A novel analytical pipeline quantifying variance in foot morphology and function using statistical shape modelling and a 26-segment foot model

Zach Martyn Stephen Welshman

Submitted in accordance with the requirements for the degree of
Doctor of Philosophy

The University of Leeds
School of Mechanical Engineering

July 2021

The candidate confirms that the work submitted is his/her own and that appropriate credit has been given where reference has been made to the work of others.

Acknowledgements

I would like to thank the patients who make such research possible and the EPSRC who financially supported my PhD.

I would like to thank everyone who helped me to complete this project. In particular my supervisors Professor Anthony Redmond, Dr Claire Brockett, Dr Michael Backhouse and Dr Graham Chapman. Additionally, Dr John Arnold who helped with data collection in the gait laboratory and Dr Carole Burnett in the acquisition of medical images.

Abstract

The aim of this thesis is to outline an approach applying a statistical shape model and developing a 26-segment patient specific foot model to identify relationships between foot posture and function. The premise of structural and functional variance between different foot arch types exists, however an analytical pipeline using segmentations from medical images integrated into a 26-segment multi-body foot model capable of computing foot function could help address the gaps in knowledge. The proposed method aims to answer questions applied to extremes of foot posture. Knowledge around variance in position and morphology between foot postures is answered using a statistical shape modelling approach to bones of the hindfoot, midfoot and medial ray. Further knowledge relating to motion of the medial ray joints including ankle plantarflexion, subtalar eversion, talonavicular dorsiflexion, talonavicular abduction, talonavicular eversion and first metatarsophalangeal dorsiflexion is generated. The thesis was constructed to enable academics and researchers to apply similar, musculoskeletal modeling pipelines to the foot and ankle in future, and for clinicians to build upon these preliminary findings between foot postures to describe clinical populations using a larger number of patients. Using variations in extremes of foot postures, the thesis shows empirical positional shape differences between high and low arch foot types comparable to the clinical notion of medial longitudinal arch being a significant contributing factor to variance. In addition, subtle morphological differences were also present for each of the bones analysed. Using statistical parametric mapping, the thesis further shows kinematic differences at each of the medial ray joints analysed demonstrating the sensitivity of the 26-segment model to variance in foot postures. The significance of this thesis is in combining two modeling approaches to understand and start to quantitate the relationship between foot structure and function, where flat, normal and high arch foot types showed systematic differences.

Table of Contents

List of Tables

List of Figures

List of Abbreviations

1D – One dimensional

3D – Three dimensional

3DMFM – three dimensional multisegment foot model

ABT – AnyBody Technology

ACL – Anterior cruciate ligament

AMMR – Anybody managed model repository

AMS – Anybody modeling system

AMTI – Advanced Mechanical Technology Inc

C3D – Co-ordinate 3 dimension

CAST – Calibrated anatomical systems technique

cm – Centimetre

CoM – Centre of mass

CT – Computerised tomography

DICOM – Digital imaging and communication in medicine

DL – Deep learning

FOV – Field of view

FPI – Foot posture index

GM – Glasgow-Maastricht

GPA – Generalised Procrustes analysis

Hz – Hertz

IDE – Integrated development environment

IC – Inter condylar

ISB – International society of biomechanics

IM – Inter-malleolar

kg – Kilogram

LC – Lateral condyle

LM – Lateral malleolus

MC – Medial condyle

ML – Machine learning

MM – Medial malleolus

mm – Millimetre

MRI – Magnetic resonance image

MR – Magnetic resonance

MSK – Musculoskeletal

N – Newtons

NRRD – Nearly raw raster data

OA – Osteoarthritis

PC – Principal component

PCA – Principal component analysis

PD – Proton density

PDM – Point distribution model

RBF – Radial basis function

REC – Research ethics committee

RoM – Range of motion

RSS – Robust statistical segmentation

SCS – Segment co-ordinate system

SSM – Statistical shape model

STA – Soft tissue artefact

STJN – Subtalar joint neutral

STL – Standard tessellation language

TE – Time to echo

TR – Repetition time

TT – Tibial tuberosity

VST – Vicon skeleton template

VTK – Visualisation toolkit

Chapter 1 Introduction

1.1 Introduction

The structure of human foot posture varies substantially within the general population. Variation across postural differences is typically associated with altered gait and foot kinematics and has been repeatedly identified using multisegment foot models (Hunt and Smith, 2004; Cobb et al., 2009; Levinger et al., 2010; Saraswat et al., 2014; Buldt et al., 2015; Caravaggi et al., 2018; Kruger et al., 2019). Dynamic measures of the foot such as plantar pressure loadings have been linked to differences between foot types (Burns, Crosbie, et al., 2005; Hillstrom et al., 2013; Buldt et al., 2018) and neuromuscular imbalances have also been noted (Burns, Redmond, et al., 2005). Variations from normal in foot types are often described as either low or high arched, low arch foot types have been reported to have a fallen medial longitudinal arch with hindfoot valgus, while high arch foot types have a characteristically increased arch with hindfoot varus (Franco, 1987; Ledoux et al., 2003; Kim, 2017). A high arch foot type has links with overuse injuries in long endurance athletes as described by Burns, Keenan, et al., (2005), similarly lower extremity overuse injuries have also been associated with low arch foot types as found by Kaufman et al., (1999). Despite literature highlighting gross structural differences between foot types and indicating risk factors, kinematic differences between opposite ends of a foot posture spectrum are not reported consistently within the literature.

Capturing, quantifying, and exploring variation between shape and function is not a new phenomenon, however, progression in understanding has been limited mainly because it is difficult in a complex structure like the foot to capture the level of detail required to answer questions linked to foot structure and function between low and high arch foot types. The use of state of the art medical imaging techniques has been able to quantify

systematic variations in positional and shape anatomy within human organs including bones, deep brain structures, cardiac structures and soft tissues such as the kidney, liver and the prostate (Heimann and Meinzer, 2009; Bowes et al., 2015). Medical image based shape analysis algorithms have been particularly successful with bones and have established relationships between anatomical features of the hip bones and the onset, incidence and progression of osteoarthritis (Lynch et al., 2009; Waarsing et al., 2010; Lindner et al., 2013). However, relative to other bones within the body, literature on the shape analysis of bones of the foot is limited, and there is a particular deficit of discourse focusing on characterising differences between discrete populations (Melinska et al., 2015; Telfer et al., 2016; Melinska et al., 2017; Moore et al., 2019). Although, more recently of general statistical shape modelling (SSM) of foot bones have been developed (Grant et al., 2020; Krähenbühl et al., 2020).

For many years functional biomechanical analysis has been used to help understand motion of bones and forces of joints within the body as reported by Leardini et al., (2017). Clinically, this approach has been a key functional measure of success for orthopaedic interventions and has enabled stratification of populations with specific diseases, such as osteoarthritis within the hip. Biomechanical hip models have been used for investigating total hip replacements (Manders et al., 2008) and other research has distinguished alterations in gait associated with leg length inequalities after total hip replacement (Renkawitz et al., 2016). Further within the knee, biomechanical models have been used to evaluate a subject specific modelling framework which predicts load during a total knee arthroplasty (Chen et al., 2016). Advances in musculoskeletal (MSK) modelling have allowed clinicians and researchers to advance engineering and clinical research enabling a better understanding of the biomechanics of the human body (Carbone et al., 2015).

Within MSK foot modelling, a number of clinical foot models exist, each with varying levels of complexity (Apkarian et al., 1989; Kadaba et al., 1990; Kidder et al., 1996; Leardini et al., 1999; Rattanaprasert et al., 1999; Carson

et al., 2001; Hunt, Smith, et al., 2001; MacWilliams et al., 2003; Simon et al., 2006; De Mits et al., 2012; Saraswat et al., 2012; Oosterwaal et al., 2016) and each with a specific application or target towards capturing ‘normal function’ or pathological variation. The complexity of dynamic foot models can arise from several attributes of MSK modelling including the number of bones used to define the model and the definition of the axis of rotation of the bone segments. Further complexity is added when computing inverse dynamics where muscle and joint reaction forces are calculated, or pressure data is used to distribute kinetic forces to individual bone segments. In addition computational biomechanical foot models have been used to capture differences between specific foot types (Hunt and Smith, 2004; Cobb et al., 2009; Levinger et al., 2010; Saraswat et al., 2014; Buldt et al., 2015; Caravaggi et al., 2018; Kruger et al., 2019), which has helped with the development of understanding the natural motion of the foot and identifying strata within pathological foot populations and which has subsequently helped with targeting and developing more appropriate treatments.

The overarching aim of this thesis is to use advanced image acquisition and processing techniques to analyse variance in position and morphology within the foot and then link motion analysis data. The focus is on comparing differences between low and high arch foot types using a statistical shape modelling approach. A novel outcome of this work is to identify principal modes of variation in shape and morphology targeting the medial ray bones; this will be achieved with a multi-domain and individual shape mode. Furthermore, integrating shape model bone representations into an analytical pipeline which adapts a state of the art 26-segment patient specific foot model (Carbes et al., 2011; Oosterwaal et al., 2011; Oosterwaal et al., 2016), allows new, patient specific kinematic models to be created. These patient specific foot models are aggregated based on pathology specific to foot motion including low, normal and high arch foot types. Overall, this approach provides a novel analytical pipeline to investigate the relationship between the positional and morphological characteristics and motion analysis of joints in the foot of high, normal and low arch foot types. This

approach uses statistical shape models with a detailed 26-segment foot model to understand the differences at the extremes of foot posture.

1.2 Aims and objectives

The project was broken down into work packages with specific aims and objectives. The two main aims of this thesis are i) to capture variation in position and morphology of bones in the hindfoot, midfoot and the medial ray of low, normal and high arch foot types using statistical shape modeling and ii) to model the biomechanical differences in kinematics between low, normal and high arch foot types using MSK modeling software. A schematic of the interlinkage between each work packages is detailed in Figure 1.

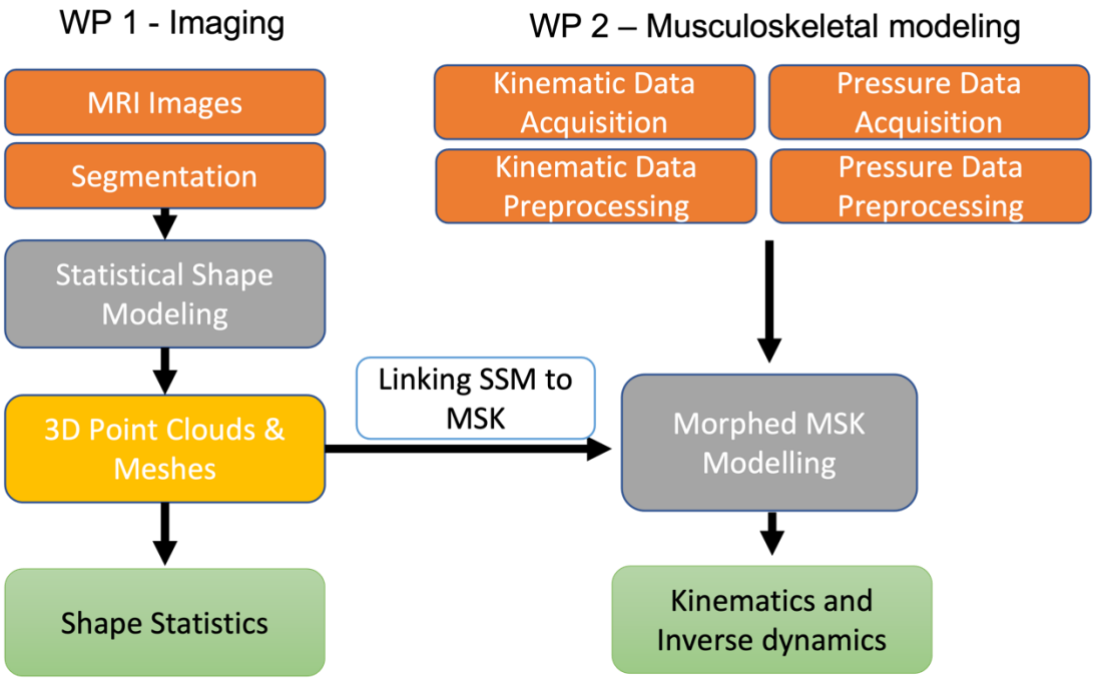

Figure 1 Describing a high-level overview of the linkage between work package 1 and work package 2 with potential derivable outputs in green.

Work package 1 – Imaging

Aims:

1) To study the relationships between overall foot type and bone shape by characterising positional and morphological changes of the talus,

calcaneus, navicular, medial cuneiform and first metatarsal in three targeted foot arch types; high, normal and low arch using statistical shape models.

2) In the context of the thesis, provide an analytical pipeline to facilitate scaling and morphing of a subject specific 26-segment multi-body foot model using 12 statistical shape models of bones including calcaneus, talus, navicular, cuboid, three cuneiforms and 5 metatarsals.

Objectives:

1) Obtain MRI images of target populations, high, normal and low arch foot types.

2) For shape analysis of the medial ray, segment MRI scans of bones including the talus, calcaneus, navicular, medial cuneiform and first metatarsal from MRI scans to develop 5 statistical shape models to infer shape characteristics between extremes of foot posture.
3) For patient specific scaling of a 26-segment foot model, segment bones including calcaneus, talus, navicular, cuboid, three cuneiforms and 5 metatarsals from MRI scans to develop 12 statistical shape models to match geometries of a patient specific foot model.

<u>Work package 2 – Musculoskeletal analysis</u>

1) The aim of this work package is to apply imaging with the statistical shape models derived from work package 1, with the addition of motion analysis data collected from the foot to develop a 26-segment model capable of modelling differences between high, normal and low arch foot types. Joint angles include ankle plantarflexion, subtalar eversion, talonavicular dorsiflexion, talonavicular abduction, talonavicular eversion, and dorsiflexion at the first metatarsophalangeal joint.

<u>Objectives:</u>

1) Obtain kinetic and kinematic data relating to high, normal and low arch foot types using detailed motion capture hardware and software applied to the foot.

2) Modify a currently available 26-segment foot model to quantify high, normal and low arch foot types. Ensure that the model can calculate ankle plantarflexion, subtalar eversion, talonavicular dorsiflexion, talonavicular abduction, talonavicular eversion and dorsiflexion at the first metatarsophalangeal joint.
   a. Output biomechanical analyses of the joint angles to determine whether the 26-segment foot model can quantify statistically relevant differences between high, normal and low arch foot types.

1.3 Software and resources

The main software and resources used in the thesis are broken down into two categories, shape analysis and dynamic multi-body foot model motion analysis. MRI scans were obtained from the NIHR Leeds Biomedical Research Centre at Chapel Allerton Hospital; ethical approval was obtained through REC reference number: 17/YH/0261. In chapter three Image data was collected and processed into segmentations, using 3D Slicer (Kikinis et al., 2014) and specifically the robust statistical segmentation (RSS) algorithm developed by Gao et al., (2012).

In chapter four Segmented images were processed into a SSM model using ShapeWorks v 6.1 (Cates et al., 2017) software developed at the University of Utah (https://github.com/SCIInstitute/ShapeWorks). In chapter five an aspect of sensitivity testing associated with point correspondence MeshLab software (2012.12) (P. Cignoni, M. Callieri, M. Corsini, M. Dellepiane, F. Ganovelli, 2008) was used to pick points on the surface of the mesh.

In chapter six the multibody-modeling software used to measure biomechanical analysis used AnyBody Managed Model Repository (AMMR) version 1.6.6 and complementary modelling Integrated development

environment (IDE) with the (AnyBody Modelling System (AMS). From the AMMR the specific foot model used was the Glasgow-Maastricht (GM) foot model (Oosterwaal et al., 2011; Oosterwaal et al., 2016).

1.4 Thesis overview

Chapter two is a literature review providing background materials on the bones of the foot, the medial ray, and on clinically observed variation between low and high arch foot types. An overview of statistical shape modelling with applications to pathologies and variance between low, normal and high arch foot types considering the talus, calcaneus, navicular, medial cuneiform and first metatarsal is provided. Clinical foot gait analysis is discussed in addition to multisegment foot modelling, with a focus on kinematics at the ankle, talonavicular and metatarsophalangeal joints of low and high arch foot types.

Chapter three outlines patient data capture and processing techniques, starting with medical image acquisition and detailing a segmentation method. Also detailed is the motion capture reflective marker labelling template for the 26-segment GM foot model and gait laboratory set-up.

Chapter four describes low, normal and high arch foot types and the process for constructing statistical shape models of the bones. A study on shape analysis differences for the medial ray bones as a multi-domain and individual statistical shape model including the talus, calcaneus, navicular, medial cuneiform and first metatarsal is detailed. In addition, this method is applied to 12 bones including the calcaneus, talus, navicular, cuboid, three cuneiforms and 5 metatarsals for the purposes of scaling and morphing the 26-segment foot model.

Chapter five describes the refinement of the GM foot model into a 26-segment foot model with the addition of a new virtual gait laboratory and pressure collection method. Furthermore, sensitivity studies are set out to compare the current scaling methodology with two alternatives, a manual point correspondence and an automatically generated point correspondence derived from the statistical shape model. In addition, a small sensitivity study

was carried out comparing the kinematics of 3 subjects, one low, high and normal arch type participants to capture differences in the kinematics and interpolation of the pressure data being incorporated into the 26-segment foot model foot.

Chapter six contains a kinematic study on thirteen subjects from low, normal and high arch foot types and a statistical parametric mapping analysis of joints including ankle plantarflexion, subtalar eversion, talonavicular dorsiflexion, talonavicular abduction, talonavicular eversion and first metatarsophalangeal dorsiflexion.

Chapter seven is an overall discussion of the work and conclusions drawn from the results and suggestions for future work are offered.

Finally, Appendix A details a graphical comparison of joint outputs available from the GM foot model aggregated by low, normal and high arch foot types and Appendix B contains a table of summary information of joints from the 26-segment foot model.

Chapter 2 Literature Review

2.1 Clinical need

Across the general population, foot shape varies significantly as do many biological characteristics associated with foot type and function. The structure and position of the bones within the foot form the global foot architecture and results in a spectrum of foot postures ranging from pes cavus (high arched) through neutrally aligned (normal arch), and pes planus (low arch). Due to the interconnected nature of structures in the foot and ankle, each type of foot has specific visible and functional features. These different characteristics contribute to different plantar loading patterns, as can be seen clinically or through technological approaches such as pressure distribution from pressure mat equipment as described detailed by Hillstrom et al., (2013). Low arch deformities can present as congenital or acquired, flexible or rigid, adult or paediatric. A severe adult acquired flatfoot deformity can be commonly caused by posterior tibial tendon deficiency (Kohls-Gatzoulis et al., 2004). Typical characteristics of low arch feet can include a supple midfoot with heel valgus (Shibuya et al., 2010). At the opposite end of the hypothetical spectrum, a high arched foot presents itself as stiff through the mid foot with an inward pointed heel in a varus position (Hillstrom et al., 2013). Visible differences can be seen between these characteristic foot types in Figure 2 with the most obvious observation being the height of the mid-foot relative to the ground.

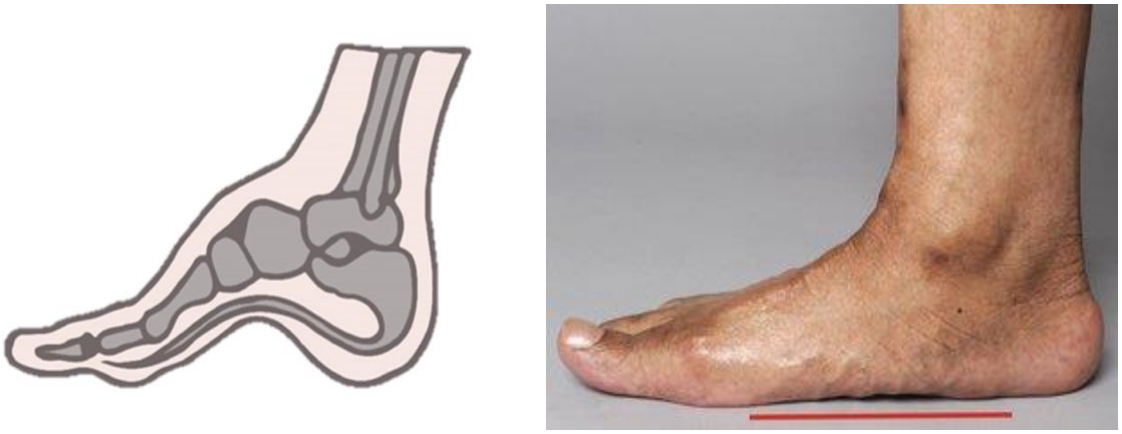

Figure 2 Showing a high-arched (pes cavus) foot type (left) accessed from https://www.kentcht.nhs.uk/wp-content/uploads/2016/12/Forefoot-equinus-00998-v3.pdf and a flatfoot (pes planus) foot deformity (right) accessed from https://www.nhs.uk/conditions/flat-feet/

2.1.1 Classification of foot type

There are several ways to perform static lower extremity measurements to classify the foot (Razeghi and Batt, 2002) and more recent 1D – convolutional neural networks have been used to classify cavus, normal and planus foot types (Mei et al., 2020). Even with many measurement methods, little research exists to support the correlation between static measurements and dynamic foot function. The difficulty in comparing static measurements with dynamic function lies in the complex anatomical make-up of the foot and how the bones in the foot move during the gait cycle. Notably, measurements such as subtalar joint neutral (STJN) introduced as a theory by Root et al, have been used historically and are presently taught in educational settings (Landorf et al., 2001). STJN is used as a means of finding the neutral position to characterise morphology and biomechanical function. However, the validity of this approach has been questioned (Jarvis et al., 2017). The Foot Posture Index (FPI) developed by Redmond, (2005) is a tool that has been used clinically and is a foot measurement score that has normative values against which variation in population foot structure has been compared (Redmond et al., 2008). Although the FPI score has

reference values and is used in routine clinical practice, it has limitations in the sensitivity to small changes in foot bones. The FPI is adequate for classifying overall foot structure and type, but data informing the contribution of the subtle changes occurring in individual structures is sparse, limiting a more detailed understanding.

2.2 Foot and ankle complex

2.2.1 Bones

The human foot consists of twenty-six bones and thirty-three joints including the tibia and fibula (Gray, 1918), shown in Figures 3 and 4. The complex geometry of the foot allows both stability and sufficient mechanical leverage to facilitate walking or running.

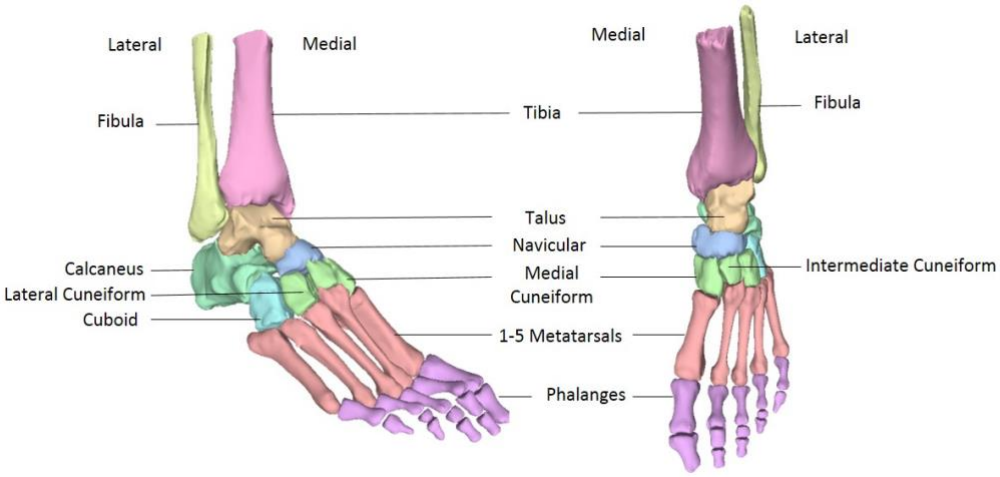

Figure 3 Showing bones of a non-weight bearing foot and ankle. Created in MeshLab with segmented MRI scans

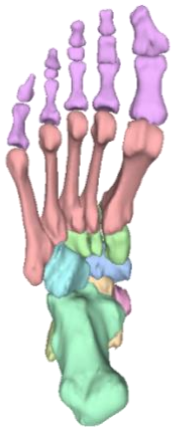

Figure 4 Showing bones of the foot from an inferior view

2.2.1.1 Hindfoot

The human hindfoot, which is typically defined as the calcaneus and talus, but can include the navicular, is usually first part of the foot to make contact with the ground while walking. The role of the calcaneus is to provide leverage from the superior gastrocnemius muscle via the Achilles tendon. Sitting superior is the talus, which transmits forces between the tibia in the lower leg and the rest of the foot. Both calcaneus and talus have an irregular shape with several bony prominences and grooves on their surface to allow for load transfer through muscles and tendons. In high arch foot types hindfoot varus and forefoot adduction has been noted (Aminian and Sangeorzan, 2008; Kim, 2017) and clinical manifestations of a subtle cavus foot can include chronic lateral ankle instability (Chilvers and Manoli, 2008). On the other end of the hypothesised foot posture spectrum, low arch foot populations have shown a hindfoot valgus (Franco, 1987; Ledoux et al., 2003) and clinical indications of a severe planus foot have been associated with posterior tibial tendon dysfunction (Dyal et al., 1997; Kohls-Gatzoulis et al., 2004).

2.2.1.2 Medial ray

The medial, or first ray of the foot has been defined in a number of ways within literature (Ring et al., 2019). The medial ray typically consists of the first metatarsal, medial cuneiform, navicular and talar head and makes up the medial longitudinal arch, described in the next section. As characteristics of cavus and planus foot types are predominately along the medial ray it is assumed that the greatest difference in bone position and orientation and kinematics at the joints will observed along this arch.

The specific role of the navicular is less well known; however, it plays a role maintaining the arch and transferring loads through the foot and also where the tibialis posterior attaches it aids in supporting the arch (Kohls-Gatzoulis et al., 2004). In a cavus foot, the midfoot can be measured by the pitch and the height of the navicular, where it has been observed to be ‘high’ relative to the floor (Aminian and Sangeorzan, 2008), in comparison to a planus foot where it is observed to be ‘low’ relative to the floor. The medial cuneiform is one of three cuneiforms that are a found in the midfoot and has shown success as a candidate in deformity correcting osteotomies (Mortimer et al., 2020) due to its role in rotating the forefoot.

The first metatarsal resides distal to the medial cuneiform and has a role in creating an arch and providing ligament and tendon insertion points, which generate leverage for muscle forces and support weight bearing. In cavus foot types, the first metatarsal has been perceived as one of three main contact points on the ground along with the calcaneus and fifth metatarsal (Schuberth and Babu-Spencer, 2009), while flat footed types have been associated with metatarsal stress fractures (Simkin et al., 1989).

2.2.2 Arches of the Foot

Conceptually, the foot has a series of structural arches that help support the weight of the body in a standing position. The arches are formed by the tarsal and metatarsal bones and strengthened by the surrounding ligaments and tendons. The arch of the foot can be sub-divided into medial arch, see

Figure 5 and lateral arch, see Figure 6 and runs anteriorly from the calcaneus to the base of the metatarsals on each side of the foot. The medial arch is made up of the calcaneus, talus, navicular and medial, intermediate and lateral cuneiforms with the first, second and third metatarsals (Gray, 1918).

The main purpose of the medial arch shown in Figure 5 is elasticity, which is due to the height and number of small joints between the bones. This elasticity contributes to a proposed ‘windlass mechanism’ of the foot described by Hicks, (1954) which allows bones in the medial ray to vary in rigidity and optimise energy efficiency during forward propulsion.

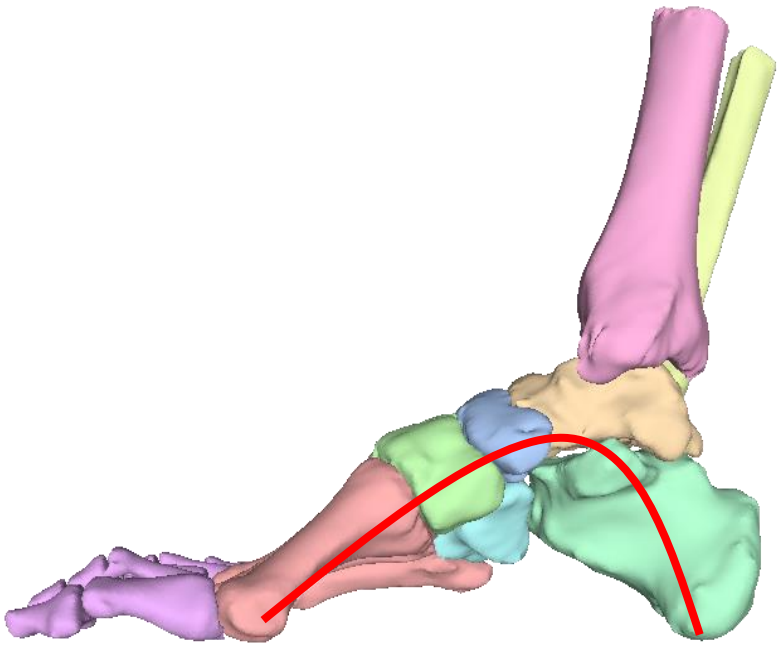

Figure 5 Showing the medial arch indicated in red with bones of the foot Created in MeshLab with segmented MRI scans from Imorphics

The lateral arch, shown in Figure 6, is less obvious than the medial arch and is composed of the calcaneus, cuboid and fourth and fifth metatarsals. It starts at the talcocancaneal joint and runs through the calcaneocuboid joint, which can lock and prohibit movement. This arch is supported by the long

plantar and plantar calcaneocuboid ligaments with the extensor tendons. Both the medial and lateral arches contribute to the longitudinal arch which is made up by the calcaneus, cuboid, third cuneiform and third metatarsal (Gray, 1918).

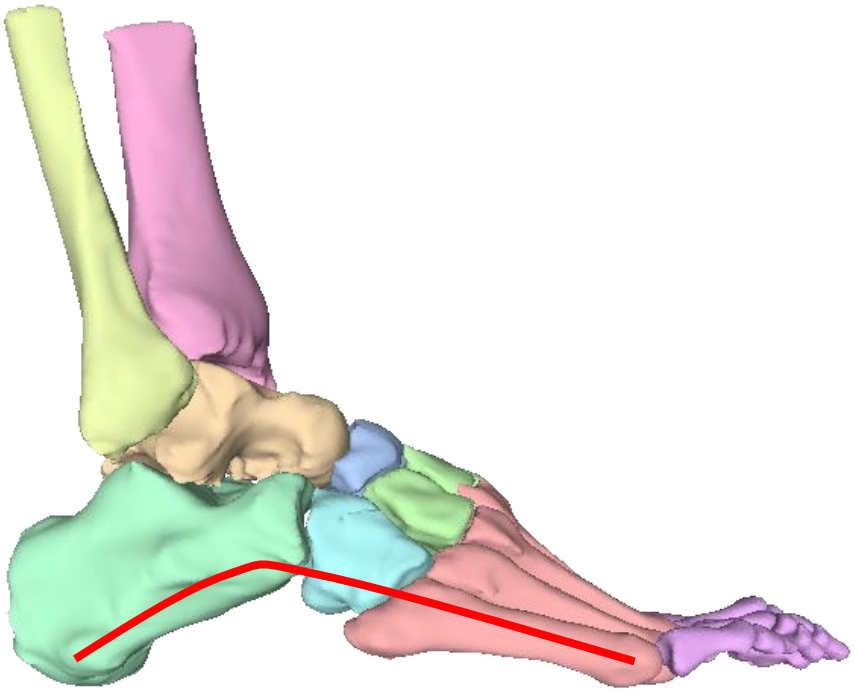

Figure 6 Showing the lateral arch indicated in red with bones of the foot, created in MeshLab with segmented MRI scans from Imorphics

The transverse arch runs perpendicular to the longitudinal arch and is formed by the shape of the anterior of the three cuneiforms and cuboid shown in Figure 7, which run to the head of the five metatarsals.

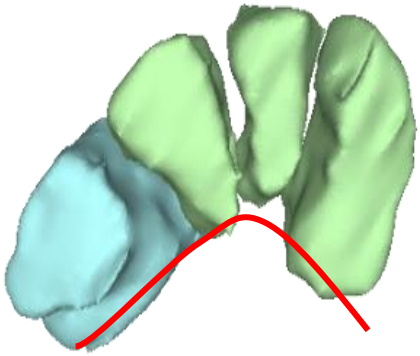

Figure 7 Transverse axis indicated in red through an anterior-posterior view of the three cuneiforms and cuboid bones, created in MeshLab with segmented MRI scans from Imorphics

The lateral, medial, transverse tarsus and metatarsus arches can be seen in Figure 8 and form a triangular structure from an inferior view of the foot

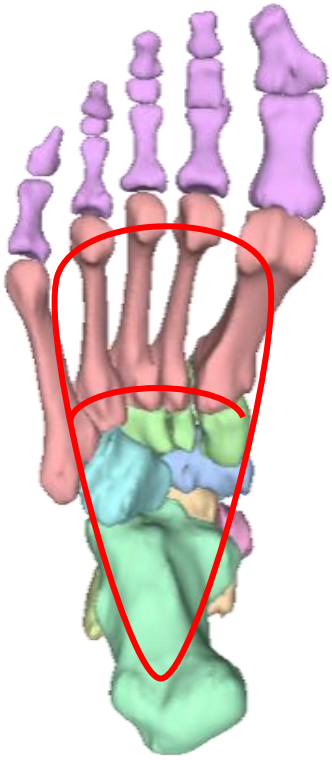

Figure 8 Showing medial, lateral and transverse arches from an inferior view of the foot, created in MeshLab with segmented MRI scans from Imorphics

In all foot types, medial, lateral and transverse arches can be measured to help classify the foot. Morphological differences between high and low arch foot types can be visually striking. Figure 9 (left) shows a mediolateral radiograph of a left pes cavus foot. Changes along the medial ray of a high arch foot type from the calcaneus through to the head of the first metatarsal show a visibly higher arch when comparing the same bones of a right pes planus, see Figure 9 (right) in a mediolateral view.


Figure 9 Mediolateral radiograph of pes cavus. Source: https://radiopaedia.org/cases/pes-cavus (left) Mediolateral radiograph of pes planus. Source: https://radiopaedia.org/cases/pes-planus (right)

2.3 **Medical Imaging**

2.3.1 Acquisition

Multiple technologies exist for taking medical images, including CT (computerised tomography), MRI (magnetic resonance image) or X-Ray. CT scanning has been widely applied to feet in a clinical context. Within research settings, foot CT scanning has been used for a range of different static loads and foot types to capture morphology (Oosterwaal et al., 2011) and is best for capturing bones in medical imaging. Although CT scanning is faster than MRI it requires relatively high doses of ionising radiation and is not widely used in the absence of clinical reasons, MR imaging can achieve similar levels of detail for bone tissue and more detail relating to soft tissues of the foot, but with no radiation exposure for the patient. Long image scanning durations present challenges, for example the foot must be kept

still to avoid image artefact, as the foot is a distal body part this can be difficult to achieve. To mitigate image artefact and increase fidelity, specific foot coils have been created to increase image resolution and keep the foot relatively stable improving image quality. MRI has also been shown to be effective in diagnostic imaging of MSK disease (Sharma et al., 2018), diabetic foot disease (McCarthy et al., 2017), and also analysing foot deformities (Winfeld and Winfeld, 2019) and is the most common modality when capturing images of the foot to identify ligamentous or tumorous tissue (Hughes et al., 2019).

2.3.2 Segmentation

Segmentation can be described as the separation of the image background from the foreground to extract regions of interest for analysis. The process of segmenting consists of partitioning a digital image into meaningful regions which are ideally homogenous with respect to a gray-level or texture (Sonka et al., 1993c). All biomedical image software applications can transform a raw image such as CT, MRI or X-Ray into binary segments. Segmentation methodologies are plentiful and can involve filtering, thresholding and more complex techniques (Oliveira and Tavares, 2014). In medical imaging, segmenting regions of interest from a set of MRI scans is a difficult task. The difficulty in segmenting images comes from defining what is important in an image and what can be discarded (Sonka et al., 1993b). Segmentation techniques can be divided into 3 groups; global knowledge which is, firstly, histogram based and uses thresholding techniques, secondly edged based segmentations which mark the edges of an object and are results of large differences in grey-level colour and texture, the most common problems of this type of segmentation is caused by image noise (Sonka et al., 1993a). Thirdly, region-based segmentations are better suited to images containing noise and where the grey-scale values drop off relative to the seed points in the initialisation are difficult to detect. In region-based segmentations the main aim is to divide the image into areas of homogeneity which can be based on grey-level, texture, colour, shape etc. All three forms give slightly

different information - edged based and region-based results can be combined depending on the important features required of the segmentation.

2.3.3 Statistical shape models

Statistical shape models (SSM) are numerical descriptors of geometric properties for a class of objects. Within SSMs the mean and variance are used to determine the average shape and distribution of instances of all other shapes. The location of a shape instance within a population is determined by how the shape model represents features of variance of the population; such features in bone shape analysis may include anatomical elements on the bones. The need for clinical experts to build high-quality SSMs involves manual generation of the ‘ground truth’ data and is currently an essential task for humas to solve. Presently, automation of these segmentation tasks are challenging given how SSM algorithms rely on manual segmentations to generate models, in addition while semi-automated methods exist, they still require human-in-the-loop approaches to ensure that spurious areas of the medical image have not been included in the final segmentation. When there are fewer ground truth data examples, the clinical appropriateness degrades, and segmentation error is more likely. In the context of medical imaging, a shape model is required to fit a shape instance through a process involving super imposition. This is typically done using Procrustes analysis, which results in a definition of the characteristic shape variance of the shape instance in relation to the class of shape instances being analysed. This type of analysis is usually carried out for shape representation (van de Giessen et al., 2010; Vincent et al., 2010; Lu and Untaroiu, 2013; Neogi et al., 2013). This is most useful where organs have been segmented and a class of objects with identified labels such as a pathologic shape or healthy shape can be quantified for statistical differences, known as a supervised learning approach.

Generating a SSM typically follows the workflow shown in Figure 10. Data is acquired as pixels, or a volume, through segmentation, which are converted into binary images. Literature discussing SSMs, in particular point

distribution models (PDM) described by Cootes et al., (1995), optimise a set of corresponding points on the boundaries, or surfaces of shapes. This approach has merits, as it is easy to assign points to surfaces aligned based on their centre of mass (CoM), however in three dimensions a manual approach to achieving correspondence, especially on irregular human anatomy is challenging. PDM's have shapes aligned based on their CoM which allows corresponding points between shapes to be processed through an alignment process to a common reference shape. The most popular method of alignment is Generalised Procrustes Analysis (GPA) (Goodall, 1991 and Dryden and Mardia, 1998). GPA aims to minimise the mean squared distance between shapes.

Figure 10 is a schematic representation of a general workflow for constructing a statistical shape model. It represents the general approach to creating models and a more specific approach to capturing anatomical variation between shapes anatomy relating to patients. Shape and density distribution of bones are obtained by adding contributions of principal modes of variation to the average shape or bone density.

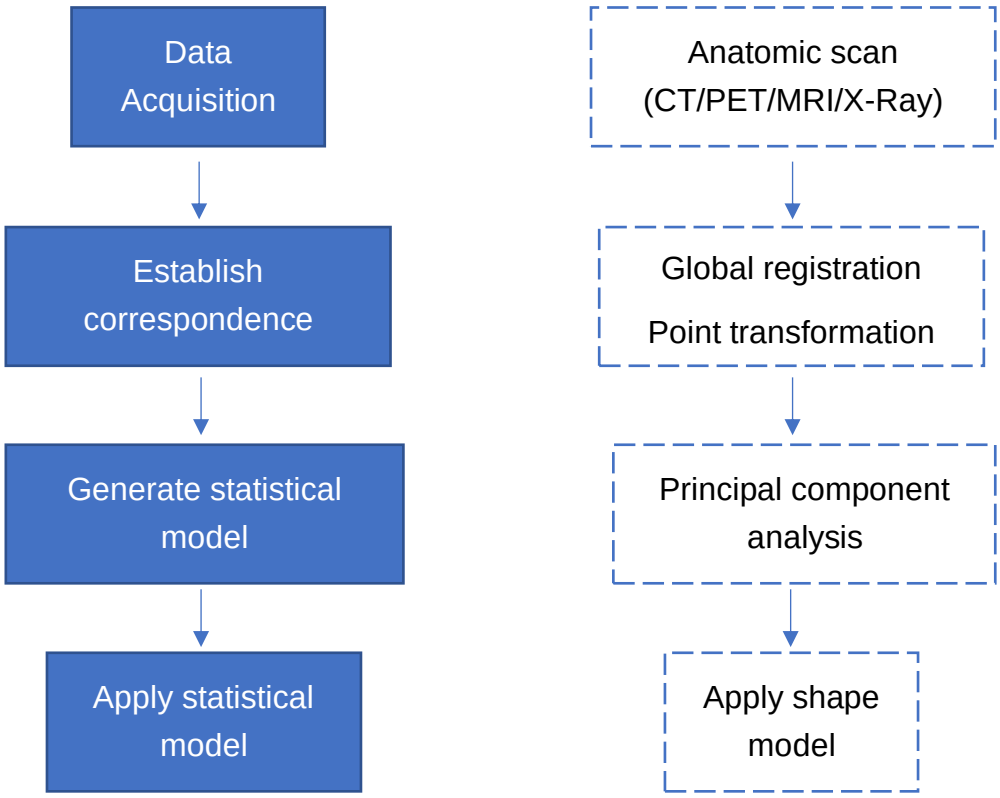

Figure 10 Showing a typical framework for generating a statistical model from population data (left) and applied for tissue morphology (right) adapted from Bischoff et al., (2014)

In orthopaedics, statistical models have been applied to quantify changes in bone morphology. For example in the hip, to measure geometric variation between those with osteoarthritis (OA) and asymptomatic age-matched participants reported in Groves, (2015). In the knee, SSMs have been used to measure shape of distal femurs with OA from radiographs to predict the onset of the disease (Neogi et al., 2013) and also in the knee for identification of specific risk factors for anterior cruciate ligament (ACL) injury using MRI (Pedoia et al., 2015). Interestingly, shape analysis has revealed differences in different ethnic groups and also differences between genders within the same ethnic region as described in Mahfouz et al., (2012).

2.3.4 Statistical shape models of the foot and ankle

Due to the complexity of the bones in the foot and ankle there have been a limited number of statistical shape models developed. Such models include those made up of bones or multiples of bones (Melinska et al., 2015; Telfer et al., 2016; Melinska et al., 2017; Moore et al., 2019; Krähenbühl et al., 2020). SSM's have also been developed with aggregated functional segments (Grant et al., 2020). Of these studies a small number focus on the morphological differences between low and high arched foot types (Telfer et al., 2016; Moore et al., 2019) demonstrating limited literature that analyses morphological variance between foot postures.

2.3.4.1 Calcaneus

Work carried out by Melinska et al., (2015) and Melinska et al.,(2017) detailed methods of unifying anatomical features of the cuboid, navicular and talus bones using spherical harmonics. Others have looked at principal component analysis (PCA) based models of bones in the hind foot (Moore et al., 2019; Krähenbühl et al., 2020) to analyse variance between foot types and within a general population. Of those that have researched morphological differences using PCA based techniques (Moore et al., 2019; Krähenbühl et al., 2020), few have aimed to describe morphological variation between foot pathologies (Moore et al., 2019).

Krähenbühl et al., (2020) studied hindfoot bones of twenty-seven asymptomatic healthy individuals to determine a baseline for which pathological foot types could be compared. They found the calcaneus first mode of variation (accounting for approximately 24% variation) to relate to an increased anterior-posterior length, corresponds to a decrease in calcaneal pitch. In addition, the first principal component (PC) had an increased slope of the posterior facet articulating surface within the subtalar joint and increased prominence of the lateral and medial processes of the calcaneal tuberosity. Similarly and targeted towards variance in foot type

and sex, Moore et al., (2019) with a population of 40 participants (23 male : 17 female), found 38% variance captured by the first two components. The first PC (21.3% variance) coincided with variation along the height and length of the calcaneus and showed the low arch foot type to have decreased height and increased length. PC 2 described by Moore et al., (2019), accounting for 16.4% variance, represented changes to the height and width of the bone. Neutrally aligned feet were statistically different to low arch feet, as neutral feet had higher scores implying anatomical features of increased height and decreased width.

2.3.4.2 Talus

The first two PC's of the talus bone described in Krähenbühl et al., (2020) account for approximately 30% of variation. They found the first PC described approximately 16% variance and could be attributed to the presence and absence of the talar posterior process prominence. The differences in the second PC included the radius of curvature for the posterior facet. Moore et al., (2019) found the first two PC's describe 33% variance but did not report the anatomical importance as this feature was not statistically relevant between the groups. In addition, Moore et al., (2019) described the high-arched group with extended lateral and medial tubercles and also noted bony prominences on the posterior talus in the cavus group compared to neutrally aligned feet.

2.3.4.3 Navicular

Navicular drop has been identified as a feature of flat foot populations by Caravaggi et al., (2018) and could have relevance to the medialised talar head altering the loading of the navicular bone. The higher relative position of the navicular tuberosity in cavus feet has been clinically observed by Kim, (2017). Moore et al., (2019) reported 35% variance captured by the first two PC's in the navicular bone. PC 1 was aligned with the width and height and significant difference were found between low and normal arch foot types. The anatomical relevance of the second PC was not reported.

2.3.4.4 Metatarsals

In five separate SSM's of the five metatarsals bones derived from 65 CT foot scans, Telfer et al., (2016) hypothesised that significant differences would exist in 3D metatarsal geometry between foot type and sex. Mean shape and PC's that contribute to the geometric differences of metatarsal bones were presented by Telfer et al., (2016) and showed all metatarsals to have significant shape differences ($p<0.01$) including pes cavus, neutrally aligned, symptomatic and asymptomatic pes planus foot types. Despite conceptual consensus that most variation between foot types occur along the medial ray of the foot, Telfer et al., (2016) was not able to confirm this theory as the study only consisted of individual metatarsal bones. However, the first metatarsal PC 1, described approximately 30% variance, was related to frontal and sagittal plane cross-sectional area, while PC 2 described approximately 12% variance aligned with the sagittal angle of the distal and proximal heads.

Shape analysis of all bones that make up the medial ray of the foot would be required to determine the principal modes of variation in cavus and planus foot types, to date studies have considered the hind foot separately to the midfoot for statistical shape modeling of flat and high arch foot populations. Further no studies have compared a combination of hind and midfoot bones of patients between low, normal and hight arch foot types, highlighting a significant gap in the literature. In addition, studies are focused on morphological variance using Generalised Procrustes Analysis between bone shapes and fail to confirm the primary hypothesized positional variance concerning the medial ray of the foot.

2.4 Clinical gait analysis

Gait analysis is a scientific method used to capture information to observe and record objective parameters of human gait (Mayich et al., 2014). By comparing relative motion of body parts, clinicians can better assess the motion of bone segments relative to one another, for example how the calcaneus moves in relation to the tibia, or the proximal phalanx moves in

relation to the first metatarsal and decide on an appropriate treatment pathway for the patient (Lobmann et al., 2001). Gait analysis for the foot is less well defined, but when implemented as part of the clinical treatment pathway can provide basic information on the movement of the hind, mid and fore foot (Carson et al., 2001). Although whole foot evaluation has been well established, motion analysis of individual bones has been less successful due to the limitation of motion capture systems and skin surface makers being placed on a patient's foot.

Gait analysis is sub-divided into *phases, periods* and *events* to isolate different aspects of the gait cycle. The gait cycle consists of a stance phase and a swing phase, where the stance phase makes up approximately 60% of the gait cycle and the swing phase the remaining 40 %. Within these phases are periods with identifiable events.

During the stance phase the lower extremity and pelvis rotate and translate over the weight bearing foot. In this phase the foot goes through three events, heel strike as seen in Figure 11 A, mid-stance as seen in Figure 11 B/C, and toe-off as seen in Figure 11 D. During heel strike or the first 'rocker', the dorsiflexor muscles contract eccentrically and allows the ankle to transition to plantar flexion. During the second 'rocker', the tibia rolls forward over the ankle to allow for forward movement of the body, meanwhile the foot remains planted in situ. During the third 'rocker', the foot plantar flexes at the ankle, and the metatarsophalangeal joints dorsiflex.

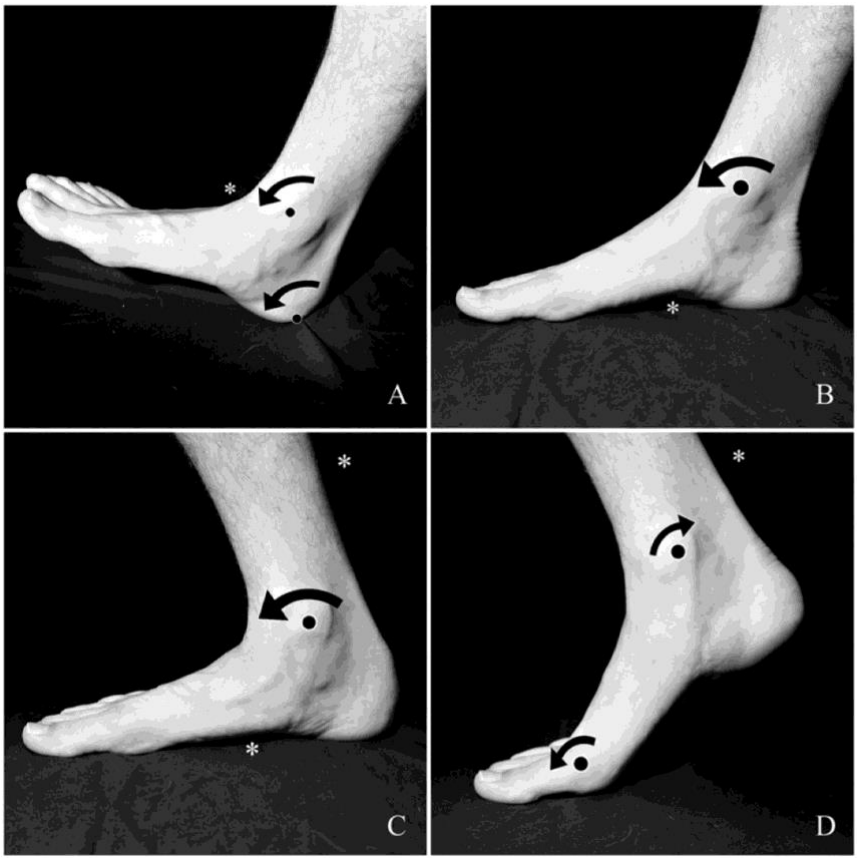

Figure 11 The 3 rockers of gait. (A) During the first rocker, the heel strikes the ground, the foot rotates around this, and the ankle joint axis to come to rest in the flat foot position. Contraction of the anterior compartment muscles* controls this motion. (B) During the second rocker of gait, the tibia is brought “up and over” the talus, rotating around the ankle joint. The intrinsic muscles of the foot and tibialis posterior fire* to maintain a medial longitudinal arch. (C) The terminal portion of the second rocker signals the powerful triceps surae to contract. (D) During the third rocker, the ankle plantar flexes over a fixed forefoot (about the metatarsophalangeal joints) ending in toe-off, initiating the swing phase of gait. Figure taken from Mayich et al., (2014)

2.5 **Foot models**

Computational dynamic foot modelling is a technique used to measure the kinematics and kinetics of the foot using gait analysis. It aims to use data collected from passive or active markers placed on the lower limb and foot with infra-red cameras installed in a gait laboratory to derive information on the relative motion of the makers. These markers are then used as a proxy for computationally derived rigid segments in the foot. Foot models vary in the number of segments used to define a foot, similarly there are different perspectives on the concept of neutral and a how to define a neutrally aligned foot as a reference point (Rankine et al., 2008; Novak et al., 2014). Foot models have been used to characterise normal functioning feet (Carson et al., 2001) and have also been explored with pathological populations (Hunt and Smith, 2004; Cobb et al., 2009; Levinger et al., 2010; Saraswat et al., 2014; Buldt et al., 2015; Caravaggi et al., 2018; Kruger et al., 2019), demonstrating the need for capturing normal and pathological foot function. This would have benefit in clinical practice; however, it is recognised that foot modelling is costly in terms of time and resource.

Capturing detailed foot mechanics is a challenge due to the complexity of the movement in the bones of the foot and the limitations of clinical gait analysis such as marker placement leading to inaccurate angular calculations, skin motion artefacts and camera set-up (Shultz et al., 2011). Soft tissue artefact (STA) in foot modeling is a well-known issue affecting kinematic outputs (Leardini et al., 2005) and in particular it has been reported that STA introduces clinically relevant error, as McGinley et al., (2009) defined at > 5 degrees in the context of reliability and refers to the variation found across repeated measures. Schallig et al., (2021) reported clinically relevant STA for the Oxford Foot Model (OFM) and Rizzoli Foot Model (RFM) models at extreme foot positions. Recently, an analysis of STA of a the GM foot model in Oosterwaal, (2016) demonstrated that the effect of soft tissue motion on marker positions ranged from 1.9 – 6.7 mm. However, the study was not able to quantify the subsequent impact on a relative marker motion during a typical walking gait cycle, as the study was static

and the foot was horizontally loaded using a specialised jig that underwent a CT scan.

Several methods have been proposed to overcome skin and STA including the use of intracortical bone pins with opto-reflective markers attached to the tip. These bone-pins are placed directly into the bones of interest and are therefore thought to track movement more accurately and are considered the gold standard (Westblad et al., 2002; Arndt et al., 2007; Nester et al., 2007; Lundgren et al., 2008). However, this method is invasive, not clinically practical and has ethical implications, although it has been useful for model validation and studies of small numbers.

Reflective markers on the foot can be combined to create biomechanical models which have been referred to as a 3D multi-segment foot model (3DMFM). These 3DMFM's range from 1 (Apkarian et al., 1989) to 26 segments (Oosterwaal et al., 2016). Classically, gait analysis considered the foot as one rigid segment connected to the shank and pivoting at the ankle joint (Apkarian et al., 1989), but more recently 3DMFM's have been developed to characterize dynamic foot kinematics *in vivo* (Kidder et al., 1996; Rattanaprasert et al., 1999; Leardini et al., 1999; Hunt, Smith, et al., 2001; Carson et al., 2001; MacWilliams et al., 2003; De Mits et al., 2012; Oosterwaal et al., 2016) and there are now multiple studies using 3DMFM's which focus on pathological differences (Hunt and Smith, 2004; Cobb et al., 2009; Levinger et al., 2010; Saraswat et al., 2014; Buldt et al., 2015; Caravaggi et al., 2018; Kruger et al., 2019). However, there is considerable variation between these models in terms of the composition of numbers of segments and number of markers used to define the coordinate systems. For example, the hind foot has been modelled as one segment composing of the calcaneus (Leardini et al., 1999; Hunt, M. Smith, et al., 2001; Leardini et al., 2007). Other hind foot models consist of the talus and calcaneus (Rattanaprasert et al., 1999; Carson et al., 2001; De Mits et al., 2012; Saraswat et al., 2012) or have the talus included in the mid foot (MacWilliams et al., 2003).

3DMFM's have been created using different approaches. For example Leardini et al., (2007) used a three segment plus shank CAST (calibrated anatomical systems technique). Clusters of markers are used to calibrate bony landmarks and a static reference trial has been used to identify a reference posture for the foot, during a walking trial segment motion can be referenced to this position. However, it has been reported that the foot may not reach anything approaching a 'neutral' position in some cases (Menz, 1995; Buldt et al., 2015). The advantage of using the CAST method is that it minimises skin motion artefact of individual markers, as previously mentioned. However, skin motion artefact is only minimised in the area the cluster of markers are placed and is subject to the area having little soft tissue. Other anatomically based methods require markers to be placed directly onto the bony prominences of the foot, for example the four segment plus shank model produced by Leardini et al., (1999). This method provides an alternative approach to describing severely deformed postures but is also more prone to skin motion artefacts.

The Oxford Foot Model (OFM) described in Carson et al., (2001) is a commonly used foot model and consists of three segments plus the shank. It defines the hind foot as the calcaneus and talus, while the forefoot segment includes cuneiforms cuboid, metatarsals and the hallux. An obvious limitation in the OFM is that motion occurring between the hind foot to mid foot and mid foot to the forefoot is not captured due to the bones being defined as groups and joint kinematics not being analysed. Although the OFM is very useful it does not provide information on intrinsic bones or subtle differences in kinematic and muscle force differences that could exist in descrete foot populations. Comparing normal and deformed foot function between multiple foot models becomes increasingly difficult when the number of segments increases. In addition, kinematic outputs of similar joint angles between models may significantly differ making kinematic motions difficult to interpret.

More complex models that capture the movement of bones in the midfoot exist (MacWilliams et al., 2003; Oosterwaal et al., 2011; De Mits et al., 2012;

Saraswat et al., 2014). Of these models the Ghent foot model (De Mits et al., 2012) has 5 segments plus the shank. The segments were constructed with the talus and calcaneus as the hind foot, the navicular cuboid and cuneiforms as the midfoot, the medial forefoot as the first metatarsal, the lateral forefoot as second through fifth metatarsals and finally the hallux. This segment configuration allows the medial ray of the foot to be evaluated which is important as energy is absorbed in this portion of the foot (Saltzman and Nawoczenski, 1995) and it is also the hypothesised area of largest difference between cavus and planus foot types. An interesting difference is the reference position used in the Ghent foot model. The reference method is to put the participant into a tandem stance with the foot of interest in front and allow the subtalar joint to remain in a relaxed position, this is different to the detailed 26-segment GM foot model which does not make use of a standing reference; this is due to the implementation and model application (Oosterwaal, 2016). MacWilliams et al., (2003) defines an 8 segment plus shank model consisting of the talus, navicular and cuneiforms as one segment, with the cuboid and calcaneus being separate segments. Interestingly, the lateral and medial forefoot were divided into two segments with the remaining three segments being the lateral toes, medial toes, and hallux. Alternatively, MacWilliams et al., (2003) considers the talus, navicular and cuneiforms as one segment, which omits motion at the talonavicular joint, which is important in normal foot function. Table 1 below shows details of foot models and the composition of segments.

This thesis aimed to create an analytical workflow that can capture the differences in movement of the small bones between foot postures using the 26-segment foot model described in chapter five.

The 26-segment model developed in this thesis is an adapted version of the model described by Carbes et al., (2011) and Oosterwaal et al., (2011) which was applied to ‘healthy’ populations in Oosterwaal et al., (2016). This model allows very detailed foot kinematics to be derived in the gait cycle as all the bones are used in the analysis, albeit only during the stance phase. However, as with all computational modelling there is usually a need to

understand how to develop models, usually thorough software to get the most out of these advanced MSK models. The benefit of being able to adapt a template computational foot model opens the possibilities for developing the modelling simulations in ways that are more specific for clinical use cases or, as in this thesis to develop the capability of foot model for detailed analysis and comparison of potential pathologies. This is especially pertinent where patient specific foot models are being developed, for example incorporating individual patient bones in a dynamic foot model simulation, which can lead to a more personalised understanding of the patient.

Table 1 Showing foot models that measure foot dynamics with the number and name of segments

Model	Number of segments	Segments
Helen Hays (Kadaba et al., 1990)	1 plus shank	Shank Foot
Apkarian et al. (Apkarian et al., 1989)	1 plus shank	Shank Foot
Rattanaprasert (Rattanaprasert et al., 1999)	3 plus shank	Shank Hind foot: calcaneus Forefoot (MT1 base and head, MT2 head) Hallux: proximal phalange
Hunt (Hunt, Smith, et al., 2001)	2 plus shank	Shank Rear Foot: calcaneus FF (MT5 base and head MT1 head)

Milwaukee (Kidder et al., 1996)	3 plus shank	Shank Hind foot: calcaneus, talus, navicular Forefoot: cuboid, cuneiforms metatarsals Hallux: proximal phalange
Carson (Oxford) (Carson et al., 2001)	3 plus shank	Shank Hind foot: calcaneus and talus Forefoot: metatarsals Hallux: proximal phalange
Leardini (Leardini et al., 1999)	4 plus shank	Shank Hind foot: calcaneus and talus Midfoot: navicular, cuboid and cuneiforms Forefoot: metatarsals
De. Mitts (Ghent foot model) (De Mits et al., 2012)	5 plus shank	Shank Hind foot: calcaneus and talus Midfoot: navicular, cuboid and cuneiforms Medial forefoot: first metatarsal Lateral forefoot: 2-5 metatarsals Hallux: proximal phalange

McWilliams(MacWilliams et al., 2003)	8 plus shank	Seg 1: talus, navicular and cuneiforms Seg 2: cuboid Seg 3: calcaneus Seg 4: lateral forefoot Seg 5: medial forefoot Seg 6: lateral toes Seg 7: medial toes Seg 8: hallux
Saraswat (Saraswat et al., 2012)	3 plus shank	Hind foot: calcaneus Forefoot: base of MT1 head of MT1, head of MT5 Hallux: proximal phalange

2.5.1 Normal foot kinematics

Determining a baseline from which pathological populations can be compared is a challenge in foot biomechanics, due to the plethora of methodological designs and metrics reported. Literature on normal foot kinematics exists for different joints but varies by joint definition i.e., reference frames.

2.5.1.1 Ankle joint

Ankle joint kinematics can be measured by comparing the talus to the tibia (Simon et al., 2006; Arndt et al., 2007; Nester et al., 2007; Lundgren et al., 2008), calcaneus to the tibia (Arndt et al., 2007; Nester et al., 2007; Lundgren et al., 2008; Oosterwaal et al., 2016), calcaneus to the talus (Arndt et al., 2007; Nester et al., 2007) and the hind foot described as the combined

talus and calcaneus to the lower leg (tibia and fibula) (De Mits et al., 2012). As the measurement of these joints differs between studies comparison between them is possible, but the interpretation is challenging.

Sagittal plane – plantarflexion/dorsiflexion

Oosterwaal et al., (2016) reported excursion of 17° in ankle plantarflexion/dorsiflexion in healthy participants. Results from *in vivo* studies De Mits et al., (2012) and Simon et al., (2006) showed a mean RoM (SD) of 11.8° (4.44); 22.2° (1.8) respectively. MacWilliams et al., (2003) who studied kinematics of adolescent gait reported a mean range of motion (RoM) of approximately 15° (results derived from a graph). An *in vitro* cadaver study by Nester et al., (2007) showed a wider mean RoM of 23.9° (8), and bone pin study Lundgren et al., (2008) showed a mean RoM of 17.0° (2.1), however the small sample size of six participants reduced the study power. Two cadaver studies, Simon et al., (2006) and Nester et al., (2007) had 10 and 13 participants respectively and showed higher RoM's compared to *in vivo* studies, however forces applied in cadaver studies are difficult to validate due to the invasive nature. Simon et al., (2006) had a target population of elderly females who demonstrated less static RoM, similar to younger participants reported by Nigg et al., (1992). However, MacWilliams et al., (2003) studying a target population of adolescent feet reported results contradicting the notion of reduced flexibility in elderly populations. Discrepancies in reported mean RoM are challenging to compare directly, due to different methodologies being applied between studies. Therefore, general comparisons of reported results would be more appropriate, unless the exact same model was used. Where populations are comparable, it is thought that differences in reported kinematic results can be related to the definitions of the joint axis or segments of the foot, which has been discussed previously by Buldt et al., (2013). Additionally, the limited number of patients used in the aforementioned studies were not adequate to capture the natural variation in the populations.

Frontal plane – eversion/inversion

Considering frontal plane movement, a mean excursion for subtalar eversion/inversion of 12.9° was found by Oosterwaal et al., (2016), similar to findings reported by De Mits et al., (2012) who reported a mean RoM (SD) of 14.9° (6.55), while Simon et al., (2006) showed less mean RoM 10° (0.3), similar to Nester et al., (2007) which reported a mean RoM of 9.7° (5.2), approximately equivalent to Lundgren et al., (2008), who reported a mean RoM of 9.8° (1.8). As previously noted, specific comparisons of exact figures do not indicated agreement, due to methodological approaches, but can provide a useful guidance.

2.5.1.2 Talonavicular joint

Due to the challenges around isolating the contributions to the motion of the talus and the navicular, studies capturing motion at this joint are limited to an in vitro study (Nester et al., 2007), bone-pin studies (Arndt et al., 2007; Lundgren et al., 2008) and previous literature applying the GM foot model (Oosterwaal et al., 2016).

Sagittal plane – plantarflexion/dorsiflexion

Sagittal plane movements reported by Oosterwaal et al., (2016) and Nester et al., (2007), found excursion (SD) of 14.6° and 12.2° (7.1) respectively. Bone-pin study by Arndt et al., (2007) reported a mean RoM 6.5° (2.9), similar to findings by Lundgren et al., (2008) who reported a mean RoM of 8.4° (1.1), these studies consisted of healthy and small samples of participants which reduced the impact of the findings. Furthermore, considerable variations exist in the pattern of motion in the study by Arndt et al., (2007) and Lundgren et al., (2008) study, the movement at this joint is particularly difficult to capture. Frequently used models such as the OFM arguably do not have the ability to report the angles at this joint, which although is a smaller joint in the foot, could highlight subtle kinematic differences between normal and non-normal kinematic outputs.

Frontal plane – eversion/inversion

Normal foot type kinematics in the frontal plane RoM of the talonavicular joint presented in a cadaver model Nester et al., (2007) showed excursion (SD) of RoM of 12.2° (7.1), whereas bone pin studies by Arndt et al., (2007)

and Lundgren et al., (2008) reported mean RoM 13.5° (4.1) and 14.9 ° (6.1) respectively. A twenty six segment with foot model described in Oosterwaal et al., (2016) reported a mean RoM of 9.3° which is less than the other studies. However, discrepancies between invasive and non-invasive foot models could be due to the difference in passive loads from cadaver studies or small number variance seen in bone pin studies for healthy populations.

Transverse plane – abduction/adduction
In transverse plane movement of the talonavicular joint, normal foot type kinematics reported by Nester et al., (2007) a mean RoM (SD) of 16.8° (9.2), similar to bone-pin study by Lundgren et al., (2008b) who reported a mean RoM of 16.3° (6.5), however smaller values were found by Arndt et al., (2007) reporting a mean of RoM 8.7° (1.4). The 26-segment GM foot model described in Oosterwaal et al., (2016) reported a mean RoM for talonavicular abduction/adduction of 14.6° similar to cadaver and bone-pin studies, showing some agreement between bone pin and non-invasive methods when analysing healthy populations.

2.5.1.3 First metatarsophalangeal joint

Sagittal plane – plantarflexion/dorsiflexion
In vitro study by Nester et al., (2007) showed average first metatarsophalangeal plantarflexion/dorsiflexion joint movement with a mean RoM (SD) of 44.2° (8.0) and other studies using multi segment foot models De Mits et al., (2012), MacWilliams et al., (2003) and Simon et al., (2006) found a mean RoM of 54.7° (10.3), 40° (approx., derived from graph) and 42.1° (1.1) respectively. In comparison Oosterwaal et al., (2016) reported a population mean RoM of 40.0° using the 26-segment GM foot model, roughly in agreement with other results reported in the literature for normal healthy populations.

2.5.2 Pathological foot kinematics

There are numerous studies that describe the kinematic data of pathological populations using foot models and fluoroscopy (Saraswat et al., 2014; Buldt

et al., 2015; Caravaggi et al., 2018; Wang et al., 2019; Kruger et al., 2019). Hunt and Smith, (2004) developed a simple 2 segment plus shank model that consisted of a rear foot portion as the calcaneus and a forefoot portion as the base and head of the fifth metatarsal and the head of the first metatarsal. They compared flat and normal feet during stance in a relatively small population of 18 normal males who had a mean age of 25, SD 5; Range (18-38) whereas the pes planus group had 15 participants and a mean age of 26; SD 7; Range (19-43). This model does not provide the levels of detail needed to adequately describe the differences in the small bones of the foot between pathological foot types, but does incorporate the medial longitudinal arch height which is a simple method used to classify a flat or high-arched foot (Hawes et al., 1992). However, when comparing the two populations Hunt and Smith, (2004) showed no differences between the groups in the frontal plane rear foot motion and at the ankle joint motion as described by International Society of Biomechanics recommendations (Wu et al., 2002). In contrast, in a study by Levinger et al., (2010) using the OFM studying 10 normal and 9 (mean age of 20.1 years ± 1.3) found planus foot types foot types had greater peak plantar flexion and adduction in the forefoot and had internal rotation of the rear foot in the late stance phase of gait compared to the normal group. While clinically useful, this model does not describe movement of the small bones in the first ray of the foot, which is where the hypothesised largest variation occurs between typical arch height and flat arch foot types. In this thesis kinematics between the small bones of the foot in the medial ray are modelled, which could address some limitations of the OFM.

Saraswat et al., (2010) created a foot model for clinical use that consisted of a three-part multi segment model that was scaled to match a subject and was driven by kinematic inputs to estimate kinematics and internal muscle forces. In a follow on study by Saraswat et al., (2012) developed a method for a foot model based on an anatomically registered technical coordinate system in paediatric planovalgus feet previously described by Saraswat et al., (2013) to investigate kinematics of normal and planovalgus feet during walking. In the paediatric foot Saraswat et al., (2014) found no difference in

ankle eversion RoM, or in midfoot flexion compared to the control group; instead, reported comparable full RoM results in line with findings by Carson et al., (2001). Comparison of segment kinematics is difficult as marker set up between the two models is different with Saraswat et al., (2013) having markers placed on the forefoot at the base and head of the first metatarsal, head of the fifth metatarsal and the hallux as a triad on the big toe. Table 2 below summarises the results of studies that characterise function of morphological variations of foot types.

Table 2 Showing foot models that describe kinematic differences between normal and pathological foot types with the number of patients, age distribution, findings and limitations.

Model	Pathological population	Number of patients	Age: years, SD, range	Findings	Limitations
Hunt (Hunt and Smith, 2004)	Flat Vs Normal during stance phase	15 male's planus or pronated foot posture 18 Normal	Normal arch: 25 ± 5 Low arch: 26 ± 7	No differences between groups at ankle joint and rear foot motion	Simple model not capable of capturing subtle movement of and adequate number of joints. All male participants
Oxford Foot Model (Levinger et al., 2010)	Normal Vs Flat Arched	19 participants 10 Normal (6 male and 4 female) 9 Pes Planus	Normal arch: 24.3 ± 8.7 Low arch: 20.1± 1.3	Planus foot demonstrated greater peak plantar flexion and abduction in forefoot and	Reliable clinical model, but still not detailed enough to demonstrate the movement

		(7 male and 2 female)		internal rotation of rear foot in late stance	of the first ray where other models have (Leardini et al., 2007)
Saraswat (Saraswat et al., 2014)	Normal Vs Planovalgus	20 Pediatric participants 10 typically developed (TD) 10 planovalgus (PV)	Normal arch: 10 7 female, 3 male, average age 10.6 ± 1.6 10 Low arch: 3 female, 7 male, average age 10.6 ± 1.9	No difference in ankle eversion ROM No difference in midfoot flexion. Comparable full RoM results with Carson et al (Carson et al., 2001)	Different segment definitions and so not comparable in some aspects. Study is on pediatric foot

2.5.2.1 Ankle joint

Sagittal plane – plantarflexion/dorsiflexion

Of the papers reporting ankle joint kinematics between low, normal and high arch foot groups include Buldt et al., (2015), Caravaggi et al., (2018) and Kruger et al., (2019). Buldt et al., (2015) showed the normal and high arch group to have similar RoM, while the low arch group had less RoM. Caravaggi et al., (2018) also found the normal group to have a greater RoM in comparison to the planovalgus group. A recent study by Kruger et al., (2019) using the Milwaukee foot model (Kidder et al., 1996) analysed kinematic outputs using a locally weighted regression smoothing with alpha-adjusted serial t-test analysis (LAAST), found significant differences between groups across the time series. Kruger et al., (2019) found significant differences between all groups for stance phase of gait, except for terminal stance between the normal and flat groups, with the spatiotemporal differences between high and flat groups between 0 and 76% of stance phase.

Frontal plane – eversion/inversion

Considering subtalar eversion Buldt et al., (2015) found cavus foot types to have less frontal plane RoM than normal and low arch foot types. In another study Caravaggi et al., (2018) found normal foot types to have less RoM than planus foot types, but with smaller magnitudes and wider standard deviations in reported values. In contrast Kruger et al., (2019) used a continuous time-series analytical method and found significant differences between rectus (normal) and low arch foot types with the exception of terminal stance for normal and planus foot types. Kruger et al., (2019) also reported a statistical difference between 0% and 100% of stance for low and high arch foot types. The foot model used by Kruger et al., (2019) used anatomically relevant calibration of patients and aligns to the conjecture of variation between foot populations. This thesis captures similar anatomically calibrated variation; however, efforts were made to improve on this by using individual bones segmented from MRI scans and registered using a SSM.

2.5.2.2 Talonavicular joint

Sagittal plane – plantarflexion/dorsiflexion

Fluoroscopy techniques have been used to both analyse the talonavicular joint and measure differences between adult acquired flat foot and normal foot types (Wang et al., 2019). In this study the sagittal plane measurements of the flat foot population had a mean RoM of 13° (6) and the normal arch foot reported a mean RoM of 7° (3), which could be explained by the stiffness of high arch foot types through the midfoot (Younger and Hansen, 2005; Barnes et al., 2008; Aminian and Sangeorzan, 2008) leading to less RoM. Conversely, flatfooted structures can be characteristically more flexible (Cobb et al., 2009) which could indicate the wider RoM.

Considering frontal plane movements (eversion/inversion) of the talonavicular joint, Wang et al., (2019) found similar RoM measurements for both flat and normal groups 25° (9) and 21° (5) respectively, indicating there is little difference between the foot types, however the flatfoot group had double the standard deviation of the normal foot group. Similarly for movement in the transverse plane (abduction/adduction), Wang et al., (2019) found the flat group to have a similar RoM to the normal group with a mean RoM of 17° (13) and 16° (4) respectively, although the flat group had more than three times the standard deviation indicating more variance within the group.

2.5.2.3 First metatarsophalangeal joint

Sagittal plane – plantarflexion/dorsiflexion

In studies analysing differences between foot pathologies of the first metatarsophalangeal joint, Buldt et al., (2015) found that the high arch foot population had the greatest RoM compared to the low or normal foot arch types. However, in contrast to these findings Caravaggi et al., (2018) reported normal the foot arch type to have a greater RoM than the low arch foot type. Both studies examined adolescent feet, however each of the studies used a different method to determine a low, normal and high arch

foot type. Different models were also used to define segments from which the kinematic motion was derived, which may have impacted the interpretation of the results. Saraswat et al., (2014) used a 3-segment foot model and an independent time-point t-tests and found that the hallux flexion of planovalgus foot type had significantly less first metatarsophalangeal plantarflexion/dorsiflexion than the typically developed foot types for adolescent populations. The differences between planovalgus and typically developed foot types were observed between approximately 30% and 40% and 77% and 100% of stance phase, indicating differences are present using an advanced MSK foot model.

2.5.3 Joint Coordinate Systems

The major differences in foot models are variation in location of the markers as they are placed on the foot and definitions of the composition of segments. Other differences include calibration to the surroundings and the segment co-ordinate system (SCS). Considering the tibiotalar and subtalar joint kinematics there a several methods used to define SCS's (Lenz et al., 2021) and many more for other joints in the foot.

Different foot models use different SCS's making comparison between model segments difficult. The SCS defines the axis of rotation in 3D space about which motion is measured and is fixed within a body or segment. The SCS describes the position and orientation of the segment which is influenced by the placement of markers. The position of the SCS system is critical in the interpretation of kinematic results. There are a number of different definitions of anatomical reference frames for the ankle joint (Cappozzo et al., 1995; Liu et al., 1997; Carson et al., 2001; Wu et al., 2002) and even more for segments further down the foot. There exists a standardized method from the International Society of Biomechanics (ISB) for measuring the talocrural and subtalar joints which together form the ankle joint complex (Wu et al., 2002).

Within the ISB recommendations there is a standard definition of anatomical planes of the tibia/fibula. In Figure 12, the frontal plane is made up from connecting inter- malleolar (IM) (the inter-malleolar point located midway between medial-malleolus (MM) and lateral-malleolus (LM)), medial condyle (MC) (the most medial point of the medial tibial condyle) and lateral condyle (LC) (the most lateral point on the border of the lateral tibial condyle). The torsion plane is constructed using IC (the inter-condylar point located midway between the MC and LC), MM (the tip of the medial malleolus) and LM (the tip of the lateral malleolus). While the sagittal plane is made up perpendicular to the frontal plane and contains the long axis of the tibia/fibula and connecting IC to IM through the tibial tuberosity (TT). The last plane is the transverse plane which is a mutual plane perpendicular to the frontal and sagittal planes. This thesis has made efforts to take into consideration segment co-ordinates used within the aforementioned literature. The 26-segment foot model uses co-ordinates relative to the bones however and while this is a slight deviation from other SCS’s it arguably provides more anatomically relevant joint motion.

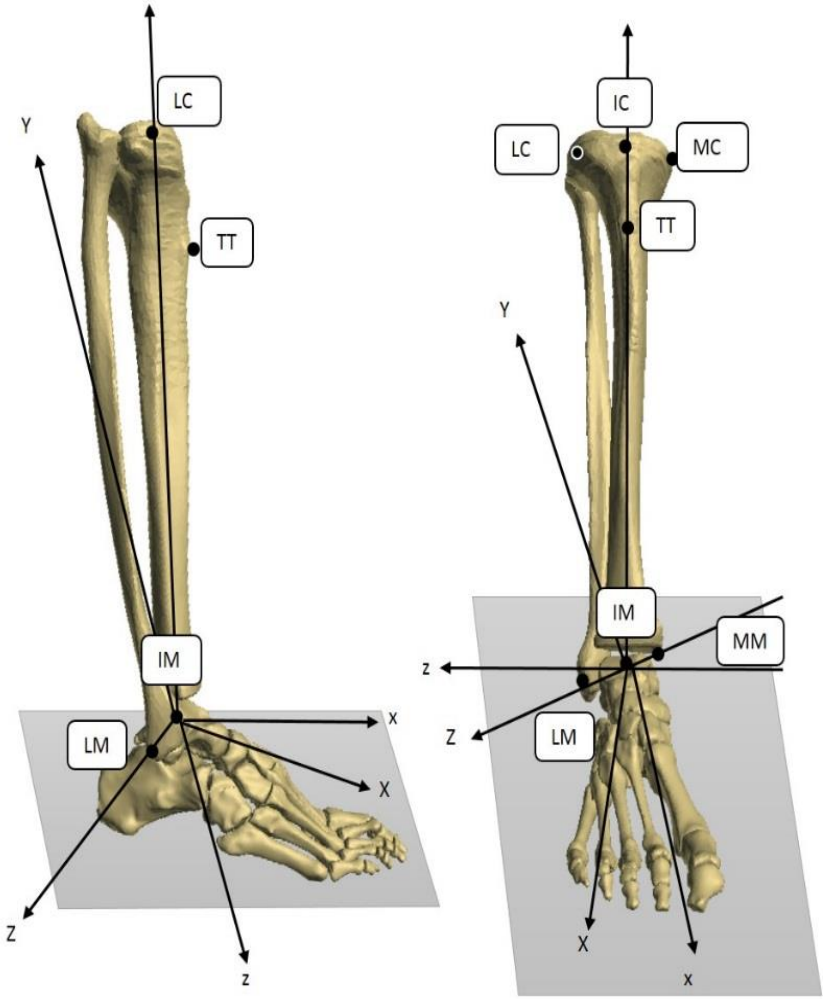

Figure 12 Illustration of the tibia/fibula coordinate system (XYZ) and the calcaneus coordinate system (xyz) with the ankle joint complex in the neutral position.

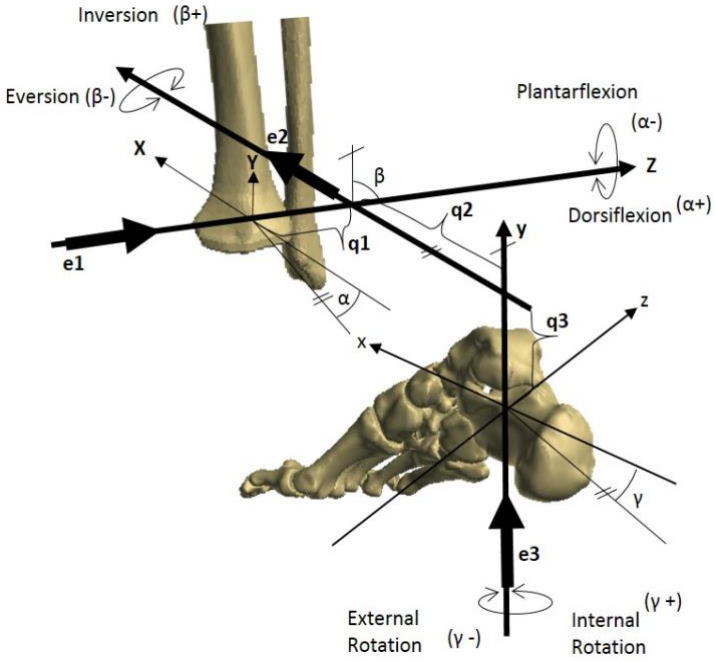

Figure 13 Illustration of the JCS for the right ankle joint complex.

The ISB also has specific recommendations for the for the calcaneus described in Figure 13 and denoted in Tables 3 and 4.

Table 3 Showing the ISB coordinate system for the calcaneus bone (Figure 13)

Notation	Definition within the coordinate system
o	The origin coincident with that of the tibia/fibula coordinate system (O) in the neutral configuration.
x	The line coincident with the long axis of the tibia/fibula in the neutral configuration, and pointing cranially.
y	The line perpendicular to the frontal plane of the tibia/fibula in the neutral configuration, and pointing anteriorly.
z	The common line perpendicular to x- and y-axis.

Table 4 Showing the Joint coordinate system and motion for the ankle complex

Notation	Definition of the coordinate system and motion
e_1	The axis fixed to the tibia/fibula and coincident with the Z-axis of the tibia/fibula coordinate system. Rotation (α): dorsiflexion (positive) or plantarflexion (negative). Displacement (q_1): medial (negative) or lateral (positive) shift.
e_3	The axis fixed to the calcaneus and coincident with the *y*-axis of the calcaneal coordinate system. Rotation (γ): internal rotation (positive) or external rotation (negative). Displacement (q_3): correspond to compression (positive) or distraction (negative).
e_3	The floating axis, the common axis perpendicular to e_1 and e_3. Rotation (β): inversion (positive) or eversion (negative). Displacement (q_2): anterior (positive) or posterior (negative) drawer.

2.6 **Musculoskeletal Modelling**

Computational or mathematical models of the MSK system help researchers understand the relationship between parts of the body, as well as the mechanical means by with injuries and disease affect natural function. Currently, the use of these virtual models in clinical practice is limited as the process to create such models can be lengthily and computationally expensive. However, there have been advances in this technology in the lower limb with models successfully assessing a range of treatments and interventions (Fang et al., 2007; Chao et al., 2007; Blana et al., 2008). One of the main limitations yet to be overcome is that only a few validated modelling systems are available. These systems are in the form of commercial and open-source versions including, Anybody Modeling System (Damsgaard et al., 2006) and OpenSim (Seth et al., 2011).

AnyBody Technology (ABT) is a commercial modelling system with a professionally managed repository AMMR and complementary modelling IDE. This software is designed to work in an inverse dynamic system that takes inputs from motion and external force measurements such a force platform in a gait laboratory, but can also interact with other 3D physical objects such as sitting position to analyse the impact on hip joint reaction forces (Van Houcke et al., 2017). With kinematic and kinetic data joint angles, reaction forces, muscle activities and contact stresses between bones throughout the gait cycle can be computed. The process for using motion capture data in the AMS starts with a MSK template geometry and motion capture trial data as inputs. A process called parameter identification initializes an optimization of the model markers and physically placed markers in directions that are free to optimize as opposed to fixed and not free to optimize. This optimization is important as the free directions account for a clinician not knowing the distance between the bone, and the marker physically place on the foot. As the markers are optimizing for local bone co-ordinates, the length of the segments is also adapting to the marker positions. The result of the optimization is to update the anthropological parameters while minimizing soft constraints (markers) subject to the hard

constraints (joints). Following convergence, for each timestep the markers can be tracked, and joint angles derived from thee system, and saved for further inverse dynamic analysis. Over-determinate kinematic models described by Andersen et al., (2009) are implemented in the AMS have more markers than degrees of freedom to be solved. This creates two groups of constraints; hard constraints, typically joints which must be satisfied and soft constraints, typically markers (but can be used for other categories) that should be satisfied. Figure 14 demonstrates calculating kinematics in the anybody model in the context of human joint analysis.

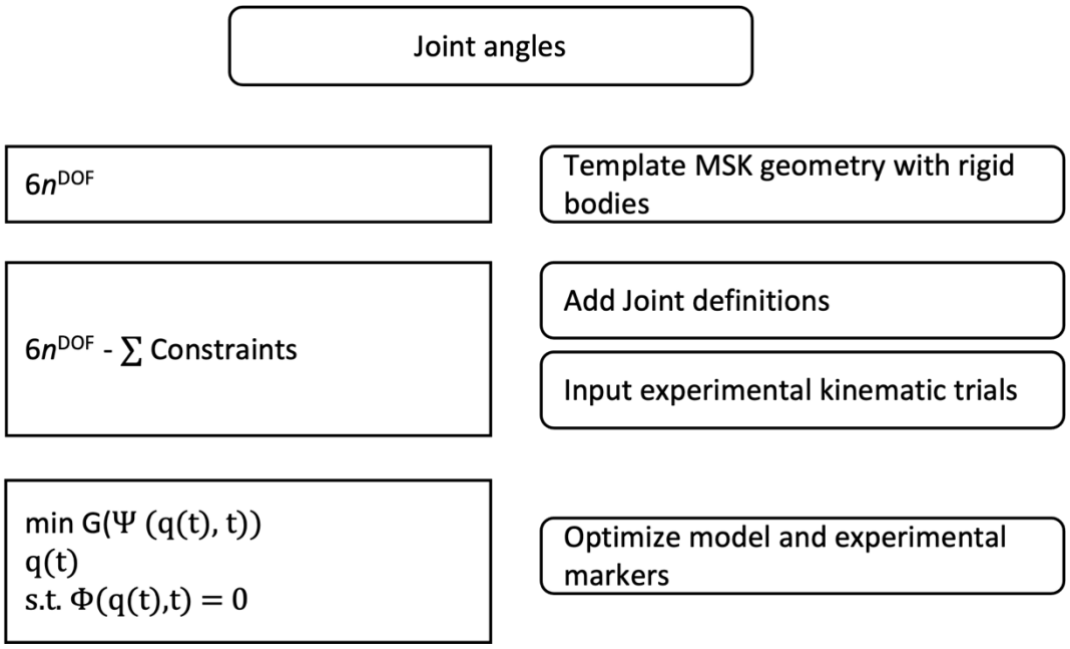

Figure 14 Showing the joint angles for kinematics derived from the anybody modelling system are calculated from rigid bodies, where the joints, as hard constraints and experimental markers as soft constraints are optimised with respect of the residual of the hard constraints equal to 0.

Inverse dynamics in the AMS system, which in addition to net joint moments allows the calculation of muscle and joint forces using angles output from kinematic analysis. Of interest are the joint reaction forces within a model as this information can be used to understand forces going through human joints during, for example activities of daily living, which can have an impact the design of clinical interventions for joints targeted for treatment.

As AMS models are based upon average anthropometric human shapes they do not account for individual differences in either kinematic or inverse dynamic analysis. Within a kinematic analysis the motion angles are defined relative to each segment and can more accurately be accounted for with personalised bone shapes derived from medical images using the patients joint centres (Marra et al., 2015). The AMS software implements non-linear scaling and morphing algorithms that allow segmented medical images as STLs to be used as an input to the modelling process. Using geometries that more closely match the patient increases the detail of the model, of which could provide more accurate information on the patients if adequately validation.

Verification and Validation of kinematics in MSK models.

Human kinematic model verification aims to demonstrate the equations being used are being solved correctly. The AMS is a commercial software package that has been tested extensively, albeit internally. Due to the commercial nature, it is common for paid for software to lack complete transparency of the suite of tests used. This can lead to ambiguity in the approaches taken to verify even what might be referred to as simple algorithms.

Human kinematic model validation aims to demonstrate the results from a kinematic analysis using a model are indicative of what would be expected in a real human motion. Considering kinematics in the foot and ankle, Lenz et al., (2021) highlights how advances in bi-planar fluoroscopy have helped evaluate the motion foot joints *in vivo*. This provides a validation benchmark for which multi-segment models can be evaluated against for derived kinematic motions. However, this type of validation for each patient is time consuming and results in a model valid only to that patient. This validity does not take into consideration the dynamic alterations and changes that occur to a patient or population over time, however, is a gold standard in validation of kinematic models.

Verification of patient specific bone morphing using STLs

MSK modeling aims to predict muscle and joint forces to derive information to often complex biomechanically posed challenges. Generally, these MSK models are based on one average cadaver specimen and as a modular component this geometry can be personalised to match an individual subject, for example, using medical images to derive patient information has been implemented in the AMS, the radial basis function (RBF) (Buhmann and Buhmann, 2003) to transform corresponding surface points using an affine RBF interpolation/extrapolation. A bounding box is used around each bone to prevent poor inter/extrapolations of the RBF function before a rigid-body transformation back to the musculoskeletal model. To verify this process it would be necessary to compare the geometry from the morphed STLs to the original STLs derived from the medical images and also the muscle attachments on the bones (Pellikaan et al., 2014).

In the case of the detailed 26-segment foot model several inputs are needed to solve mathematical problems that represent the most clinically useful information, such as joint reaction forces and muscle activations. The detailed model also uses information from pressure pad data to distribute force plate measurements, when investigating inverse dynamics. However, in the context of this thesis only kinematics were explored. For detailed 26-segment foot model using the AMS, a patient specific image of the bones from MRI or CT modalities can be used to scale and morph a template model using bone segments and motion markers. Previous literature using the GM foot model used bones segments derived from CT scans and a foot surface scan to scale the model to fit the patient, however this thesis details a scaling and morphing method using bones segmented from MRI scans.

2.6.1 The Glasgow-Maastricht Foot model

The most detailed musculoskeletal model of the foot at present is a result of a European Union funded project, AFOOTPRINT which involved several collaborators. The modelling aspect of this project was carried out by ABT, specifically Carbes et al., (2011) and Oosterwaal et al., (2011) who used a combination of finite element and inverse-dynamics software to create a forward dynamic model which was further evaluated by Oosterwaal et al.,

(2016). The GM foot model, see Figure 15 was aimed at describing the biomechanical effects of orthotic devices, but also is capable of describing internal loads of the foot (Tørholm et al., 2013; Al-Munajjed et al., 2016). The GM model can achieve this through the manipulation of kinematic rhythms described by Wolf et al., (2008), these rhythms act as constraints within the model to achieve kinematic over-determinacy (Andersen et al., 2009). Currently this is the only MSK foot model that allows each of the bones in the foot to be analysed as individual bone segments.

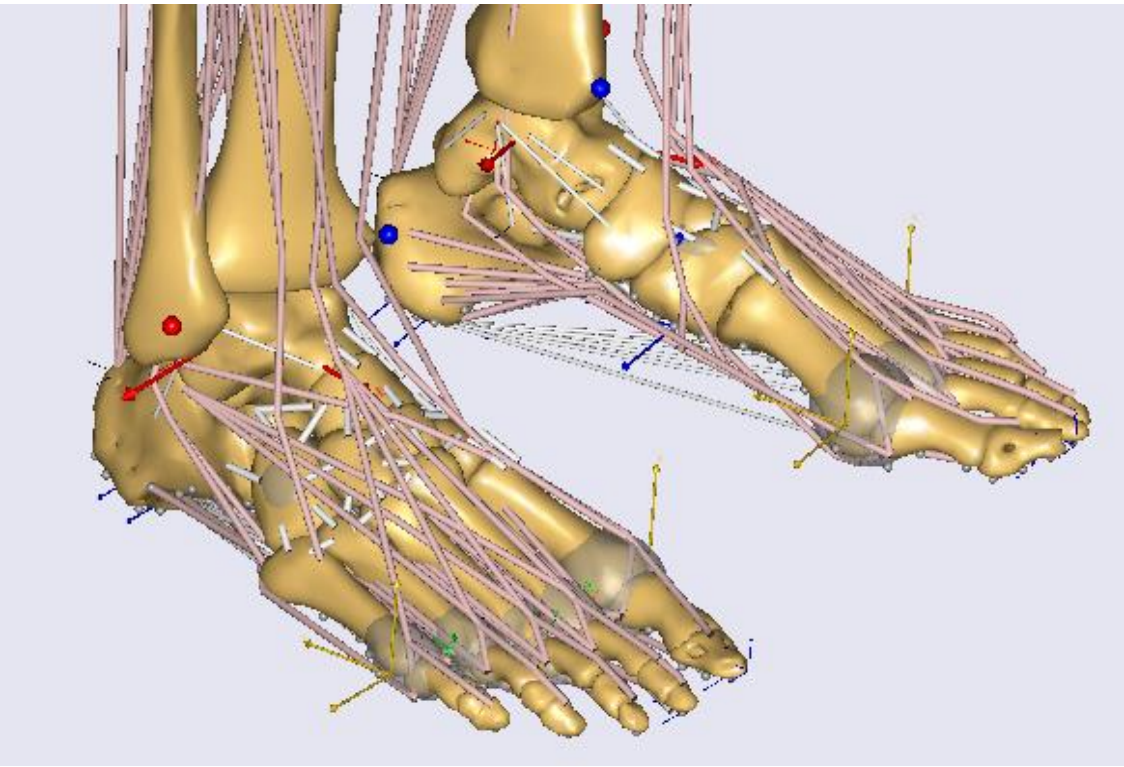

Figure 15 The Glasgow-Maastricht foot model

The GM foot model has been compared to cadaver studies but lacks clinical validation in the calculation of intersegment angles. This is challenging due to the number of methods and differing clinical applications used to develop kinematic models of the foot (Leardini et al., 2019).

Within the GM model, the joints are defined as revolute, spherical or universal based on the perceived anatomical requirements of that joint in the foot. Although many useful parameters can be tailored for clinical use, this

can result in a larger number of degrees of freedom. To reduce the degrees of freedom kinematic constraints have been applied in the form of seven kinematic rhythms or functional units based on a methodology developed by Wolf et al., (2008). These functional units are based on the motion that occurs as a result of ligaments crossing over multiple joints. In the GM model these rhythms represent the motion of two or more joints in the foot and are adaptable to model specific foot deformities. Also included in the foot model are inter-tarsal joints e.g., cuboidnavicular, cuneocuboid and three cuneiforms. Although these are not explicitly defined, they are modelled as gliding joints with an ellipsoid fitted to the lateral side of the tarsal bones. Any interaction between these bones is controlled by a contact algorithm which eliminates the possibility of the ellipsoids intersecting and inter-segment penetration.

2.7 **Summary**

To summarize, the literature suggests that foot posture varies from low to high arch foot type, with subtle subcategories identified along the spectrum. Nomenclature for this clinical variation in foot posture includes cavus, cavovarus, cavoid, planus, planovalgus all pertaining to variations of a notional extreme. Enhanced imaging acquisition methods, such as MRI and CT modalities provide information on a patient's specific bone and soft tissue geometry. These images can be processed and converted into a geometric shape distribution to capture variance within healthy and pathological populations providing information on shape characteristics in latent space. To date there is limited literature describing shape variation in the medial ray bones in combination, where clinically the arch is a significant diagnostic factor in decision making. In addition, a detailed 26-segment foot model has been developed and applied to healthy populations with some kinematic outputs comparable to cadaver and bone-pin studies but has not been fully explored in the context of foot pathologies.

There also exists a gap in the literature describing an analytical pipeline combining statistical shape analysis and a 26-segment foot model to investigate research around differences in the structural and functional characteristics that may exist between extremes of foot posture.

This thesis aims to develop an engineering pipeline that will use patient specific images transformed into a statical shape model to capture variance in low, normal and flat arch types. In addition, the thesis will use SSM's as the basis to scale and morph a 26-segment foot model that will be used to derive kinematics of low, normal and high arch foot types, with a focus on the hind, mind and medial ray of the foot.

Chapter 3 Generating patient specific input data for statistical shape analysis and a dynamic 26-segment musculoskeletal foot model

3.1 Introduction

This chapter will describe the methods for generating data that was used in the statistical shape modelling and a 26-segment foot model described in chapters four, five and six. The patient specific data generated was divided into two sections, with the first detailing MR image acquisition and extraction of bone morphology and the second describing gait and pressure data acquisition. A total of eighteen patients with variations in Foot Posture Index scores (Redmond, 2005) were collected. A subset of three patients were used as the basis to develop workflows for the statistical shape model, described in chapter four and to develop the 26-segment foot model detailed in chapter five. The further fifteen patients were categorised by their FPI and used to capture variance between arch type and shape characteristics. The patient data used in this thesis was collected as part of a larger study on midfoot OA, with anonymisation and with ethical procedures followed in accordance with REC reference number: 17/YH/0261.Thirteen patients were used to capture variance in kinematic analysis between extremes of foot posture, detailed in chapter six.

Data from each patient was collected over an 18-month period. Image data, gait analysis and pressure data were collected from the NIHR Leeds Biomedical Research Centre, Chapel Allerton Hospital, Leeds, UK. Table 5 shows the characteristics of patients used in shape and kinematic analysis. Patients were selected to include an equal number per low, normal, and high arch categories.

Table 5 Detailing the cohort of patients used in the studies, with age in years, Sex as Male or Female, height in centimetres (cm), weight in kilograms (kg), Foot posture index (FPI) as an integer and arch type as low normal and high.

Patient	Age (years)	Sex	Height (cm)	Weight (kg)	FPI	Arch type
1	63	Female	168	87	-4	High
2	59	Female	167.5	71.5	-2	High
3	65	Female	162	68.9	-3	High
4	81	Female	157	58.7	0	High
5	67	Female	178	74.9	-3	High
6	77	Female	159	73.9	4	Normal
7	75	Male	169	57.3	3	Normal
8	56	Male	178	72.9	3	Normal
9	70	Female	167	69.3	4	Normal
10	40	Female	167	92.1	1	Normal
11	80	Male	166	68.9	10	Low
12	70	Male	166	73.7	11	Low
13	68	Female	165	52	6	Low
14	60	Female	153	65	6	Low
15	70	Female	164	58.8	5	Low

3.2 **Data acquisition methods**

The methods that were developed in this chapter provide image, motion and pressure data on a range of foot posture index scores that were later used

as input data in both a statistical shape model and a 26-segment foot model. The methods and results generated will provide a workflow that can be applied in the future to a larger number of patients and will demonstrate a feasible approach in the development of a pipeline to combine statistical shape and kinematic analysis.

The stages in the generation of bone morphologies involved image acquisition and segmentation of different foot types to extract the bone morphology. To generate motion data a previously published model described in Carbes et al., (2011) and Oosterwaal et al., (2011) was adapted and used to create the 26-segment foot model capable of capturing gait analysis data in a different laboratory. In addition to motion capture, kinematic and kinetic data, pressure data was collected from the patient to integrate the distribution of pressure forces applied to the foot, into the 26-segment foot model. A workflow for methods that generate data for shape analysis and MSK analysis can be seen in Figure 16.

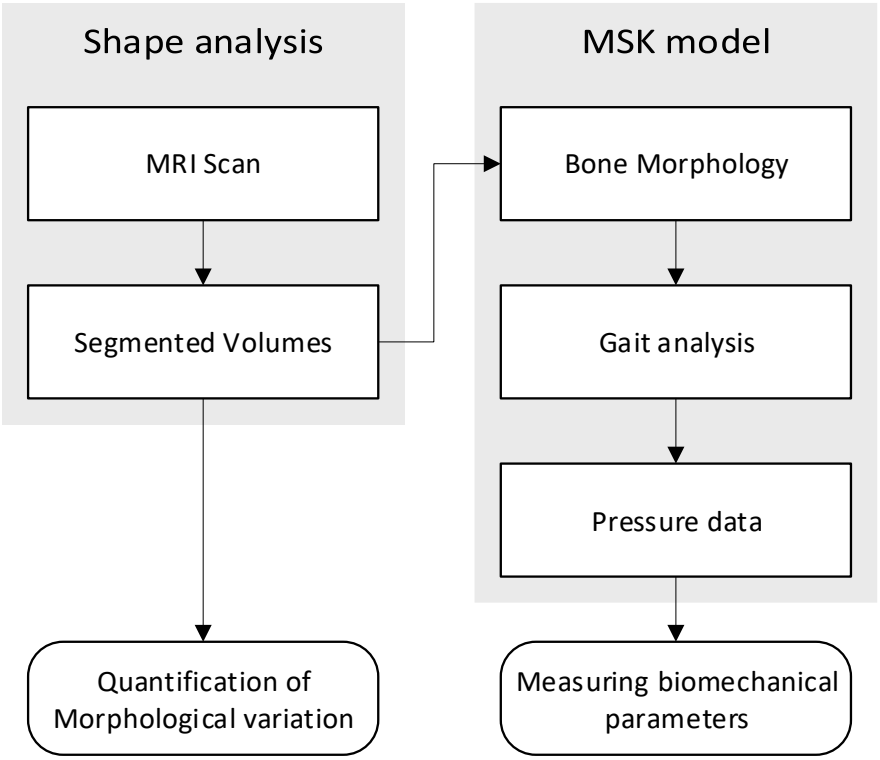

Figure 16 An overview of the generation of patient data for shape analysis and MSK analysis and their use in the modelling workflow

3.2.1 Generation of patient bone morphology

MR Images in this thesis were collected in a larger study focusing on mid-foot OA with predefined protocols and images sequences optimized for this purpose. The image sequences were used as the basis to define the patient's bone geometry

3.2.1.1 Image acquisition

Morphologies of patient's high, normal and low arch foot types were generated from MRI scans of right feet. The patient's foot was scanned using a Siemens 3T Magnetom Verio large bore scanner with an 8 Channel foot and ankle coil to enhance the image resolution. The image volumes were constructed with a 7 min, 3D PD SPACE sequence with a Repetition Time (TR):1000, Time to Echo (TE): 36, flip angle 120, echo train length 62, 0.5mm slices, FOV of 199 x 199 mm, matrix 315 x 384. The patient MR data was anonymised with ethical procedures followed in accordance with REC reference number: 17/YH/0261.

3.2.1.2 Segmentation

Image segmentation and investigative visualisations were performed on MR images converted to a Digital Imaging and Communication in Medicine (DICOM) format. Binary image volumes of bone morphology were reconstructed into image volumes using software package 3DSlicer (Kikinis et al., 2014) and specifically the robust statistical segmentation (RSS) algorithm developed by Gao et al., (2012) that is based on a label map and active contour approach to segmentation. Bone morphology from the talus, calcaneus, navicular, medial cuneiform, intermediate cuneiform, lateral cuneiform, cuboid and metatarsals 1-5 were extracted.

The segmentation process involved placing generalised seed region points through the image stack as a label map using the paint editor in 3DSlicer. Figure 17 shows the seed points overlaying the calcaneus bone in the a)

transverse plane, b) sagittal plane and c) frontal plane. This label map acts as an initial starting point for the RSS algorithm to propagate.

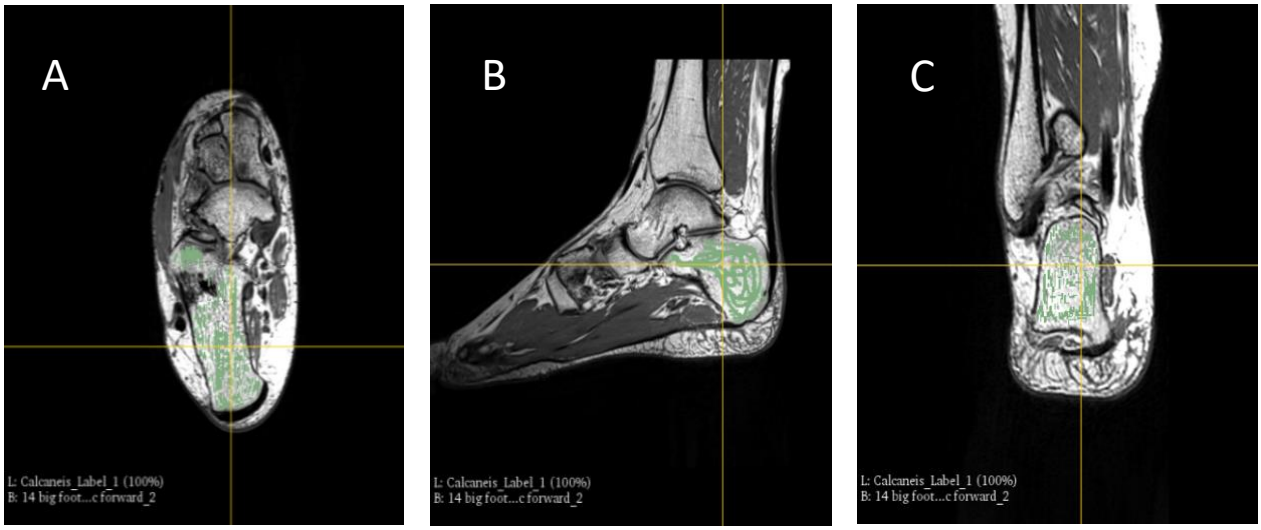

Figure 17 Representing seed points on a calcaneus bone of an MR image of a right foot

Parameters including expected volume, intensity homogeneity and boundary smoothness were adjusted until the output volume covered the entire boundary of the bone with no leakage or missed boundaries. When the entire bone was not completely segmented, the seed label map was updated, and the RSS algorithm was applied. The RSS algorithm is run on the label map and evolves across the boundary of the bone and produces a volume. Figure 18 shows a) the transverse plane, b) sagittal plane and c) coronal plane of the segmented volume overlay on a calcaneus bone.

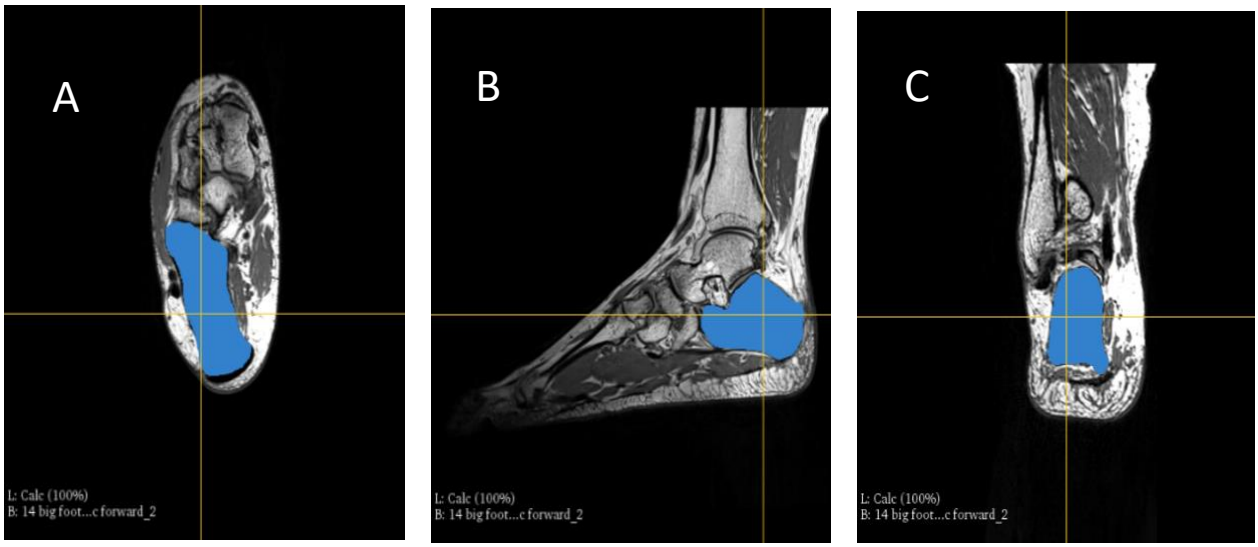

Figure 18 Representing segmented calcaneus volume overlayed on an MR image of a right foot

3.2.2 Generation of patient motion capture and pressure data

Kinematic data was collected at 200Hz using an eight-camera system (Vicon MX, Oxford, Metrics, UK) and kinetic data was generated from an integrated force platform AMTI force plate at 1000Hz. Multi-segment foot kinematics for right feet were captured using a motion capture marker set up as previously described in the GM foot model (Carbes et al., 2011; Oosterwaal et al., 2011) and detailed in Table 6 with the addition of a CAST (Cappozzo et al., 1995), which uses rigid clusters of four non-orthogonal makers placed laterally on both the thigh and shank. Markers were placed on the subject's foot, shown in Figure 19. For each trial auto gait event detection was obtained from the force platform using threshold values of 10N for heel strike and toe off.

Figure 19 Motion capture marker set up of the foot for the GM foot model.

3.2.2.1 Labelling kinematic data for batch processing

To facilitate batch processing of labelled kinematic data, a customised Vicon Skeleton Template (VST) was created in Vicon Nexus based on an initial subject, see Figure 20. Forty-six markers were labelled on the patient's pelvis and right lower limb, shown in Table 6. To create the labelling template, virtual segments were formed and linked from the pelvis to the distal foot shown by the colours in Figure 20. Following auto-labelling of the static trial, walking trials for each subject were reconstructed and batch labelled per patient. Gaps found in the trials were filled using the spline gap filling tool in the software and finally a 6Hz Butterworth filter was applied to reduce the noise in the walking trials. When this processing step resulted in a marker that could not be interpolated successfully, the trial was discarded.

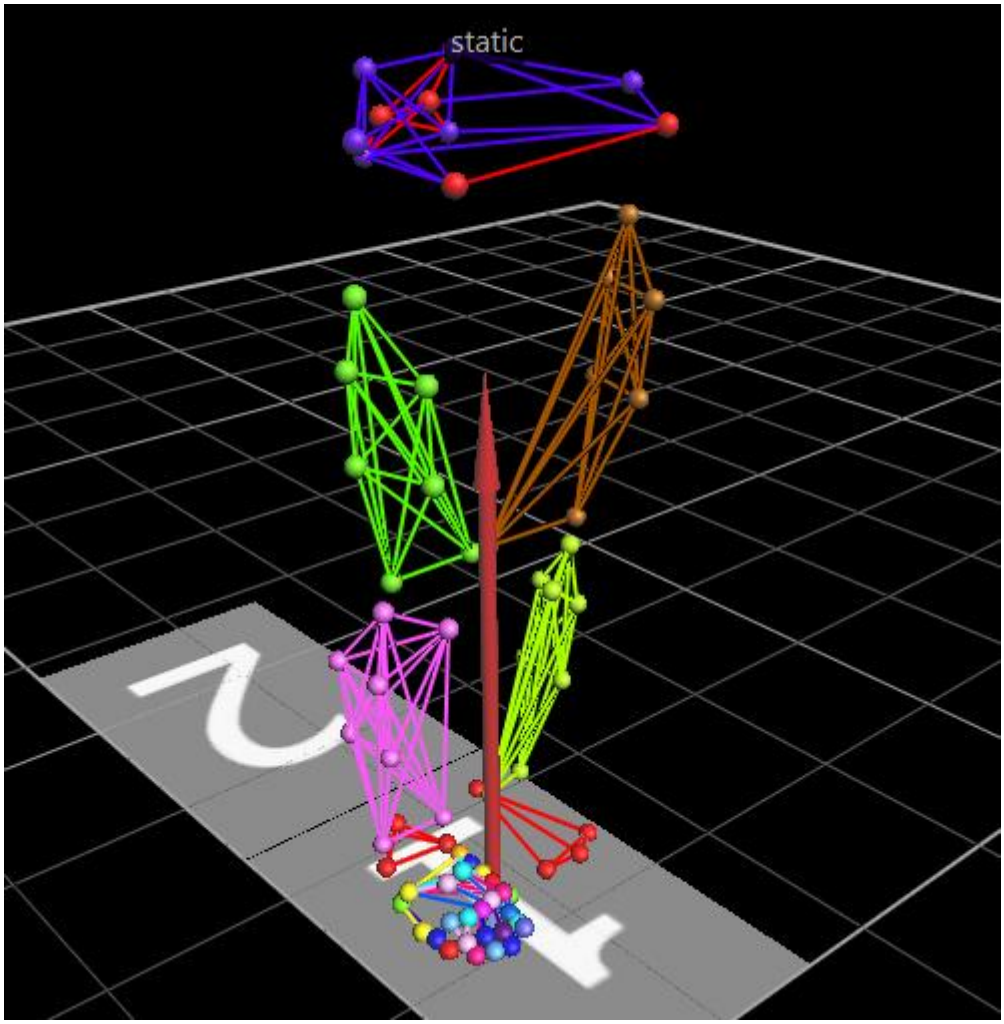

Figure 20 Labelled static trial with the kinematic markers coloured from nexus vicon that was used to collect motion data from the makers, as indicated by sperical nodes in the image, connected with striaight lines that make up a segment.

Table 6 Overview of kinematic model landmarks and label names

Bony Landmark	Label name
Right iliac crest	RASIS
Left iliac crest	LASIS
Right posterior Iliac crest	RPSIS
Right anterior Iliac crest	LPSIS
Right greater trochanter	R_GTROC
Thigh 1	R_THI_1
Thigh 2	R_THI_2
Thigh 3	R_THI_3
Thigh 4	R_THI_4
Lateral knee	R_LKNEE
Fibula head	R_FIB_HEAD
Tibial tuberosity	R_TIB_TUB
Leg 1	R_LEG_1
Leg 2	R_LEG_2
Leg 3	R_LEG_3
Leg 4	R_LEG_4
Lateral malleolus	R_LAT_MAL
Medial malleolus	R_MED_MAL
Inferior calcaneus	R_INF_CAL
Superior calcaneus	R_SUP_CAL
Medial calcaneus	R_MED_CAL
Lateral calcaneus	R_LAT_CAL
Navicular tuberosity	R_NAVIC

Cuboid	R_CUBOID
Lateral cuneiform	R_LAT_CUN
Intermediate cuneiform	R_INT_CUN
Proximal 1st metatarsal	R_PROX_1ST_MET
Central 1st metatarsal	R_CEN_1ST_MET
Medial 1st metatarsal head	R_MED_1ST_MET
Lateral 1st metatarsal	R_LAT_1ST_MET
Proximal 5th metatarsal head	R_PROX_5TH_MET_HEAD
5th metatarsal head	R_5TH_MET_HEAD
4th metatarsal head	R_4TH_MET_HEAD
3rd metatarsal head	R_3RD_MET_HEAD
2nd metatarsal head	R_2ND_MET_HEAD
Hallux 1st	R_HALLUX_1
Hallux 2nd	R_HALLUX_2
Hallux 3rd	R_HALLUX_3
Proximal 2nd phalanx	R_PROX_2ND_PHAL
Proximal 3rd phalanx	R_PROX_3RD_PHAL
Proximal 4th phalanx	R_PROX_4TH_PHAL
Proximal 5th phalanx	R_PROX_5TH_PHAL
Distal 2nd phalanx	R_DIST_2ND_PHAL
Distal 3rd phalanx	R_DIST_3RD_PHAL
Distal 4th phalanx	R_DIST_4TH_PHAL
Distal 5th phalanx	R_DIST_5TH_PHAL

3.2.2.2 Pressure data acquisition

Pressure data was generated using an Emed q-100 pressure plate developed by Novel, gmbh to record at a frequency of 100Hz placed on top of the force platform, shown in Figure 21. As the pressure plate hardware has a larger dimension than the force platform a 2mm thick sheet of polymer the same area as the force plate was placed between the pressure plate and force platform with double-sided tape. The aim of which was to eradicate any chance of the full load of the subject being distorted by the overhanging pressure plate on ground that was not the force platform. Accuracy was maintained through each trial collection by calibrating the vertical reaction force using the Cal Tester method. Finally, the pressure data collected was exported as a comma separated values (CSV) file.

Figure 21 Image of pressure platform set up in the laboratory used to collect pressure data from patients that could be used in the 26-segmentfoot model

3.3 Discussion

3.3.1 Bone morphology discussion

The aim of the bone morphology aspect of this chapter was to develop a methodology to extract segmentations of patient's bones from an MRI scan to be used subsequently in this thesis. Firstly, as an input to several statistical shape models detailed in chapter four and secondly, as a patient specific morphing for a 26-segment foot model described in chapter five. Using MR images has an advantage over CT as there is no ionising radiation exposure endured by the patient, while still producing data that is capable of capturing bone volume and other anatomical tissues that can be extracted for quantitative purposes. This imaging protocol was sufficient to generate bone images of the talus, calcaneus, three cuneiforms, cuboid and five metatarsals, however omitted the distal phalanges due to the 8-channel foot coil losing signal.

The task of segmenting regions of interest is a challenging aspect of extracting bone morphology from any medical image. In the end application, that is aiming to produce data for shape and MSK kinematic analysis, cartilage was included in the segmentations. Including this soft tissue could have an impact on morphological variation between foot types but should not have an impact on positional or orientation variance. In addition, including the cartilage in the segmentations should not impact kinematic motions derived from the patient specific foot model, however a sensitivity test would be needed to confirm this theory. Segmenting bones from MRI scans including the cartilage remains a consideration for the work in this thesis.

The quality of the segmentations was judged by the author's experience of implementing the robust statistical segmentation algorithm developed by Gao et al., (2012) on 216 bones in the segmented datasets, this is a result of segmenting 12 bones from eighteen patients. Implementing the RSS algorithm required tuning through the adjustment of parameters to ensure full bone coverage was achieved. On rare occasions when the algorithm was not encapsulating the entire areas of bone, seed label map points were

updated, this was likely due to the variance in pixel volumes for the bone across the label map not covering the variance seen in the part of the image containing the region of interest.

Segmentations of the foot volumes were carried out using the RSS algorithm (Gao et al., 2012), which is an extension tool available within 3D Slicer. This tool has been used to segment various organs in the body using modalities including MRI and CT scans (Gao et al., 2012). The advantages of this method include the semi-automatic approach using seed points, an active contour approach, open-source availability and its implementation in 3D Slicer. Due to the use of a foot coil in image acquisition the intensity of MR images dropped towards the distal end of the foot, however as the algorithm uses seed points from individual bone label maps this did not affect the quality of the output. Typically, filters to normalise the intensity across the image are used as a pre-processing step in segmentation of medical images, however in this workflow no filters were applied. Using pre-processing filters could decrease the time to segment the images, reduce the number of seed points, decrease the likelihood of segmentation leakage and manual updates to the label map, however the approach taken in the methods produced acceptable segmentations.

The RSS algorithm allows for adjustment of parameters concerning homogeneity intensity and boundary smoothness and so these parameters along with initial seed points were optimized to improve segmentation outputs. This semi-automatic segmentation algorithm depends on the subjectivity of the user to ensure that all aspects of the bone volume have been covered. Despite subjective bias being introduced with segmentation, the approach taken to segment the image was appropriate, due to the open-source design and the time taken to segment twelve bones per foot was reduced when compared to a manual process alone.

The use of the RSS algorithm on MR images of the foot demonstrates its wide applicability. Further optimization of MR pre-processing could be explored in the future. Although the segmentation process applied in this workflow is quicker than a fully manual alternative, other methods such as

the application of machine learning (ML) or deep learning (DL) models could be more efficient with a larger dataset. However, both approaches require large training sets of manually segmented images to initiate a segmentation solution.

3.3.2 Kinematic data discussion

The aim of capturing gait and pressure data from patients in this chapter was to develop methods to generate C3D (Co-ordinate 3 dimension) and pressure data files that can be used as patient specific inputs for the 26-segment foot model, developed in chapter five. Previously developed methods (Carbes et al., 2011; Oosterwaal et al., 2011) were used as a basis and developments were made to the to adapt the GM foot model to be applicable to an alternative virtual gait laboratory set-up.

The kinematic GM foot model (Carbes et al., 2011; Oosterwaal et al., 2011) was developed to measure the kinematic profile of all the bones and joints in the entire foot and ankle. Adjustments to the protocol were made to include a CAST marker set, where extra markers on the thigh and shank improve the accuracy of the eversion and inversion of the lower limb due to the increase in tracking markers. However, due to the number of makers on the foot this may have unnecessarily increased the time to label a full trial and caused issues when optimising the 26-segment foot model detailed in chapter five and applied to low, normal and high arch foot types, detailed in chapter six. A challenge associated with the processing of kinematic data is placing makers on bony landmarks. This was overcome by a trained and experienced podiatrist palpating bone to accurately place markers on the targeted bony landmarks. Gap filling and marker reconstruction parameters were optimised to achieve an accurate kinematic trial. As some of the markers on the foot were closely co-located, parameters in the label reconstruction from the VST template were optimised to generate the markers for each trial and once labelled a Butterworth filter was applied to the trajectories of the markers.

Kinematic models of the foot and ankle when using opto-reflective markers are subject to STA as skin is an elastic material and the markers on the foot

aim to track the motion of the underlying a rigid bone that does not move in tandem with the skin. Previous work carried out by Oosterwaal, (2016) using the GM foot model investigated STA and found the effect on marker positions ranged from 1.9 mm – 6.7 mm, with midfoot markers exhibiting more motion, but with no significant difference. Due to the size of the foot, it can be difficult to place markers exact distances from the bones, which can amplify STA movements calculated at a joint due to inertial effects of walking. As STA's are common to all kinematic models and cannot be adequately measured without the combining markers placed on the patients' foot while they are being scanned by MRI or CT it was not measured or recorded in this thesis and remains a limitation. This thesis attempted to capture the sensitivity study of this kinematic method between one low, normal and high arch foot type, detailed in chapter five.

3.3.3 Force and plantar pressure discussion

The aim of generating force and pressure data was to use it with the 26-segment foot model, seen in chapter five. The pressure plate was placed on top of the force plate to collect both kinetic and pressure data simultaneously. An addition of the polymer sheet to account for the overhang of the pressure platform was appropriate to ensure global resultant force vectors were collected from the force plate accurately. This could have impacted the dissipation of forces through the pressure platform and the polymer sheet, however the impact of this adaption was not captured. Combining force and pressure plates is the current method used to work with the GM foot model, although there are many unknowns when incorporating pressure into a MSK foot model, attempts were made to understand the sensitivity to these adaptations for extremes of foot posture in chapter five.

3.4 Limitations

The methods detailed in this chapter outline how the data was collected and limitations do exist. Patients were selected based on the data collected for a study of mid-foot OA patients, this introduced constraints on the

geodemographics of the patients the pipeline would be developed, and MRI sequence applied to the patients was optimized for the purposes of identifying mid-foot OA from a medical image and not to segment bones form MRI scans. There were no definitive characteristically matched groups, such as age, sex, height, body mass index or geography which are likely to have an impact on shape variance or movement analysis between low. normal or high arch foot groups. However the justification for this lack of matching was due to the focus of the thesis, which is to outline a methodological pipeline that can be applied to quantifying variance between foot postures using state of the art techniques.

To potentially improve the performance of the bone segmentations an alternative MRI image acquisition such as a T2 weighted image that defines the edges of the bones well and has been used to analyse bone marrow lesions (Dube et al., 2018) could have been used to mitigate against leakage seen in the PD SPACE sequence applied to the MR images in the data collection or improved speed of segmentation. However, the MRI sequence data was collected as part of a larger study on midfoot OA performed and the protocol had been defined. In addition the PD SPACE scans have been used to differentiate between bone, hyaline cartilage, and fibrocartilage which, although not investigated in this thesis could be used be investigated to quantify variance between foot types, loading patterns and pathomechanics cartilage degradation.

3.5 **Conclusion**

The aim of this chapter was to develop and apply methods to segment bones from MRI scans in a range of foot postures. This data will be used in the analysis of position and morphology through the development of SSM's detailed in chapter four. In addition, kinematic, kinetic and pressure data collection methods were developed to generate motion profiles from C3D files and resultant forces from a force platform. Further, pressure distributions from a pressure platform were collected for later use in a 26-segment foot model described in chapter five. In conclusion these

processing steps were successfully applied to generate appropriate patient specific data for quantitative shape and kinematic analysis of low, normal and high arch foot types.

Chapter 4 Application of statistical shape modelling to extremes of foot posture

4.1 Introduction

Variations from a ‘normal’ foot type have been associated with changes in foot function during gait (Menz et al., 2013), however the reason for this is unclear. High arch foot types are reported to exhibit structural changes such as hindfoot varus accompanying forefoot adduction (Aminian and Sangeorzan, 2008; Kim, 2017), whereas low arch foot types have previously been reported to have a hindfoot valgus with forefoot abduction. Differences in posterior tibial tendon function and plantar pressure have also been observed between cavus and planus foot types (Dyal et al., 1997; Kohls-Gatzoulis et al., 2004; Buldt et al., 2018). Previous literature reports that biomechanical differences between low and high arch foot types exist, therefore investigating a cause-and-effect relationship between morphological features with recognised functional differences is of interest to clinical and research communities. Statistical modeling of 3D geometry has been applied to quantify morphological and positional variation using SSM’s. For example, SSM’s have been developed and successfully applied to quantify variance in pathological and non-pathological foot types (Melinska et al., 2015; Melinska et al., 2017; Moore et al., 2019; Grant et al., 2020).

SSM’s use images derived from modalities such as X-Ray (Zheng, 2010), CT and MRI. This chapter uses individual bones previously segmented from MRI scans discussed in chapter three, which were used as an input for the SSM. These shapes were analysed for positional, orientation and morphological variance. PCA is a tool often applied to the corresponding points populated on shape instances, its purpose is to reduce the dimensionality of the ensembled data to a limited number of features that describe shape variance within the dataset. This data was labelled within the SSM model to facilitate a between group comparison of low, normal and high arch foot types for average morphological differences.

This study aimed to investigate relationships between overall foot type and individual bone shape of medial ray bones including the talus, calcaneus, navicular, medial cuneiform and first metatarsal. In the context of this thesis, this work will form a part of the analytical pipeline that will be used to facilitate patient specific bone morphing of a 26-segment foot model, detailed in chapter five, using the SSM's derived 3D point clouds and a template geometry from the MSK foot model.

4.2 Methods

4.2.1 Patient groups

For the SSM study between foot types, patients were divided into three equal groups based on foot posture; 5 high arch (FPI = -4 to 0); 5 normal arch (FPI 1 to 4) and 5 low arch (FPI = 5 to 12), shown in Table 7, resulting in an equal distribution of patients per group.

Table 7 Showing the FPI and foot arch types used to group patients for the statistical shape analysis study.

High arch		Normal arch		Low arch	
-4 to 0		1 to 4		5 to 12	
Subject	FPI	Subject	FPI	Subject	FPI
1	-4	6	4	11	10
2	-2	7	3	12	11
3	-3	8	3	13	6
4	0	9	4	14	6
5	-3	10	1	15	5

4.2.2 Statistical shape modeling using ShapeWorks Studio

ShapeWorks Studio v 6.1 is an open-source shape modelling software developed at the University of Utah (documentation available at https://github.com/SCIInstitute/ShapeWorks). ShapeWorks was used to analyse the bones of the foot due to the open-source nature and proven success in other anatomical areas. Shape analysis was carried out on binary image volumes generated from patient MRI scans collected in chapter three. For each of the 15 patients 5 bones; including the calcaneus, talus, navicular, medial cuneiform, and first metatarsal were used from the segmented MRI scans. These were used as the input to the SSM workflow, were a multi-domain SSM of the medial ray bones was created. In addition, individual SSM's were created for each of the 5 bones, therefore a total of 75 bones were analysed in the shape analysis study.

The registered binary image segmentations were pre-aligned in nearly raw raster data (.NRRD) file format with matching voxel spacing and imported into ShapeWorks Studio v 6.1. These images were groomed to smooth the surfaces in preparation for an optimisation of the particle correspondence between shape instances. PCA was carried out on the point clouds resulting in the generation of means and standard deviations, with vtk (visualisation toolkit) reconstructions of these point clouds visualised as meshes to show variation present in each of the bones. Figure 22 shows a workflow of each of the specific steps in the analysis.

PCA as a dimensionality reduction technique takes a dataset and computes the mean for every dimension of the 3D point matrix (d). The covariance is also calculated and used to compute eigen vectors and corresponding eigenvalues. Eigen vectors are ordered by descending eigen values to choose k eigenvectors with the largest eigenvalues to form a d x k dimensional subspace. The d x k eigenvector matrix is used to transform samples into new subspace where comparisons can be made.

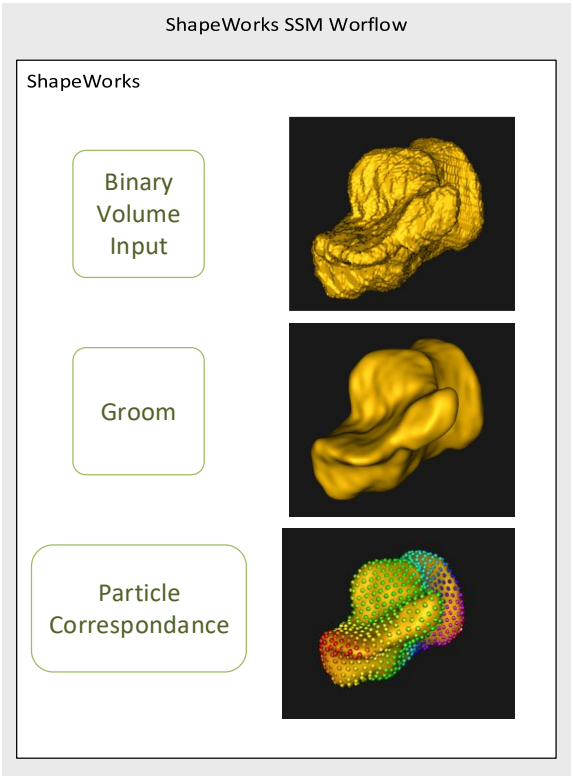

Figure 22 ShapeWorks Studio graph showing various steps involved a binary input volume groom step and particle correspondence of the PCA**.**

4.2.3 Pre-processing

Prior to running the shape analysis in ShapeWorks Studio v 6.1 the binary images volumes of similar bones were aligned using the image CoM and ICP registration. This step facilitates a faster and more accurate global alignment via the removal of translation and rotations of the images. Figure 23 (A) shows the segmented calcaneus bone imported into ShapeWorks Studio v 6.1 with visible segmentation staircase effect on the surface.

A grooming function was applied to all the bones. This step generates a smooth surface and distance transforms using a fast-marching method that is used as a basis to initialize the point-based correspondence optimisation algorithm. Built-in functionality allows the user to a) centre segmentations to a common reference axis, b) isolate background from image, c) fill holes d) antialiasing to remove the step effect of the segmentations and e) blur the distances transforms to remove artefacts' and create a smooth surface for particle optimisation. Figure 23 (B) is an image of a groomed calcaneus bone.

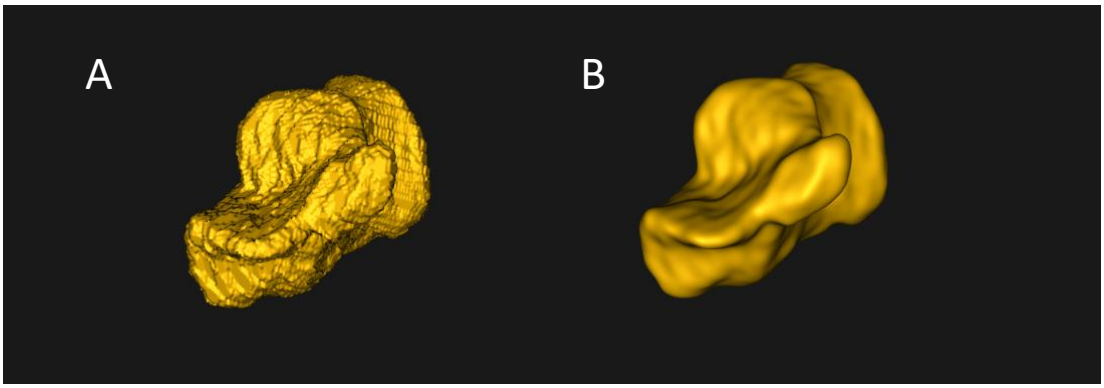

Figure 23 Showing the result of original mesh imported to ShapeWorks Studio (A) and Groomed mesh (B)

When considering the results in this chapter, shape variance for the medial ray bones including the calcaneus, talus, navicular, medial cuneiform and first metatarsal, the initial alignment was achieved by a local alignment of each domain, leading to the reference frame being specific to each bone. The rotations and translations are aligned using the centre of mass and an

ICP matching algorithm. The variation described in individual bones analyses with morphological descriptors uses a local alignment pertaining to the group of shapes with the rotation and translations also aligned using the centre of mass and an ICP matching algorithm with the addition of a Procrustes analysis to superimpose shapes onto the medioid or reference shape and therefore standardising for natural size and scale variation and the resulting variation due to morphological differences.

In preparation of the shapes surface for alignment and corresponding particle optimisation a number of filters were applied to shape. The cohort of shapes are antialiased to create a continuous-valued image and are initially aligned based on their centre of mass to remove translations, rotational alignment is achieved through an ICP rigid alignment algorithm each of the steps involves antialiasing the segmentation. For computational optimization the binary segmentations are converted to signed distance transforms. The signed distance transform indicates a voxel-based distance to the zero-level set of the shape surface and satisfies the requirements to update the located of an optimised set of particles, including a smooth surface with a foreground and background and a sign (+ / -) to indicate where the particles need to be snapped back to the surface of the image, during optimisation. As the signed distance transforms are derived from segmentations the surface will have a staircase effect which is carried through to the signed distance transform, before the signed distance transform is computed the segmentation is antialised to smooth the surface, then a 3D gaussian filter is applied on the signed distance transform to remove any residual staircase effect.

4.2.4 Particle optimisation

Once the shapes in the dataset have been groomed, an entropy-based particle optimisation algorithm is applied to facilitate correspondence among input shapes. A set of particles *z* interact with the surface of the ensemble $\mathcal{E}$, via reciprocally repelling forces to cover the geometry of *M* shapes.

$$\mathcal{E} = \mathrm{z}^1, \mathrm{z}^2, \ \ldots, \ \mathrm{z}^{\mathrm{M}}$$

This particle-based representation combines two types of random variables, a shape space variable: $\mathrm{Z} \in \mathbb{R}^{dM}$ and a particle position variable: $\mathrm{X}_n \in \mathbb{R}^d$ that encode the distribution of particles on the nth shape. Correspondences are determined by minimizing the entire ensemble and surface sampling cost function,

$$Q = \propto H(\boldsymbol{Z}) - \sum_{n=1}^{N} H\,(X_n),$$

Where Q is the cost function minimised using gradient descent, the optimiser aims to minimize the global information in the model while maintaining the sampling of the shape surface geometry. H is an entropy estimation of the shape distribution in the shape space and $\propto$ is the relative weighting of the correspondence term. Relative weighting balances correspondence with surface sampling, the trade-off between points corresponding between shapes and how well the points cover the surface of each shape. By increasing the relative weighting, point correspondences are distributed over areas with low variability and when lower values of relative weighting are used, more variability of the surface is captured, however correspondence between shapes reduces. Full details of the optimisation algorithm can be found on GitHub (http://sciinstitute.github.io/ShapeWorks/workflow/optimize.html). GPA (Goodall, 1991; Dryden and Mardia, 1998) is applied to negate size and compared morphologies between shapes. If Procrustes analysis is not applied, resultant variation is due to size or positional and orientational features of variance.

When morphological variation was investigated, a Procrustes interval was applied to align the shapes to a common reference frame during the optimisation. Finally, PCA based reconstructions of the optimised particles are visualised using VTK-based isosurfacing and Preview-based mesh quality control.

This step involves defining the number of particles to be placed on the shapes surface. Table 8 shows the bone analysed as groomed meshes, the

total number of particles used and indicates the shape usage with shape analysis and patient specific scaling and morphing, as seen in chapter five.

Table 8 Number of particles and number of points for each bone used for correspondence, inclusion in shape analysis and inclusion in chapter five scaling and morphing.

Bone as groomed mesh	Number of particles	Shape analysis	Chapter five Scaling and morphing
Talus	2048	Yes	Yes
Calcaneus	2048	Yes	Yes
Navicular	1024	Yes	Yes
Cuboid	1024	No	Yes
Medial Cuneiform	1024	Yes	Yes
Intermediate Cuneiform	1024	No	Yes
Lateral Cuneiform	1024	No	Yes
Metatarsal 1	2048	Yes	Yes
Metatarsal 2	1024	No	Yes
Metatarsal 3	1024	No	Yes
Metatarsal 4	1024	No	Yes
Metatarsal 5	1024	No	Yes

Parameters such as relative weighting were optimised to improve the correspondence among the shapes. Starting regularisation was set between 5 % and 10 % of the highest eigen value and ending regularisation was set at 10% of the starting regularisation. The Procrustes interval was applied to align the shapes to a common reference frame during the optimisation. Finally, PCA based reconstructions of the optimised particles are visualised using VTK-based isosurfacing and Preview-based mesh quality control. Figure 24 (A) shows an input Calcaneus (B) a groomed Calcaneus and (C) a PCA reconstructed Calcaneus.

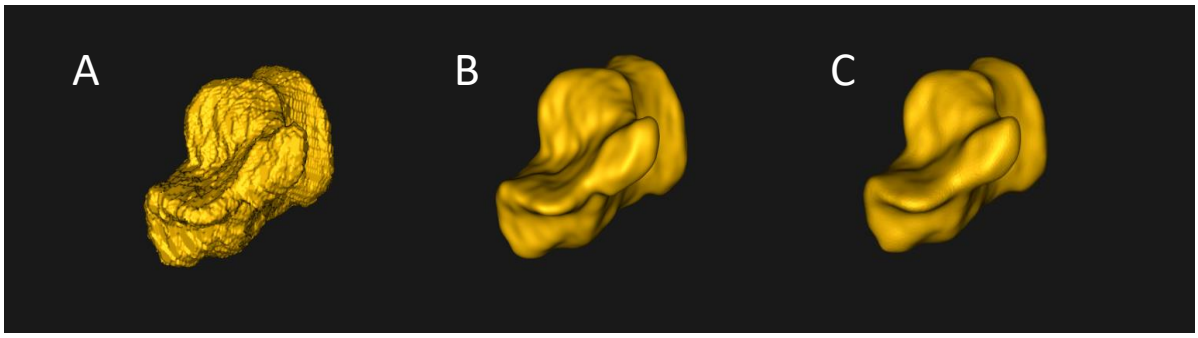

Figure 24 Showing (A) the binary volume input calcaneus, (B) the groomed calcaneus and (C) the PCA reconstructed calcaneus

4.2.5 PCA Surface reconstruction from ShapeWorks

The transformations of the segmentation involve manipulating the original segmentation and analysed PCA reconstructed surfaces from the particle system. The process of reconstructing patient geometries from the PCA particle system involves a template-deformation approach. The triangulated iso surface generated from distance transformations of the population space particle system and are warped from the mean distance transformation to each patient using a thin plate spline and radial basis function.

Section 5.3.1.2 and specifically Table 9 compares the RMS error between surface vertices of the segmented bones and the SSM generated patient bones that represents the specificity of the shape modelling process to accurately spawn PCA meshes that represent the input shape.

4.3 Results from quantification of bone shape changes in the foot

PCA was carried out on bones including the calcaneus, talus, navicular, medial cuneiform and first metatarsal bones from 15 patients categorised into 3 groups depending on arch type: low, normal and high. Fourteen PCs were generated for each bone and variation in shape of the total population is indicated by the percentage difference captured in the PC's. Overall foot shape was compared between high and low arch foot types for orientation and positional variance and morphological variation was analysed separately. The mean shapes of each of the bones were compared to see anatomical areas of each bone that may vary between the low and high arch groups. Overall, positional changes in the orientation of each of the bones accounts for most of the variance seen in the data however, subtle changes in morphology may also exist between low, normal and high arch foot types may also exist.

4.3.1 Shape changes in bones of the medial ray

The multi-domain or multi-shape SSM included the calcaneus, talus, navicular, medial cuneiform and first metatarsal of all the patients, initially without Procrustes Analysis enabled i.e. the variation was due to orientational differences, the total variation in the data set is visualised in Figure 25, showing a superior view of the principal mode of variation with the mean and ± 2 standard deviations and Figure 26 showing a medial view of the principal mode of variation with the mean and ± 2 standard deviations. The image shows the first mode of variation to be associated with rotation and orientation of each of the bones and a decrease in the radius of the medial longitudinal arch at +2 standard deviation and an increase in the medial longitudinal arch at -2 standard deviation.

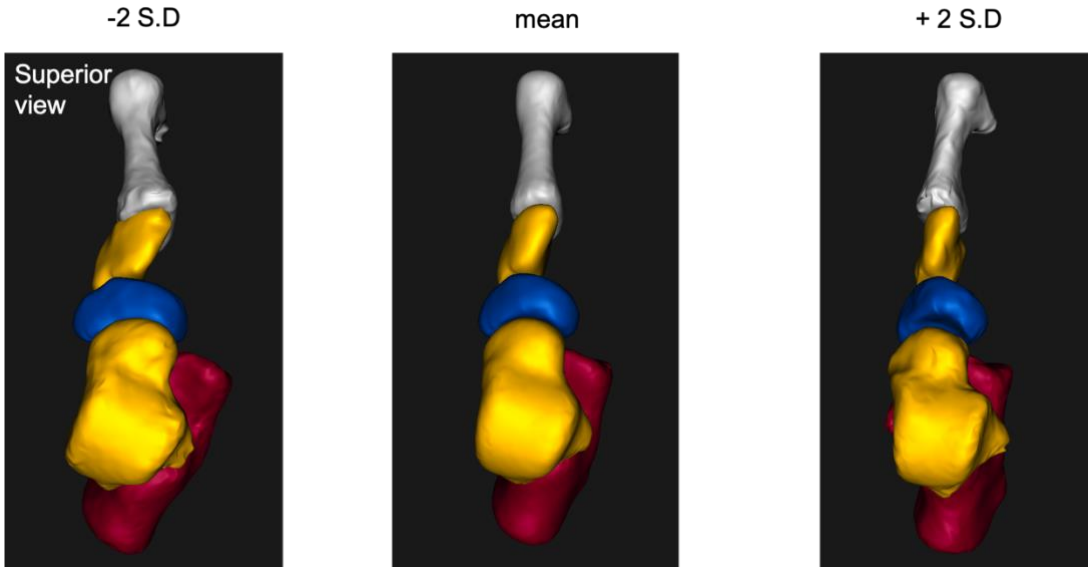

Figure 25 Superior view of multi domain shape model of the first PC of calcaneus talus, navicular, medial cuneiform and metatarsal 1 with mean and ± 2 standard deviations

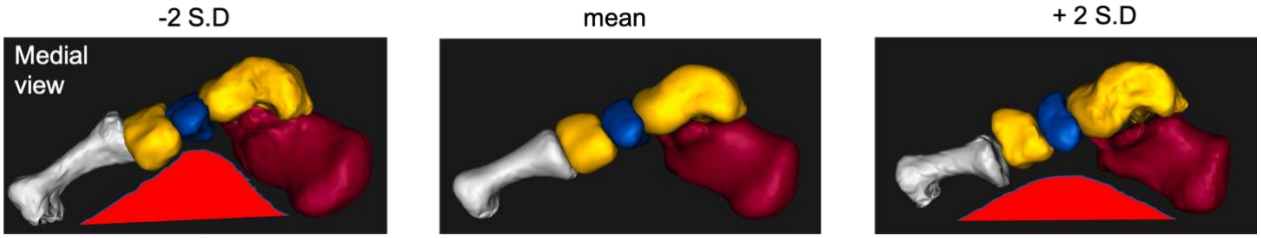

Figure 26 Superior view of multi domain shape model of the first PC of calcaneus talus, navicular, medial cuneiform and first metatarsal with mean and ± 2 standard deviations

Further analysis in mean differences between flat and high arch types are presented in Figure 27 as a visual inspection of average differences. In Figure 28 mean difference between the low and high arch foot types are presented, where the mean low arch foot differences are indicated by the red colour, where the colour is blue, this represents no difference between

the groups. Figure 28 shows differences in orientation and position of the low arch foot type compared to the high arch foot type.

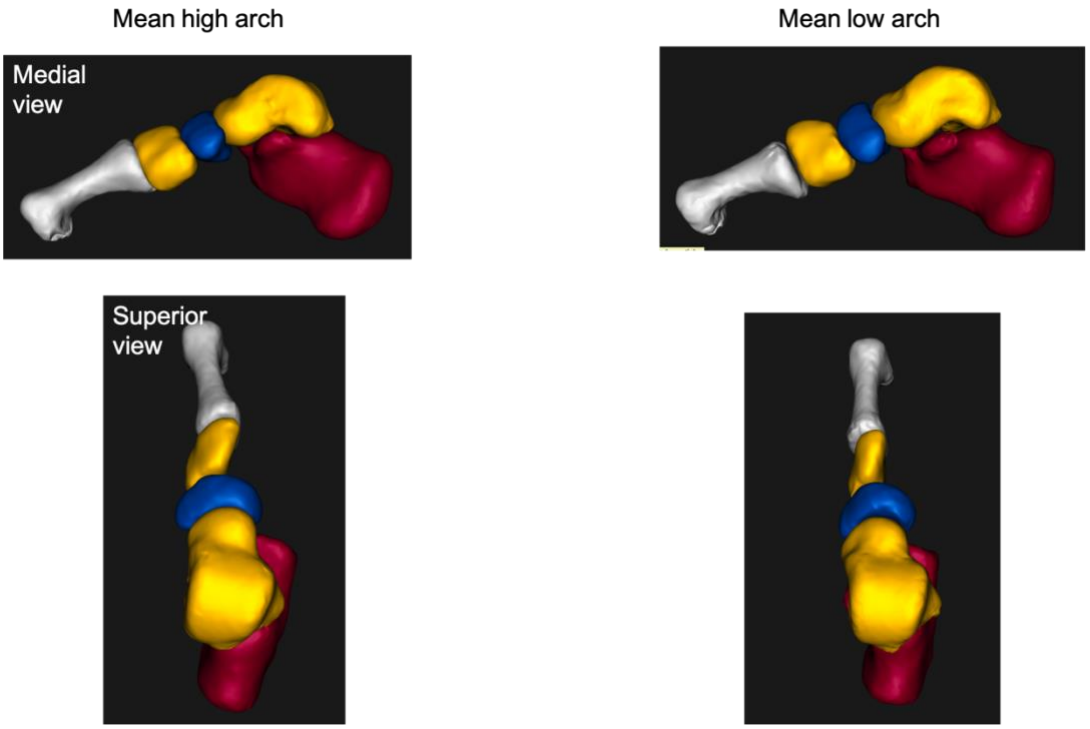

Figure 27 Showing the mean low arch medial ray bones (right) and mean high arch medial ray bones (left)

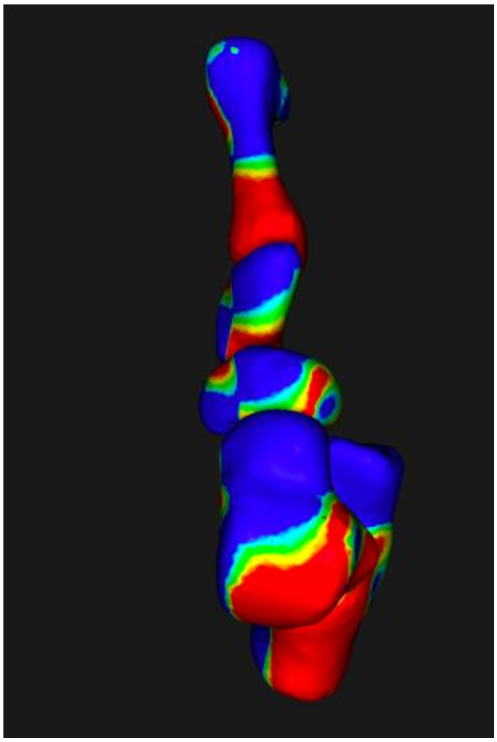

Figure 28 Posterior view of the mean differences between low and high arch foot types. Red indicates the low arch foot orientation and position, and blue indicates the high arch foot orientation relative to the low arch bone.

Using GPA and focusing on morphological variation between low and high arch foot types, a comparison shows the low arch group to have morphological differences shaded in red/yellow compared to the high arch group, where areas are shaded in dark blue, there was not an average difference between groups, shown in Figures 29 and 30. For the mean low arch group the morphological differences for the calcaneus and talus were on the posterior lateral aspect and anterior medial aspects; for the navicular the mean difference was on the anterior medial aspect; for the medial cunneiform the mean difference was greatest on the anterior medial and posterior lateral aspect; and for the first metatarsal the greatest differences were observed on the posterior medial and lateral aspects and the anterior medial aspect.

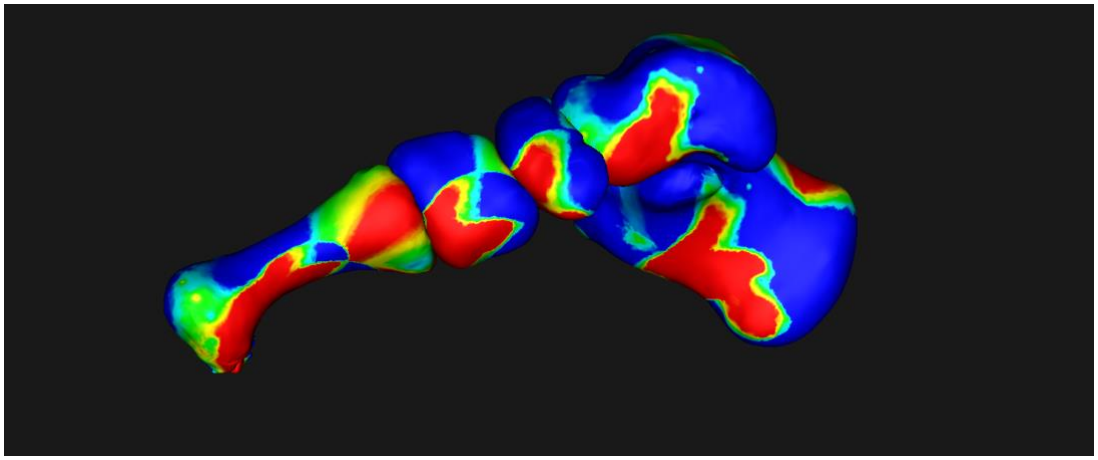

Figure 29 Medial view showing morphological variation between low and hight arch foot types. Red indicates the low arch foot morphological differences and blue indicates the high arch foot morphological differences relative to each other

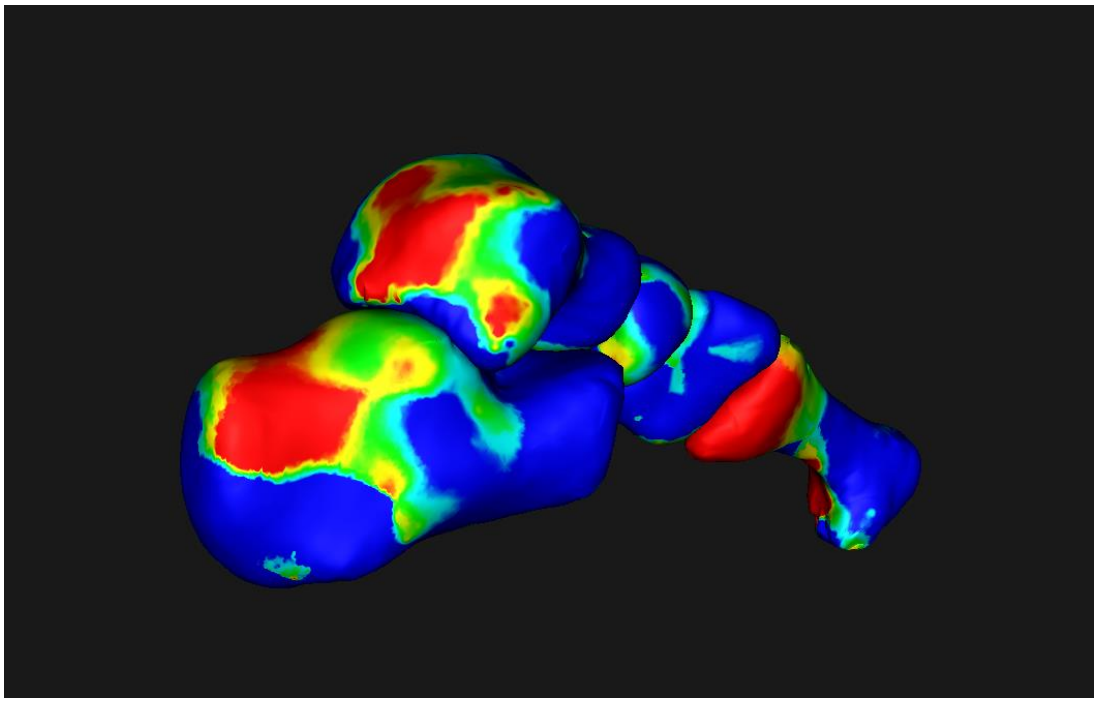

Figure 30 Posterior lateral view showing morphological variation between low and hight arch foot types. Red indicates the low arch foot morphological differences and blue indicates the high arch foot morphological differences relative to each other.

4.3.1.1 Calcaneus shape analysis

The first PC in the data set without Procrustes analysis was responsible for the valgus/varus rotation. Figure 31 demonstrates the mean and ± 2 standard deviations from the mean calcaneus shape and presents the first two PC's that describe variation within the dataset. The second PC in the dataset relates to the calcaneal pitch.

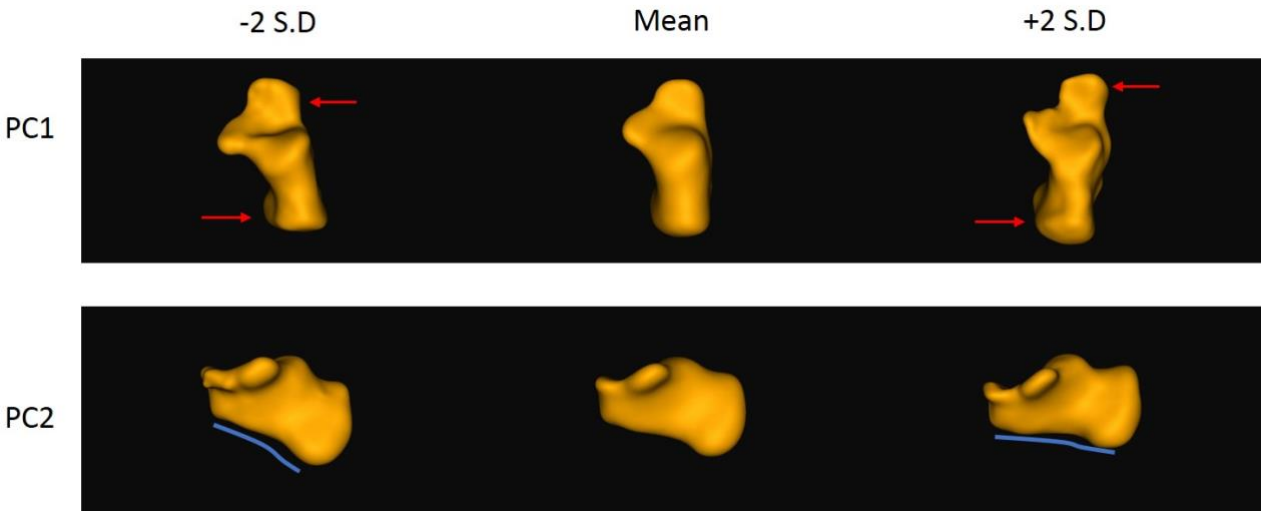

Figure 31 PC's 1 and 2 describing positional variation in 15 calcanei. The red arrows in PC 1 indicate the aspect of the bone that varies most. The blue line in PC 2 shows the inclination seen in the bone**.**

Extracting PC values from the analysis revealed that the calcaneus bones, described by 14 PC's, had the first three PC's describing 77.1% of the

position and orientation variation (PC1 = 50.6%, PC2 = 19.0%, PC3 = 7.5%) shown in Figure 32.

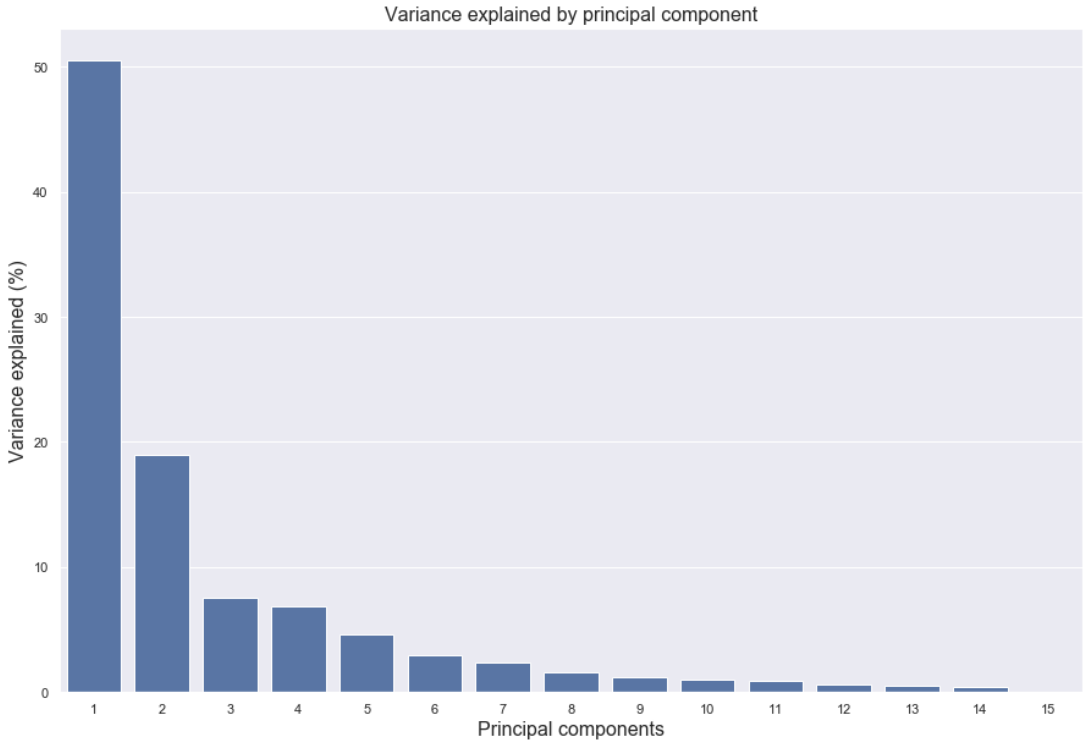

Figure 32 Cumulative variation of the Calcaneus bone explained by PC analysis

PC scores of the foot populations for the calcaneus bone were extracted from the analysis and categorised into three subgroups, a low, normal, and high arched foot type, represented in Figure 33. Potential class boundaries for groups can then be inferred from the latent space defined as the result of the dimensionality reduction in PCA.

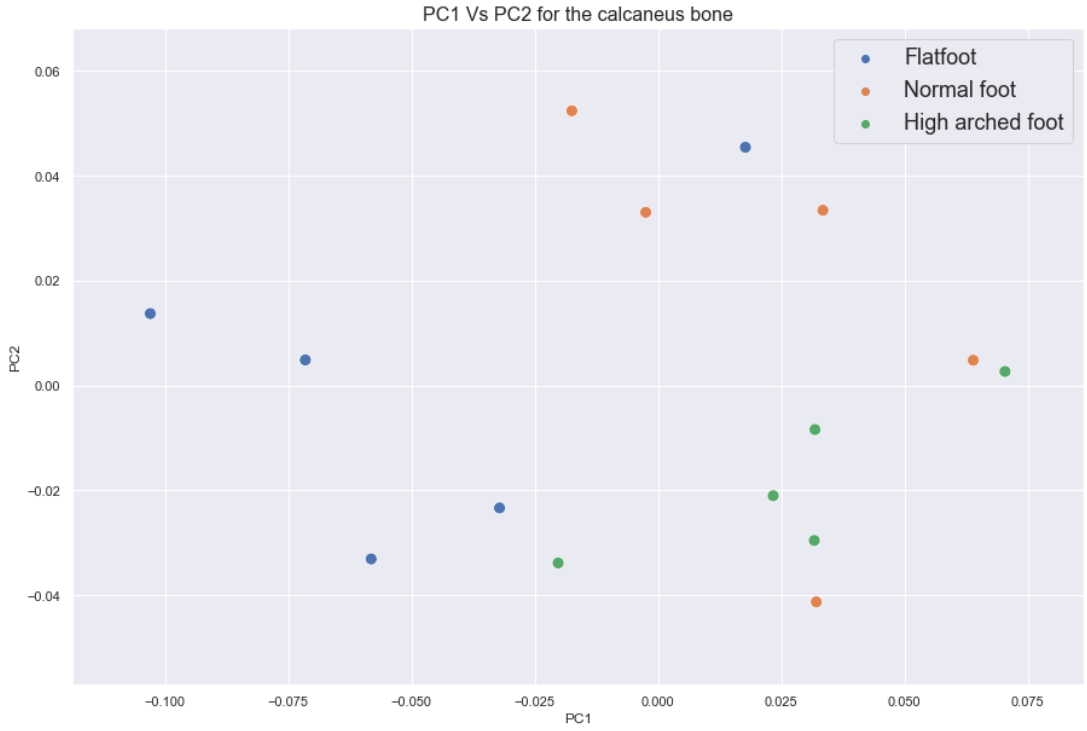

Figure 33 PC1 and PC2 scores of calcaneus bones categorised by three-foot population groups low, normal and high arch.

PC scores of the calcaneus bones show the low arch group to be linked with lower PC1 scores and the high and normal groups to share similar, but greater PC scores, presented a kernel density plot in Figure 34. The second PC in the dataset, presented in Figure 35 shows the high arch group to occupy a tighter range of lower PC scores and the normal and low arch groups are more dispersed across the distribution of the second PC space.

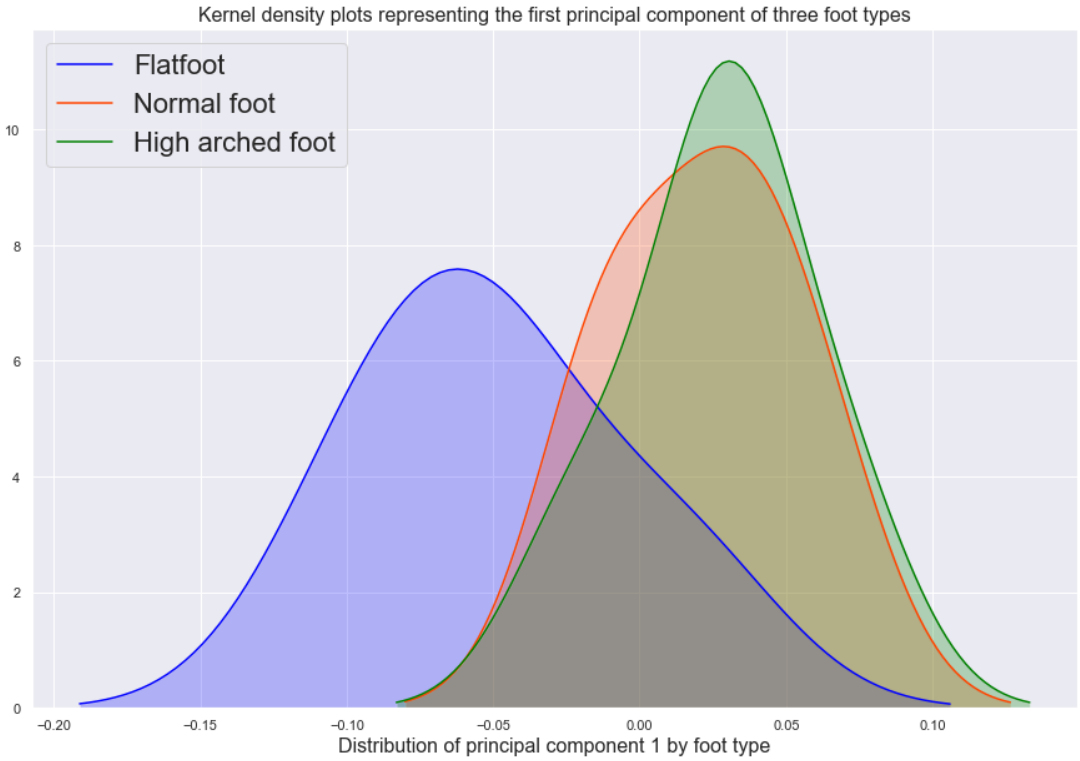

Figure 34 Showing PC 1 grouped by low, normal and high arched foot types for the calcaneus bone

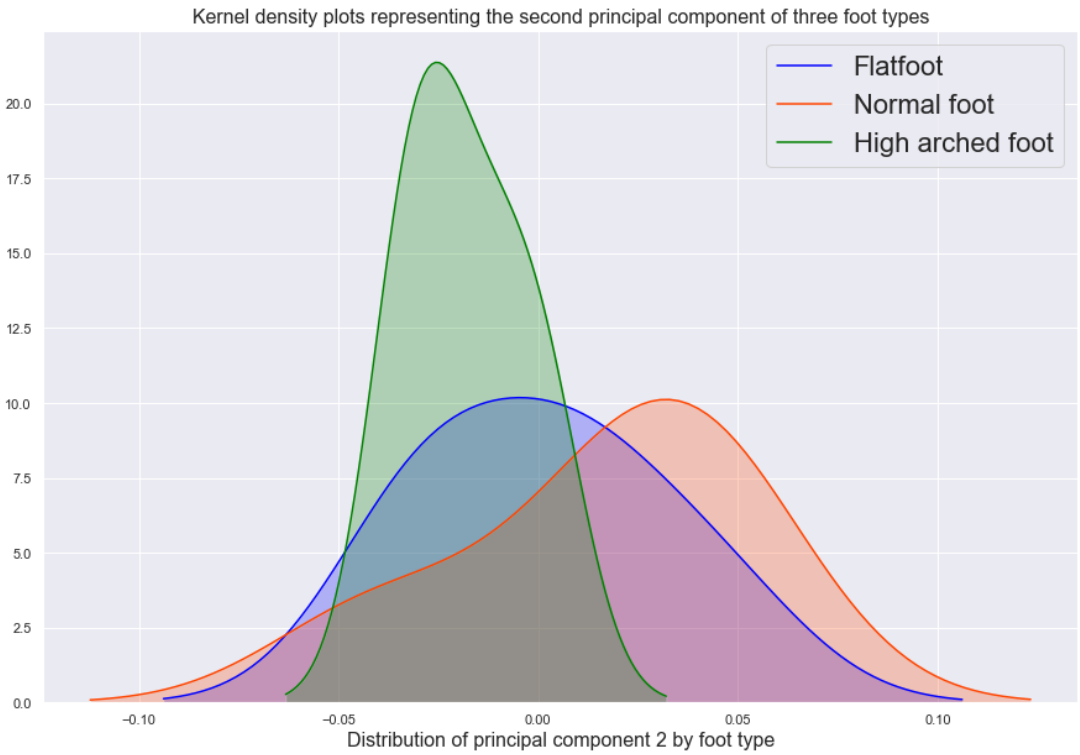

Figure 35 Showing PC 2 grouped by low, normal and high arched foot types for the calcaneus bone

Focusing on morphological variance within the calcaneus bone, when controlling for size, orientation and applying Procrustes analysis during the particle optimization on shape works v 6.1, morphological variations in the total calcaneal dataset can be described. The calcaneal data show the first principal mode of variation (31% variance) to be associated with the height of the posterior mass, visualised in Figure 36.

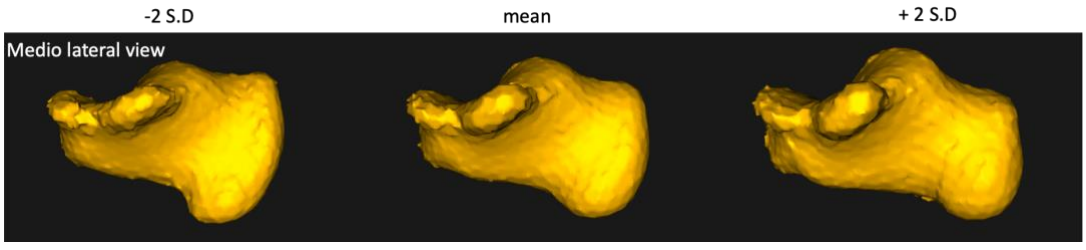

Figure 36 Showing the first principal mode of variation showing changes in morphology within the population for the calcaneus bones

From a morphological perspective, comparing mean difference in shapes for the low and high arch populations for the calcaneus bone, visualised in Figure 37 show areas of anatomical variation between the mean representations of the low and high arch foot types. Considering the calcaneus, generally low arch foot types have morphological variations on the anterior medial and posterior lateral aspects, superior aspects of the posterior talar articulating surface and sustentaculum tali of the calcaneus bone compared to the high arch foot type.

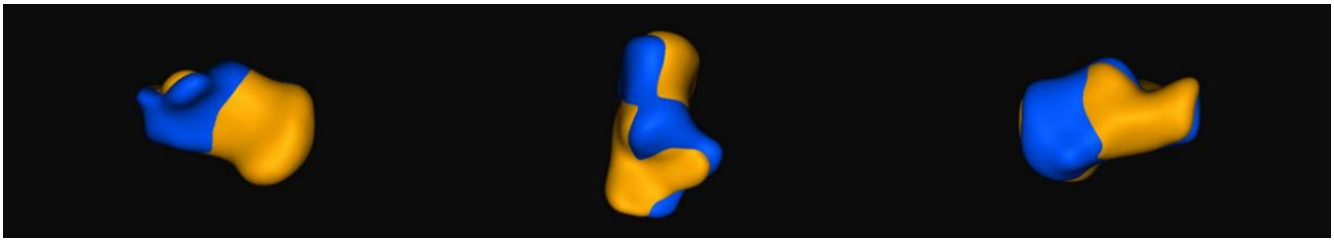

Figure 37 The mean low arch (blue) and mean high arch (orange) populations for the calcaneus bone

4.3.1.2 Talus shape analysis

The first PC in the talus data set without Procrustes scaling is visualised in Figure 38 and appears to be linked to a positional change of medial lateral angle of the talar dome, and the redistribution of bone on the medial and lateral sides if the talar head. The second PC is responsible for the anterior posterior tilt of the talus bone.

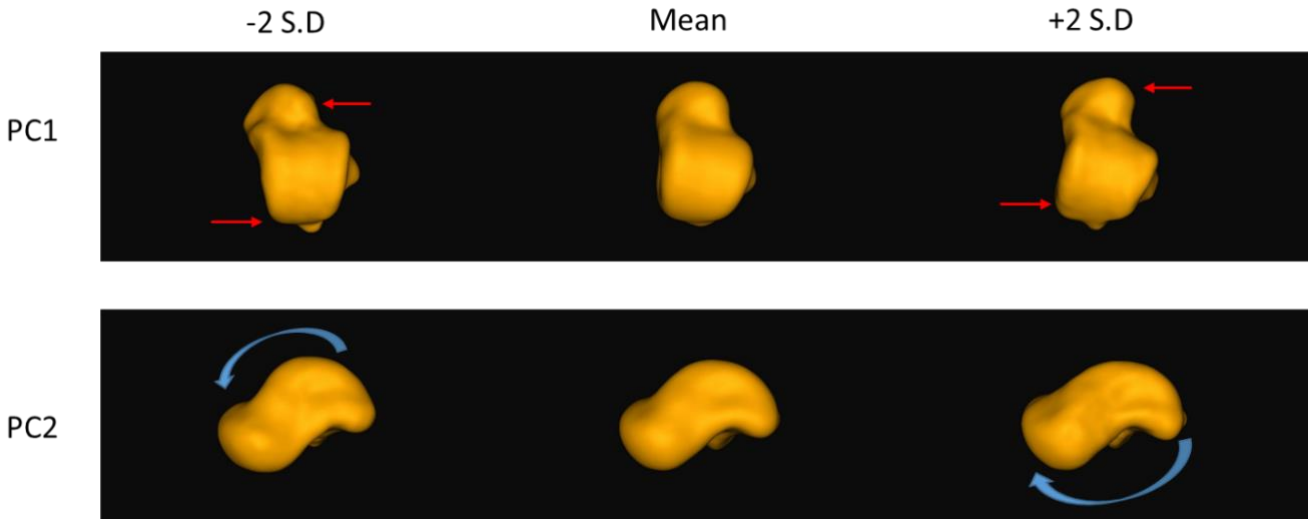

Figure 38 PC's 1 and 2 describing variation of 15 talus bones. The red arrows in PC 1 indicate the aspect of the bone that varies most. The blue arrow in PC 2 shows the direction of the rotation seen in the bone.

Investigating positional and orientational variance, the talus bones were described by 14 PC's. The first three PC's described 75.8% of the variation (PC1 = 50.9%, PC2 = 16.0%, PC3 = 8.9%) presented in Figure 39.

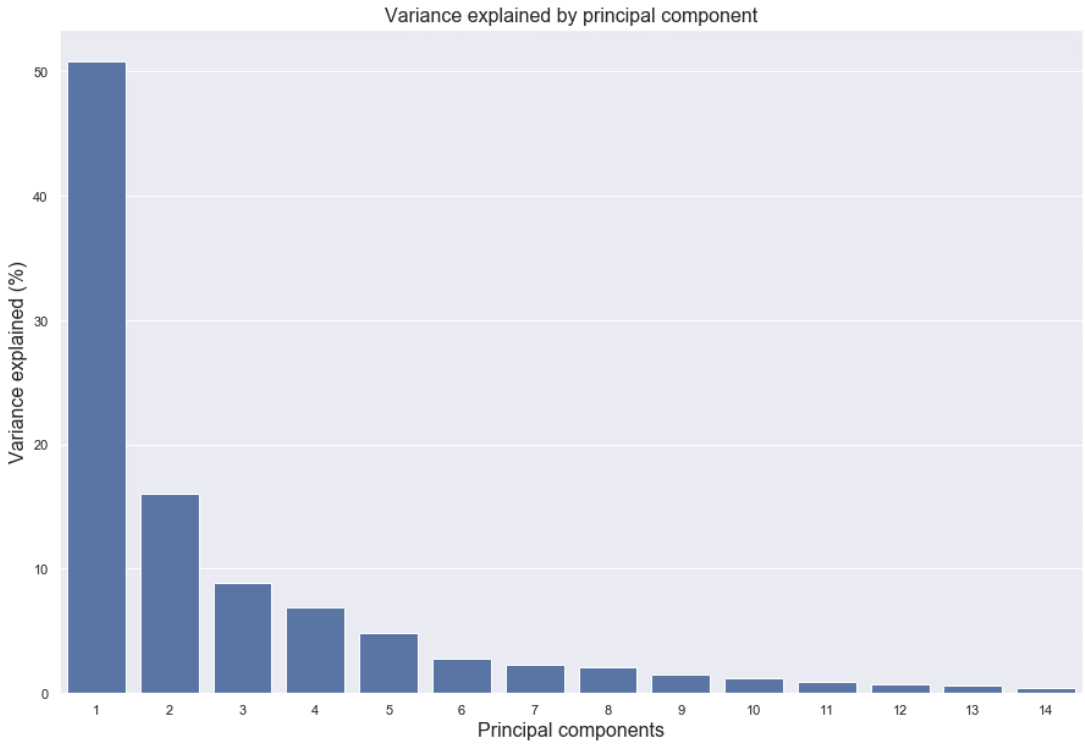

Figure 39 Variation of the talus bones explained by PC analysis

PC scores of the foot for the talus bone were extracted from the shape analysis and divided into three subgroups: low, normal and high arch foot groups. These categories could then be visualised in a 2d graph representing orthogonal PC's and facilitating the possible investigation on anecdotal boundaries in latent space, as presented in Figure 40.

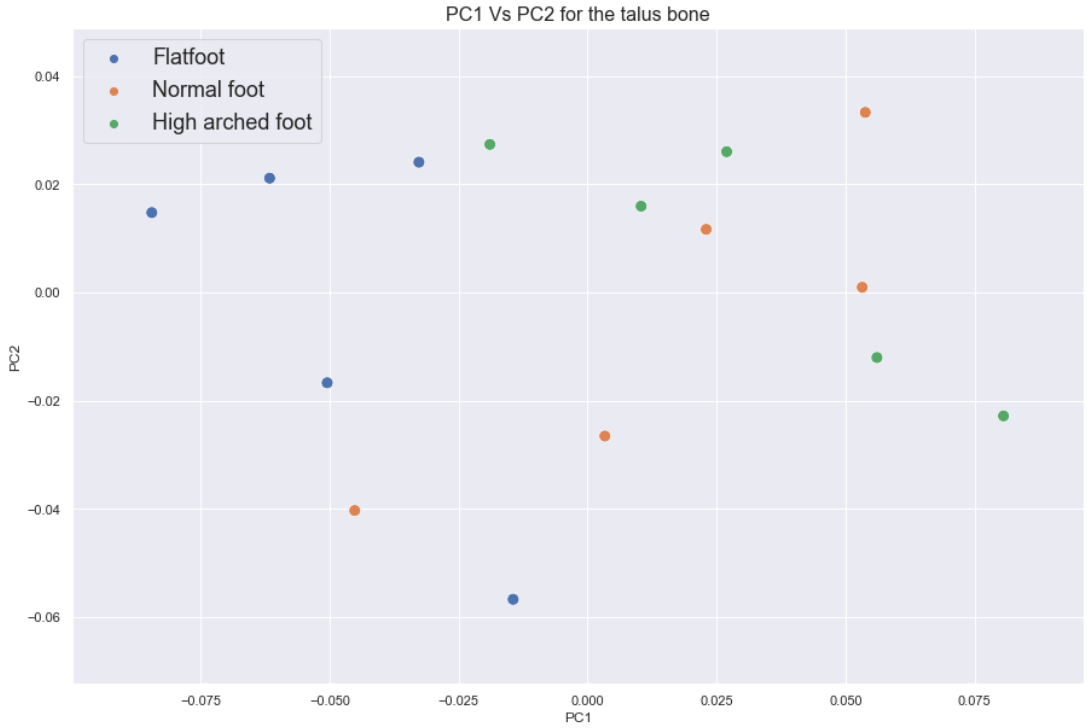

Figure 40 PC1 and PC2 scores of talus bones categorised by three-foot population groups low, normal and high arch types.

An analysis of PC scores of the talus bones describing positional variance show the low arch group to be linked to lower PC1 scores and the high and normal arch groups to share similar, but greater PC scores. The first PC for groups low, normal and high are visualised in a density plot in Figure 41. The second PC in the dataset shows, presented as a kernel density estimation plot in Figure 42, showed all groups share similar scores in the second PC space.

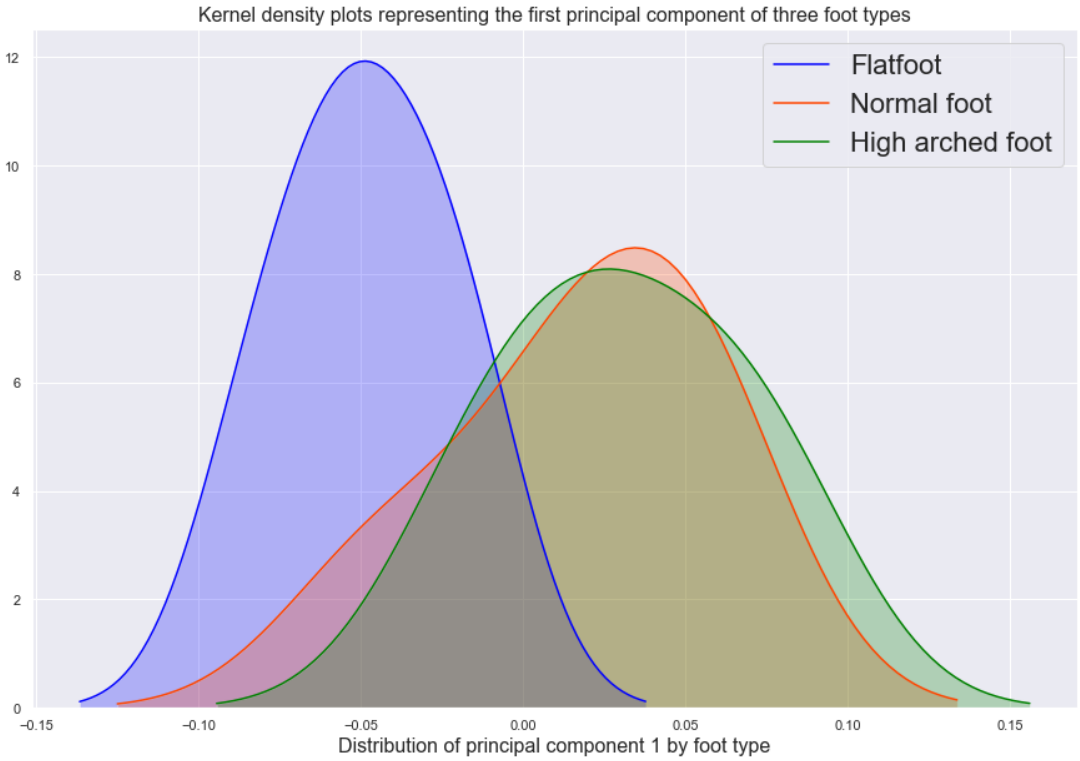

Figure 41 Showing PC 1 grouped by low, normal and high arched foot types for talus bones

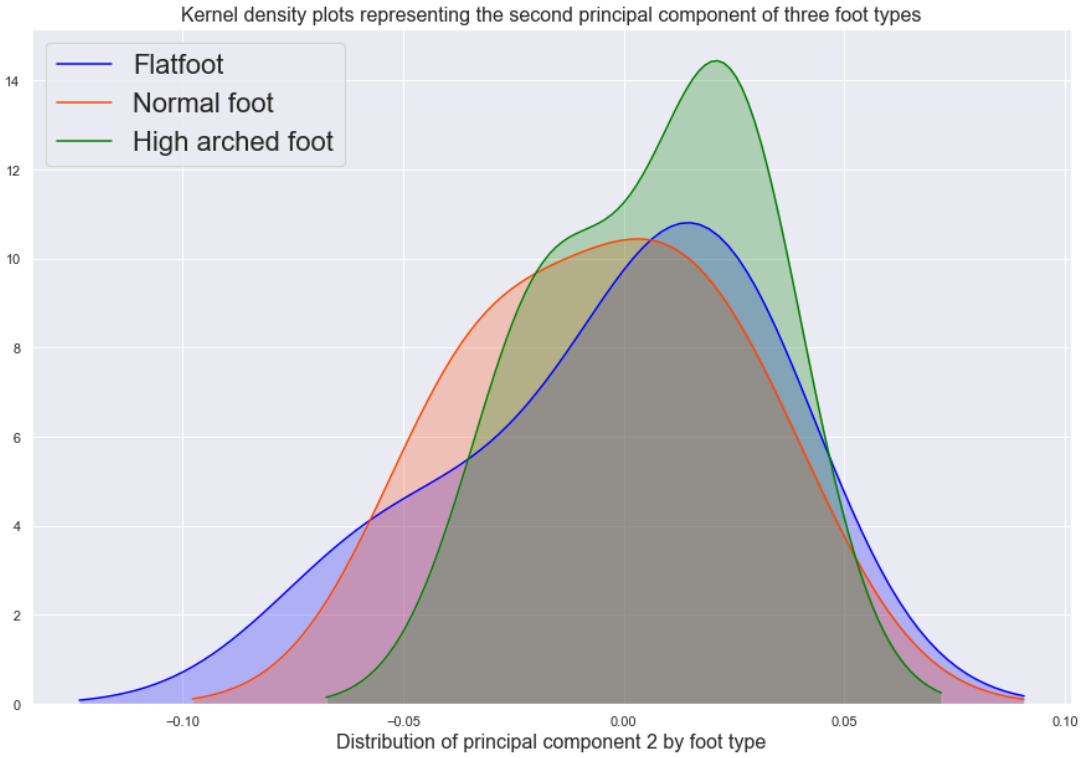

Figure 42 Showing PC 2 grouped by low, normal and high arched foot types for the talus bones

Further analysis on the morphological variation within the talus, showed that controlling for size and orientation, morphological variations in the total talus data could be found. The first PC was responsible for 23.9% of the variance within the dataset and was linked with the height and length of the talar dome and the lateral tubercle, visualised in Figure 43, which shows the morphological mean shape with - 2 standard deviations, associated with a shortening in length and increase in height of the talus, and + 2 standard deviations associated with an increase in length, but decrease in height of the talus bone.

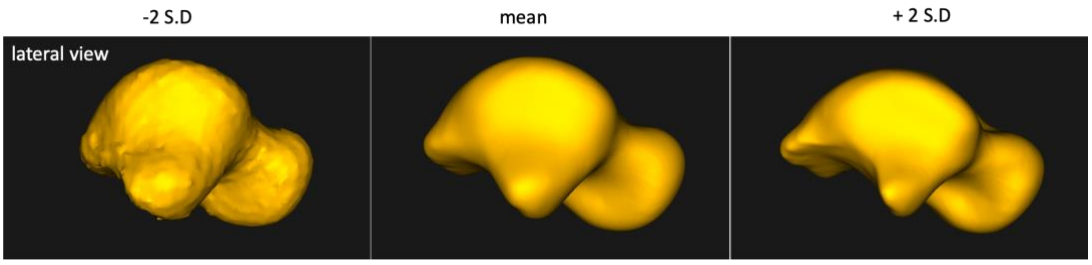

Figure 43 The first principal mode of variation showing changes in morphology within the all the talus bones

Mean morphological shapes for the low and high arch populations is presented in Figure 44. The images show areas of anatomical variation between the mean representations of the respective populations for the talus bone. The images indicate the low arch foot populations to have morphological bone additions on the anterior medial aspect of the talus and posterior lateral aspect, including the lateral process, relative to the high arch foot population.

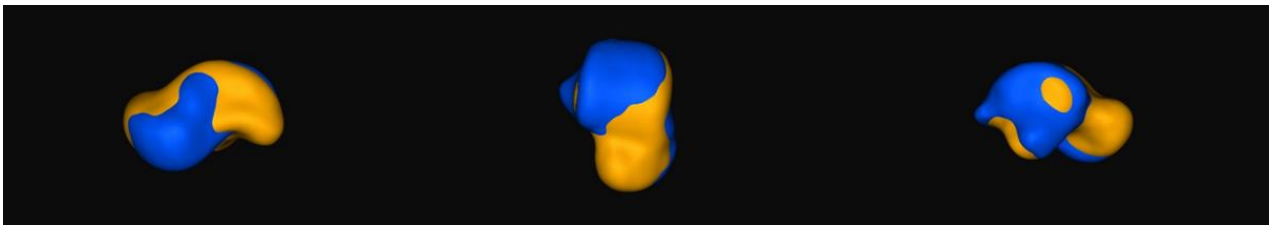

Figure 44 Showing the mean low arch (blue) and mean high arch (orange) populations for the talus bone

4.3.1.3 Navicular shape analysis

The first PC in the navicular data set without Procrustes scaling was linked to a mediolateral rotation and change in position. At – 2 standard deviations, the bone rotates slightly medially and at + 2 standard deviations, the bone rotates, slightly laterally. Also linked to the first PC is a change to the medial aspect of the navicular bone, where at – 2 standard deviations the medial aspect of the bone drops inferiorly and at + 2 standard deviations the medial aspect rises superiorly. The second PC describing the navicular dataset is associated with superior and inferior tilt. Figure 45 shows a visual representation of the mean shape with ± 2 standard deviations of the navicular shape and incudes with the first two PCs that describe positional and orientation related variation within the dataset.

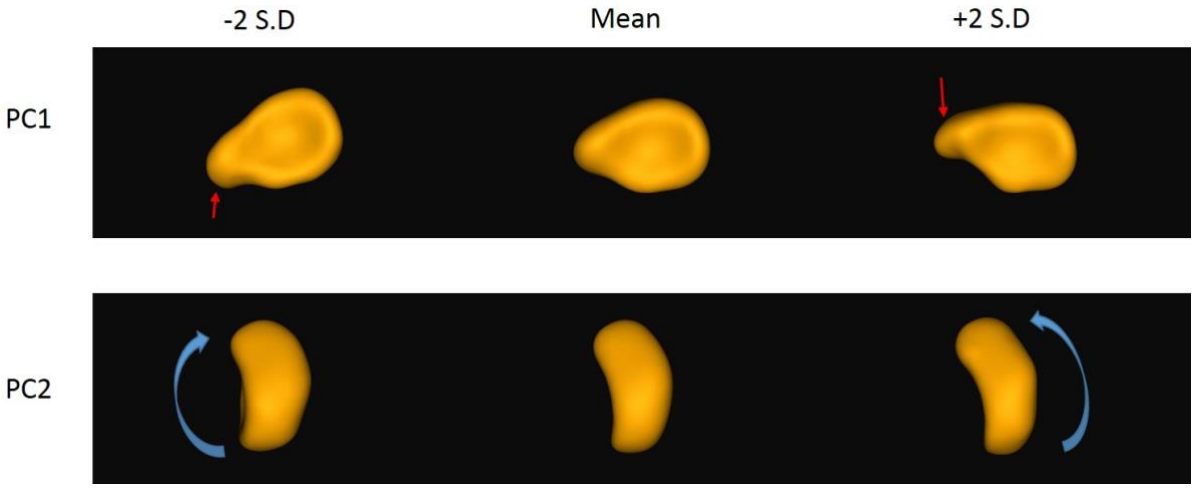

Figure 45 PC's 1 and 2 describing variation of 15 navicular bones. The red arrow in PC 1 represents the greatest anatomical area of variance. The blue arrow in PC 2 indicates the direction of rotation for the bone.

Shape analysis of the navicular bones revealed 14 PCs that described the variation in the data. The first three PC's describing 87.8% of the position and orientation variation (PC1 = 49.6%, PC2 = 31.7.0%, PC3 = 6.4%) are shown in Figure 46.

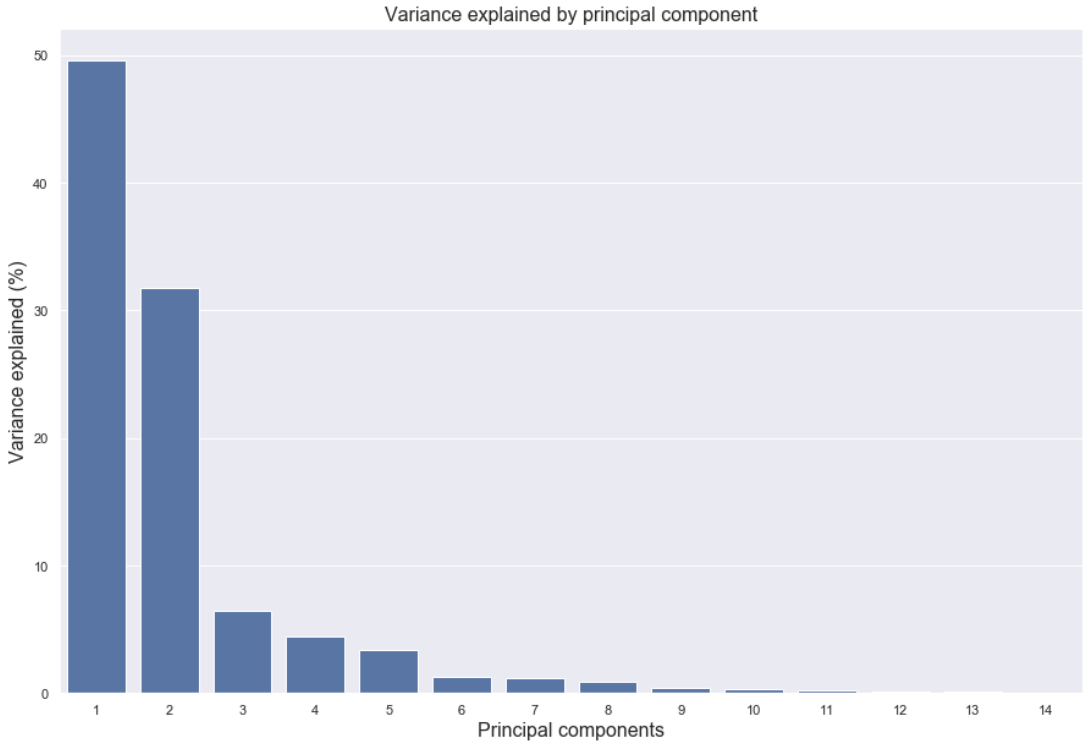

Figure 46 Variation of the navicular bones explained by PC analysis

PC scores of each of the analysed groups, low, normal and high arch populations for the navicular bone morphology were extracted from the analysis to provide a visual representation presented in Figure 47 of the patients, to help understand were potential laten space features might exist.

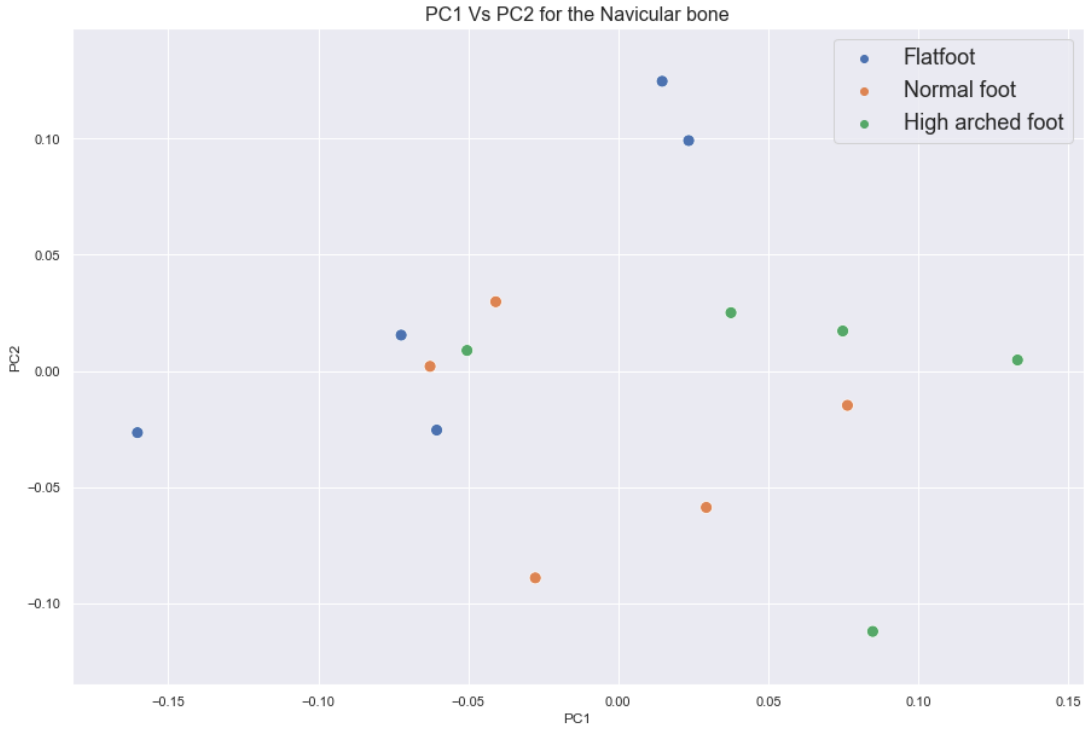

Figure 47 PC1 and PC2 scores of navicular bones categorised by three-foot population groups low, normal and high arch foot type.

For the first PC, PC scores of the navicular bones reveal all groups to share similar scores across. The low arch group tended occupy the lower end of the first PC space and the high arch groups, occupied the higher PC scores, demonstrated in Figure 48. PC 2 shows the normal and high arch groups to occupy the lower end of the second PC space and the low arch group to have more weight in the higher end of the second PC stance in Figure 49.

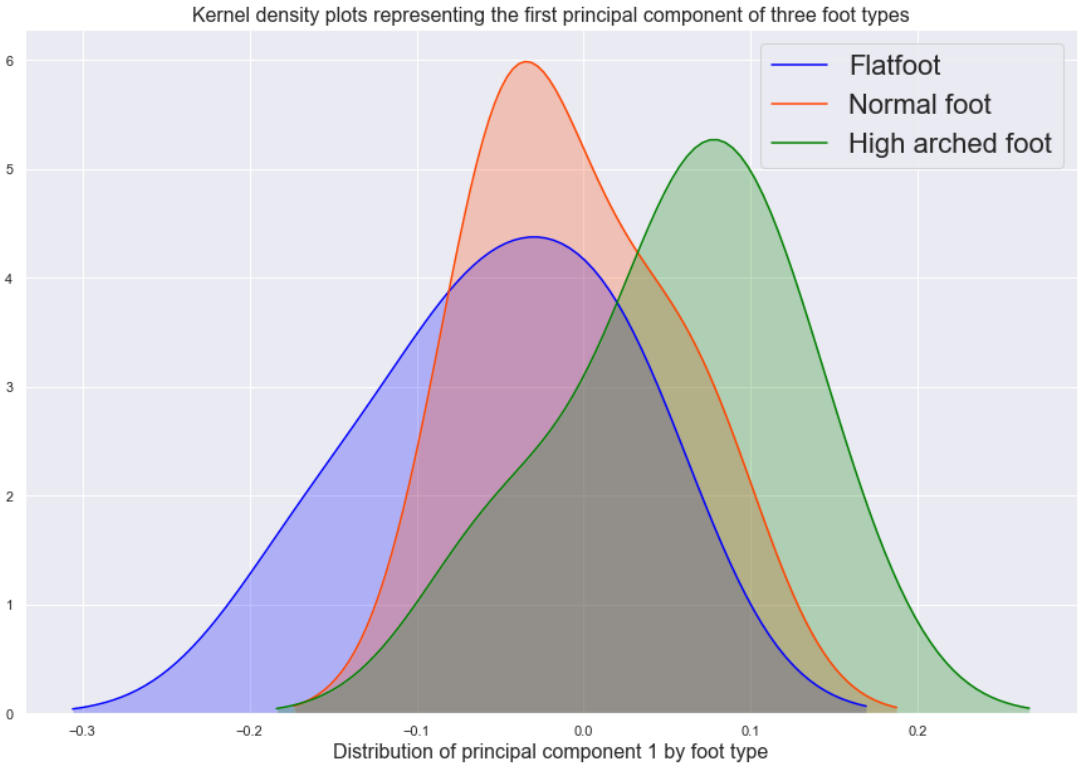

Figure 48 Showing PC 1 grouped by low, normal and high arched foot types for the navicular bones

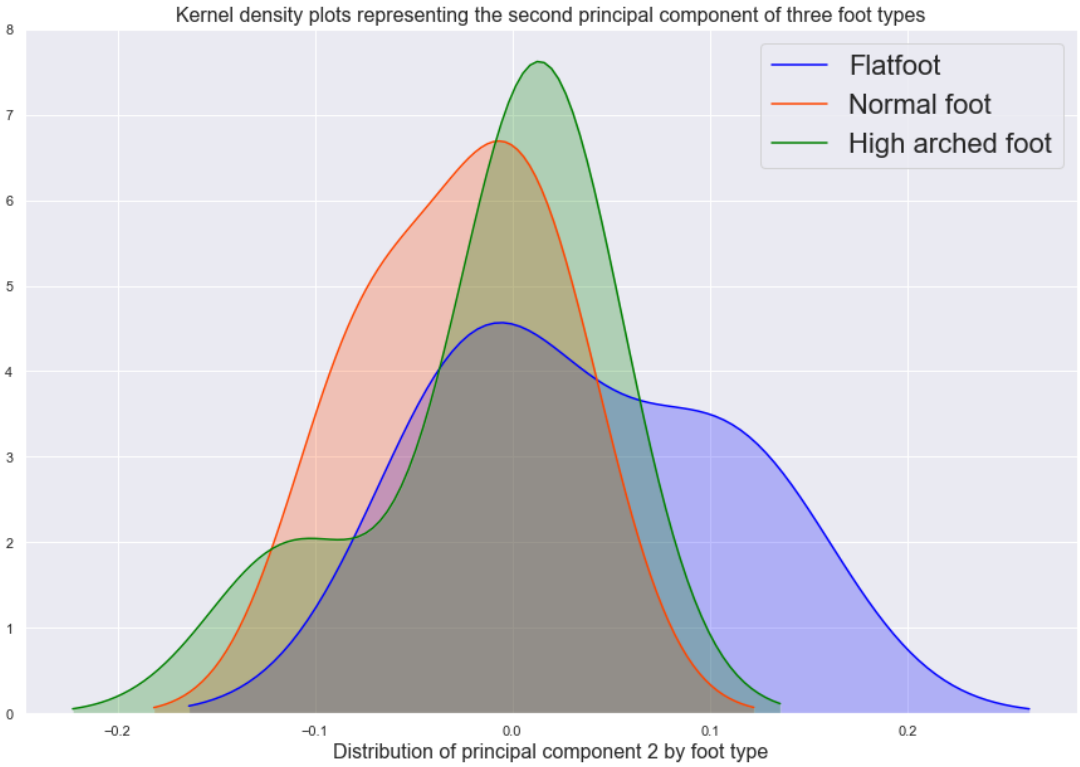

Figure 49 Showing PC 2 grouped by low, normal and high arched foot types for the navicular bones

Focusing on morphological variation within the navicular, when controlling for size and orientation, statistical shape analysis describes morphological variations in the total navicular data. The morphological differences reveal the first PC, describing 27.3%% variance in the dataset to be most closely linked to the morphology of the navicular tuberosity tubercle. In Figure 50, an anterior view of the navicular, – 2 standard deviations were associated with a rise of the navicular tuberosity tubercle and at + 2 standard deviations, a lowering of the navicular tuberosity tubercle.

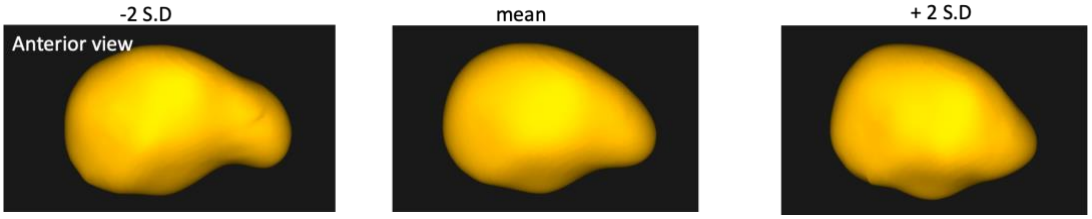

Figure 50 First principal mode of variation showing changes in morphology within the all the navicular bones

Mean shape differences for the low and high arch populations are visualised in Figure 51. Areas of anatomical variation between the mean representations of the low and high arch foot types of the navicular bone indicate the low arch foot type to have an appendage of bone on the posterior medial and anterior lateral aspects of the navicular bone compared to the high arch foot type.

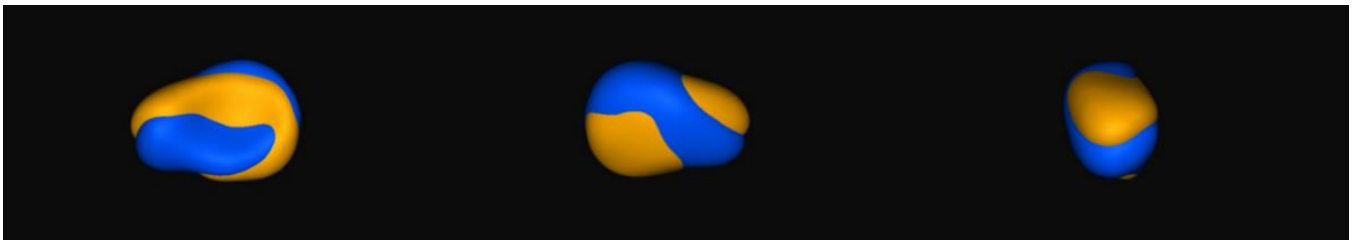

Figure 51 Showing the mean low arch (blue) and mean high arch (orange) populations for the navicular bone

4.3.1.4 Medial cuneiform shape analysis

The first PC in the medial cuneiform data, without Procrustes scaling was associated with the mediolateral tilt, with – 2 standard deviations lined to a lateral rotation and + 2 standard deviations linked to a slight medial rotation. The second PC was responsible for the subtle anterior posterior tilt, as Figure 52 demonstrates the mean and ± 2 standard deviations of the medial cuneiform shape of the first two PCs that describe the variation in the medial cuneiform dataset.

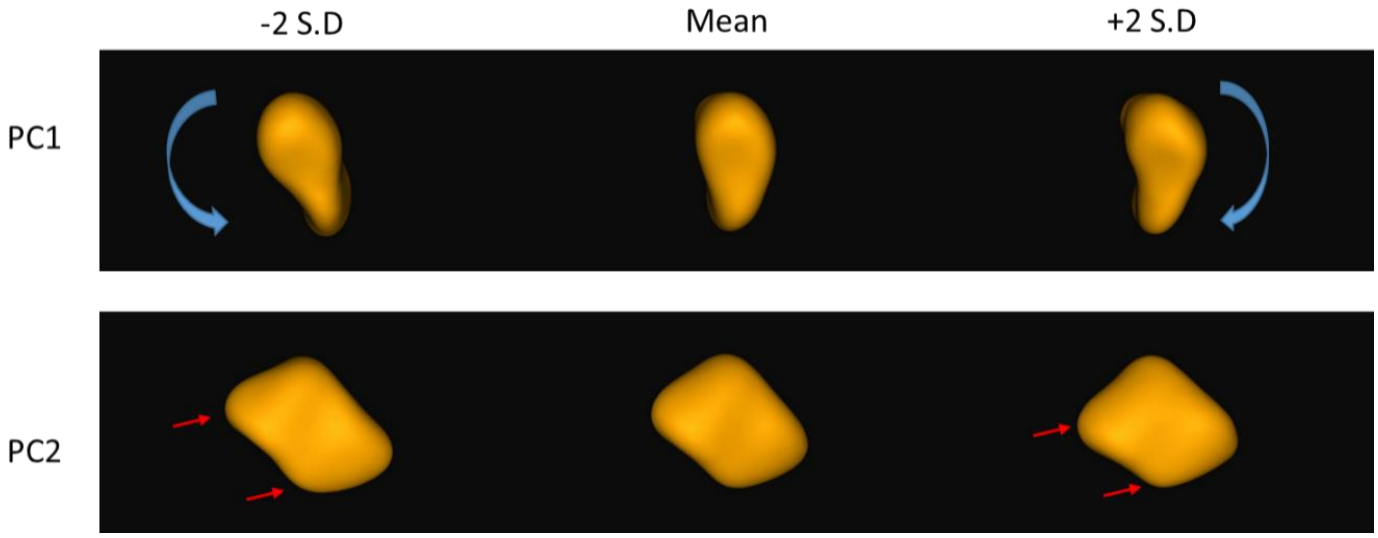

Figure 52 PC's 1 and 2 describing variation of 15 medial cuneiform bones. In PC 1 the blue arrow represents the direction of rotation for and in PC 2 the red arrows represent the area of variance

The medial cuneiform bones were described by 14 PCs with the first three PC's describing 91.6% of orientation and positional variation (PC1 = 59.7%, PC2 = 24.4%, PC3 = 7.4%), visualised in shown in Figure 53.

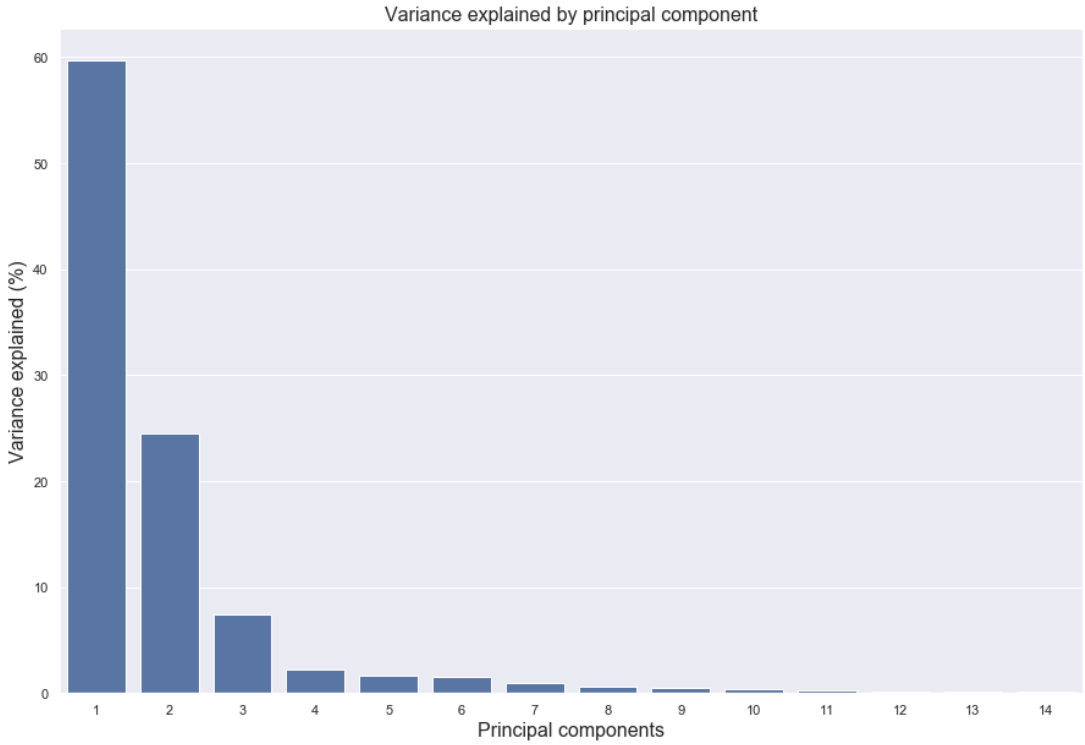

Figure 53 Cumulative variation of the medial cuneiform bones explained by PC analysis

PC scores of the three-foot types for the medial cuneiform bones were extracted from the shape analysis and divided into three subgroups: low, normal and high arch foot types. This is visualised in Figure 54.

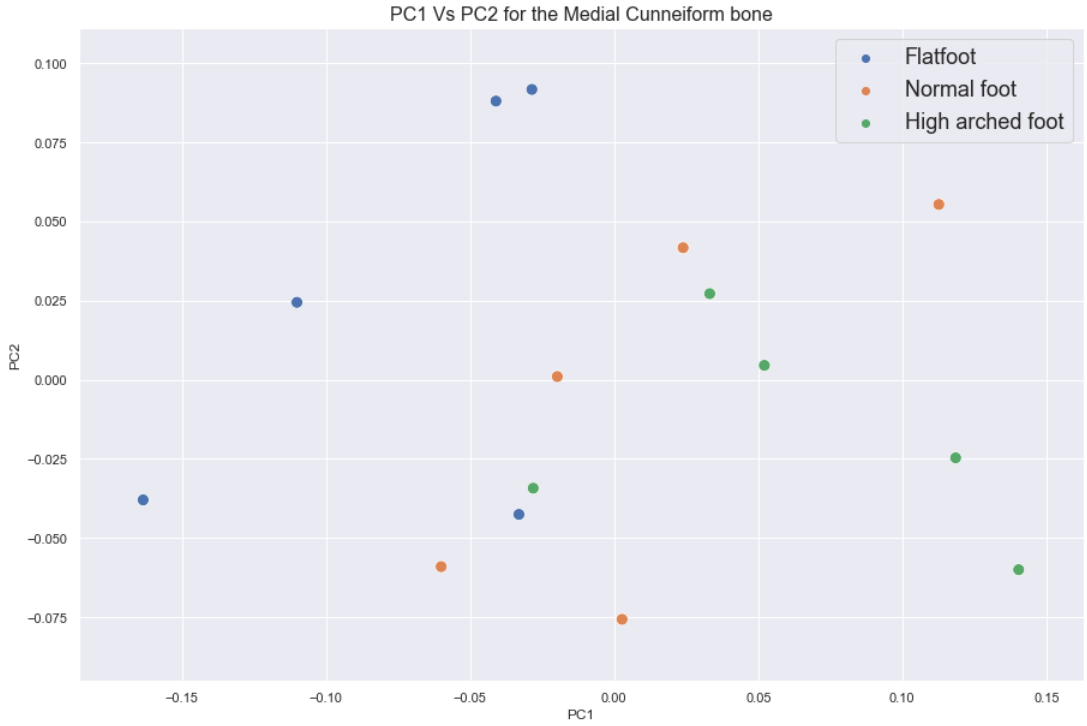

Figure 54 PC1 and PC2 scores of medial cuneiform bones categorised by three-foot population groups low, norm and high arched foot types**.**

For the first PC scores of the medial cuneiform bones show the low arch group to occupy the more of the lower end of the PC space. The normal and high arch groups occupied the higher end of the PC space, presented in Figure 55. The second PC in the dataset shows all groups to share similar of PC scores, with the high arch group occupying a smaller range in the second PC space, visually represented in Figure 56.

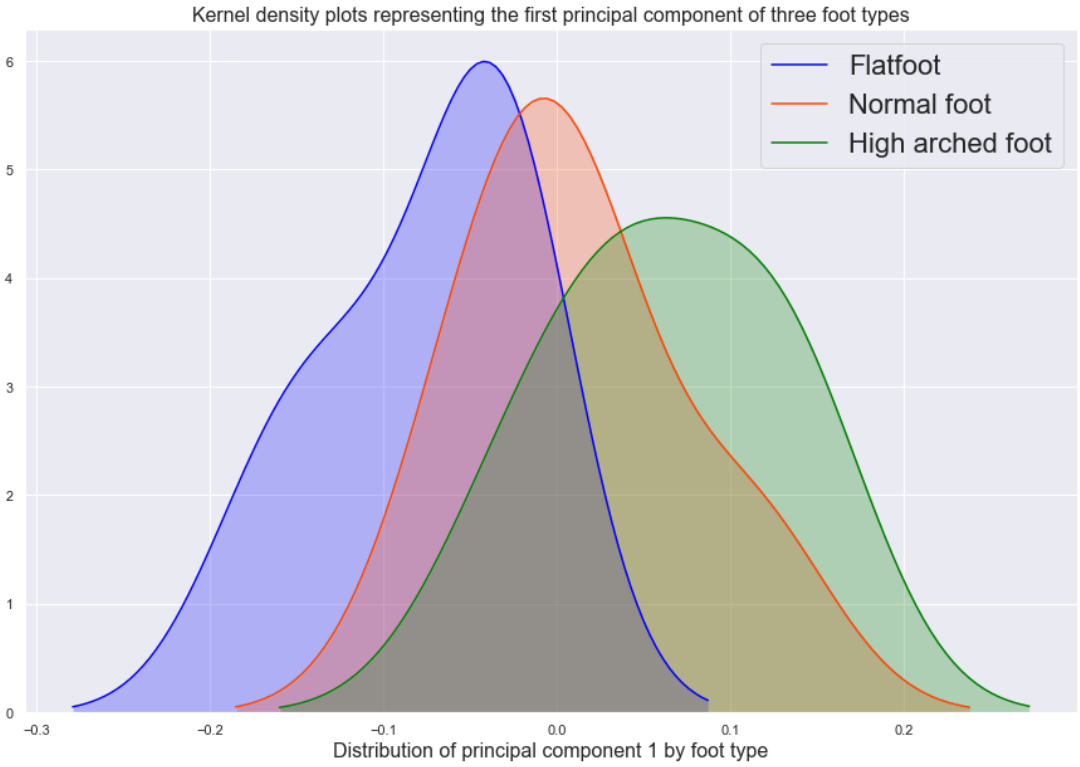

Figure 55 Showing PC 1 grouped by low, normal and high arched foot types for the medial cuneiform bones

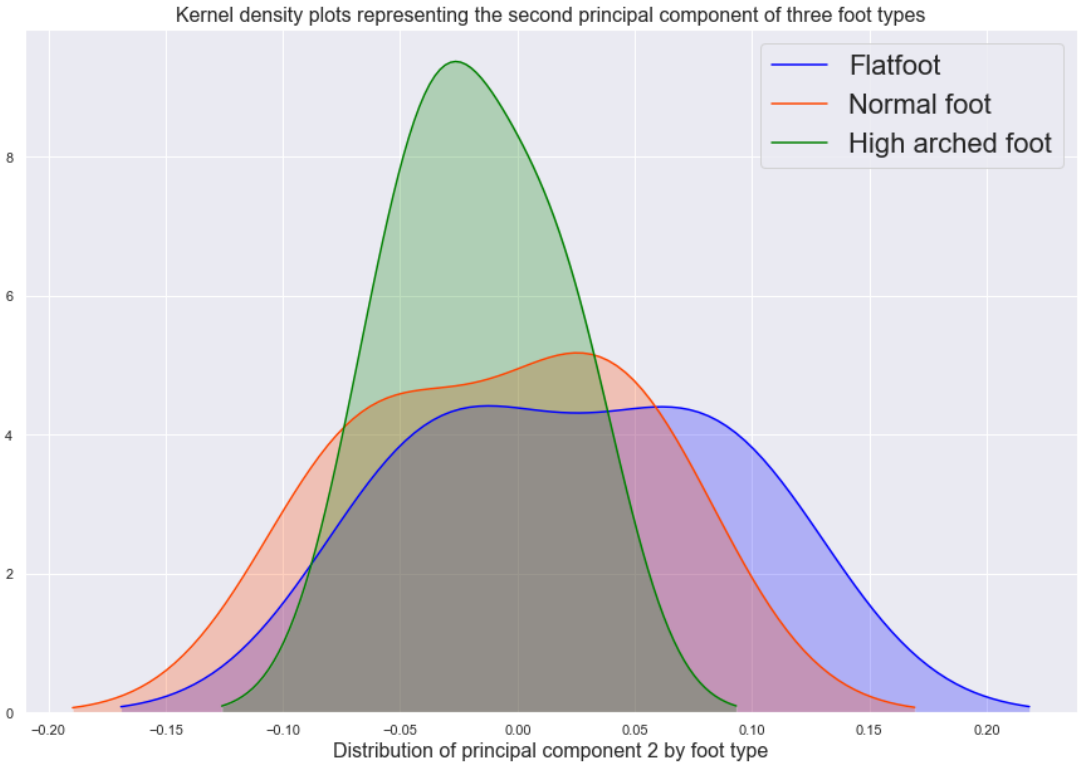

Figure 56 Showing PC 2 grouped by low, normal and high arched foot types for the medial cuneiform bones

With a focus on morphological variation within the medial cuneiform, when removing the effect of size and orientation on the shapes, morphological variations in the total medial cuneiform bone presented the first principal mode of variation, describing 30.7% variance to be associated with the morphology of the superior aspect of the posterior surface. Figure 57 shows at – 2 standard deviations, a retraction of the superior aspect of the posterior surface, while at + 2 standard deviations, there is relative morphological appendage on the superior aspect of the posterior surface.

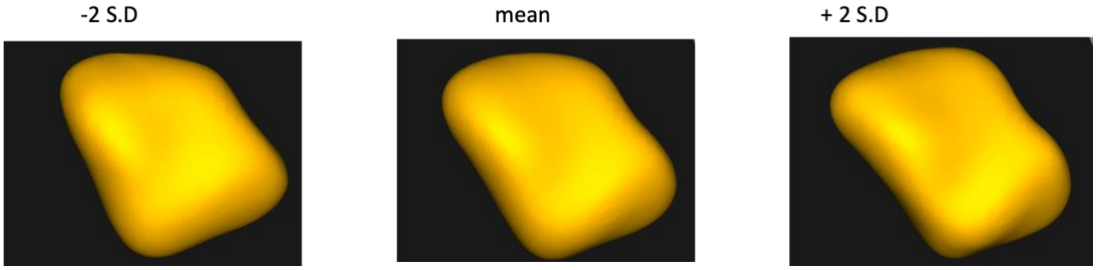

Figure 57 Showing a medial view of the first principal mode of variation showing changes in morphology within the all the medical cuneiform bones

Mean shape of the low and high arch foot types were extracted. Mean differences between the extremes of posture in Figure 58 demonstrate areas of anatomical variation between the mean representations for the medial cuneiform bone. The low arch population showed morphological addition of bone on inferior medial and superior lateral aspects of the bone.

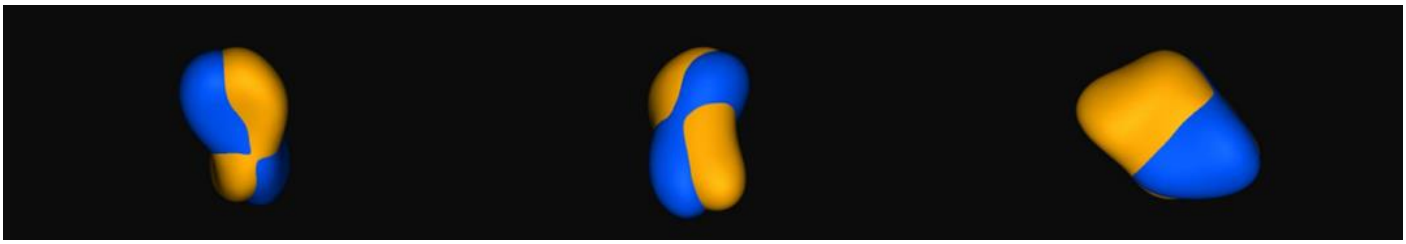

Figure 58 Showing the mean low arch (blue) and mean high arch (orange) populations for the medial cuneiform bones

4.3.1.5 First metatarsal shape analysis

The first PC in the first metatarsal bone data set was linked to positional changes in medial lateral rotation of the bone. At – 2 standard deviations, the metatarsal bone rotated laterally and at + 2 standard deviations the metatarsal rotates, medially. The second PC was linked to the anterior-posterior tilt of the metatarsal. Figure 59 demonstrates the mean and ± 2 standard deviations of the medial cuneiform shape with the first two PCs that describe variation within the dataset.

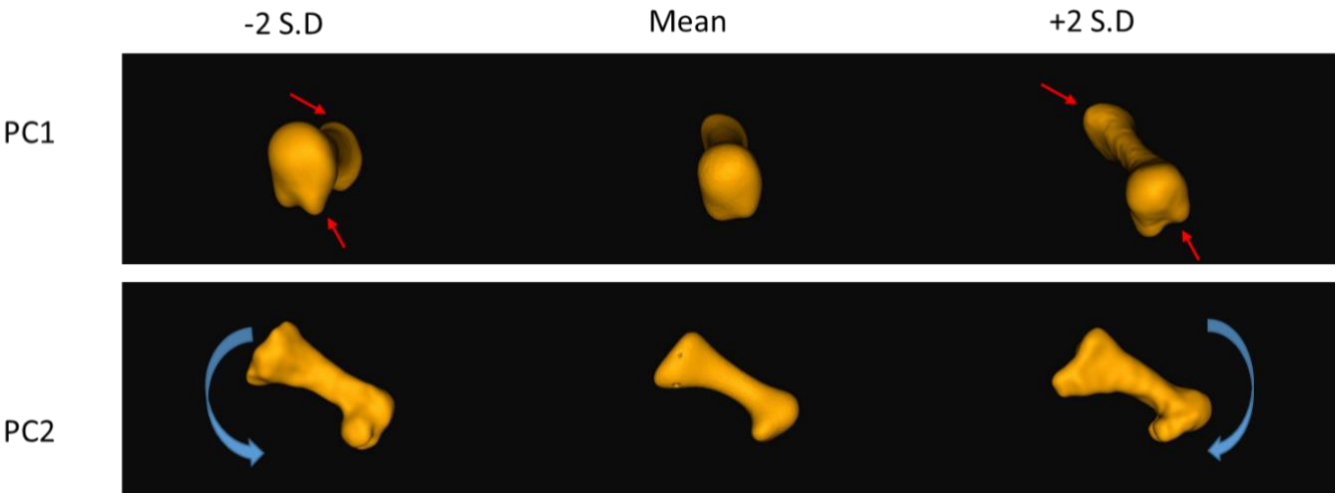

Figure 59 PC's 1 and 2 describing variation of 15 first metatarsal bones. The red arrows in PC 1 represent the anatomical area of largest variance and in PC 2 the blue arrow represents the direction tilt of the bone.

PCA of the first metatarsal bones was described by 14 PCs. The first three PCs describing 83.5% of the positional and orientation variation (PC1 = 40.6%, PC2 = 27.8%, PC3 = 15.1%) shown in Figure 60.

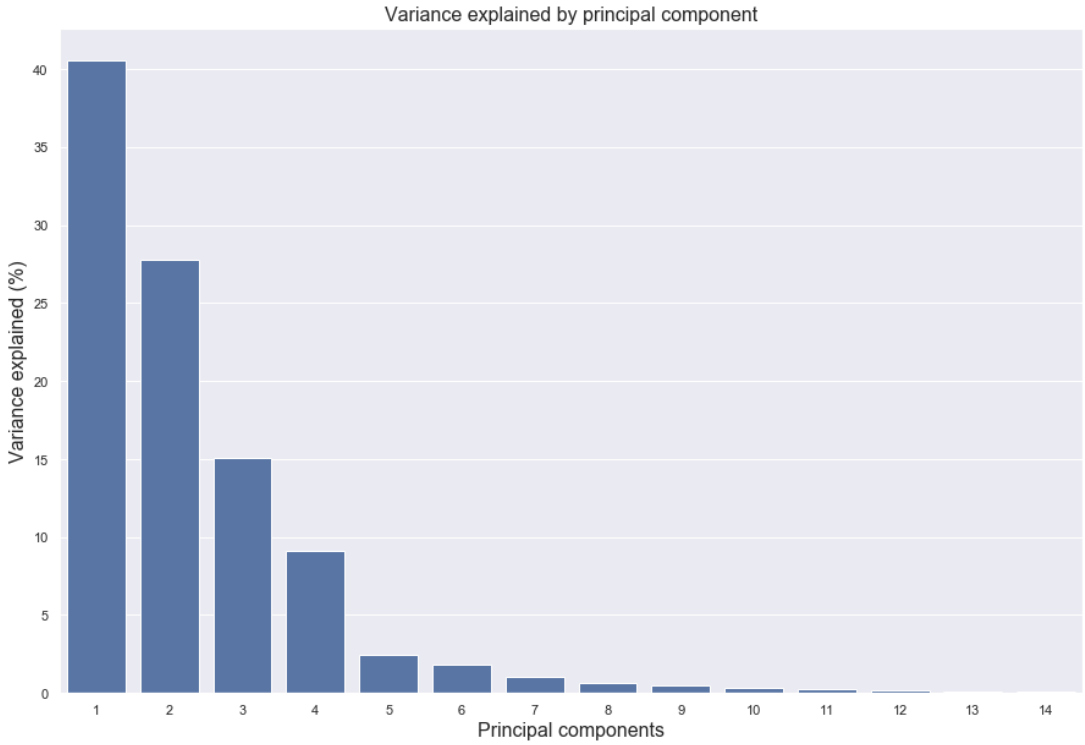

Figure 60 Variation of the first metatarsal bones explained by PC analysis

Extracting PC scores of the three-foot types for the medial cuneiform bones and divided into subgroups; low, normal and high arch foot were visualised in Figure 61.

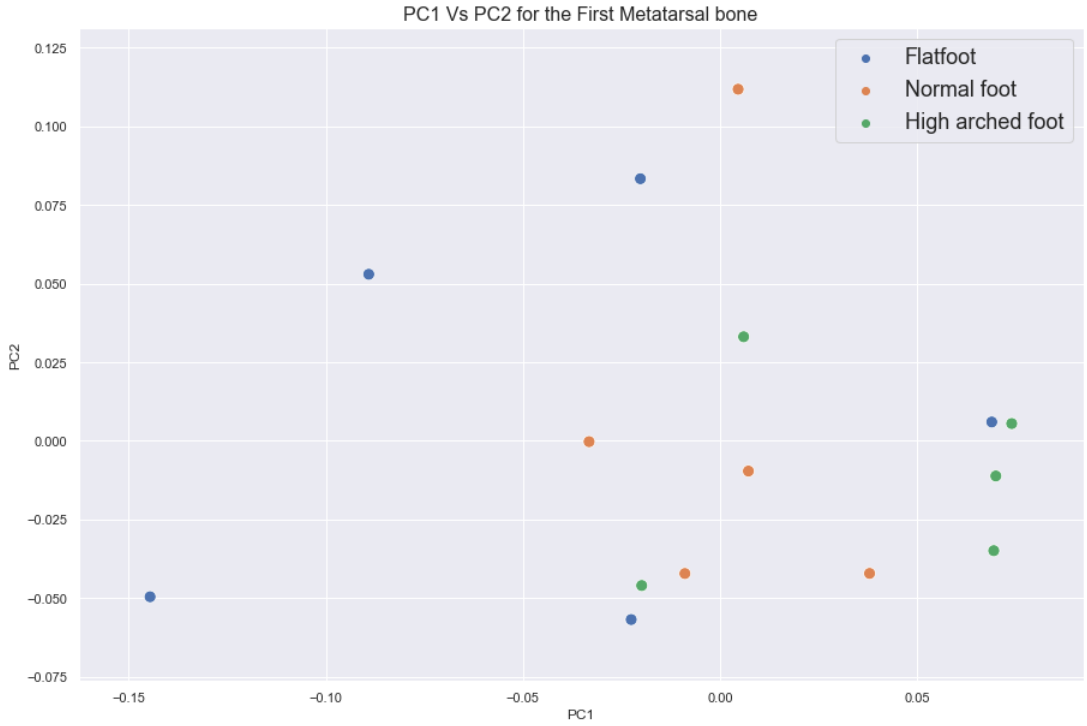

Figure 61 PC1 and PC2 scores of first metatarsal bones categorised by three-foot population groups low, norm and high arch foot types.

PC scores of the metatarsal 1 bones show the low arch group to occupy the entire fist PC range, presented with a notable tail in the lower PC1 scores. The high and normal arch groups to shared similar PC scores, with the high group also occupying the higher tail of PC 2 scores, presented in Figure 62. The second PC in the dataset shows that all groups share similar PC scores in the middle. The high arch PC scores occupy a tighter band compared to the normal and low arch foot types that have shape variations that occupy the entire spectrum of the PC 2.

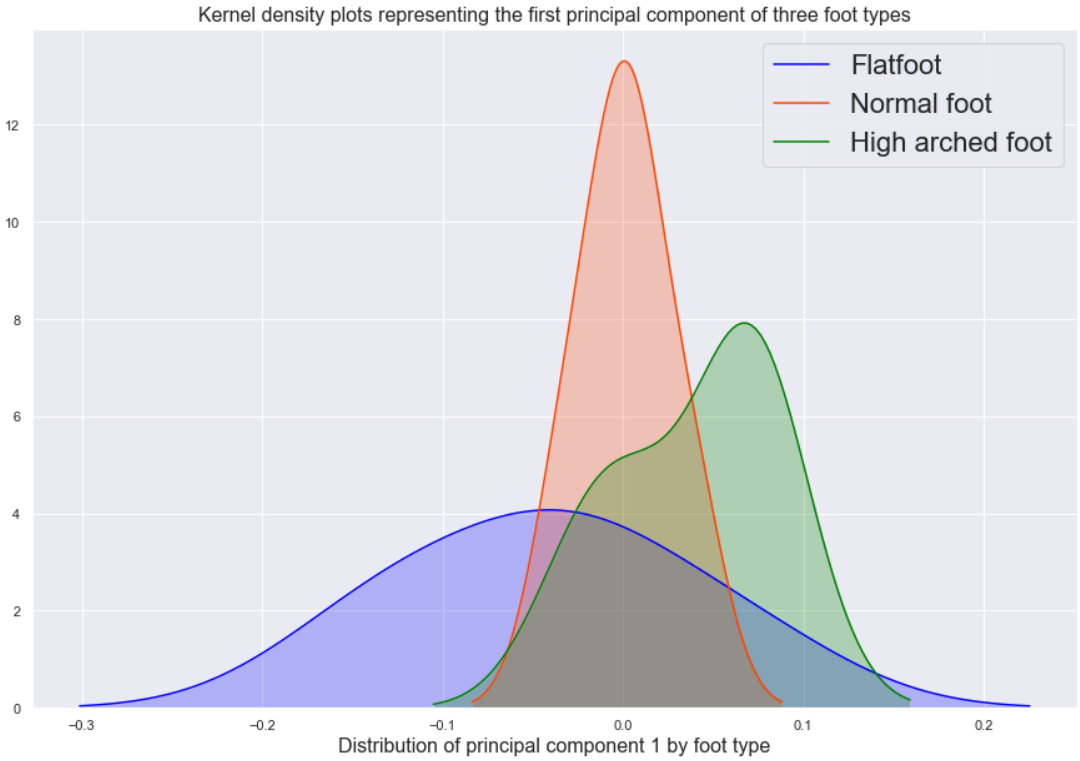

Figure 62 Showing PC 1 grouped by low, normal and high arched foot types for the first metatarsal bones

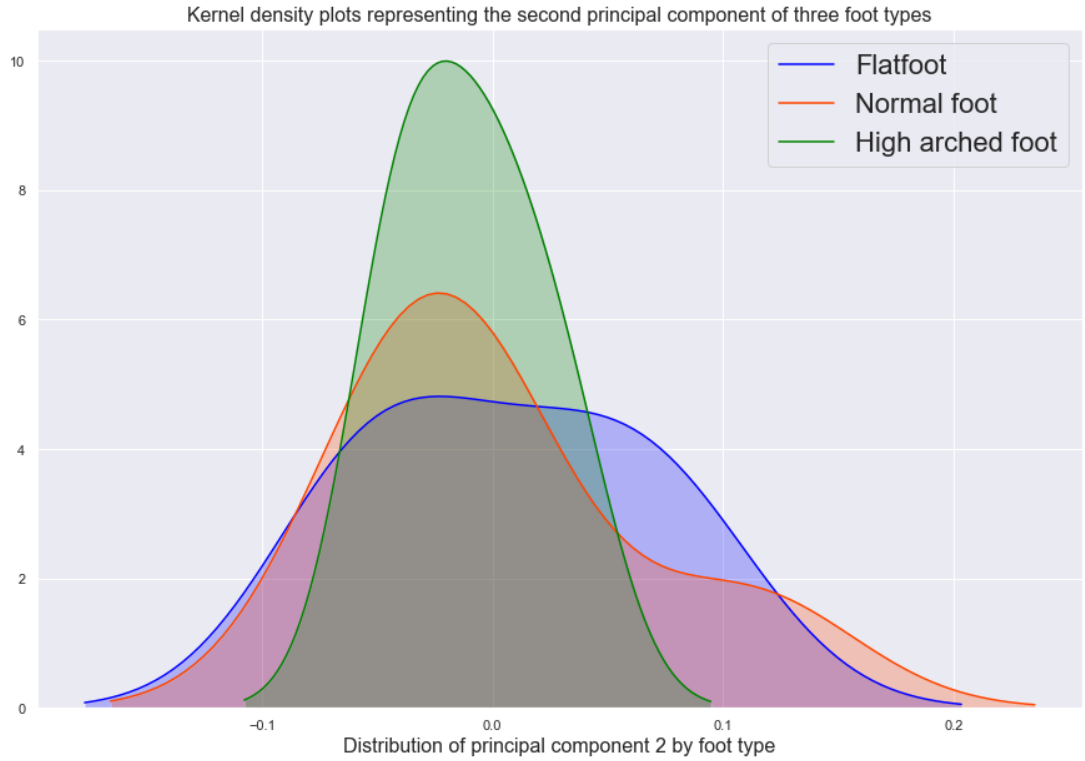

Figure 63 Showing PC 2 grouped by low, normal and high arched foot types for the first metatarsal bones

Considering, the first metatarsal and controlling for size and orientation, and therefore analysing morphological variations, the total medial cuneiform data reveal the first principal mode of variation, describing 45.0% of the variance to be associated with the thickness of the tarsal shaft demonstrated in Figure 64 with subtle differences observed at the sesamoids. At - 2 standard deviations the thickness of the metatarsal shaft is thinker than compared to +2 standard deviations where the shafts thickness reduces.

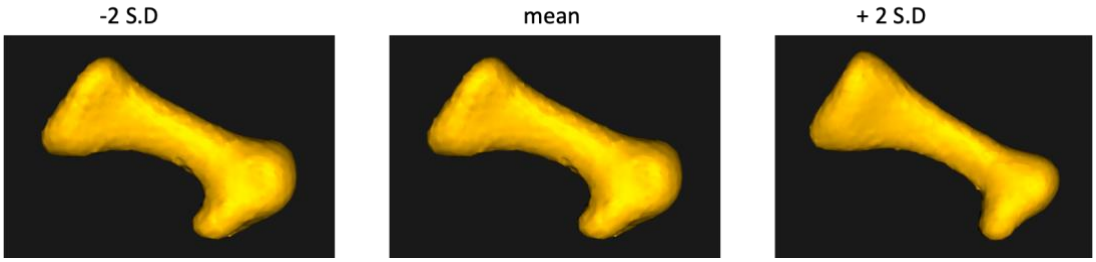

Figure 64 Representing a medial view of the first principal mode of variation showing changes in morphology within the all the metatarsal bones

Investigating the mean shape differences for the low and high arch populations shows areas of anatomical variation between the mean respective foot types for the first metatarsal bone, presented in Figure 65. The low-arch population on average have more bone present on the posterior medial aspect of the bone and the relative to the high arch foot type.

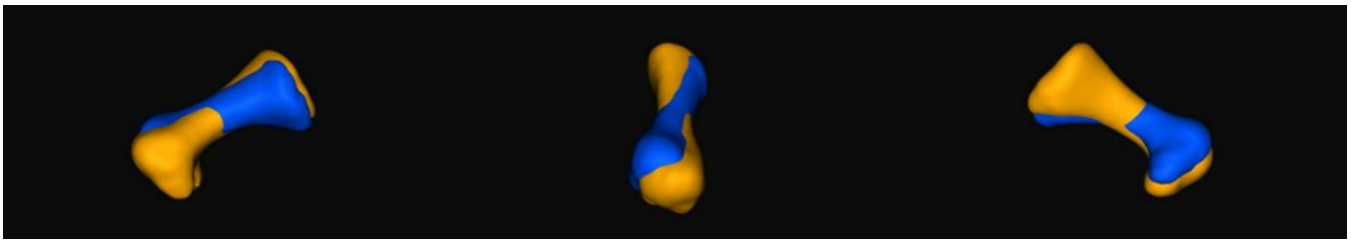

Figure 65 Showing the mean low arch (blue) and mean high arch (orange) populations for the first metatarsal bones

4.4 Discussion

This study addressed the aims set out to investigate differences in bony relationships between low, normal and high arch foot types and variation in individual bone shape of medial ray bones including the talus, calcaneus, navicular, medial cuneiform and first metatarsal.

While the process for constructing statistical shape models and specifically using ShapeWorks have been successfully applied to other bones and anatomy there are limitations with this modelling approach. One of the main limitations is in ensuring reconstructing the patient's geometry from the patient particle space into a 3D mesh or STL file is representative. There are assumptions made about the accuracy of the antialising of segmentations and 3D gaussian bluring of distance transformations in the work and assuring the filters applied do no filter important features of the patient, therefore this work would benefit from testing the sensitivity of the parameters in these intermediate steps of the SSM modeling pipeline. Further work should consider comparing the PCA spawned meshes, which will be later addressed in section 5.3.2.1 and specifically Table 9 comparing the RMS error of the surfaces between segmented bones and the SSM generated shapes representing patient geometry.

Overall a multi-domain statistical shape model, made up of the calcaneus, talus, navicular, medial cuneiform and first metatarsal was used to investigate positional and orientation variance by excluding Procrustes scaling. Non-Procrustean analysis captured positional variation between low and high arch foot types and agree with characteristic clinical observations in position and orientation with the first PC relating to the rise and collapse of the average low arch foot type relative to the average high arch foot type (Manaster, 2016; Kim, 2017; Osher and Shook, 2021) Morphological differences between foot types were also investigated, i.e., enabling Procrustes analysis that controls for scale and orientation. Morphological differences were present in all bones indicating that overall, subtle differences in bone shape exist between extremes of foot postures. The small sample size remains a limitation of the study and precludes

conclusions on the amount of variation but there were clear trends towards logical, sequential differences consistent with progression from low arch, through normal to high arch. This provides good preliminary evidence that the approach has potential for future utility in other research applications.

PCA was used to capture differences in shape, represented as 3D point clouds, between low and high arch foot types. This mathematical technique has previously been applied to characterise differences between discrete foot types in a population of military recruits (Moore et al., 2019). The statistical shape modelling workflow in this thesis investigated shape analysis with and without generalised Procrustes analysis. Firstly, analysing position and orientation variance resulted in macro differences between low and high arch types and agreed with clinical observations, where the arch is a large diagnostic feature of an extreme ‘low’ or ‘high’ foot type. Subsequently, morphological changes were then analysed to investigate if any variation existed by applying Procrustes analysis that negates size, orientation and positional variance as components in variation. The result was then related to variance in morphology between low and high arch groups. The present study addressed the aim of investigating relationships between variance in positional and morphological features linked to foot type and individual bone shape of the talus, calcaneus, navicular, medial cuneiform and first metatarsal. In addition, in the context of the thesis, developing an analytical pipeline that facilitated the automation of scaling a subject specific multi-body foot model, that is later detailed in chapter five using the SSM’s 3D point clouds. Overall, positional changes in the orientation of each of the bones accounted for variation among foot types, this was then interpreted into anatomical terminology aligning with clinical observations of a fallen and elevated arch (Manaster, 2016; Kim, 2017; Osher and Shook, 2021). When Procrustes analysis was investigated subtle changes in morphology existed for each of the bones, between low and high arch foot types.

Calcaneus

Studying orientation and positional changes, the first two PCs of the calcaneus in this work describe 69.6% of calcaneal variance. Studying changes in morphology the first two PC's accounted for 40.3% variance, compared to the 38% captured by Moore et al., (2019). Compared to Moore et al., (2019), the increase in shape variation captured in the SSM has similar model compactness i.e., more shape variation captured in fewer PCs. Moore et al., (2019) found the cavus calcanei to have more posterior mass, similar to the morphological findings demonstrated in the present study. This morphological observation links to in an increased calcaneal pitch, prevalent in high arch foot types (Kim, 2017), which could be due to the repetitive daily loading conditions on the bone in this population.

The first PC reported by Moore et al., (2019) was responsible for variation along the height and length of the calcaneus and showed the low-arch foot type to have decreased height and increased length, similar to findings by Krähenbühl et al., (2020) who studied the calcaneus bones to determine baseline for which pathological foot types could be compared. Krähenbühl et al., (2020) also found the calcaneus first mode of variation to relate to an increased anterior-posterior length, corresponding to a decrease in calcaneal pitch, an increased slope of the posterior facet articulating surface within the subtalar joint and increased prominence of the lateral and medial processes of the calcaneal tuberosity. These findings differ from the first PC without using Procrustes analysis in the present study which aligned with large positional differences in the medial lateral / varus valgus rotation when observing variance in the total population of calcaneus. However, findings by Krähenbühl et al., (2020) did agree with the variation within the calcaneus controlling for size and scale, indicating that Procrustes analysis has a significant impact on results when applying statistical shape modeling.

In this thesis, analyses that did not include Procrustes analysis, the anterior / posterior tilt of the second PC grouped the calcaneus bones from the high arch foot category in a tighter range in the PC space, indicating that subject's in this PC space have an increased calcaneal pitch, which has been previously reported by Kim, (2017) as a characteristic of high arch foot

types. The low and the normal arch groups shared a similar PC space and have less inclination than the high group which has been reported as prevalent in a low arch population (Sangeorzan et al., 1993).

In terms of bony morphology, analysis between extremes of foot posture showed the average low-arch foot population to have more pronounced areas on the lateral process, sustentaculum tali, sulcus for the flexor hallucis longus and posterior talar articular surface, while the average shape of the high and normal groups (higher and similar PC scores) exhibited extra structural variations on the medial process, sinus tarsi and the anterior process. This variation between average group shapes could indicate that subtle morphological differences between hypothetical opposite ends of the foot posture spectrum may exist. However, the reason for this difference is less clear. It could be speculated that, congenitally, humans are predisposed to a particular calcaneal bone shape, or that typical daily movement patterns are a precursor for morphological differences, and which have an impact on the morphological changes in the calcaneus. In addition, the foot has abundance of muscle, ligament and tendon tissues that, between characteristic low and high arch foot types, could impact the morphological changes observed.

Talus

The first two PCs of the talus, looking at orientation and positional variance in this work, describe 66.8%. In the morphological study, the first two PCs described 41.4% variance, compared to the 33% variance captured by Moore et al., (2019). In the study looking at orientation and positional variance the medial lateral angle of the talar dome and the redistribution of bone on the medial and lateral sides of the talar head in PC 1, showed the low arch foot population with lower scores to have a medialised and distal talar head compared to the high and normal arch groups of which, their PC 1 scores overlapped. Moore et al., (2019) found the high-arched group to have extended lateral and medial tubercles, whereas this work found the average shape of the high-arch talus to have an extended medial tubercle, while the lateral tubercle was extended in the average shape of the low arch foot type.

Moore et al., (2019) also found bony prominences on the posterior talus in the high arch group compared to neutrally aligned feet. However, the present morphological study showed the low arch population to have more bone on the talar dome, lateral malleolus and posterior mass, when compared to the high and normal arch type populations. Within the second PC space of the study focusing on positional and orientation variance, all foot groups overlap and there was no distinct region that was occupied by a particular arch type, however, a visual inspection of the average shape of the high arch foot population showed a relative flattening of the posterior process to the head of the talus compared to the low arch foot population. Uncovering the reason to these subtle changes would require additional information, such as longitudinal image study and functional movement data, however overall it could be reasonably determined that using a SSM approach was capable of generating mathematical representations of shapes for to quantify variance between foot postures.

Navicular

Studying positional differences, the first two PCs of the navicular in this work capture 81.4%. Studying morphological variance the first two PC's describe 47.9%, compared to the 35% variance captured by Moore et al., (2019). The first PC in the positional analysis was most closely attributed height of the navicular tuberosity, while the second PC was appeared to represent a medial lateral rotation. Mean differences in navicular shape represented the low arch group to tilt medially with the navicular tuberosity to dropping lower, in comparison to the mean high arch foot type. The low arch group showed a thickened lower medial posterior quadrant of the talar articulating surface when compared to average the high arch foot type. This could be described as "navicular drop", which has been previously reported in the literature to be a diagnostic feature of a low-arch foot type as reported in Caravaggi et al., (2018). On the other end of the variance scale, the higher relative position of the navicular tuberosity was observed, and in high arch foot types has also been observed clinically (Kim, 2017). Potentially impacting the morphological differences between the average high and low arch shapes in the of the

navicular in the present study is the loading conditions from the surrounding bones either side of the navicular. Anterior to the navicular are the three cuneiforms and posterior resides the talus. Considering the talus in relation to the navicular, the medialised talar head in the low arch population, may impact on the loading conditions delivered to the navicular bone, or inversely, the medial cuneiform may impact the navicular morphology.

Medial Cuneiform

To the authors knowledge, this is the first time the relationship between low and high arch foot types of the medial cuneiform has been investigated using statistical shape analysis. The first two PCs analysing positional, and orientation of the medial cuneiform describe a large proportion (84.2%) of the variance in the dataset. The medial cuneiform appears to rotate laterally in the first PC for the low arch foot type and rotate medially for the high arch group. In the average shape of the low arch foot type, the medial cuneiform indicates a subtle lateral tilt and an increase of bone on the lower left quadrant of the naviculo-medial cuneiform articulating surface in comparison to the average high arch foot type. The second PC scores show the low arch foot group to have a more pronounced anterior superior aspect and a retracted anterior inferior aspect in comparison to the average high arch foot type. As the variance described in the first two PCs of this bone was high, it could be hypothesized that classification of foot type based on morphology of the medial cuneiform alone, could be used as a classification feature of foot type. This could have potential applications in reducing the time to scan all the bones of the foot and potentially aid in the identification of treatment targets.

Metatarsal 1

The first two PCs in the positional analysis of the first metatarsal bone describe 68.4% variance of the dataset, while 50.5% variance was described in the morphological analysis. In the average shape of the low arch foot type a positional investigation of PC 1 showed the first metatarsal to rotate laterally and slightly inferiorly, relative to the first articulating surface of the medial cuneiform. This difference aligns with conjecture surrounding the

decreasing radius of the medial longitudinal arch in patients with low or fallen arches. Telfer et al., (2016) reported differences between pes cavus and pes planus, the first PC was related to frontal and sagittal plane cross-sectional area, similar to findings in the present study and interestingly the PC 2 in Telfer et al., (2016) described as the sagittal angle of the distal and proximal heads, similar to findings in this study for the first metatarsal bone. In this thesis, the average high-arched foot type exhibited positional changes that agree with clinical observations, where the first metatarsal bone is rotated medially and slightly superiorly relative to the first tarso-metatarsal articulating joint, indicating an increased radius of the medial longitudinal arch contributing to a heightened arch. The values of each of the patients in the second PC are shared by all three-foot types, indicating the variation seen in this PC alone cannot be reasonably attributed to a characteristic of either a high or a low arched foot type.

The differences between average low and high arch foot types of the first metatarsal indicated by the statistical shape analysis indicate what is conventionally observed clinically. For the average low arch foot type this is a lowering of the base (posterior extremity) of the metatarsal extremity and lateral rotation when compared to the mean shape of the high arch foot type.

4.5 **Conclusion**

The results of statistical shape modelling on the talus, calcaneus, medial cuneiform and first metatarsal reveal subtle differences between low and high arch foot types, which have agreement to anecdotal and published clinical observations. This demonstrates a quantitative approach to a clinically observed phenomena between characterising foot type, defined using a validated clinical scoring index, the Foot Posture Index (Redmond, 2005) and individual bone shape, deduced from a dimensionality reduction technique, PC analysis, for both orientation, position and morphology. In addition to analysing differences in average shape between low and high arch foot types, further work could attempt to a link between shape variation of low, normal and high arch foot types with their subsequent functional

characteristic types to help address the notional linkage of movement between individual bone shape and functional patterns. The aims of the chapter were to investigate relationships between overall foot type and individual bone shape of medial ray bones including the talus, calcaneus, navicular, medial cuneiform and first metatarsal. The work carried out in this chapter demonstrated differences between high and low arch foot types and provide a basis for part of an analytical pipeline can be used to generate patient specific bone geometry for a 26-segment foot model, detailed in chapter five.

Chapter 5 Development of a 26-segment foot model to describe biomechanical variations in different foot postures

5.1 Introduction

This chapter will discuss the methodology developed to incorporate medical image data generated in chapter three and transformed into 12 statistical shape models of bones in the foot including the calcaneus, talus, navicular, cuboid, three cuneiforms and five metatarsals in chapter four; to scale and morph the AnyBody GM foot model (Carbes et al., 2011; Oosterwaal et al., 2016), creating a patient specific foot geometry. The methods will describe the development of a scaling and morphing process for twelve bones, integration of a 46-motion marker gait analysis protocol and a process to incorporate pressure data, used in the GM foot model. The result was an adapted GM foot model capable of describing the biomechanical variation in extremes of foot posture.

Subject-specific foot models have been previously applied to a range of normal functioning (Carson et al., 2001) and pathological foot types (Levinger et al., 2010; Leardini et al., 2019) . However advanced 26-segment foot models (Carbes et al., 2011; Oosterwaal et al., 2016) have yet to be fully explored. Capturing foot mechanics is a challenge due to the complexity of the movement of individual bones, with traditional gait analysis approaches, historically modelling the foot as one rigid segment connected to the shank (Apkarian et al., 1989). More recently, other foot models, which characterise dynamic foot function have been developed (Kidder et al., 1996; Rattanaprasert et al., 1999; Leardini et al., 1999; Hunt, Smith, et al., 2001; Carson et al., 2001; MacWilliams et al., 2003; De Mits et al., 2012; Oosterwaal et al., 2016), with each varying in numbers of segments and joint definitions.

There are numerous methods available to scale biomechanical models to a specific patient. Traditional gait analysis use markers to define bone

segments, whilst advanced musculoskeletal modelling techniques can use segmented medical images to scale cadaver based models, such as has been demonstrated in the knee (Marra et al., 2015). The evolution in scaling of musculoskeletal models relies on the modeller to manually adjust parameters between the reference model and the individual subject, however, this process is time consuming and requires in-depth knowledge of specific software packages to implement. As with traditional biomechanical analysis, the 26-segment GM foot model uses motion capture data, generated from trajectories of reflective markers that have been collected in a gait laboratory. The current version of the GM foot model in the Anybody managed model repository uses the skin surface of the foot to scale and morph the template model to fit the geometry of a patient, this is the default methods of applying the model. However, the 26-segment foot model developed in this chapter uses similar kinematic and pressure data models with additional patient geometries derived from a statistical shape model. The model presented in the chapter has the potential to be use to analyse inverses dynamics of the foot and ankle . Inverse dynamics of the foot and ankle using the model developed in this chapter was not applied to the study groups containing low, normal and high arch foot types in the study. A preliminarily, proof of concept set of models were developed to verify the model's potential for future work investigating joint contact forces and muscles within the foot. The preliminary work is designed to show the complexities involved in incorporating multi-domain real-world patient data into a single foot and ankle model and where further verification and validation would be beneficial.

A sensitivity study investigating three bone morphing methods will also be carried out to justify the extra computational processing of a statistical shape model as an input to the 26-segment multi-body model. There will be three bone morphing methods compared. The default method used to scale the GM foot model, previously described by (Carbes et al., 2011; Oosterwaal et al., 2016), a manual point correspondence approach, and a statistical shape modeling approach to generating point correspondence. Only twelve of the 26 bones in the foot and ankle were used in the kinematic models due to the

limitations on the field of view of the MRI scans; this resulted in the distal portion of the foot being omitted. The imaging protocol described in chapter three was sufficient to generate bone including the talus, calcaneus, three cuneiforms, cuboid and five metatarsals with the quality of the scaling and morphing modeling within the AMS compared to the STLs generated from the segmentations created in chapter three .

Preliminary kinematic analysis on the sensitivity of these scaling methods will be compared using the ankle joint plantarflexion as the reference motion. In addition, a verification of pressure data integrated into the model will be carried out to ensure the information from the pressure data collection platform is interpolated and distributed appropriately to the bones in the foot model developed in this chapter.

5.1.1 Aims

The aim of this chapter was to utilise data generated in chapter 3, to (1) investigate the applicability and sensitivity of three bone based scaling and morphing methodologies; (2) to demonstrate the implementation of the motion and pressure data into the model and (3) test the sensitivity in kinematics of ankle plantarflexion for kinematics and resultant forces and pressure integration with the developed bone morphing methods, against the current method for scaling the GM foot model.

5.2 Materials and methods

5.2.1 Scaling and morphing of patient specific bone morphology

Patient specific bone geometries were morphed into to the 26-segment template foot model using three morphing methods and the error between the morphed bone and the medical image segmentation was compared between these methods. The method that yielded the smallest error overall was used in the kinematic analysis in chapter six. The first of these bone morphing techniques is a skin based scaling method that is the current method used to generate a patient specific foot geometry in the GM foot model (Carbes et al., 2011; Oosterwaal et al., 2016). This method picks

corresponding points on the surface of the foot, the skin, between the patient and the template repository model. The second morphing technique in the comparison was a manual corresponding point picking process on surface of the bones of the foot including the calcaneus, talus, navicular, cuboid, three cuneiforms and 5 metatarsals bones. The third morphing method involved leveraging the SSM's developed in chapter four, this approach was an automatically generated point correspondence. In addition, anatomical meshes were generated from 12 statistical shape models including the calcaneus, talus, navicular, three cuneiforms and 5 metatarsals. To implement the automatically generated point correspondence from the SSM approach, the template model STL's, were remeshed to a higher density to improve the surface topology for the morphing process. This was done by converting the bones from the GM foot model repository STL meshes, to individual binary image volumes, through generating a new surface from the image, whilst maintaining the topology template model bones. Figure 66 shows the original repository model STL bones in (a) lateral aspect and (b) superior aspect of the foot. The higher density meshes needed for an automatically generated 3D point correspondence derived from the SSM meshes as STL file are viewed in (c) the lateral aspect and (d) superior aspect of the foot. Combing the talus, calcaneus, navicular, medial cuneiform, intermediate cuneiform, lateral cuneiform, navicular, and metatarsals 1-5, the lower quality mesh had a total of 7636 vertices and

75504 faces, while the higher quality, reprocessed SSM mesh's had 90593 vertices and 181142 faces.

Two novel methods were developed in this thesis, method a and method b in Figures 67 and 68 respectively and a third was replicating a previously published methodology (Carbes et al., 2011; Oosterwaal et al., 2016). All approaches were used with the intention of generating bone geometry from MRI segmentations to morph individual patient bones into the GM model. Each of the newly developed methods was compared to the existing process based on the surface scan of the foot. The error between the patients segmented geometry and the morphed geometry were compared for the talus, calcaneus, navicular, three cuneiforms and 5 metatarsals compared between the three methods.

A schematic of method (a) is presented in Figure 66. This method was a manual corresponding point selection between the GM foot model repository bones as the source and patients segmented MR images as binary volumes converted to an STL file as the target bone geometry. Initially,

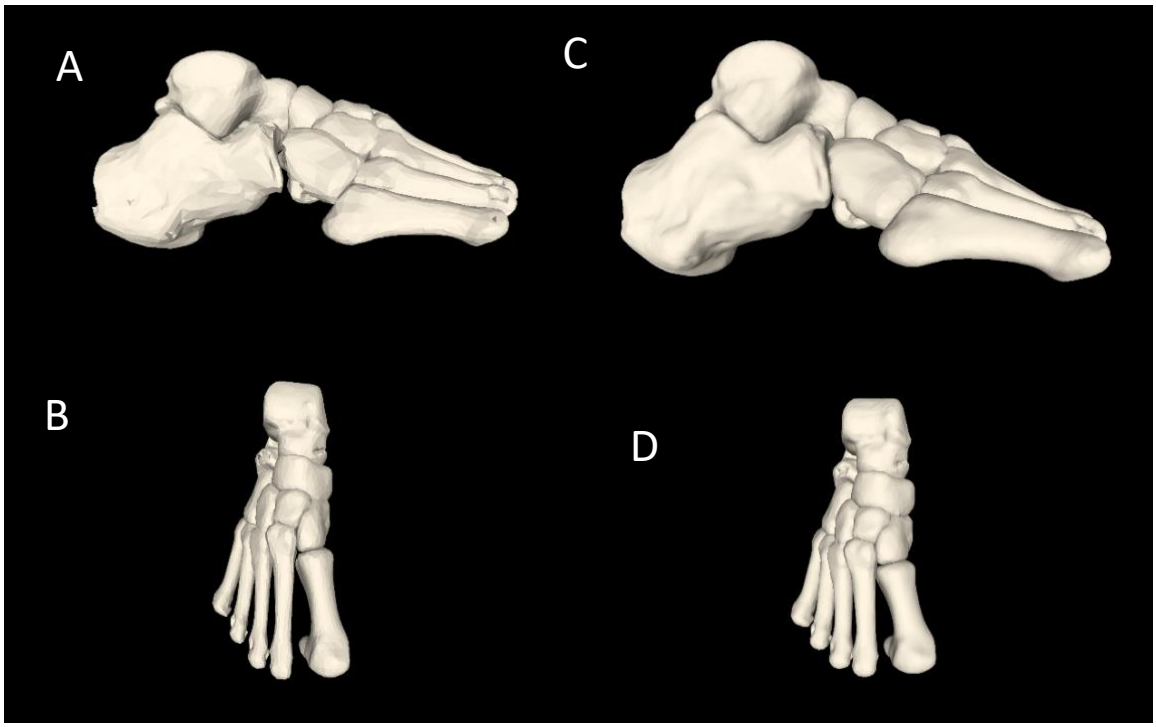

Figure 66 An image of the low-quality mesh (A) medio-lateral view, (C) Superior-inferior and the denser mesh (B) medio-lateral and (D) Superior-inferior views, generated in MeshLab

segmentations were derived using the approach detailed in chapter three and corresponding points generated using MeshLab. The corresponding point files and meshes were placed in a folder on a computer where the AMS script can pick up the geometries when processing gait analysis data

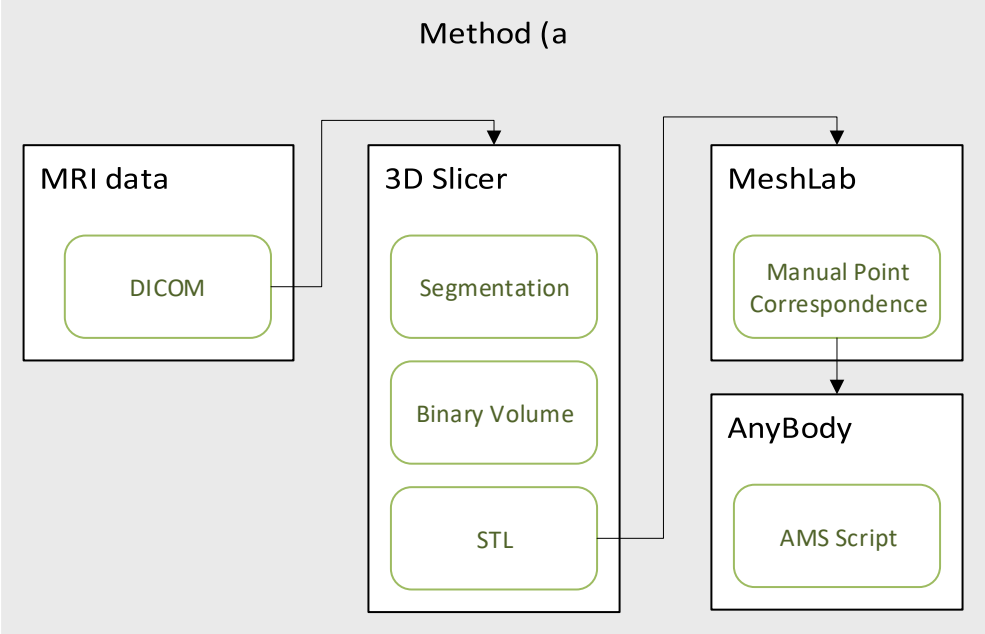

Figure 67 Workflow for generating corresponding points and STL meshes for the manual point picking scaling method

A schematic of method (b) is presented in Figure 68. This is schematic details an automatic corresponding point selection approach from a statistical shape model developed using the methods described in chapter four, with the additional, repurposed bone geometries from the template GM foot model bones. Three-dimensional point clouds and anatomical meshes were exported from the statistical shape model and again were placed into a

folder which the dynamics foot model used when processing patient gait analysis data in the AMS script.

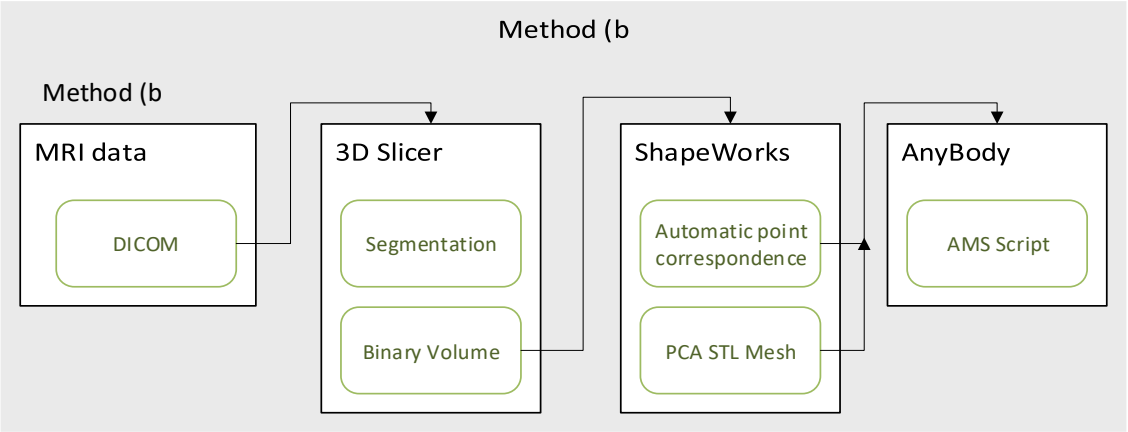

Figure 68 Workflow for generating automatically corresponding 3D point clouds and STL meshes from a statistical shape model

5.2.1.1 Segmentations

Both scaling methods (a) and (b) used the binary image volumes of the MRI segmentations from Chapter four. Method (a) used the image volumes converted to STL files and method (b) used the binary bone image volumes converted to meshes from the SSM to create the STL outputs. The foot skin surface or the patients' geometry was generated by thresholding the MR images of each of the patients to include the outer surface of the skin.

5.2.1.2 Bone morphology construction and implementation

After generating the patient's bone geometry, the implementation of transforming 3D point clouds and STL meshes into a morphed foot model from methods (a) and (b) was developed using built-in functionality within the AMS. The morphing algorithm template was constructed using the radial basis function (RBF) (Buhmann and Buhmann, 2003) and specifically the triharmonic RBF as this resulted in the smoothest surface compared to the other interpretations of the RBF. Taking an initial set of corresponding surface points, an affine RBF interpolation transformation was applied. Secondly, using the RBF transformation as a pretransformation, an iterative closest point for method (a) and a corresponding point transformation for method (b) were applied to vertices on the STL bone surfaces. A bounding

box was used around each bone to prevent poor inter/extrapolations of the RBF function before a rigid-body transformation back to the musculoskeletal model's reference frame was applied. The workflow shown in Figure 69 describes the steps taken to morph the bones into the GM foot model using the AMS morphing script.

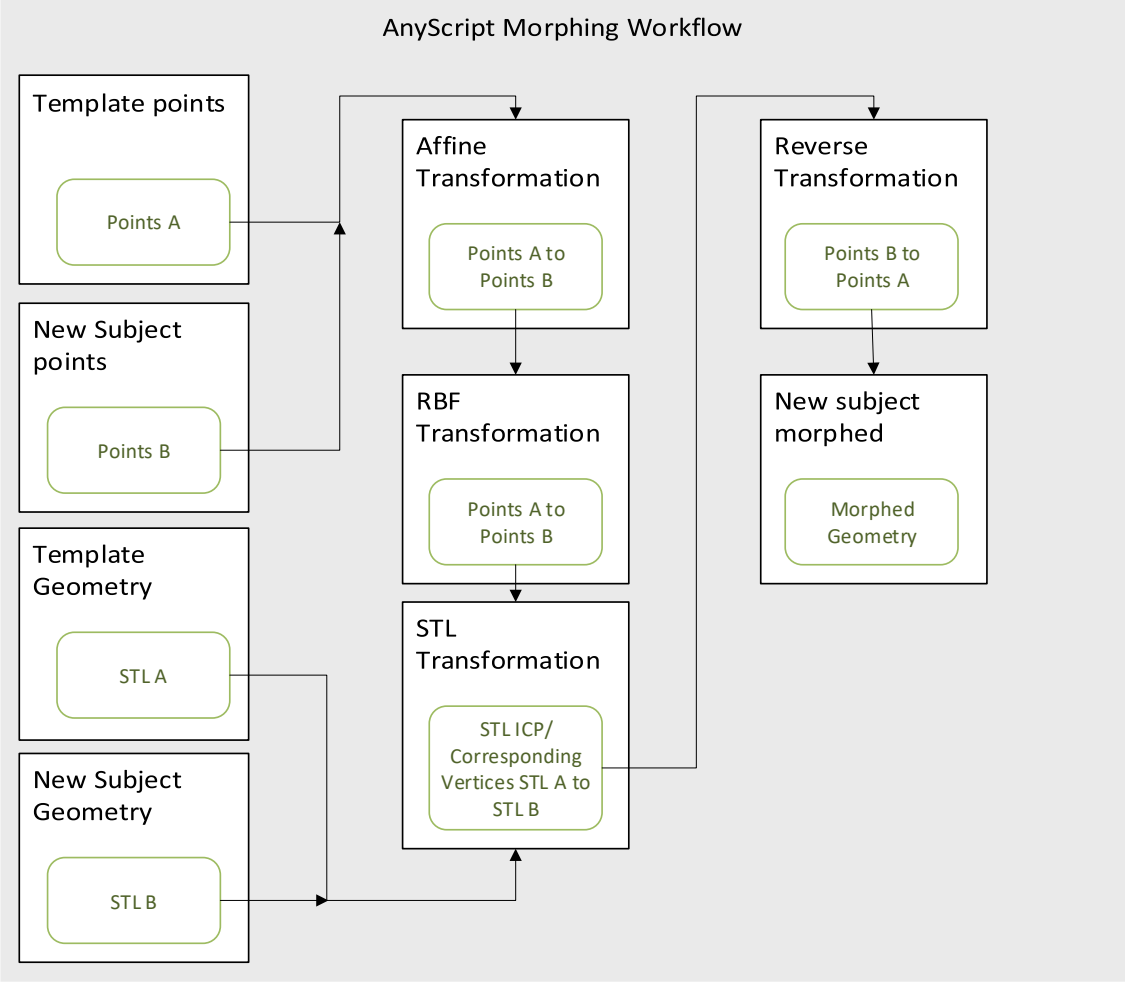

Figure 69 Workflow showing how the points and STL files from each method were used to generate a morphed geometry in the AMS.

5.2.1.3 Corresponding Point Selection

Method (a) – Manual corresponding point selection

The initial set of corresponding source and target points were manually generated in MeshLab software (2012.12) (P. Cignoni, M. Callieri, M. Corsini, M. Dellepiane, F. Ganovelli, 2008). These points are shown in

Figure 70 and demonstrate the set of the corresponding points chosen for the twelve scaled bones of the source and target foot bones. These points were used as inputs for the scaling and morphing algorithm in the AMS script.

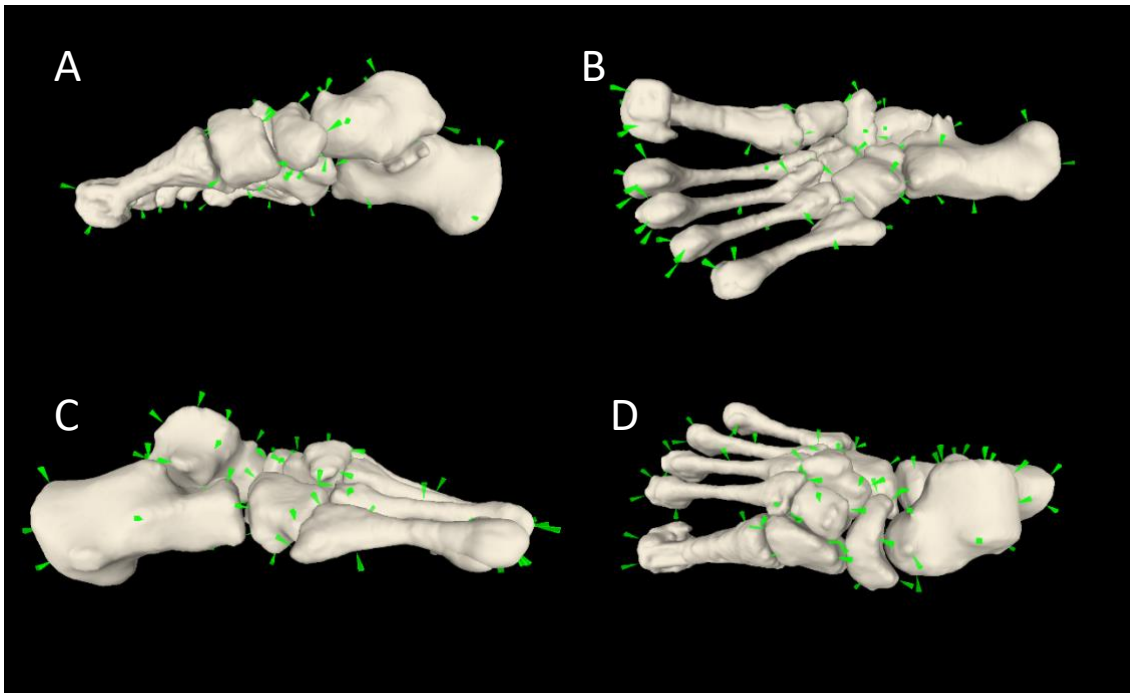

Figure 70 (A) medial, (B) Inferior, (C) Lateral, (D) Superior, view of the manual points used in method (a) generated from MeshLab.

Method (b) – Automatic corresponding point selection

The points in method (b) were generated automatically using the ShapeWorks Studio SSM software. The automatic point correspondence algorithm employed in this software is a particle based system (Cates et al., 2007) which populates each binary bone input volume with a set of densely corresponding points. This process optimises the points on each binary bone volume by computing the principal modes of variation using PCA on the aligned point clouds. The SSM reconstructs image files of the input binary bone volumes that can be converted to STL files. A visual representation of the automatic point correspondence on the PCA generated mesh is shown

in Figure 71. This is a subset of the calcaneus population made up of 4 input volumes a) GM foot b) a high-arched foot type, c) a normal arch foot type and d) a low arch foot type.

These STL meshes and points were then registered to the GM model template so that future MR segmentations as binary volumes could then be processed by the shape model and have points corresponding to the template GM model.

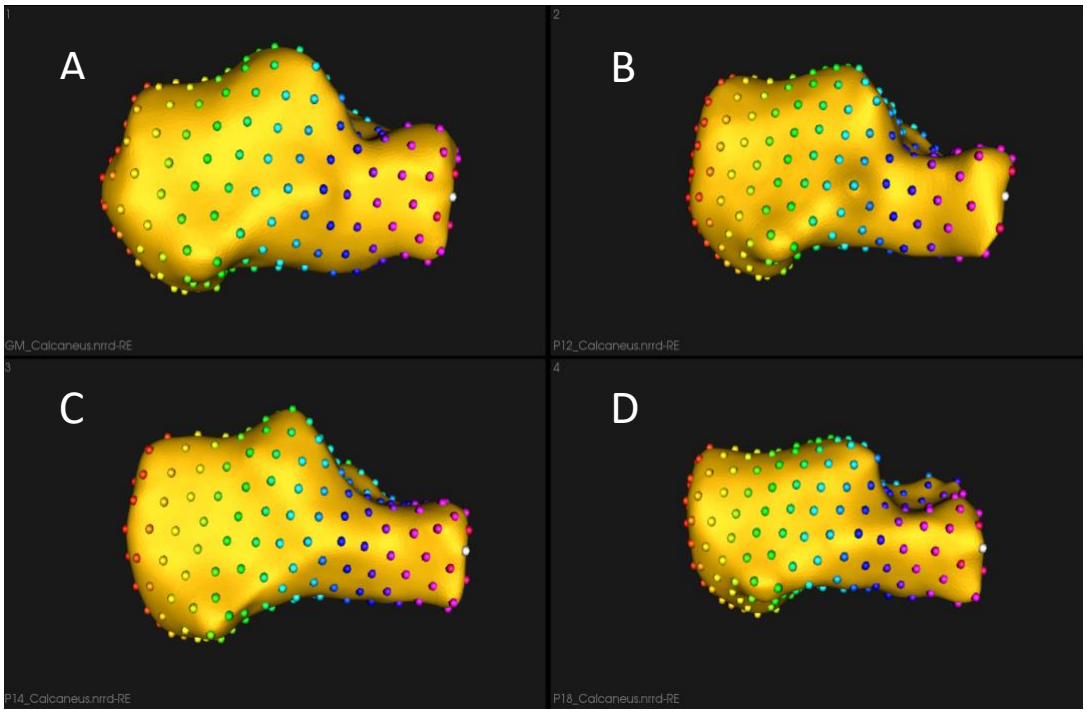

Figure 71 Automatic point correspondence and spawned PCA meshes of the calcaneus bone from Shape Works Studio software. (A) Represents the GM foot model, (B) the high arch foot type, (C) the normal foot type, (D) the flatfoot type.

Published literature on point correspondence method

The GM foot repository model from AMMR 1.6.6 uses points on the surface of the source and target foot for scaling. Patient skin surface geometries were generated for the 3-foot types used for shape modelling as way to compare the sensitivity of the current method of incorporating patient

specific foot geometries into the GM model with the individual bone morphing methods developed in this thesis. The point picking process for this method is visualised in Figure 72. As the repository model was designed to develop patient specific foot orthotics, a list of 16 anatomically relevant points were used as the source points were used to scale the skin surface of the whole foot (Oosterwaal et al., 2011), These points include:
"Heel back", "Heel plantar", "Heel medial", "Heel lateral", "Achilles tendon", "Malleolus medial" ,"Malleolus lateral", "Navicular tuberosity", "Navicular dorsal", "Midfoot lateral", "First metatarsal head lateral", "Metatarsal dorsal", "Metatarsal plantar", "Big toe tip", "Second toe tip" and the "Fifth toe tip".

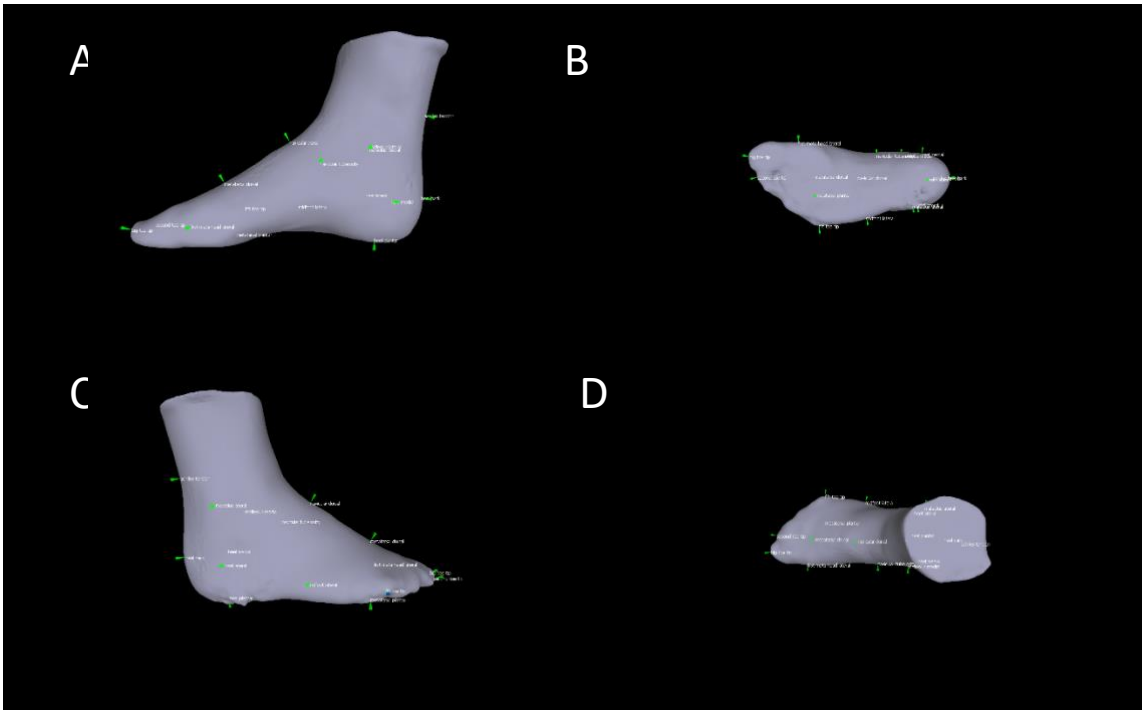

Figure 72 Current method for scaling the foot model to a new subject.

5.2.2 Motion analysis method development

Gait analysis data generated from chapter three was added to the 26-segment foot model to drive motion of the segments in addition to each of the bone morphing techniques into the model. The marker configuration and location for the GM foot model was taken from the AMMR version 1.6.6. Marker names from the model marker repository were changed to match the VST template generated in chapter three. Figure 73 demonstrate the workflow followed for implementing motion capture data into the foot model.

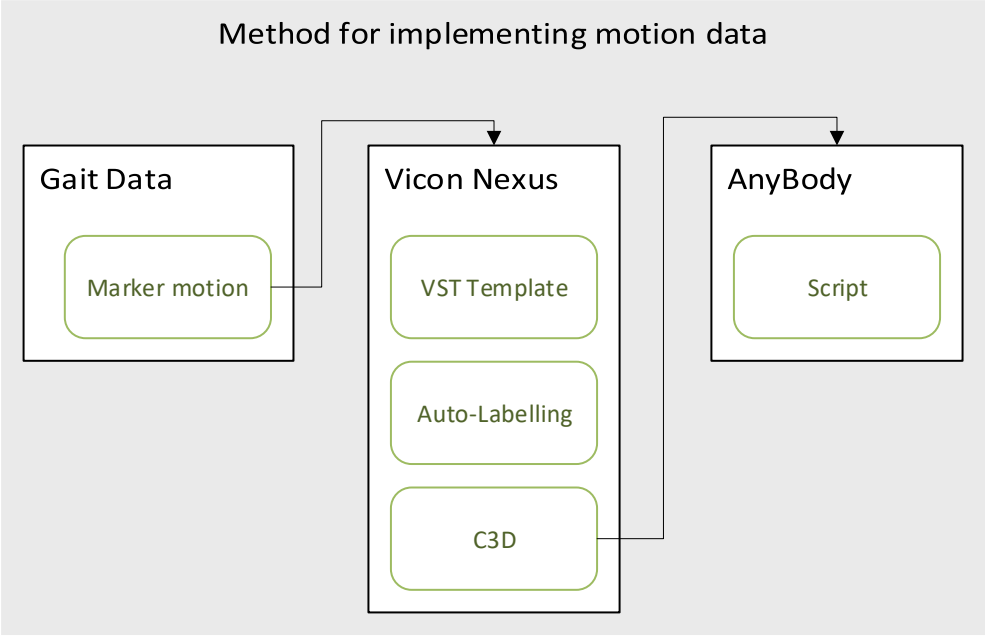

Figure 73 Workflow for generating motion capture data as an input for the foot model**.**

In addition to adding motion capture data into the 26-segment foot model, a virtual AMTI pressure force platform was developed as code and scripted into the virtual model environment. This processed was needed as the repository model was developed in a different gait laboratory. This script takes the global resultant force from the force platform and was used in the integration of pressure data. The development of this force platform facilitated the incorporation of the pressure data to be incorporated into the model, providing the capabilities to perform inverse dynamic analysis.

5.2.3 Pressure data integration development

Pressure data was generated in chapter three and implemented into the 26-segment foot model. Integrating pressure data into the model started by exporting data as a CSV file from the pressure Emed pressure software and formatting to a text file, as the text file is ingested by the model. The CSV file was converted to a text file using a python script and then cropped to a matrix size that included only the foot pressure data. The schematic for incorporating the pressure data from an external pressure platform is represented in Figure 74 as a workflow chart.

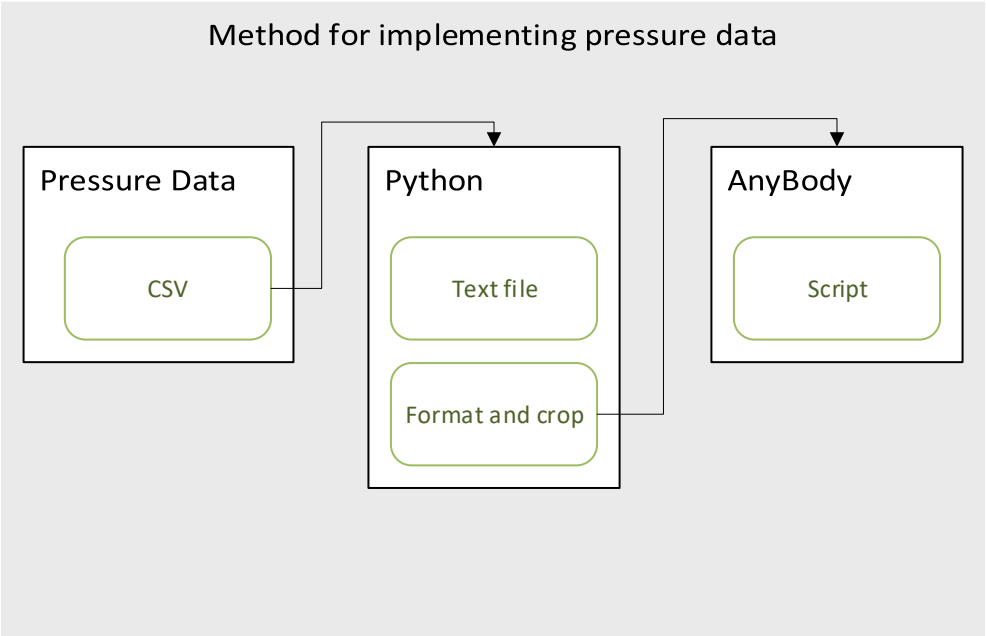

Figure 74 Workflow used in implementing the pressure data in the foot model**.**

5.2.3.1 Pressure data construction and implementation

Formatted pressure data is needed in the GM foot model to drive the inverse dynamic analysis, but not needed to analyse kinematics of the foot. Although not fully explored between foot types in this thesis, the capability was developed to demonstrate the possibility of the model with small sample of extremes of foot posture. The text file was converted to a coefficient matrix using scripts from the AMS repository model that could be applied to the 183

pressure nodes on the foot. Figure 75 shows the pressure nodes on the underside of the foot.

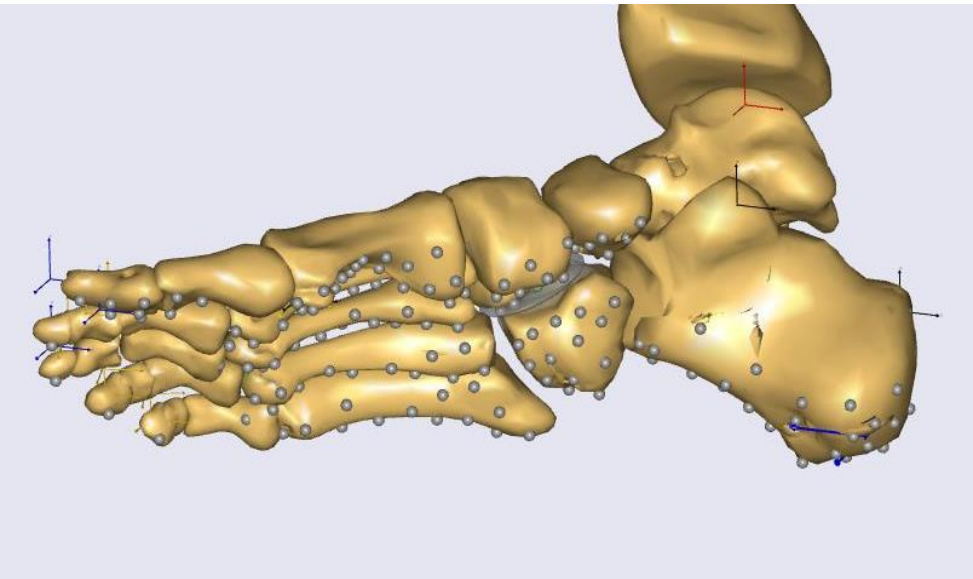

Figure 75 Showing pressure nodes on the inferior side of the foot

Within the GM foot model is a virtual pressure mat is located under the foot where a formatted pressure matrix data is placed under the foot to align with the virtual pressure mat using the python scripts. Figure 76 shows the footprint denoted by 6 black nodes, the pressure matrix, denoted by 4 blue nodes. The foot strike node, indicated by a red node and the centre of pressure denoted by a green sphere.

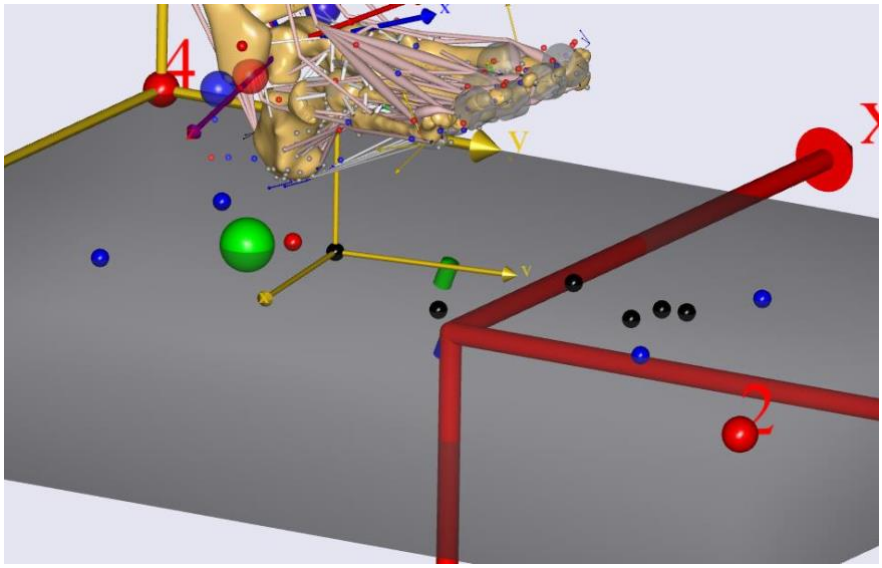

Figure 76 Showing the pressure matrix under the foot

5.3 Optimisation and evaluation of input parameters

5.3.1 Bone morphing optimisation

Generating a patient specific musculoskeletal model required morphing one bone shape into another and the sensitivity of the morphing algorithm to mesh error was analysed and compared between the previous literature used to scale the model, a manual point correspondence bone scaling approach and a statistical shape modelling scaling method to test the mesh similarity between segmentations and morphed meshes.

A root mean square error of the measurement of the distance of the nearest neighbouring vertex on the source and target meshes was used to quantify the error of the morphed meshes. The minimum and maximum root mean squared error between source and target meshes were recorded.

In this section the surface mesh error is discussed within the context of three parts. Initially concerned with 1) the error between low resolution GM template model, high resolution repurposed GM foot model and the statistical shape model generated template meshes; 2) the error between the source and target meshes for the method (a) a manual point correspondence between STL and manually assigned points; 3) the error

between source and target shape model generated meshes for method (b) using automatically generated points and 4) the error between source and target meshes for the previously published literature on scaling the GM foot model.

5.3.1.1 Initial optimization in 3D space

The bone geometry for the GM model template meshes and the patient specific meshes, were in different reference frames and of different scale. To account for this, patient specific meshes were scaled to match the AMS reference system and a manual registration with 4 manual corresponding points was applied to roughly align the patient specific meshes with the model template, before a fine iterative closest point (ICP) cloud registration was performed on the source and target point clouds. The RMS value was set to $1e^{-5}$ aimed to achieve a surface overlap of 100%.

5.3.1.2 Error between the repository model bone geometries, a newly generated model template and an SSM reconstructions of the template geometries.

As the original template model mesh of the AMMR 1.6.6 was of low quality and segmentations of new subject's bone geometry were denser, increasing the density of the model template bones while maintaining the topography was a necessary step in being able to morph the subject's geometry, otherwise morphed meshes would be inadequate. Figure 77 (a) shows a visualisation of the similarity of meshes by measuring the distance of the vertices between the higher density mesh reconstructed from binary images of the GM foot model bone geometries, and the original template mesh geometries of the GM foot model. The RMS error between the low-quality template mesh and the higher quality mesh was 1.4mm. Figure 77 (b) shows a visualisation of the similarity between the new high quality template GM

bone meshes and the SSM reconstructed meshes. These meshes had an RMS error of 1.5mm.

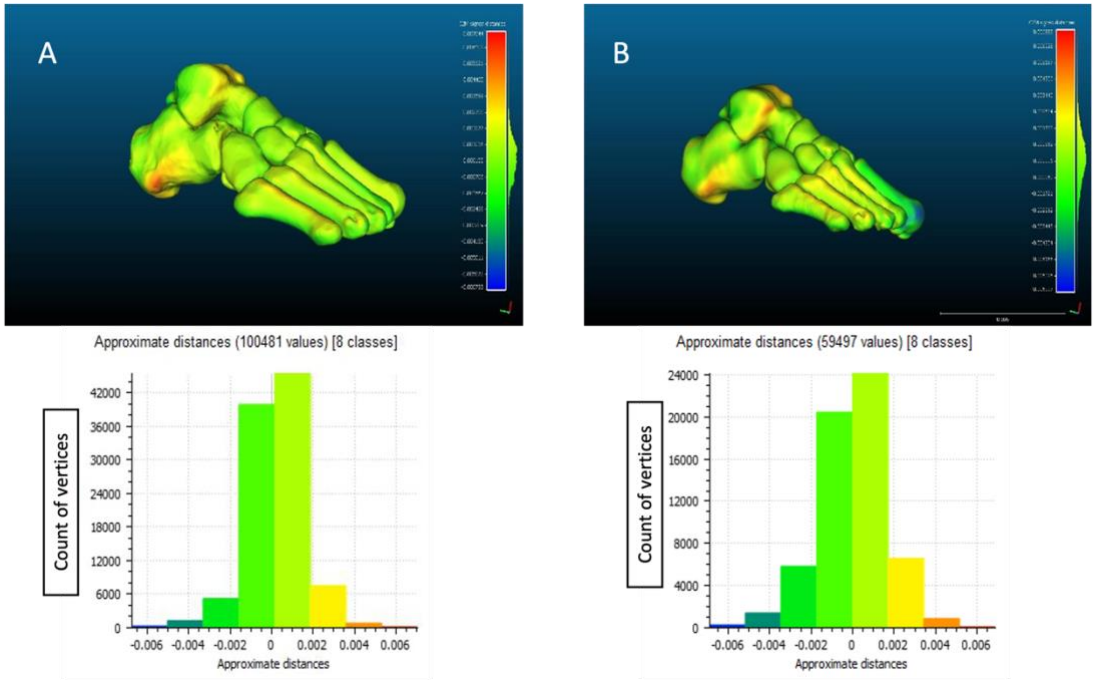

Figure 77 (A) Visualisation of the error between the template model mesh and a higher quality mesh with a graph of the distances between surface vertices in meters and (B) Visualisation of the error between the low-quality template model mesh and the shape model

Table 9 shows the RMS error between surface vertices of the segmented bones and the SSM generated patient bones, this represents the specificity of the shape modelling process to accurately spawn PCA meshes that represent the input shapes, the minimum RMS error was 0.3 mm observed for the 3rd and 5th metatarsal bones. The maximum RMS error was 2.3 mm observed on the intermediate cuneiform.

Table 9 Error between patient segmentations and shape model of the spawned patient bones in mm; min and max values describe the minimum and maximums across each of the patients for each bone.

RMS Error (in mm)					
Segmentations Vs Shape					
	Patient 12	Patient 14	Patient 18	Min	Max
Talus	0.4	0.5	0.5	0.4	0.5
Calcaneus	0.6	0.5	0.8	0.5	0.8
Navicular	0.7	0.6	0.9	0.6	0.9
Medial Cuneiform	0.7	0.7	0.7	0.7	0.7
Intermediate Cuneiform	2.3	0.8	0.8	0.8	2.3
Lateral Cuneiform	0.9	0.8	0.8	0.8	0.9
Cuboid	0.7	0.7	0.7	0.7	0.7
Metatarsal 1	0.9	0.5	0.6	0.5	0.9
Metatarsal 2	0.4	0.4	0.4	0.4	0.4
Metatarsal 3	0.3	0.4	0.3	0.3	0.4
Metatarsal 4	0.4	0.4	0.4	0.4	0.4
Metatarsal 5	0.4	0.4	0.3	0.3	0.4

5.3.1.3 Error between the morphed and segmented meshes for the method (a)

Method (a) involved generating morphed subject-specific bone geometries based on a manual point picking process. The RMS, minimum and maximum distances for each of the 12 morphed bones, between three subjects were analysed and compared in Table 10. The minimum RMS error was 0.6 mm observed on the intermediate cuneiform and 5th metatarsal and the maximum error was 3.1 mm observed on the calcaneus bone.

Table 10 Error between segmented and morphed meshes for method a – manual points picked on each bone in mm; min and max values describe the minimum and maximums across each of the patients for each bone.

RMS Error (in mm)					
Bone Scaling Vs Segmentations					
	Patient 12	Patient 14	Patient 18	Min	Max
Talus	1.1	1.1	1.3	1.1	1.3
Calcaneus	3.1	2.5	2.6	2.5	3.1
Navicular	1.0	2.1	1.2	1.0	2.1
Medial Cuneiform	0.8	0.8	0.7	0.7	0.8
Intermediate Cuneiform	0.6	0.7	0.6	0.6	0.7
Lateral Cuneiform	1.1	1.0	0.9	0.9	1.1
Cuboid	2.4	2.4	1.8	1.8	2.4
Metatarsal 1	1.8	2.0	2.0	1.8	2.0
Metatarsal 2	1.4	0.9	1.1	0.9	1.4
Metatarsal 3	1.4	0.8	0.9	0.8	1.4
Metatarsal 4	0.7	1.0	1.1	0.7	1.1
Metatarsal 5	0.9	0.7	0.7	0.7	0.9
Metatarsal 5	0.0	0.0	0.0	0.6	0.0

5.3.1.4 Error between the morphed and segmented meshes for the method (b)

Method (b) involved generating morphed subject specific bone geometries based on an automatic point correspondence process, derived from the SSM. The RMS, minimum and maximum distances for each of the 12 morphed bones, between three subjects was analysed and compared in the Table 11. The minimum RMS error was 0.1mm observed on the calcaneus, medial, intermediate and lateral cuneiforms, cuboid and 2nd to 5th metatarsals. The maximum error of 1.5mm was observed on the talus

Table 11 Error between segmented and morphed meshes for method b based on SSM generated points on each bone in mm; min and max values describe the minimum and maximums across each of the patients for each bone.

RMS Error (in m)					
Shape model morphed Vs Segmentations					
	Patient 12	Patient 14	Patient 18	min	max
Talus	1.0	1.5	1.0	1.0	1.5
Calcaneus	0.4	0.1	1.0	0.1	1.0
Navicular	1.0	1.0	1.0	1.0	1.0
Medial Cuneiform	0.1	0.1	1.0	0.1	1.0
Intermediate Cuneiform	0.2	0.1	0.7	0.1	0.7
Lateral Cuneiform	0.1	0.1	0.9	0.1	0.9
Cuboid	0.1	0.1	1.0	0.1	1.0
Metatarsal 1	0.8	0.8	0.2	0.2	0.8
Metatarsal 2	0.1	0.1	0.1	0.1	0.1
Metatarsal 3	0.1	0.2	0.1	0.1	0.2
Metatarsal 4	0.1	0.1	0.1	0.1	0.1
Metatarsal 5	0.1	0.1	0.1	0.1	0.1

5.3.1.5 Error between the morphed and segmented meshes for the skin surface to the segmented bones

This method scaled the subjects foot based on a segmented surface of the foot using predefined picked points and is currently published. The minimum error was 0.5 mm observed on the intermediate cuneiform, and the maximum error was 3.5 mm observed on the first metatarsal. The RMS error for the other bones is detailed in Table 12.

Table 12 Error between segmented and morphed meshes for the skin scaling method; min and max values describe the minimum and maximums across each of the patients for each bone.

RMS Error (in mm)					
Skin Vs Segmentations	Patient 14	Patient 16	Patient 18	Min	Max
Talus	1.3	0.8	1.2	0.8	1.3
Calcaneus	2.7	3.1	2.8	2.7	3.1
Navicular	2.0	2.4	2.0	2.0	2.4
Medial Cuneiform	0.8	1.3	0.8	0.8	1.3
Intermediate Cuneiform	0.5	1.7	0.5	0.5	1.7
Lateral Cuneiform	1.1	0.9	1.1	0.9	1.1
Cuboid	1.4	2.5	1.4	1.4	2.5
Metatarsal 1	3.5	1.8	3.2	1.8	3.5
Metatarsal 2	1.2	1.1	0.8	0.8	1.2
Metatarsal 3	0.9	0.6	0.8	0.6	0.9
Metatarsal 4	1.3	1.0	1.3	1.0	1.3
Metatarsal 5	1.8	0.7	0.9	0.7	1.8

Figure 78 shows the average bone RMS error consisting of three patients bones between the morphing methods represented at the mean and standard deviation (as error bars). The blue bar represents the RMS error of the automatic point correspondence method associated with the statistical shape model and overall lowest error. The orange bar represents the error of the manual point picking process, and the blue bar represents the error of the foot surface skin approach process to morphing bones into the GM foot model.

In summary, the AMMR repository bone meshes were of too low-quality to be used in a SSM modeling workflow, therefore efforts were made to repurpose the mesh while maintaining the topology. RMS error was calculated between the low-quality AMMR and repurposed meshes. In addition RMS of the low-quality AMMR meshes was compared against the SSM spawned meshes. Finally, The RMS error was calculated between the patient segmentations and SSM spawned meshes.

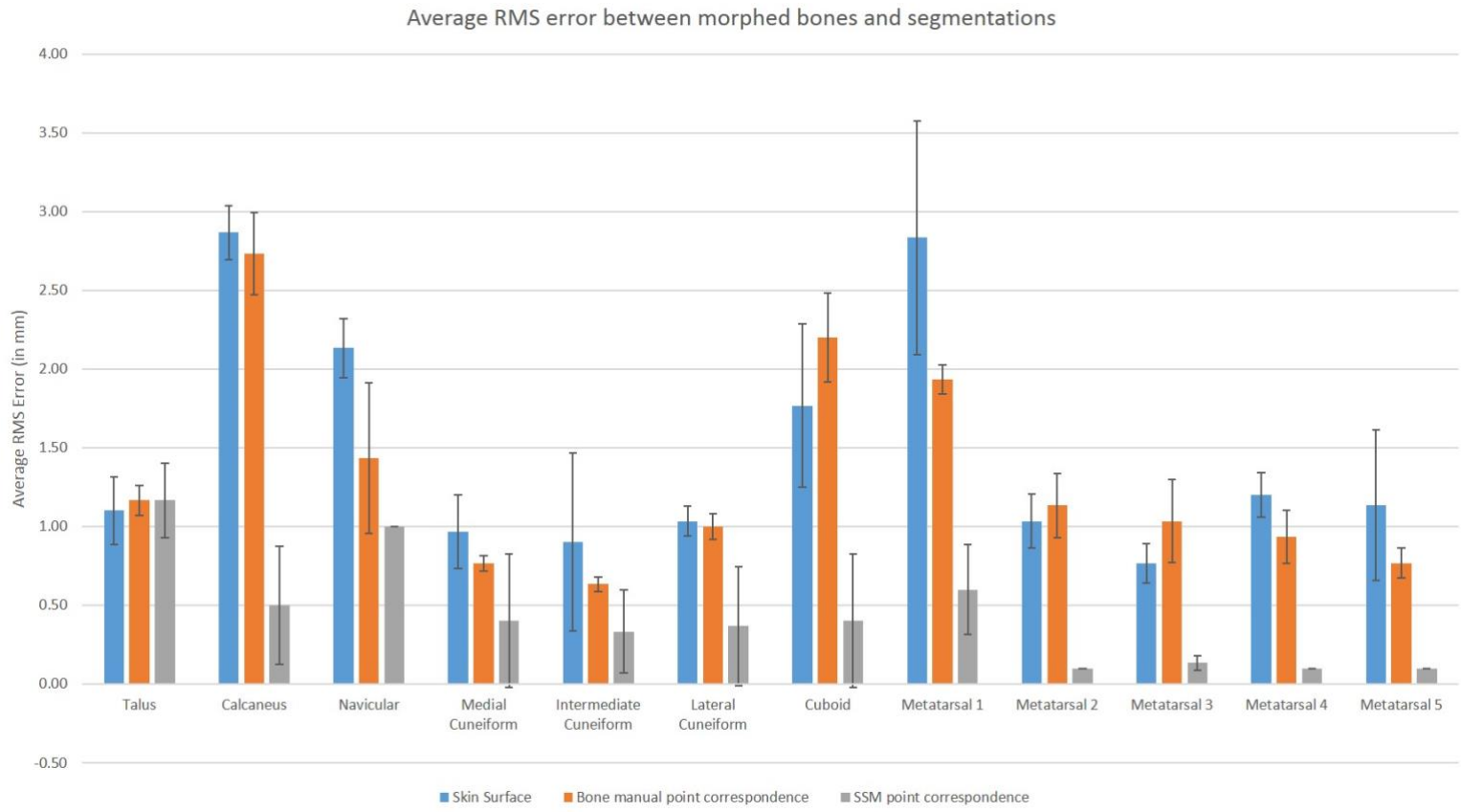

Figure 78 Graph showing the average RMS error between morphed meshes and patient segmentations of a skin scaling morphing technique (blue) a bone based manual point corresponding technique (orange) and an SSM based automatic point corresponding technique (grey)

5.3.2 Kinematic model optimisation

The 26-segment GM kinematic model from the AMMR 1.6.6 was used as the foundation in this thesis. Small changes were applied to the contact algorithms, specific to the metatarsal within the model. These contact algorithms aim to prevent the distal end of the metatarsals from intersecting, during the initialization and optimizing of markers and segments of the kinematic model. Due to the development and implementation of the SSM based scaling and morphing approach, generally there was an impact on the kinematic model's ability to solve the initial conditions. To improve the initial guess of the kinematic model and allow it to solve, the intersecting contact algorithms of the metatarsal heads were slightly increased or decreased changing the contact diameter to cover the entire width of the distal end of the metatarsal bone. The kinematic tolerances were set to $5e^{-4}$ in an over determinant system.

To test the sensitivity of the scaling methodology on kinematics, with morphing technique the least overall error, the SSM approach was compared to the published method, for the kinematic model. Ankle joint plantarflexion was used as the test motion. Figure 79 shows a graph consisting of three patients, one low, one normal and one high arch foot type. For each patient two lines are presented, the solid lines represent the kinematic output for the SSM approach, and the dashed lines represent the previously published scaling approach.

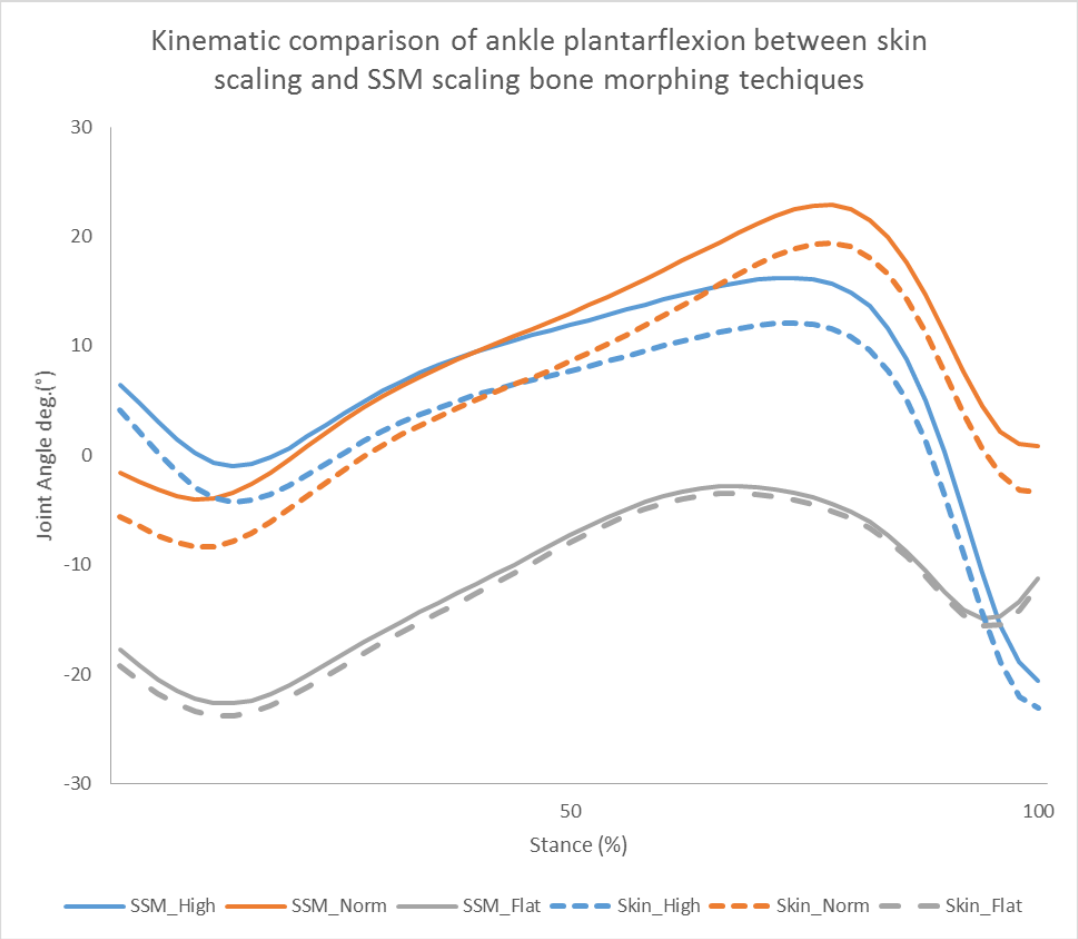

Figure 79 Graphs comparing ankle plantar flexion of one trial from three patients using the skin scaling and SSM bone morphing techniques. The low arch foot is represented in grey, the normal arch foot is represented in orange and the high arch foot is represented in blue.

The graph, shown in Figure 79 presents a comparison of two scaling techniques applied to three-foot types: low (grey), normal (orange) and high arch foot (blue) types using the same kinematic foot model. For each foot type, there are differences in the starting angles between scaling methods. The high arch foot type had a difference of +2.07 ˚, where the SSM morphing technique resulted in a higher starting value. The normal foot arch type had a difference of + 3.94 ˚, where the SSM morphing technique resulted in a higher starting value. The low arch foot type had a difference on + 1.54 ˚, where the SSM approach resulted in a higher starting value. The

differences in starting angles are due to the anatomical referencing frames between the bones changing when comparing the two scaling methods.

Correlations between the SSM scaling method and the published literature, for three-foot types; low, normal and high arch were compared at the ankle joint for plantar flexion movement. Figure 80 shows the highest correlations are observed between the same foot type and the alternative scaling method, i.e., SSM_High – the statistical shape modeling morphing approach with the high arch foot, compared to Skin_High – the published literature approach using the skin surface with the high arch foot. The least correlated variable was the high arch foot type compared to the low arch foot type, i.e., Skin_High compared to Skin_low. These results indicate the least correlated variables are between the high and low foot types and most correlated variables are between the same foot type and different scaling method.

	SSM_High	SSM_Norm	SSM_Flat	Skin_High	Skin_Norm	Skin_Flat
SSM_High	1					
SSM_Norm	0.72	1				
SSM_Flat	0.64	0.95	1			
Skin_High	1	0.70	0.62	1		
Skin_Norm	0.71	1	0.94	0.70	1	
Skin_Flat	0.63	0.95	1	0.6	0.95	1

Figure 80 Showing the correlation between two different bone morphing methods (the default skin scaling) and SSM between foot types in ankle plantarflexion. The lower the number the less correlated the variables are and the higher the number the more correlated the variables are.

5.3.3 Pressure data optimisation

The integration of the pressure data was scripted in the model to facilitate inverse dynamic analysis, which while not used in chapter 6 in the application of the foot model, was developed to show the possibility of applying the technique to extremes of foot posture. The pressure matrix was converted from a text file into a coefficient that was passed into the 26-segment foot model. The coefficient output from the model is being appropriately applied during the analysis when the value is 1 which indicates the total use of the pressure matrix, as presented in Figure 81. The FootTestSum variable, specific to the model, was normalised to 100% of stance for a comparison between three-foot types, low arch (indicated with a dotted red line), normal arch (indicated with a dashed yellow line) and high arch (indicated with a solid black line). The results from the analysis of the coefficient shows data of 3 subjects with varying foot posture to closely matching 1 though the stance phase of gait and this in then inferred as the total pressure matrix being used in the model and dropping off at terminal stance.

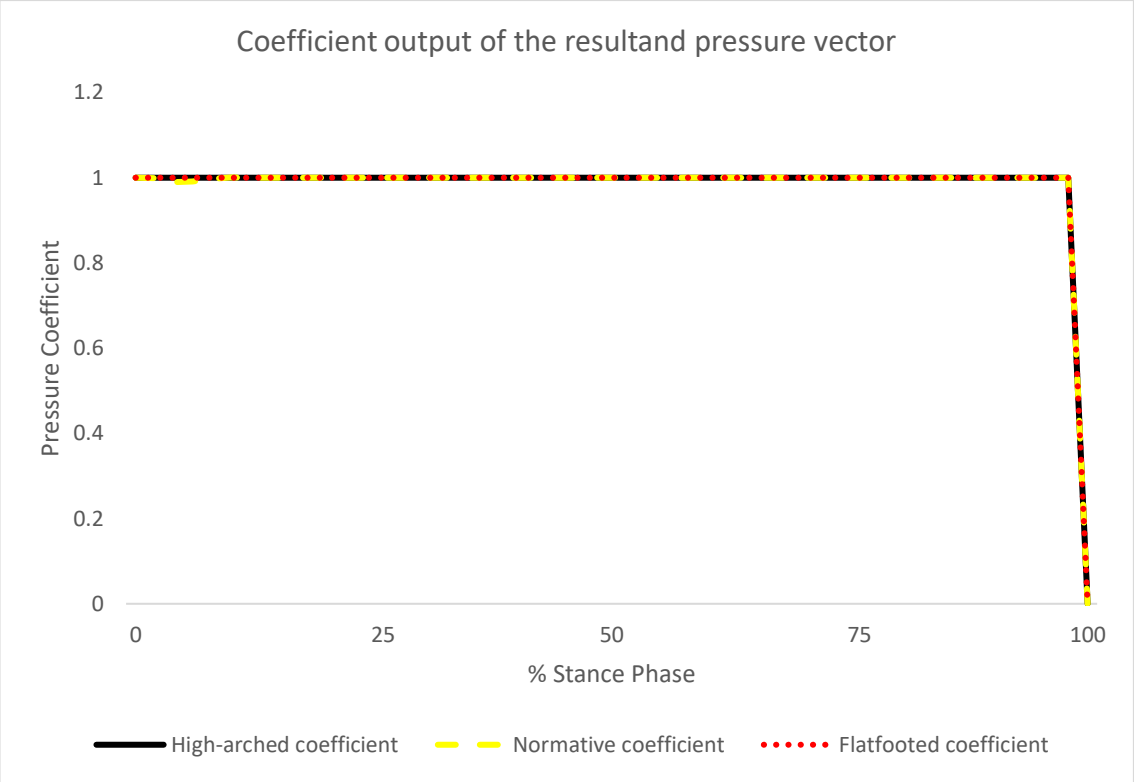

Figure 81 A graph showing the model using the coefficient vector from the pressure matrix in of a range of foot types. The low arch foot type is indicated with a dotted red line, the normal arch foot type is indicated with a dashed yellow line and the high arch foot type is indicated with a solid black line.

A comparison of the force vector outputs from the 183 pressure nodes with the kinetic data was made to show how the placement of the virtual pressure matrix under the foot was being applied in the inverse dynamic analysis. Figure 82 shows the force vector output from the pressure nodes of the 3 subjects being applied to the biomechanical model in a synchronous timeframe with the kinetic force data normalised to 100 percentage of the gait cycle. Figure 82 shows, for each foot type of low, normal and high arch, the sum of vector outputs for the pressure nodes, matches the resultant force from the force plate, indicating the force vectors to the pressure nodes are equal to the force measurements from the force platform.

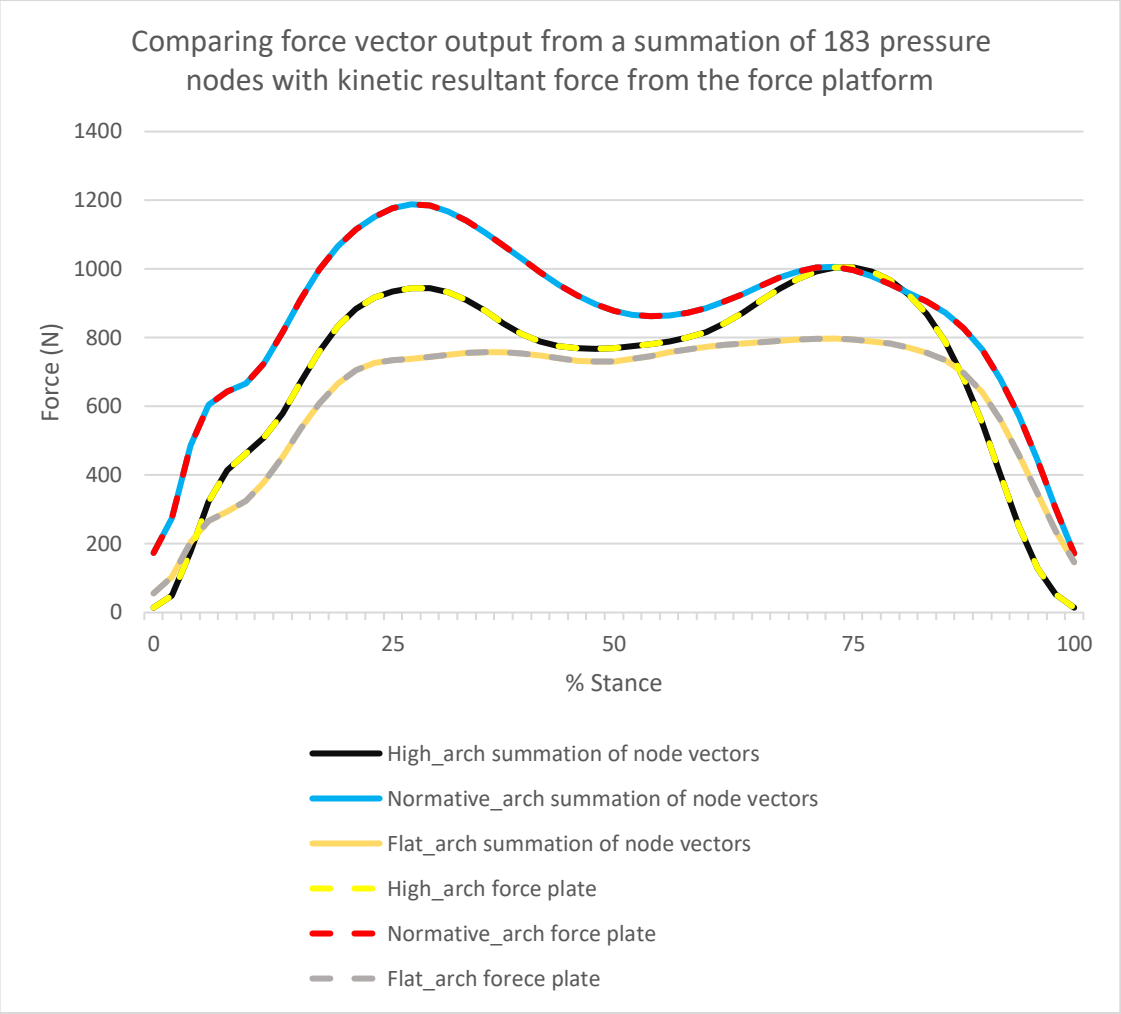

Figure 82 Comparison of the global resultant force and the combination of force vector outputs from the 183 pressure nodes. The data shows for three-foot types, the low arch pressure node summation (solid yellow) overlayed on the low arch force plate measurement (dashed grey); the normal arch pressure node summation (solid light blue) overlayed on the low arch force plate measurement (dashed red); The high arch pressure summation (solid black), overlayed on the high arch force plate measurement (dashed yellow) over a normalised percentage of stance phase.

The integration of the pressure data using a coefficient matrix uses all the available data based on the FootTestSum (an AnyBody named variable

vector for resultant pressure from the nodes) coefficient measurement and the summation of force vector outputs from the pressure nodes matches the global resultant force from the forced platform. By overlaying the two variables (Figure 82), global resultant force and summation of vector from pressure nodes in this evaluation demonstrates the pressure data was used in the model for the entire length of the study as these two overlay each other throughout the study.

5.4 Discussion

5.4.1 Bone morphing optimisation

The generation of bone morphologies was derived from segmenting MRI scans which is difference to previously literature using the CT scans. Using MRI scans has significant benefits as there is no ionising radiation exposure to the patient, however CT scans are easier to segment and work with for MSK modelling applications and segmenting MRI scans takes more refinement to get adequate shape geometries. Using MRI scans with the 26-segment foot model increases future utility for scaling and morphing soft tissues.

Generating accurate patient specific bone morphology, is an important input data source for building an MSK model that can be abstracted and applied to many pathologies. The GM model published on the AMMR 1.6.6, is scalable, by using a surface scan of the foot (Oosterwaal et al., 2016) to create patient specific geometry. This published scaling method was compared to two

other methods developed in this thesis. One method involved a manual point process and the other relied on automatically generated 3D point clouds derived from a statistical shape model developed in chapter four. Of the few papers published using the foot surface scaling method, (Jung, 2014; Oosterwaal et al., 2016; Al-Munajjed et al., 2016), only one highlights the method in enough detailed to replicate (Oosterwaal et al., 2016), with others using the same non-linear scaling technique. However, no sensitivity analysis of these scaling methods has been applied to the GM foot model. Using a surface scan of the foot, whilst useful for clinical applications, it does not capture potentially important information at the joint level required for other, more detailed applications such as understanding joint function. This could be due to the skin surface including tissues such as muscles, ligaments and fat which have to potential to impact the accuracy of the bone morphing process. When considering variation in foot posture, scaling the individual bone to the patient provides an extra level of required detail for the answering questions associated with low and high arch foot types, as there are subtle differences in the bones of the foot. The bone scaling methods developed in this thesis present a workflow, which accurately captures each subject's bone morphology, including the calcaneus, talus, navicular, cuboid, three cuneiforms and 5 metatarsals, and which has potential to contribute to a detailed understanding of the variance associated between low, normal and high arch foot types.

Scaling biomechanical models in gait analysis applications using advanced MSK modelling techniques can use segmented medical images to scale cadaver based models, such as has been demonstrated in the knee (Marra et al., 2015), based on the work by Pellikaan et al., 2014 where two cadaver specimens were analysed and the error in muscle attachment sites measured, Marra et al., 2015 made used of the Materialse NV (Leiven, Belgium). The differences between the method proposed in this thesis and Marra et al., 2015 relate to generating the corresponding points between the target and the source bone geometries and their STL representations to initialise the RBF morphing algorithm to changes the muscle insertion or origin points to match the patient. In this thesis the correspondence between

the MSK model and the patient was determined though a statistical shape modeling approach as defined in chapter 4 with error between the spawned STLs geometries and the STL segmentations presented in Table 9. Although the statistical shape modelling approach adds extra computational processing to, the added benefit is the analysis of capturing morphological variation within and between study groups and therefore enhancing the novelty of the pipeline developed in this thesis.

As AMS models are based upon average anthropometric human shapes they do not account for individual differences in either kinematic or inverse dynamic analysis. Within a kinematic analysis the motion angles are defined relative to each segment and can more accurately be accounted for with personalised bone shapes derived from medical images using the patients joint centres (Marra et al., 2015) this should be noted and mentioned as limitation within the pipeline developed and further work on the development of the MSK model presented should focus on recalling the joint centres for each patient. Furthermore, the error associated with inter/extrapolation of the RBF function could be reduced by making improvements to the bounding box to be within the latent space defined by the principal component space, i.e. by making the bounding box a ‘bounding principal component space’

The scaling algorithms developed and applied in the bone morphing process use the RBF, as pretransformation before a corresponding point STL surface match is applied to the template mesh. The template meshes include cartilage in the geometry and so further sensitivity of the effect of interpolation algorithm could be investigated for applications that require submillimetre accuracy, like the effect of cartilage thickness on joint contact forces. The RBF morphing algorithms applied to the source and target points were transformed using a non-linear affine transformation. This has the advantage of capturing local deformities in bone morphology and the location of the origin and insertion points. This RBF technique has been applied to MSK models using individual CT derived bones of the foot (Al-Munajjed et al., 2016), however the exact point correspondence was not published.

Issues with using bone STL representations derived from segmentation masks of medical images are associated with the staircase effect that occurs from the mask cause 1) an unsmoothed surface and 2) the corresponding source and target points are generated manually, which has an impact on time to generate and accuracy on area on anatomy that are difficult to demine, especially on the non-uniform shapes of foot and ankle bones. Using a SSM approach is both more efficient and more accurate demonstrated in Tables 10, 11 and 12.

An issue with using a SSM approach as a scaling approach to multibody modeling is relying on the quality of the template model geometry, and point correspondence with the patient bones. More specifically, the GM version of the TLEM 1.0 bone template geometries have some inconsistencies, such as poor mesh quality that would not be typical of human bones, these inconsistencies have been addressed in the TLEM 2.0 body template model, however the GM foot model has yet to be fully implemented into the commercial repository using this new bone geometry template. To overcome these mesh inconsistencies and to use the model template meshes in a SSM workflow, the foot template bone meshes were converted to binary images, using a surface to mask filer in 3D Slicer. This conversion from a STL mesh to binary image resulted in small amounts of mesh error, or small differences in similarity, in generating higher quality meshes from the low quality TLEM 1.0 repository mesh. A maximum RMS error of 1.4 mm was found between the low-quality AMMR mesh and high-quality template mesh, that was the repurposed for a SSM. The RMS error of 1.5 mm between the low-quality AMMR mesh and the shape model generated mesh. These results indicate less error between the AMMR meshes and the repurposed meshes, over the AMMR meshes compared to the spawned meshes from the SSM, however overall demonstrates acceptable error of geometries for a patient specific model for kinematic analysis. This error has the potential to impact results from inverse dynamic analysis, for example if the error was greatest at muscle origin or insertions points, or if the error was greatest at the articulating surface where joint reaction forces are calculated. However,

this error has less of an impact on kinematic analysis and the bones are treated as rigid bodies.

Considering the error of the morphing process between manually selecting corresponding points on the bone surfaces, the largest RMS error was 3.1 mm. This error was likely to be due to the accuracy of the correspondence between source and target meshes and the corresponding points not accurately capturing areas of high curvature. The points chosen on these bones were selected to capture areas of high curvature so further evaluation could be carried out on anatomically relevant points to improve the manual, but easily identifiable anatomical landmark on each of the bones. In contrast the SSM approach demonstrates that accuracy can be significantly improved by using an automatically generated point correspondence with ShapeWorks Studio.

Considering the mesh error between the patient segmentations and the spawned STL's from the shape model, the largest error was 1.5 mm on the Talus. This error could be due to the parameters set by the shape model in chapter two not being optimal, more specifically, the 1 standard deviation set for the shape model PCA analysis and STL reconstruction used in the shape model might not have been sufficient to capture the variation in this small developmental set of foot types. Further evaluation of these parameters could be carried out to reduce the error, however as the input to the shape model consisted of only 4 bone shapes, for development purposes, it is likely that an increase in the number of input shapes will increase the model's ability to spawn better representations of the input shapes, demonstrated in chapter four.

The range of RMS error for all morphed bones in the shape model between the published skin scaling method, manual bone corresponding point method and SSM approach were 0.5 mm – 3.5, 0.6 mm – 3.1 mm and 0.1 mm – 1.5 respectively, demonstrating that the published scaling technical is similar to the manual point picking process, however both of these methods resulted in more error than the SSM approach. Figure 78 shows that in the majority of the bones using a SSM approach result the smallest RMS error.

Similar work morphing SSM bone reconstructions to a reference model was carried out by (Nolte et al., 2016) where the thigh (femur) and shank (tibia and fibula) had a RMS error of 1.29 (0.33) mm and 1.70 (0.29) mm respectively, the study using the SSM in this thesis produced similar error. The range of error using a SSM can be explained by the capabilities of the shape modelling process to accurately correspond points on the surfaces between roughly aligned binary images and to adequately generate STL's from these 3d point clouds.

Although, comparing results of the scaling and morphing process of the bone geometry to the segmentations for the SSM was comparable to published literature in a subject specific model (Nolte et al., 2016), using an RBF inter/extrapolation; while with a bounding box aims to avoid poor extrapolations, comes with challenge that were not address in full in this thesis and remain a limitation to the kinematic results reported in chapter 6. For example, in addition to the geometric surface matching of the patient being morphed with acceptable error, the joint centres of the model are also altered in the 3D multibody model. This adjustment of the joint centres has an impact on joint axis and centres of mass of the patient, which was not compared or controlled for in the development of the model and are known to have an impact on kinematics [papers from marra and the joint axis paper]. The impact of recalculating the joint centres or the axis of rotation from each patient after the model has been morphed would be needed to increase the clinical usefulness of the foot model developed in this thesis.

5.4.2 Kinematic model optimisation

Kinematic and kinetic data collected for the 26-segment model were developed using a different method to previously published. The kinetic data in this thesis was collected using an AMTI system which require developing in the form of software scripts within the AMS and was also used in the development of the pressure integration. This development extends the used of the system to other users of the 26-segment foot model.

The kinematic model in this thesis was derived from the GM foot model from the AMMR 1.6.6 repository. Additional markers were added to the thigh and

leg segments of the GM model adding time to the marker optimisation process but increasing the accuracy of the femoral and tibial motion. However, this may have added extra time to optimize which may not have been entirely necessary given the focus of the work was on the foot.

As the SSM approach to scaling and morphing the bones was used as an alternative to the published, default skin scaling technique to morph bones of patients with varying foot postures, this process revealed mesh errors between similar patient geometries. In addition, the sensitivity of the ankle plantar flexion kinematic measure was investigated, comparing the published skin morphing approach with a SSM morphing technique. A comparison of kinematic outputs of the ankle plantarflexion measure was made to test the model's sensitivity to changes in bone morphing methods. The starting angles of the same patient between the two scaling and morphing techniques differ due to the local definition of the joint axis changing with respect to the compared scaling and morphing methods. This local change in bone and initial joint orientation is more conspicuous when comparing the high arch foot type with the low arch foot type. An investigative correlation coefficient (Figure 80) shows high correlations between the corresponding foot type and the alternative scaling method, for example the SSM high arch has a correlation of 0.99 with the skin scaled high arch measure, while the SSM high arch foot type has a correlation of 0.63 with the SSM low arch foot type for ankle plantarflexion, reinforcing the differences in starting angles to be due to the changed in bone orientation between flat and high arch foot type. This indicates that the GM foot model is sensitive enough to capture anatomical variation between extremes of foot postures in terms of altered kinematics.

Ankle plantarflexion/dorsiflexion was selected to compare the sensitivity between foot types and scaling methods as it is notionally comparable to other clinical foot models. However, the construction of bone segments and joint axes in the GM foot model is different to traditional biomechanical foot models with the GM foot model using anatomical geometry from the patient and defining the joint axis locally on the bones themselves, while in

traditional biomechanical models the segments are generated from markers positioned on the calcaneus and joint axis defined by the centre of those segments (in the OFM or the Leardini foot models for example). While a comparison between traditional foot modelling and MSK foot modelling could be done it makes little sense in the way of validating or verifying the typical kinematic profile for ankle plantarflexion. Although, comparing multiple foot models with data collected from the same patient would be interesting to investigate. Also, to more accurately validate motion at the ankle joint techniques such as real-time 3D biplanar fluoroscopy study would provide a more suitable reference. This type of study however was not carried out in this thesis and can be considered as a limitation of the work presented.

Interpreting kinematics from MSK and other biomechanical models involves the notion of a standard reference frame and ‘neutral’ position for comparative analysis within and between groups; this is a generally accepted challenge to overcome in foot biomechanics. This model developed in this chapter relied on reference frames local to the bones, of which were included in the joint. Due to the natural anatomical variation seen between low arch and high arch foot types, it was implied that differences seen between these groups would be related to anatomical changes in bone orientation, however without the recalibration the centre of the joint differences seen between groups might not be true and the model would need further development to make more fair comparisons.

The numerous approaches to co-ordinate system definition reviewed by Lenz et al., (2021) suggests that a single universal co-ordinate system should be agreed upon among researchers. Given the ambiguity surrounding the ‘true’ movement of individual bones in the foot created by individual patient differences, introducing standards for comparisons beyond the ankle complex towards the distal ends of the foot would really help the field of foot biomechanics mature and progress.

5.4.3 Pressure optimisation

Pressure data was collected using an Emed system, which different to previously published literature that used an RS scan device with the 26-segment foot model. This required development of new scripts and it also creates an additional pressure data option to the MSK foot modelling user base.

The GM foot model uses a combination of pressure data with medical imaging and 3D motion capture in the analysis of patient biomechanics. The model described in this thesis describes how the pressure data was integrated using python scripts from the model repository with several changes to the virtual environment file in order to be successfully deployed and used with an alternative gait motion laboratory set up. Changes were made to the virtual force plate with the development of a new ‘type2pressure plate’ to work with an AMTI force platform. Additionally, the AMMR model used an RS scan pressure mat for plantar pressure acquisition. To investigate the sensitivity of pressure between foot types and scaling methods the pressure acquisition for patients in this study used an Emed pressure system. The introduction of a new system in comparison to the published methodology required the development of code and scripts were created to transform Emed data into a text file that the 26-segment foot model could interpret in the context of a type2pressure plate in the virtual environment. Within the 26 - segment model the text file containing the pressure data was converted to several coefficient vectors that is then applied to the foot in the analysis. The location of the virtual pressure matrix in the AnyBody GM model was manually placed under the foot so that the pressure was delivered to the correct bones at the correct time. The virtual pressure mat was consistently placed for each patient, however the location of the foot landing for each trial varied. To ensure all the pressure data from the text file containing pressure data was distributed throughout the pressure nodes on the foot, the same modeller made visual adjustments to the pressure matrix. Acceptable placement of the matrix was deemed when the combined output vector from 183 pressure nodes matched the python

scripted coefficients and the global resultant force output. The positioning of this pressure matrix was verified by the coefficient vectors in the model being shown as active and equal to 1. Figure 81 shows that the vector force is equal to 1 throughout the study and drops off at terminal stance, indicating that all the pressure information from the text file was being used in the model. To ensure that the coefficient vector matched the global resultant forces that the patient was applying to the force platform, the summation of force vector outputs from the pressure nodes were plotted against the global resultant force from the force platform in the gait laboratory. Figure 82 shows the two measures, global resultant force and the summated forces from the pressure nodes plotted on the same graph matching each other, indicating that the pressure data is being incorporated into the model as intended. This demonstrates the model's applicability, by verifying the use of force data, for further work to address differences in muscle, joint forces between low, normal or high arch foot types. Further work could investigate the automation of placing both the virtual pressure mat and the foot pressure matrix.

5.5 Conclusion

5.5.1 Bone morphing

Remeshing the template model bones allowed for more accurate morphing of patient specific bones, however, did result in some error in comparison to the original TLEM 1.0 bone meshes. Concerning patient specific morphing error, the largest error was seen in the existing skin scaling method, the second largest error was seen in the manual point picking process and the least error was seen in the shape modelled bones. Based on the results from 3 subjects each with 12 bones, using a SSM workflow to produce patient specific bone morphologies in STL file format results in 58% reduction in maximum error over using the foot scaling method and a 52% reduction over using the manual point correspondence.

The automatic corresponding point method is more accurate at capturing morphology of patients than the manual point picking and the skin scaling method as can be observed where 11 out of the 12 bones indicated that the SSM produces the most representative patient mesh by having the least amount of error.

5.5.2 Kinematics

An analysis of the effects of bone morphing on the ankle plantarflexion kinematic measure from the GM foot model showed two things. First, for each matching foot type scaling methods had high correlations indicating that the main source of variation between scaling methods was the starting angle. Second, the correlations were the least between the extremes of arch type, indicating that the GM foot model is sensitive enough to capture local positional changes in bones and their joint orientation.

Chapter 6 Application of foot model to extremes of foot posture

6.1 Introduction

Variations in foot morphology, some quite extreme, relating to postural differences have been associated with kinematic function using several multisegment models (Hunt and Smith, 2004; Cobb et al., 2009; Levinger et al., 2010; Saraswat et al., 2014; Buldt et al., 2015; Caravaggi et al., 2018; Kruger et al., 2019). Other biomechanical parameters, such as plantar pressure have identified differences within foot types (Burns, Crosbie, et al., 2005; Hillstrom et al., 2013; Buldt et al., 2018) in addition neuromuscular imbalances have also been noted (Burns, Redmond, et al., 2005). An excessively supinated foot is a characteristic often associated with a high arch foot and has been linked with overuse injuries in long endurance athletes (Burns, Keenan, et al., 2005). Similarly, lower extremity overuse injuries have also been associated with an over pronated feet (Kaufman et al., 1999) characterised by low medial arches. Low arch foot types have been reported to have a reduced medial longitudinal arch with hindfoot valgus, while high arch foot types have a characteristically increased arch with hindfoot varus (Franco, 1987; Ledoux et al., 2003; Kim, 2017). Despite literature highlighting the gross structural differences between foot types and indicating these as risk factors for injury, kinematic differences between hypothesized ends of a foot posture spectrum are not consistent within the research.

6.1.1 Aim

The aim of this chapter is to apply the processed MRI scans developed into a statistical shape model from chapter four in order to generate patient specific geometry that can be integrated into the 26-segment foot model developed in chapter five. In addition, gait analysis of low, normal and high arch foot types collected in chapter three will be used to drive motion of the foot bone segments. Integration of subject-specific bone geometries with detailed gait analysis will be used to assess the applicability of the 26-segment foot model in determining the possibility of the presence of systematic, foot-type-related kinematic differences in the joints of the hindfoot, midfoot and medial ray, including ankle plantarflexion, subtalar eversion, talonavicular dorsiflexion, talonavicular abduction, talonavicular eversion and first metatarsophalangeal dorsiflexion. The aim of the analysis was on medial ray kinematics due to the medial longitudinal being a hypothesised primary diagnostic feature of foot type. Specifically, the focus was on demonstrating the sensitivity of the 26-segment foot model developed in chapter five to detect systematic differences between low, normal and high arch foot types.

6.1.2 Objectives

The objectives of the chapter are to a) apply the statistical shape model developed in chapter four to generate patient specific geometry and b) analyse kinematics of foot joints including ankle plantarflexion, subtalar eversion, talonavicular dorsiflexion, talonavicular abduction, talonavicular eversion and first metatarsophalangeal dorsiflexion to determine whether systematic statistical differences can be identified between foot-type groups.

6.1.3 Hypothesis

Null hypothesis:

There are no systematic differences in the kinematic motions (dependent variables) of medial ray joints including foot joints including ankle plantarflexion, subtalar eversion, talonavicular dorsiflexion, talonavicular abduction, talonavicular eversion and first metatarsophalangeal dorsiflexion between low, normal and high arch foot types (independent variables).

Alternative hypothesis:

Systematic differences exist between medial ray kinematic motions (dependent variables) of medial ray joints including ankle plantarflexion, subtalar eversion, talonavicular dorsiflexion, talonavicular abduction, talonavicular eversion and first metatarsophalangeal dorsiflexion between low, normal and high arch foot types (independent variables).

6.2 Methods

A total of 13 patients in the study were divided into three groups; 5 high arch (FPI = -4 to 0); 4 normal arch (FPI 1 to 4) and 4 low arch (FPI = 5 to 12) as shown in Table 13. Patients undertook a series of walking trials at a self-selected speed in the gait analysis laboratory during which lower-limb kinematics and kinetics were collected using methods described in chapter three. Data from each patient was collected over 18 months from Leeds Biomedical Research Centre, Chapel Allerton Hospital, Leeds, UK, REC reference number: 17/YH/0261.

Kinematic data was collected at 200Hz using an eight-camera system (Vicon MX, Oxford, Metrics, UK) and kinetic data was generated from an integrated force platform AMTI force plate at 1000Hz. Multi-segment foot kinematics for right feet were taken using a motion capture marker set up previously, as described in chapter three and based on work by Carbes et al., (2011) with the addition of a CAST markers for femur and tibial motions. Markers were placed on the subject's right foot as previously described in chapter three.

For each trial, automatic gait event detection was obtained from the force platform data, using threshold values of 10N for heel strike and toe off.

Table 13 Showing grouping of patients used in the analysis

High		Normal		Low	
-4 to 0		1 to 4		5 to 12	
Subject ID	FPI	Subject ID	FPI	Subject ID	FPI
1	-4	6	4	11	10
2	-2	7	3	12	11
3	-3	8	3	13	6
4	0	10	1	15	5
5	-3				

6.2.1 Data analysis

Intersegment angles including ankle plantarflexion, subtalar eversion, talonavicular dorsiflexion, talonavicular abduction, talonavicular eversion and first metatarsophalangeal dorsiflexion were extracted from the 26-segment lower-body foot model of the right foot developed in chapter five, that is an iterative version of work described by Carbes et al., (2011) and Oosterwaal et al., (2011) in a model published in the AMMR. Previously described inputs which drive the model, such as the number and location of the retroreflective markers are described in chapter three were used. Bone geometries in the MSK model were scaled from a statistical shape model pertaining to the participant. Methods to generate bone geometries were detailed in chapter four and the implementation of patient specific scaling process to morph the template 26-segment foot model is detailed in chapter five.

Kinematic time series between the three-foot types were derived from the MSK foot model and normalized to 100% of the stance phase (between

heel-strike and toe-off). Heel-strike was determined when the resultant force from the force platform registered 10N and toe-off was signalled when the force platform was less than 10N. Mean RoM and standard deviation was calculated over a minimum of 2 successful trials as defined by no marker dropout, with the minimal and maximal RoM calculated for each low, normal and high arch groups and minimal and maximal joint angles, to compare between low, normal and high arch types. Averaged kinematics were calculated for each participant. Grand means across participants within the group were then calculated to allow comparisons between foot types, this analysis was done using code developed and hosted in the GitHub repository (https://github.com/zwelshman/GMfoot-Kinematics-Analysis). Foot joints that were compared in detail included the ankle, talo-navicular, naviculo-medial cuneiform and first metatarsophalangeal joints. All other joint angles were calculated and presented in Appendix B.

Outputs for the three foot-type groups were first graphed to establish whether any joint/motion combinations appeared to yield systematic progressions in values i.e., low to normal to high arch foot types. To provide some statical analysis, despite the small sample size exploratory comparison of group means was undertaken using statistical parametric mapping (SPM) package. A statistical parametric mapping package SPM1D (documented at https://spm1d.org) developed using python and code related to the analysis (documented (https://github.com/zwelshman/GMfoot-Kinematics-Analysis/SPM1D) was applied to time normalised stance phase data. For each point in the time-series the t statistic was calculated, leading to the test statistic SPM{t} (Pataky, 2012; Pataky et al., 2013; Pataky et al., 2015). The significance level was set $\alpha = 0.05$ and the *t* critical threshold calculated based on temporal smoothness of the input data through Random Field Theory. This analysis is underpinned in work described by Pataky et al., (2015) assumptions including the appropriate criteria for normally distributed data. The kinematic data analysed using SPM has sample sizes per group, therefore tremendous caution is advised in the statistical interpretation of the results presented later in the chapter. Data derived from the 26-segment foot model was assumed to be normally distributed. While

the sample size of each low, normal and high arch foot types was small, resulting in lack of statistical power the applicability of SPM produces useful information. This method was used in an exploratory manner therefore to indicate which groups and at what point in the time series a statistically relevant difference might be observed and could be targeted in future studies.

6.3 Results

Kinematic profiles of the motions data derived from all joints of the GM model are shown in Appendix A. Each graph shows the average kinematic profile for each of the foot types. Average, minimum and maximum RoM's were calculated for three groups and all kinematic measures derived from 26-segment foot model in Appendix B.

More detailed SPM analysis was performed on the targeted hindfoot, midfoot and medial ray joints of the foot, including ankle plantarflexion, subtalar eversion, talonavicular dorsiflexion, talonavicular abduction, talonavicular eversion and first metatarsophalangeal dorsiflexion Results for naviculo-medial cuneiform abduction, naviculo-medial cuneiform dorsiflexion, first tarsometatarsal dorsiflexion, first tarsometatarsal abduction were not presented in the results as they are a function of talonavicular dorsiflexion, talonavicular abduction.

6.3.1 Ankle joint dorsiflexion / plantarflexion

The mean (SD) values for ankle dorsiflexion/plantarflexion excursion for high, normal and low arch groups were 15.6° (1.06) 14.19° (3.51); 16.79° (2.92), respectively, see Appendix B. The low arch cohort had the greatest mean ankle dorsi / plantar flexion RoM compared to the high group, which had a greater RoM than the normal group, shown in Figure 83. When viewing the graph in Figure 83 there was clear evidence of a general systematic progression of values for the motion-time series, with the flat

group being lower overall, the normal group residing centrally within the distribution and the high arch group yielding more dorsiflexed values overall.

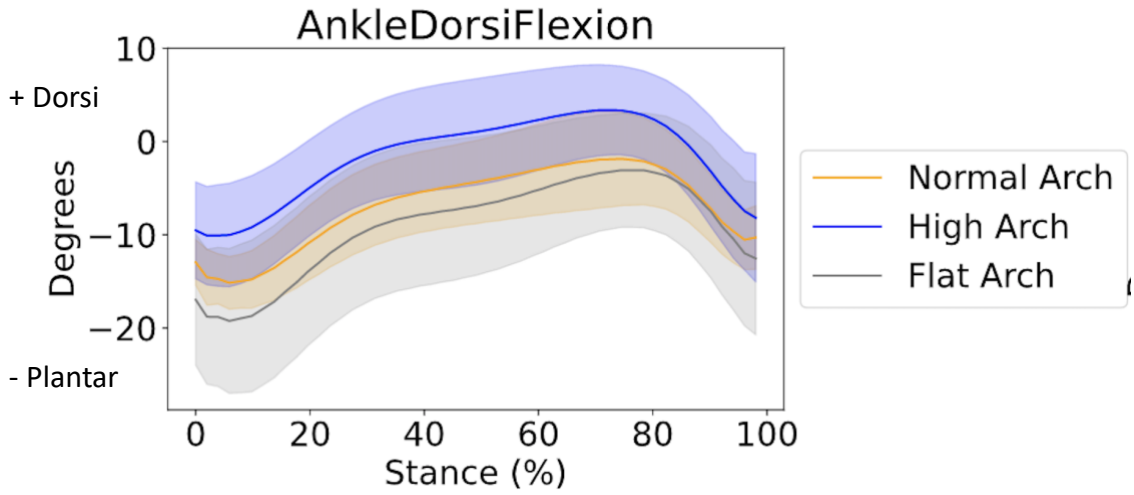

Figure 83 Showing ankle plantar/dorsiflexion kinematic profiles for high (blue), normal (orange) and low arch (grey) foot groups with 1 standard deviation.

The SPM analysis indicated statistically significant difference between the high and low and high and normal arch foot types (Figure 84). The high arch group demonstrated significantly increased ankle dorsiflexion compared to the low arch throughout the stance phase (0-76%) with the supra threshold cluster exceeding the threshold t^* = 2.741 with a *P*-value = 0.001. Statistically significant differences were also observed between high and normal arch types, where the high arch group demonstrated greater ankle dorsiflexion compared to the normal arch foot type (7-36%), with the supra threshold cluster exceeding the threshold t^* = 2.791 with a *P*-value = 0.017. No statistically significant differences were evident during the whole stance phase between normal and low arch foot types.

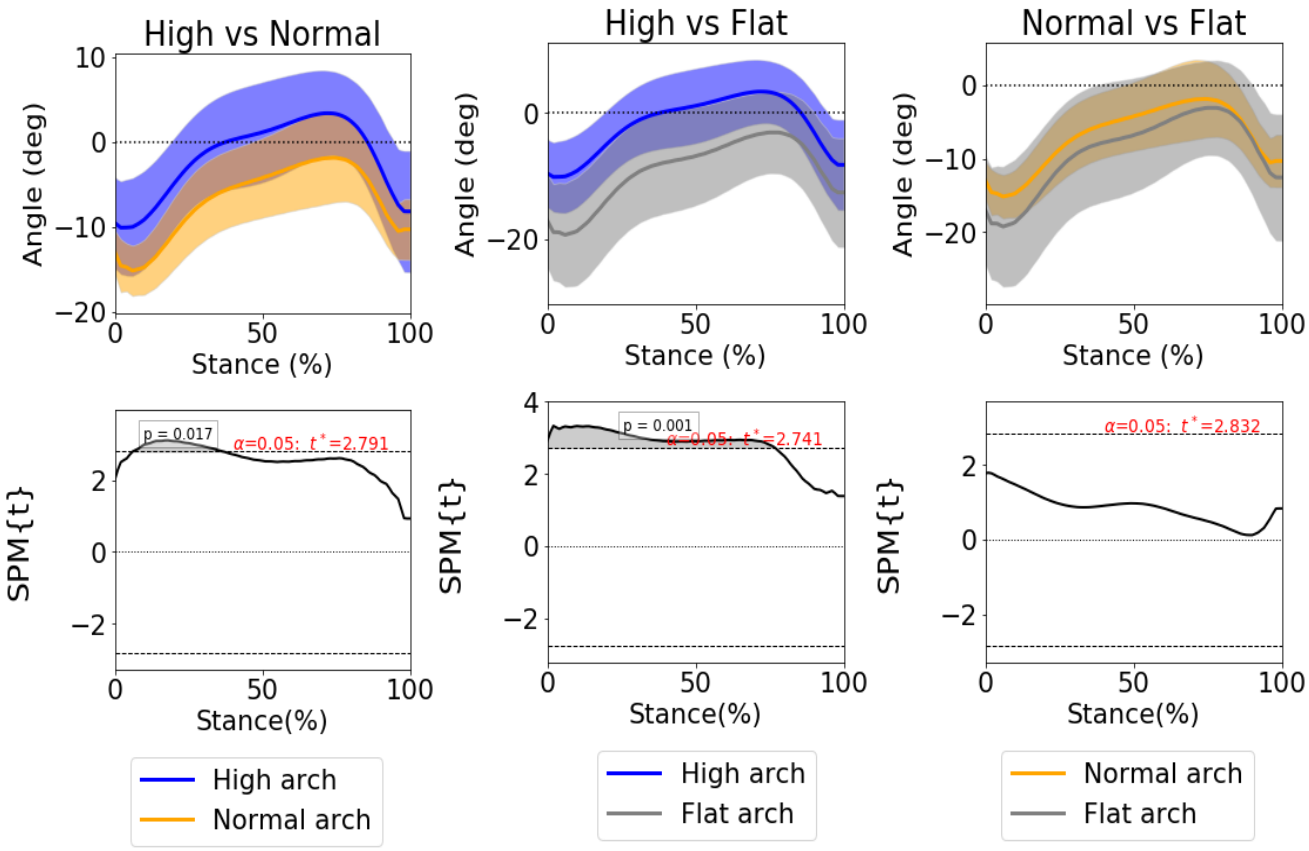

Figure 84 Showing statistical parametric mapping (SPM) t-test analysis between high (blue), normal (orange) and low arch (grey) groups as a percentage of stance phase of gait for ankle dorsi/plantar flexion. Statistical differences are shown between high and normal and high and low arch groups.

6.3.2 Subtalar eversion / inversion

Initial visual inspection of the graph in Figure 85 indicated systematic progression of values for the motion-time series, with the high group being lower overall, the normal group residing centrally within the distribution and the low arch group yielding more eversion values overall. Each of the foot types began in an everted position and became less everted throughout stance phase of gait. The total population for the subtalar eversion/inversion showed a mean (SD) excursion of 13.51° (4.0), with high, normal and low arch groups presenting with 14.57° (2.96); 12.35° (4.99); 13.36° (3.66) degrees respectively, as seen in Appendix B. The high cohort had the greatest mean RoM compared to the low arch group, which had a greater average RoM than the normal group, shown in Figure 85.

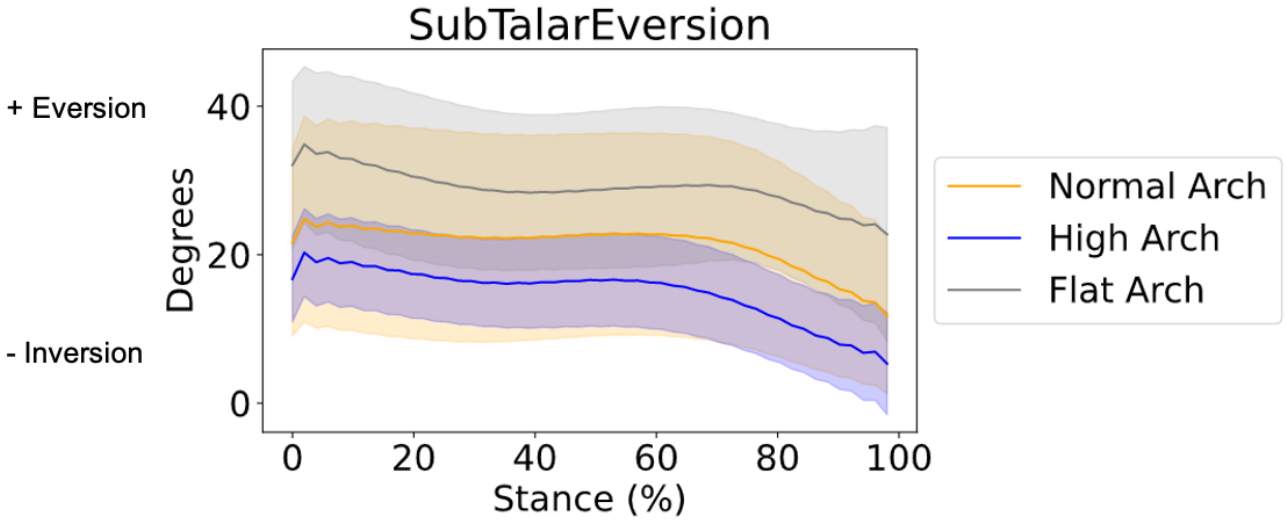

Figure 85 Showing subtalar eversion/inversion kinematic profiles for high (blue), normal (orange) and low arch (grey) foot groups with 1 standard deviation

The SPM analysis showed a statistically significant difference between the high and low arch foot types (Figure 86). The high arch group had significantly less eversion compared to the low arch group throughout the stance phase (0-100%) with the supra threshold cluster exceeded the

threshold t^* = 2.590 with a P-value < 0.001. No statistically significant differences were evident during the whole stance phase between high and normal arch types and normal and low arch foot types.

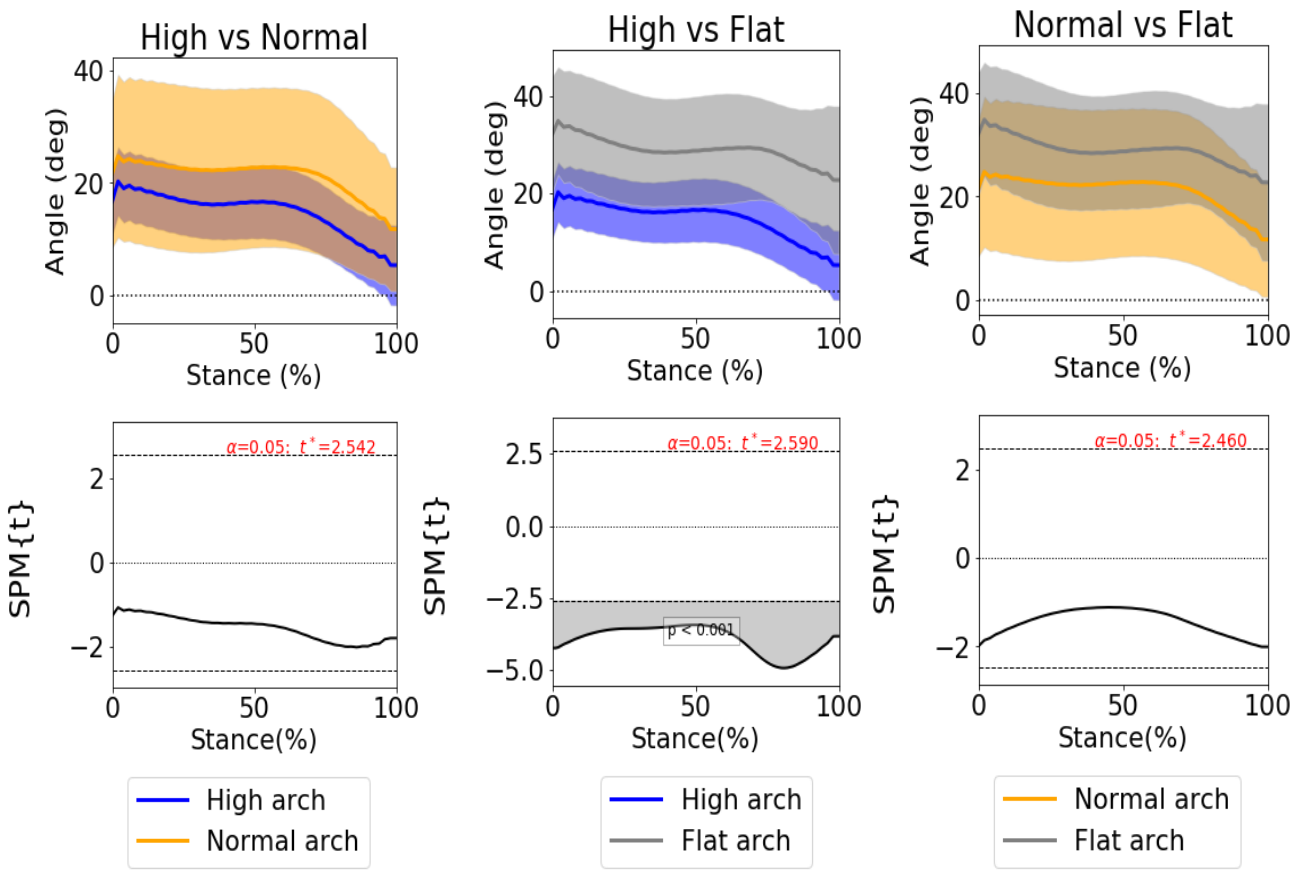

Figure 86 Showing statistical parametric mapping (SPM) t-test analysis between high (blue), normal (orange) and low arch (grey) groups as a percentage of stance phase of gait for subtalar eversion/inversion. Statistical differences are shown between high and low arch groups.

6.3.3 Talonavicular dorsiflexion / plantarflexion

Visually inspecting the graph in Figure 87 showed systematic progression of values for the motion-time series, with the high group being lower overall, the normal group lying centrally within the distribution and the low arch group yielding more dorsiflexion values overall.

The total population for talonavicular dorsiflexion/plantarflexion showed a mean (SD) of 8.09° (4.29) degrees, with high, normal and low arch groups presenting with 5.65° (2.57); 11.04° (2.97); 8.19° (5.16), respectively, shown in Appendix B. The normal cohort had the greatest mean RoM compared to the low arch group, which had a greater average RoM than the high group, shown in Figure 87.

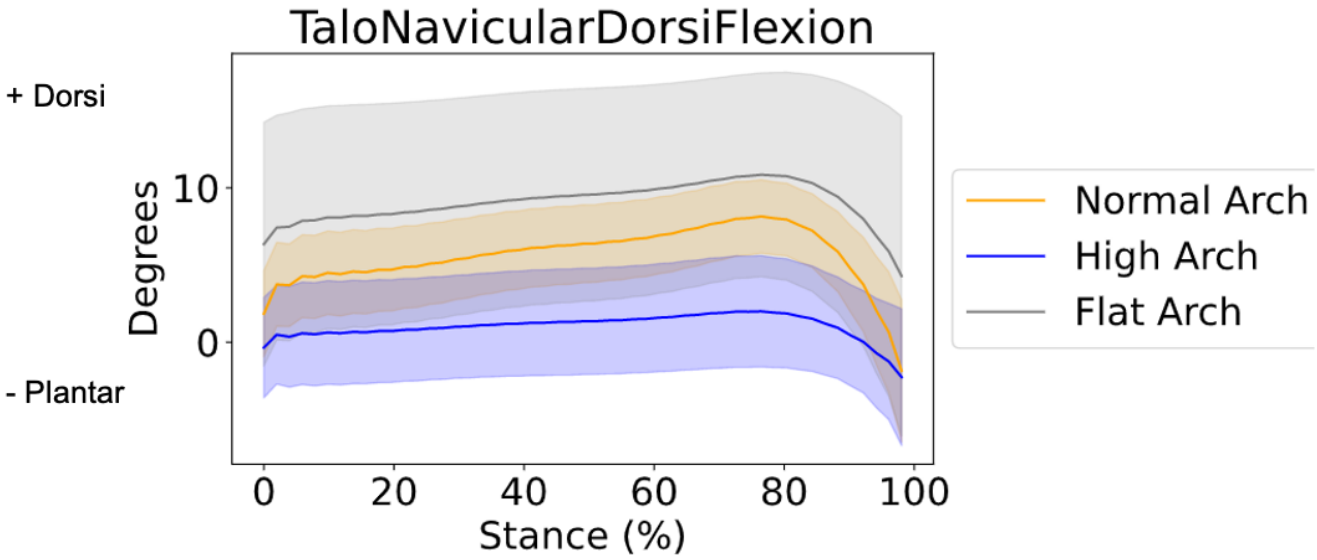

Figure 87 Showing talonavicular dorsiflexion/plantarflexion kinematic profiles for high (blue), normal (orange) and low arch (grey) foot groups with 1 standard deviation

Figure 88 shows the SPM analysis to result in a statistically significant difference between the high and low arch foot types and high and normal arch types. The high arch group demonstrated significantly less talonavicular dorsiflexion compared to the low arch group throughout the stance throughout the stance phase (0-95%) with the supra threshold cluster

exceeding the threshold t^* = 2.616 with a *P*-value = 0.006. The high arch group demonstrated significantly less talonavicular dorsiflexion compared to the normal arch foot type throughout stance (3-92%) with the supra threshold cluster exceeded the threshold t^* = 2.679 with a *P*-value < 0.001. Between normal and low arch foot types, no statistically significant differences were observed.

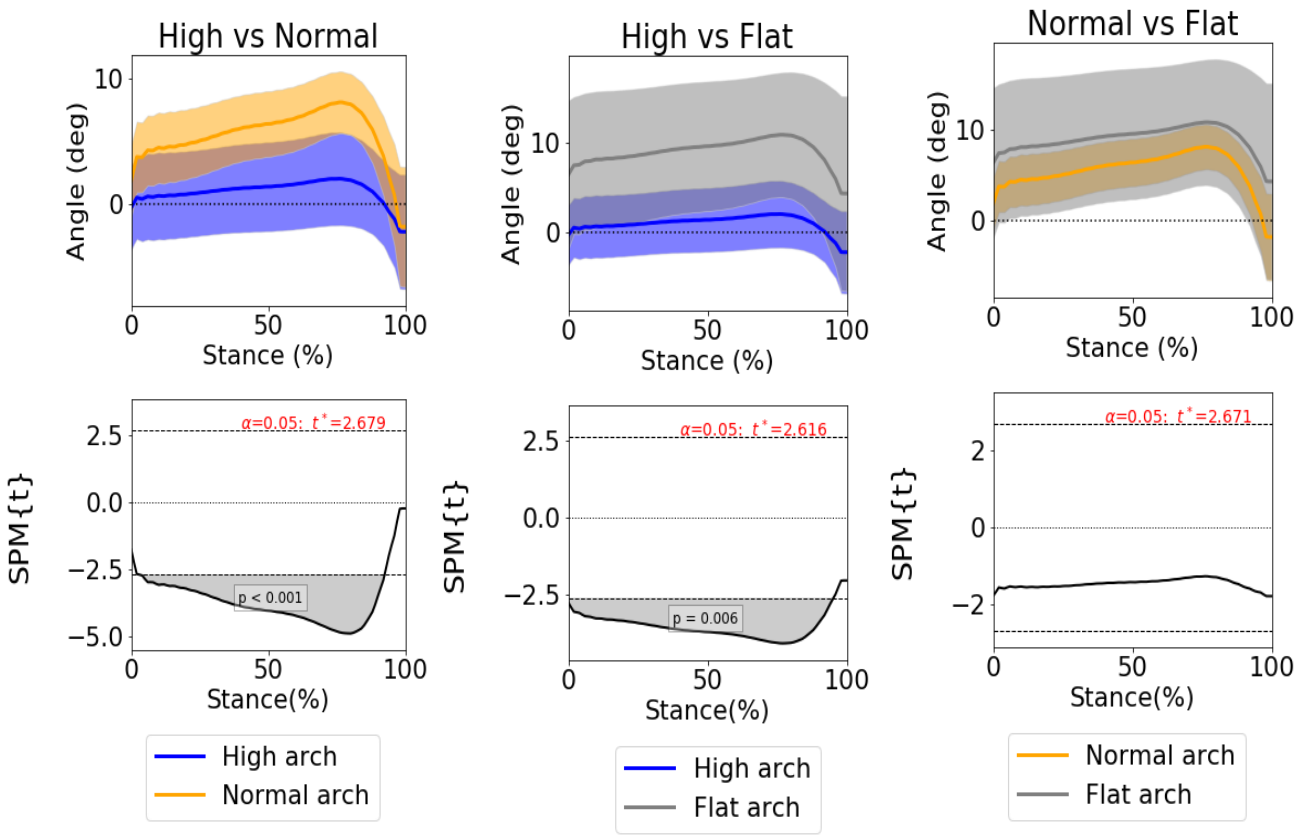

Figure 88 Showing statistical parametric mapping (SPM) t-test analysis between high (blue), normal (orange) and low arch low arch (grey) groups as a percentage of stance phase of gait for talonavicular plantar/dorsiflexion. Statistical differences are shown between high and normal and high and low arch groups.

6.3.4 Talonavicular eversion / inversion

Visually inspecting the graph in Figure 89 showed systematic progression of values for the motion-time series, with the high arch group being lower

overall, the normal group falling centrally within the distribution and the low arch group yielding more eversion values overall.

The total population for talonavicular eversion/inversion showed a mean (SD) excursion of 11.53° (4.73) degrees, with high, normal and low arch groups presenting with 10.18° (2.36); 11.84° (5.24); 12.13° (6.09) degrees, respectively, shown in Appendix B. The low arch cohort had the greatest mean RoM compared to the normal group, which had a greater average RoM than the high group, shown in Figure 89.

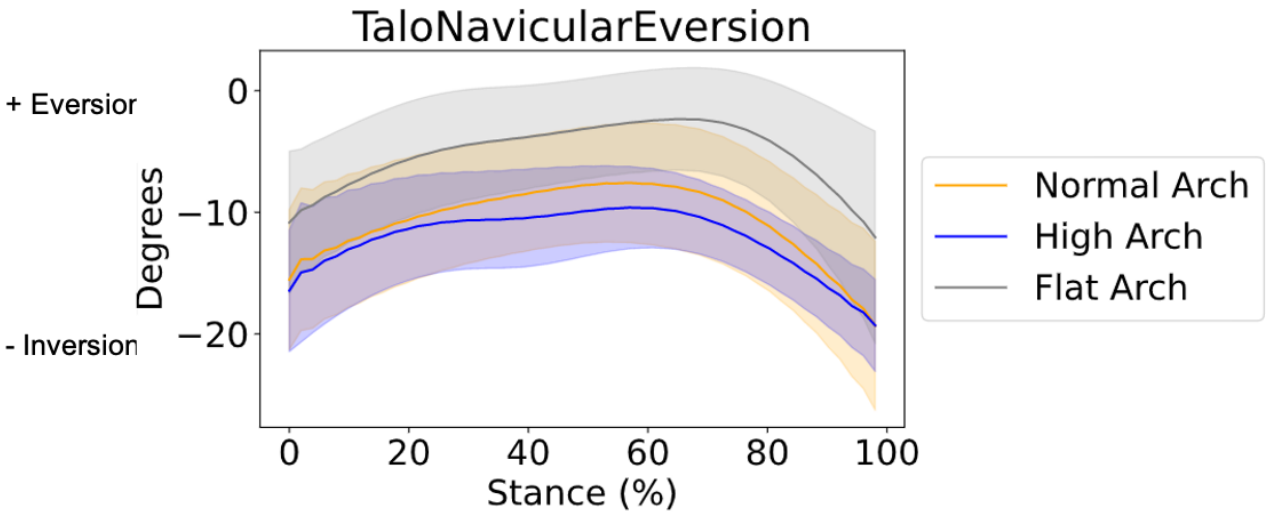

Figure 89 Showing talonavicular eversion/inversion kinematic profiles for high (blue), normal (orange) and low arch (grey) foot groups with 1 standard deviation

Figure 90 shows SPM analysis revealed a statistically significant difference between the high and low ach foot types and normal and low arch types. The high arch group demonstrated significantly less talonavicular eversion compared to the low arch group throughout stance (14-97%) with the supra threshold cluster exceeded the threshold $t^* = 2.762$ with a P-value > 0.001. The normal arch group demonstrated significantly less talonavicular eversion compared to the normal arch foot type throughout stance (64-90%) with the supra threshold cluster exceeding the threshold $t^* = 2.668$ with a P-value =

0.034. No statistical differences were observed between high and normal arch foot types.

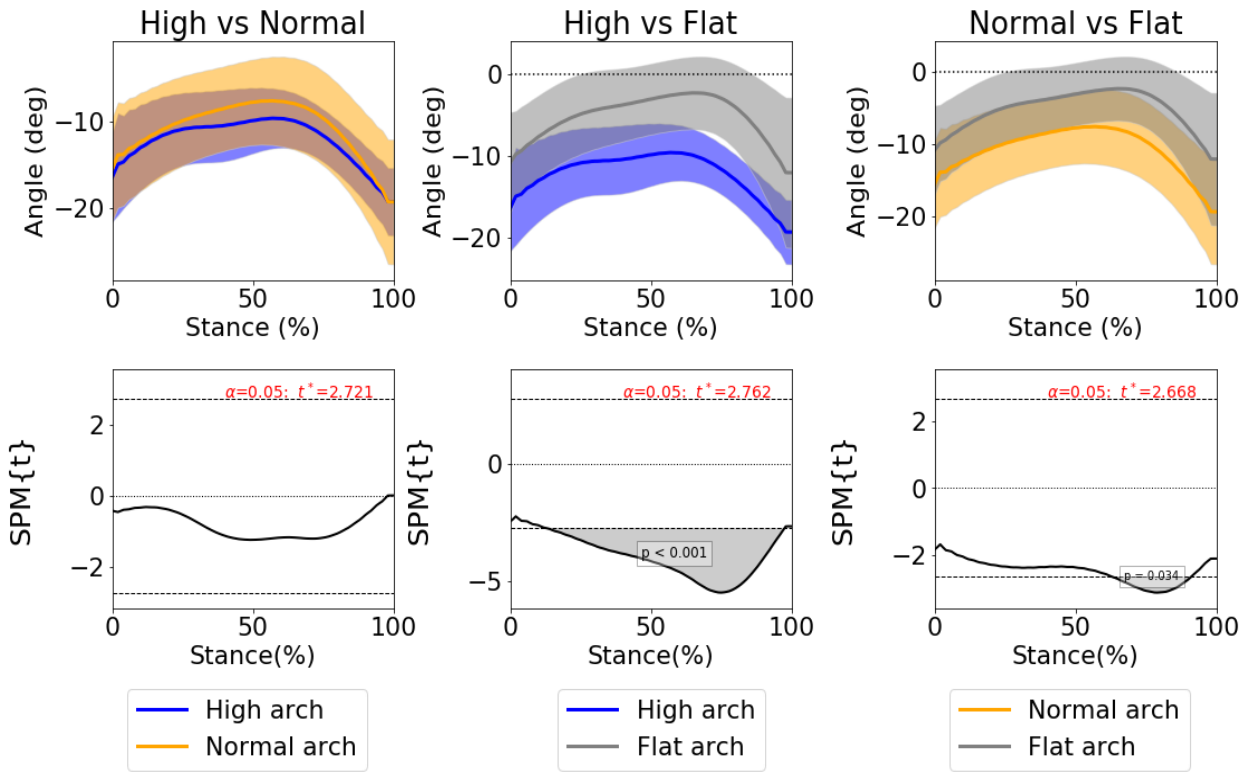

Figure 90 Showing statistical parametric mapping (SPM) t-test analysis between high (blue), normal (orange) and low arch (grey) groups as a percentage of stance phase of gait for talonavicular eversion/inversion. Statistical differences are observed between high and low arch groups.

6.3.5 Talonavicular abduction / adduction

Visually inspecting the graph in Figure 91 showed some systematic progression of values for the motion-time series, with the high arch group being lower overall and the low and normal type groups yielding more abduction values overall.

The total population for talonavicular abduction/adduction showed a mean (SD) excursion of 16.0° (4.53) degrees, with high, normal and low arch groups presenting with 18.21° (3.22); 14.18° (4.96); 15.05° (4.34) degrees, respectively, showed in Appendix B. Figure 91 shows the high cohort had

the greatest mean RoM compared to the low arch group, which had a greater average RoM than the normal group.

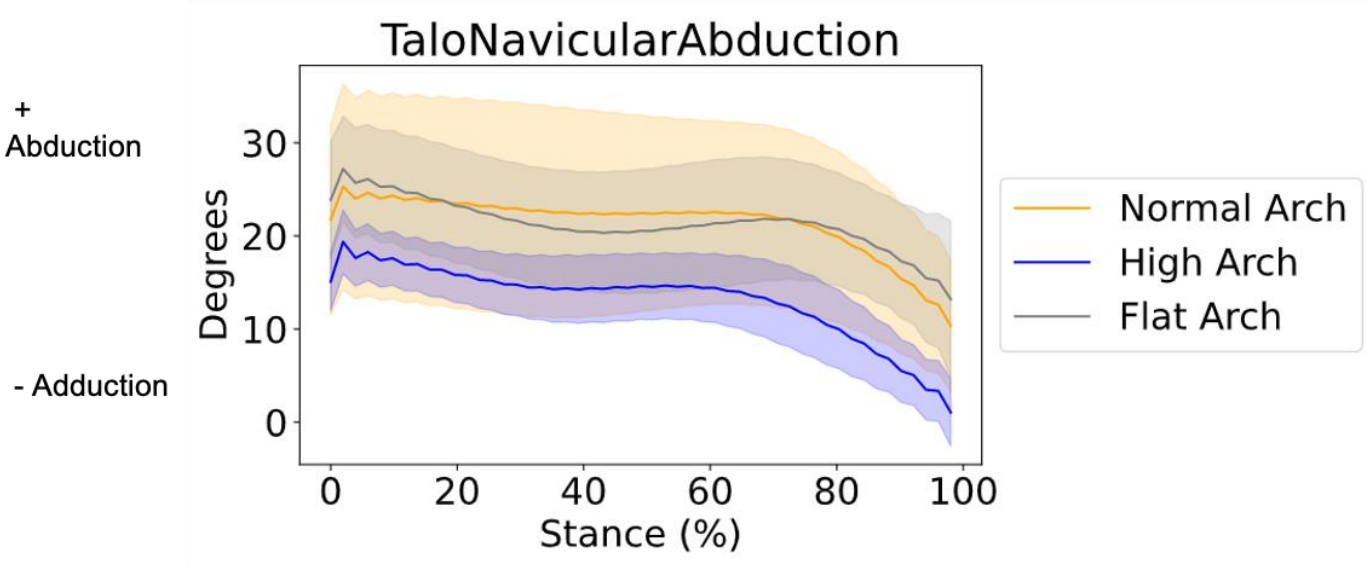

Figure 91 Showing talonavicular abduction/adduction kinematic profiles for high (blue), normal (orange) and low arch (grey) foot groups with 1 standard deviation

Figure 92 shows SPM analysis reporting statistically significant difference between the high and low ach foot types and high and normal arch types. The high arch group demonstrated significantly less talonavicular adduction compared to the low arch group throughout the stance throughout the stance phase (0 - 40% and 56% - 100%) with the supra threshold clusters exceeding the threshold t^* = 2.869 with a P-value = 0.007. The high arch group demonstrated significantly less talonavicular adduction compared to the normal arch foot type throughout stance (61-100%) with the supra threshold cluster exceeding the threshold t^* = 2.745 with a P-value = 0.026. No statistically significant differences were observed between normal and low arch foot types.

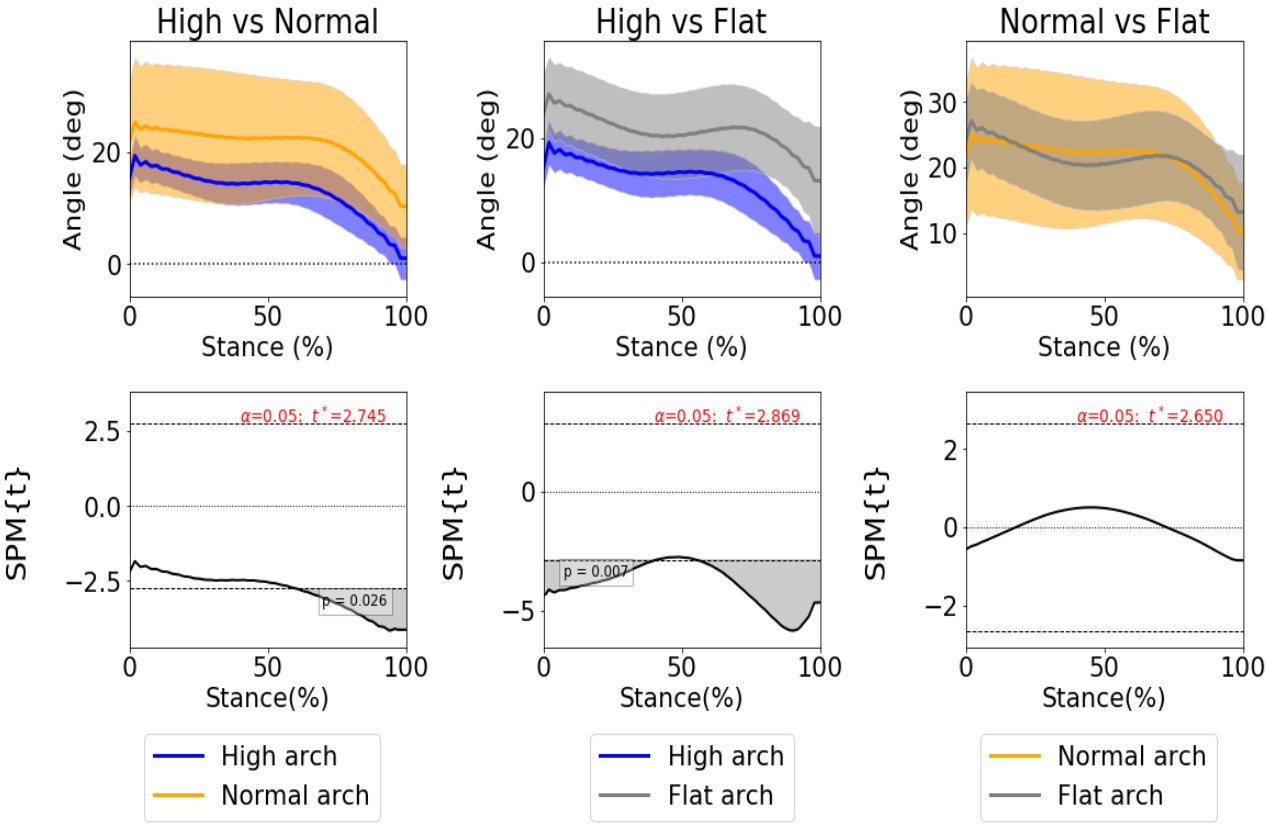

Figure 92 Showing statistical parametric mapping (SPM) t-test analysis between high (blue), normal (orange) and low arch (grey) groups as a percentage of stance phase of gait for talonavicular abduction/adduction. Statistical differences are noted between high and normal and high and low arch groups.

6.3.6 First metatarsophalangeal dorsiflexion / plantarflexion

Visually inspecting the graph in Figure 93 showed some systematic progression of values for the motion-time series, with the low arch group being lower overall and the high and normal groups yielding more dorsiflexion values overall.

The total population for first metatarsophalangeal dorsiflexion/plantarflexion showed a mean (SD) excursion of 39.8° (8.74) degrees, with high, normal and low arch groups presenting with 36.89° (7.92); 44.14° (3.81); 39.33° (11.21) degrees, respectively, shown in Appendix B. The normal cohort had

the greatest mean RoM compared to the low arch group, which had a greater average RoM than the high group, shown in Figure 93.

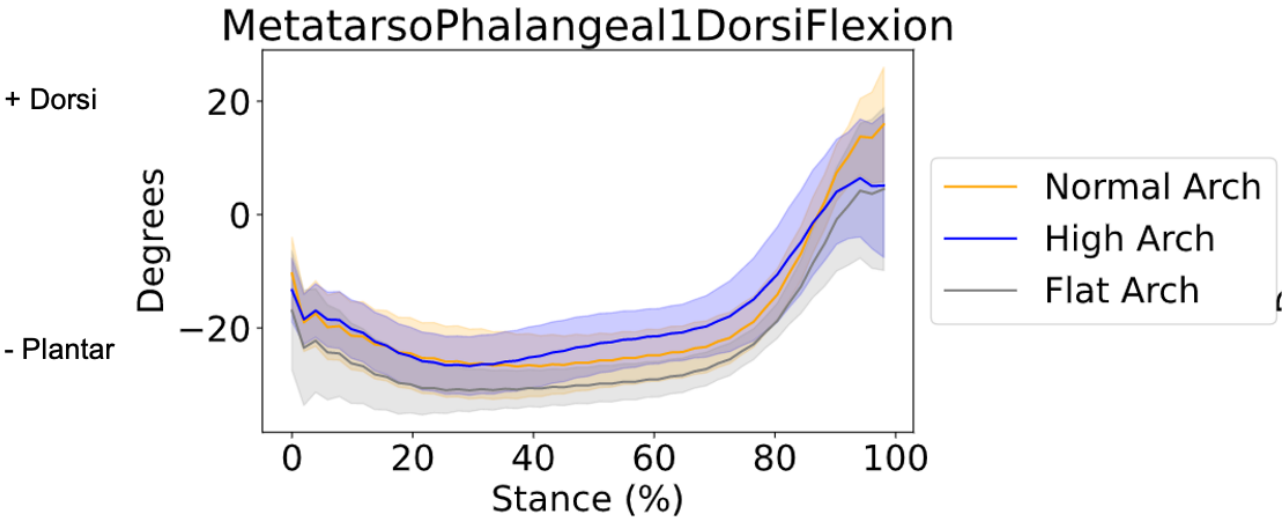

Figure 93 Showing first metatarsophalangeal plantar/dorsiflexion kinematic profiles for high (blue), normal (orange) and low arch (grey) foot groups with 1 standard deviation

Figure 94 shows SPM analysis and revealed a statistically significant difference between the high and low arch foot types. The high arch group demonstrated significantly more first metatarsophalangeal dorsiflexion compared to the low arch group throughout the stance throughout the stance phase (42 - 79%) with the supra threshold clusters exceeding the threshold $t^* = 2.986$ with a P-value < 0.001. No statistical differences were observed between high and normal and normal and low arch foot types.

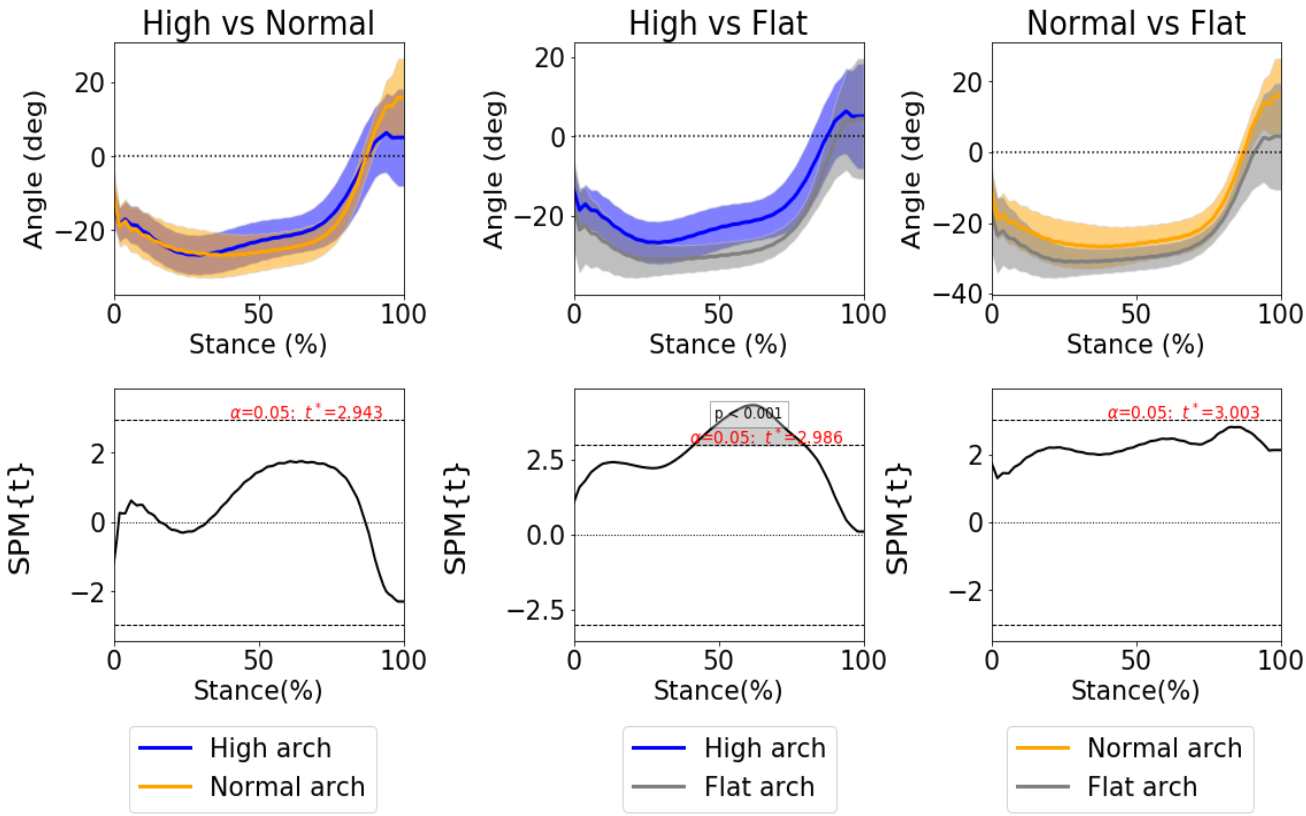

Figure 94 Showing statistical parametric mapping (SPM) t-test analysis between high (blue), normal (orange) and low arch (grey) groups as a percentage of stance phase of gait for first metatarsophalangeal plantar/dorsiflexion. Statistical differences were noted between high and low arch groups.

6.4 **Discussion**

The aim of this chapter was to investigate the application of a 26-segment foot model to determine whether systematic differences could be identified between low, normal and high arch foot types. This was achieved by creating patient specific bones derived from the statistical shape model developed in chapter four. Specifically, each individual bone that makes up the hind and fore foot, excluding the phalanges were morphed from a template model geometry creating a patient specific model from point sets generated from the SSM. The foot model developed in chapter five was also applied using kinematic data collected in chapter three, as inputs and applied to drive the motion of the foot segments, from which intersegment angles were calculated in the stance phase of the gait cycle. Visual inspection, descriptive statistics and statistical parametric mapping was then used to explore for any differences between foot-types between medial ray joints of low, normal, and high arch foot groups. Overall findings suggest that there was a general recurring picture of differences, where evident, being systematic and progressing flat to normal to high as predicted by the clinical theory. For some joint/motion combinations high arched feet were the relative outlier while for others the low arch group was most obviously different. Unsurprisingly, some combinations yielded similar degrees of difference between the groups and some little difference at all (Table 14). For several foot joints and anatomical planes systematic differences in kinematics between low and high arch foot groups could be identified either throughout or at particular parts of the stance phase of the gait cycle. The medial ray is of interest to the clinical communities, the results reported at least one significant difference in a plane of motion between high and low arch foot groups, while for other joints discrete differences could not be identified due to overlapping kinematic angles due to greater variance in the study populations.

Summary hypotheses

The null hypothesis was that no differences existed in the kinematic motions (dependent variables) of medial ray joints including ankle plantarflexion, subtalar eversion, talonavicular dorsiflexion, talonavicular abduction, talonavicular eversion

and first metatarsophalangeal dorsiflexion between low, normal and high arch foot types (independent variables) summarised in Table 14.

Table 14 Showing a summary of kinematic measure, group type comparisons and differences between groups from statistical parametric mapping analysis

Kinematic measure	Arch type comparison	Differences between groups
Ankle plantarflexion	High – Normal	Differences were present
	High – Low	Differences were present
	Normal - Low	No differences were present
Subtalar eversion	High – Normal	No differences were present
	High – Low	Differences were present
	Normal - Low	No differences were present
Talonavicular dorsiflexion	High – Normal	Differences were present
	High – Low	Differences were present
	Normal - Low	No differences were present
Talonavicular eversion	High – Normal	No differences were present
	High – Low	Differences were present
	Normal - Low	Differences were present
Talonavicular abduction	High – Normal	Differences were present
	High – Low	Differences were present

	Normal - Low	No differences were present
First metatarsophalangeal dorsiflexion	High – Normal	No differences were present
	High – Low	Differences were present
	Normal - Low	No differences were present

6.4.1 Ankle dorsiflexion / plantarflexion

The results demonstrated in this chapter largely agree with previous, previously state of the art methods in reported values for normal ankle excursion (MacWilliams et al., 2003; Lundgren et al., 2008; De Mits et al., 2012; Oosterwaal et al., 2016), however contrary to these findings, other studies (Simon et al., 2006; Nester et al., 2007) report greater values. The present study showed normal ankle dorsiflexion/plantarflexion excursion (SD) of 14.9° (3.51), comparable to Oosterwaal et al., (2016) who reported a RoM of 17° . A similar pattern of results was obtained by a study by MacWilliams et al., (2003) RoM of 15° (derived from graph), De Mits et al., (2012) RoM 11.8° (4.44), and bone pin study (Lundgren et al., 2008) RoM 17.0° (2.1). However values indicated in the present study, see Appendix B, are notably lower than reported by *in vitro* cadaver study by Nester et al who reported a mean RoM of 23.9° (8) and Simon et al who reported a mean RoM of 22.2° (1.8).

Differences in reported ankle dorsiflexion exist between multi-segment foot models and have been attributable to the differences in numbers of segments and definition of the joint axis reported in literature (Buldt et al., 2013). Comparing Nester et al study with thirteen cadaveric specimens to the present study, reveals a larger RoM with cadaveric foot than the dynamic multi-segment foot model. The differences could in part be assignable to forces applied in cadaver studies being much greater than are achieved *in vivo* causing RoM at the ankle to increase. Also in Simon et al study larger RoM values were reported, however this study a had younger target

population with a mean age of 30 years, ranging from 19 – 43 years. The larger RoM in both Nester et al and Simon et al could be due to sample differences wherein elderly females have been reported to demonstrate less static RoM compared to younger groups (Nigg et al., 1992). While the study by MacWilliams et al., (2003) found a RoM which more closely aligned with the results from the multi-segment foot model of this study, the target population was mainly adolescent feet, which contradicts the notion of reduced flexibility in elderly population. These observations indicate some level of agreement between bone pin studies and the simulated foot model in the present study. Discrepancies of reported mean RoM are challenging to compare directly, due to the different methodologies between studies. Therefore, general comparisons of reported results would be more appropriate, unless the same model was used, and considering ankle dorsiflexion, the RoM and kinematic profile measure in the present study align well with results from Oosterwaal et al which evaluated a similar 26-segment kinematic model used to derive kinematics in this chapter.

Importantly, the null hypothesis proposing no significant difference between high and low arch foot groups is refutable when using the biomechanical methodology described in chapter five, therefore can be rejected in favour of the alternative hypothesis. This suggests statistical differences exist for ankle dorsiflexion between high and low arch groups and also high and normal arch groups. The model also demonstrates its ability to detect foot type related differences when kinematic outputs for multiple other joint/motion combinations are analysed visually, descriptively and with exploratory statistical parametric mapping. Within the foot groups SPM revealed the high arch group to demonstrate significantly increased ankle dorsiflexion compared to the low arch throughout the stance phase (0-76%) with the supra threshold cluster exceeding the threshold $t^* = 2.741$ with a P-value = 0.001. Significant differences observed between high and normal arch types demonstrated greater ankle dorsiflexion in the stance phase of gait (7-36%) with the supra threshold cluster exceeding the threshold $t^* = 2.791$ with a P-value = 0.017. Kruger et al., (2019) found significant differences between normal and high arch, and high and low arch types in the stance phase of gait for ankle dorsiflexion, excluding terminal stance between the normal and low arch groups, this concurs with the

present study. However, Kruger et al also found differences between normal and low arch foot types and this was not observed within the present study. Data produced in this study, showed pathological populations in ankle joint sagittal plane motion to have mean RoM (SD) of 15.6° (1.06); 14.9° (3.51); 16.79° (2.92) for high, normal and low arch groups respectively. The low arch foot demonstrated greater RoM than the normal or high arch groups. Previous literature from Buldt et al., (2015), Caravaggi et al., (2018) and Kruger et al., (2019) reported conflicting kinematics for sagittal plane ankle motion for cavus and planus foot types. The study by Buldt et al found low arch foot types have less RoM than high and normal arch foot types, similarly, Caravaggi et al found normal group kinematics to have greater RoM compared to low arch foot type.

When considering anatomical variance between foot populations, a characteristic high arch foot is typically more dorsiflexed (Aminian and Sangeorzan, 2008; Kim, 2017). This is schematically represented in Figure 95 A, where the ankle joint is compared to a low arch foot in Figure 95 B. The results in this study indicate the high arch group’s ankle dorsiflexion starting angles at heel strike to be more dorsiflexed than the low arch group. This observation could relate to the natural pose of the high arch foot, similar results were reported by Kruger et al., (2019) the results in this study could be explained by the less rigid nature of the low arch foot adopting a more plantar flexed position at heel strike (Aminian and Sangeorzan, 2008; Kim, 2017) (Ledoux et al., 2003).

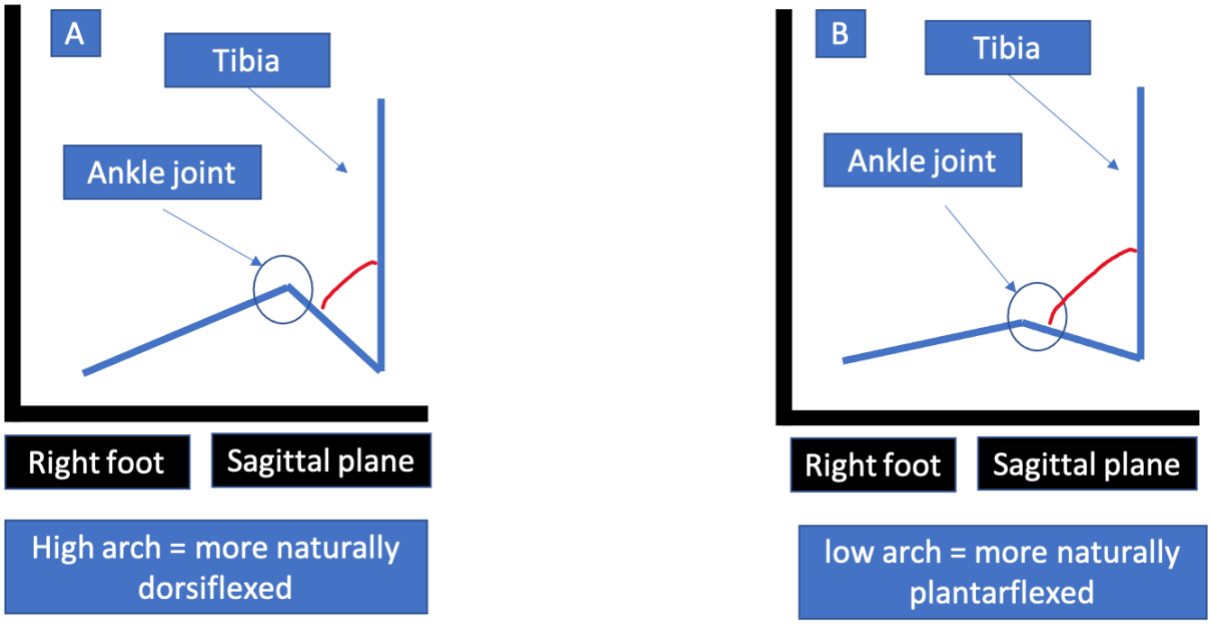

Figure 95 Showing relative differences between of the ankle joint between foot types, A: Describing the high arch foot type as more naturally dorsiflexed and B: the low arch foot type as more naturally plantarflexed

Quantifiable differences in kinematics for ankle dorsiflexion between the high and low arch and high and normal foot types could partly be explained by systematic differences in morphology, as found in chapter four. In chapter four the calcaneus and talus associated with ankle plantarflexion moved in relation to their foot groups, in other words, for both bones the low arch group showed a medial and posterior rotation, and the high arch group a lateral and anterior rotation. SPM shows increasing systematic differences at particular times in the stance phase of gait, with the greatest significant difference seen between the high and low arch groups for the first 75% of stance. The next greatest difference was seen between the high and normal groups, which had differences at the initial phase of stance. These findings provide a foundation for the methodology developed with the small subset of low, normal and high arch foot types and could be applied to a large cohort of high and low arch populations.

6.4.2 Subtalar eversion / inversion

The results generated from the biomechanical model for normal frontal plane ankle excursion (SD) in this study were 12.35° (4.99), which is generally consistent with data from previous literature for subtalar eversion (Simon et al., 2006; De Mits et al., 2012; Oosterwaal et al., 2016) However, cadaver and bone pin studies Nester et al., (2007) and Lundgren et al., (2008) and multisegment foot model (MacWilliams et al., 2003) reported slightly less RoM compared to the present study findings. It is encouraging to compare the normal group reported mean RoM of subtalar eversion with the most comparable to resulted from the GM foot model described in Oosterwaal et al which reported a mean RoM 12.9 °. Data from De Mits et al study were also comparable to the present study where a mean RoM of 14.9° (6.55) was reported. However, data from Simon et al, showed less motion 10° (0.3), which was similar to the study by MacWilliams et al who found a mean RoM of 7° (derived from graph). In addition, studies by Nester et al and Lundgren et al reported a mean RoM of 9.7° (5.2) and 9.8° (1.8) respectively.

Outputs derived from the biomechanical model indicated systematic differences between foot groups can be found for subtalar eversion by the low arch group having the greatest mean starting angle followed by the normal and then high groups. The null hypothesis for subtalar eversion can be rejected in favour of the alternative hypothesis suggesting that significant differences exist between high and low arch foot groups at specific time points in the stance phase, as indicated in the SPM results.

Kinematic RoM in subtalar eversion showed, high, normal and low arch groups mean RoM of 14.57° (2.96); 12.35° (4.99); 13.36° (3.66), respectively. The high arch cohort had the greatest mean RoM compared to the low arch group, which had a greater mean RoM than the normal group. The present study disagrees with previous work by Buldt et al., (2015) who reported the cavus foot type to have less RoM than normal and low arch foot types. This study’s results suggest high arch foot types have greater RoM than planus and normal foot types. However, the main aim of this work was to determine if the modelling pipeline , linking chapters four and five was capable of identifying systematic differences between extremes of foot posture. It is

speculated that the differences between the study by Buldt et al., (2015) and the present study could be due to the application of different models and the reference frame used for subtalar neutral, which in terms of the clinical application of 3D models, is a debated topic (Jarvis et al., 2017). Subtalar eversion values in the present study are in agreement with Caravaggi et al., (2018) from the perspective of normal foot types having less excursion than low arch foot types. Caravaggi et al also showed subtalar kinematics of normal and low arch foot types to overlap in their standard deviations and not to demonstrate statistically relevant differences; this thesis found similar results using a continuous time-series analysis with SPM. Contradictory to findings from Kruger et al., (2019) the present study was not able to find differences between normal and low arch foot types for subtalar eversion, this could be due to the different definitions of the segments used to capture the joint movement. Kruger et al., (2019) used multiple bone segments to measure hindfoot inversion-eversion, whereas the model in the present study used the talus and the calcaneus only. The results in the present study agree with the study Kruger et al findings that statistical differences between high and low arch foot types exist across the entire stance phase. The Milwaukee model used by in the study by Kruger et al to evaluate the foot types applied an anatomically relevant calibration of patients, which is different to the 26-segment foot model developed in chapter five that used a patient specific bone scaling and morphing technique. Using individual bone segments to compare kinematics between foot types represents anatomical differences more appropriately as information is not captured in the patients' geometry when grouping multiple bone segments together as a hindfoot.

Natural variance in anatomy between foot populations is clinically described as a high arch foot presenting more inverted / less everted (schematically Figure 96 A) at the ankle joint. In comparison to a low arch foot (schematically Figure 96 B) which is described as in a more everted / less inverted position at standing rest.

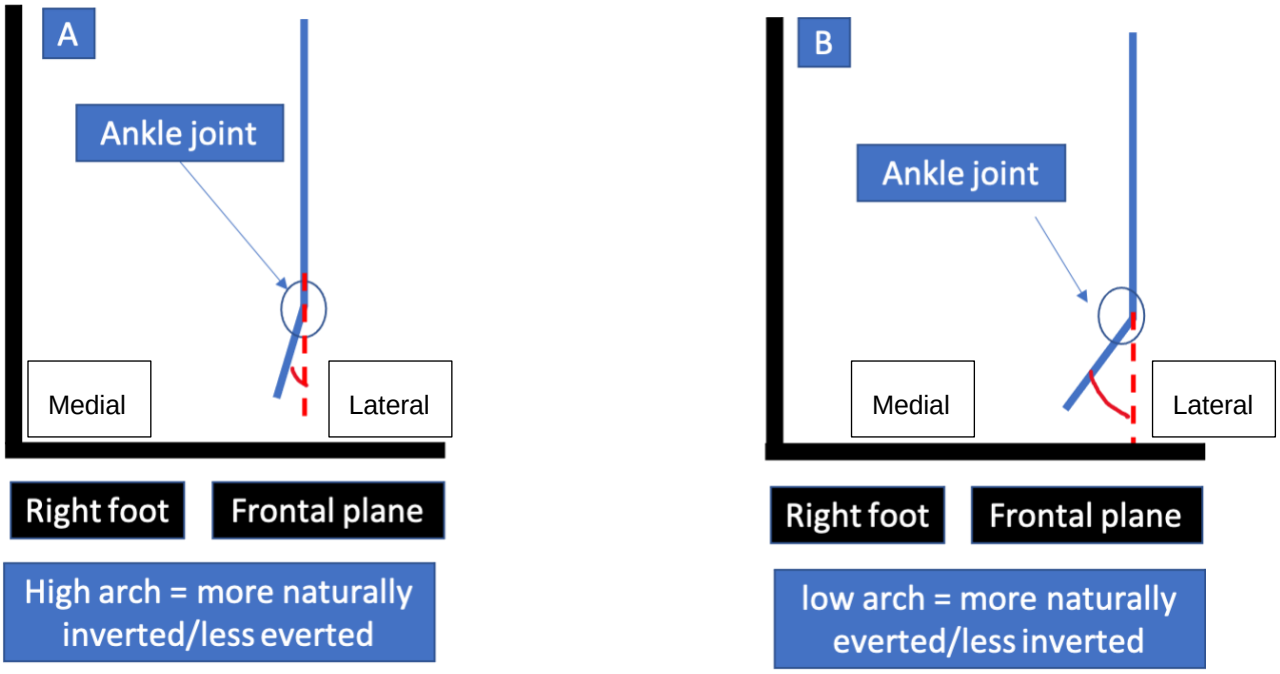

Figure 96 Showing relative differences of the ankle joint between foot types, A: Describing the high arch foot type as more naturally inverted/less everted and B: the low arch foot type as more naturally everted/less inverted

Differences for subtalar eversion between the high and low arch foot types could be related to systematic differences in morphology between foot populations as previously reported in chapter four. Specifically, where the primary bones, the calcaneus and talus, for subtalar eversion spatially relate to their foot groups i.e., bones for the low arch group show a medial and posterior rotation leading to more eversion and, for the high group rotate laterally and anteriorly, leading to less eversion, or even inversion. This systematic difference might go some way towards explaining the starting angle differences in the biomechanical model outputs between groups. Statistical parametric mapping shows relevant differences between high and low arch foot groups at particular times in the stance phase of gait, with the greatest significant difference between the high and low arch groups across the entire stance phase. These findings extend the promise of using the foot model engineering pipeline described in this thesis to a larger sample of patients of high and low arch populations.

6.4.3 Talonavicular dorsiflexion / plantarflexion

Consistent with previous literature, normal results from for sagittal plane movement of the talonavicular joint excursion (SD) of 11.04° (2.97) was comparable to Oosterwaal et al., (2016) and Nester et al., (2007) findings, however study values were higher than those reported by Arndt et al., (2007) and Lundgren et al., (2008).

Due to the challenges around isolating the talus and the navicular, studies capturing motion at this joint are limited to *in vitro* studies (Nester et al., 2007), bone-pin (Arndt et al., 2007; Lundgren et al., 2008) and previous literature using the GM model (Oosterwaal et al., 2016). Reported values from the study by Oosterwaal et al and Nester et al reported ranges of motion 14.6° and 12.2° (7.1) respectively, slightly higher than what was reported in this study, however comparable because the standard deviations are similar. In contrast, studies reporting values less than the present study are bone-pin studies; by Arndt et al reported a mean RoM (SD) 6.5 ° (2.9), similar to the study by Lundgren et al who reported a RoM 8.4° (1.1).

While the present study reported the normal foot arch type mean RoM comparable to Nester et al., (2007), discrepancies exist between bone pin studies because an agreement for normative talonavicular dorsiflexion has not yet been established. The kinematic profile of the talonavicular joint reported in Oosterwaal et al., (2016) was similar to the 26-segment foot model used in the present study, although the differences in RoM between the studies could be explained by different target populations.

In line with the overall hypothesis suggesting systematic offsets between foot types, kinematic analysis of talonavicular joint shows the low arch group to have the greatest mean starting angle and the high group to have the lowest mean starting angle, with the normal group values in-between. Kinematic RoM in the sagittal plane for talonavicular dorsiflexion showed, high, normal and low arch groups mean RoM (SD) of 5.65° (2.57); 11.04° (2.97); 8.19° (5.16) degrees respectively. This is the first time that SPM has been applied to the talonavicular joint to investigate a hypothesis focused on low arch and high are foot types. As single metric such as total excursion does not consider all the nuance of time series analysis and employing techniques

like SPM help account for temporal variation over the stance phase. For talonavicular dorsiflexion SPM showed statistically significant differences across a large proportion of the stance phase. Significant differences ($p < 0.001$) were observed between the high and normal groups for 3% - 93% of stance and high and low arch groups ($p = 0.006$) for 0% - 95% of stance. Counter intuitively, there was a greater statistical difference between the high and normal groups than the high and low arch groups, although this observation could be explained by the variance of the low arch group being higher than the other groups and the small sample size. Statistical differences were not observed between normal and low arch foot groups. Comparing RoM , the high group had a smaller RoM than the low arch group which could be explained by the stiffness of high arch foot types through the midfoot (Younger and Hansen, 2005; Barnes et al., 2008; Aminian and Sangeorzan, 2008) leading to less RoM. Coinciding low arch foot structures can be characteristically more flexible (Cobb et al., 2009) and the wider RoM which has been indicated using fluoroscopy techniques in a study by Wang et al., (2019) found low arch foot population have a mean RoM 13° (6) and normal foot types have a mean RoM of 7° (3), however the present study disagrees as the normal group has a mean RoM greater than the low arch foot group. These differences could be due to the methodologies used to initially label a foot type as low, normal or high arch.

Clinically a high arch foot is described as being more naturally plantarflexed / less dorsiflexed (Aminian and Sangeorzan, 2008; Kim, 2017), this is demonstrated in Figure 97 A which shows a schematic of the talonavicular joint. The low arch foot is clinically described as more dorsiflexed / less plantarflexed positioned at standing rest (Ledoux et al., 2003), this is represented in Figure 97 B which shows a low arch foot schematic. The results in the present study indicate high arch group talonavicular starting angles at heel strike to be less dorsiflexed than the low arch group, this could relate to the natural postural differences highlighted between high and low arch foot types.

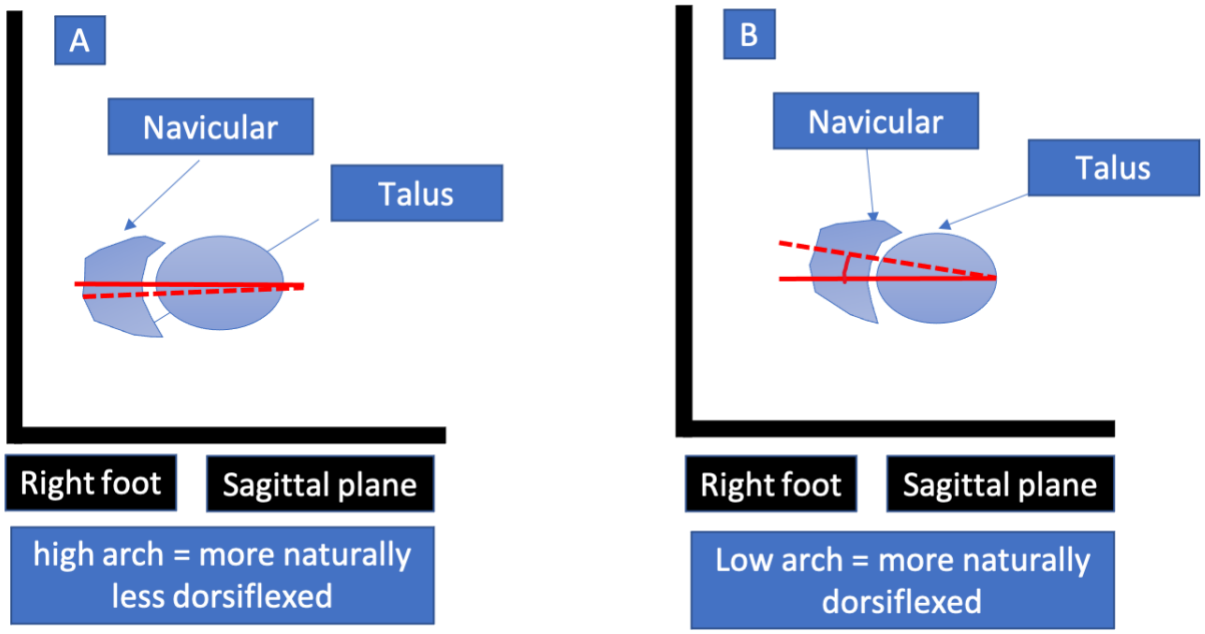

Figure 97 Showing relative differences of the talonavicular joint between foot types, A: Describing the high arch foot type as more naturally less dorsiflexed and B: the low arch foot type as more naturally dorsiflexed.

Differences for talonavicular dorsiflexion between the high and low arch foot types could be indicative of systematic differences in morphology between foot populations. Specifically, where the primary bones the talus and navicular spatially relate to their foot groups i.e., bones for the low arch group show a medial and posterior rotation leading to more dorsiflexion and, for the high group rotate lateral and anteriorly leading to less dorsiflexion at this joint described in chapter four. The differences in kinematics derived from the 26-segment foot model, could provide a foundation to exploring relationships between morphology and movement. Statistical parametric mapping shows relevant differences between high and low arch groups for talonavicular dorsiflexion at particular times in the stance phase of gait. A similar proportion of significance was found along the time series between 0% and 95% for the high and low arch groups, compared to the high and normal arch groups for which differences between high and normal arch groups were observed between 3% and 93%.

6.4.4 Talonavicular eversion / inversion

The results generated from the foot model in this thesis for normal talonavicular excursion (SD) was 11.84° (5.24) which is generally comparable to previous literature reporting this kinematic motion (Arndt et al., 2007; Nester et al., 2007; Lundgren et al., 2008)

A cadaver model based study by Nester et al., (2007) showed a mean talonavicular excursion (SD) of 12.4° (5.0), whereas bone pin studies by Arndt et al., (2007) and Lundgren et al., (2008) reported mean RoM 13.5° (4.1) and 14.9° (6.1) respectively and the GM foot model used in a study by Oosterwaal et al., (2016) multi-segment foot model reported a mean RoM 9.3°. Despite the mean talonavicular joint RoM from the present study being closer to the cadaver model there was greater variance, thus indicating the data for this motion was more dispersed, this could potentially be explained by the diversity in foot posture of the study population. The kinematic profile for talonavicular eversion followed a similar waveform to previously reported literature using a similar model in a study by Oosterwaal et al.

For each of the high, normal and low arch groups the RoM (SD) was 10.80° (2.36); 11.84° (5.24); 12.13° (6.09), respectively. Fontal plane motion for talonavicular joint indicated the high group to have less mean RoM than low arch or normal groups. Statistical parametric mapping revealed statistical differences between the high and low arch groups between 14% and 97% of stance and between the normal and low arch groups between 64% and 90% of stance, no statistical differences were seen between high and normal foot types. These findings could be explained by the flexibility of the midfoot, as high arch foot types are more rigid which in turn leads to less RoM permitted at the joint. Whereas more flexibility in the midfoot for low arch foot types could facilitate larger RoM.

High arch feet are more naturally inverted / less everted at the talonavicular joint this is represented in Figure 98 A, in comparison low arch feet are more everted / less inverted at standing rest, demonstrated in Figure 98 B. The results in the present study indicate the high arch group talonavicular starting angles at heel strike as less everted than the low arch group and aligns to the conjecture of natural pose

differences between high and low arch foot types (Franco, 1987; Ledoux et al., 2003; Kim, 2017).

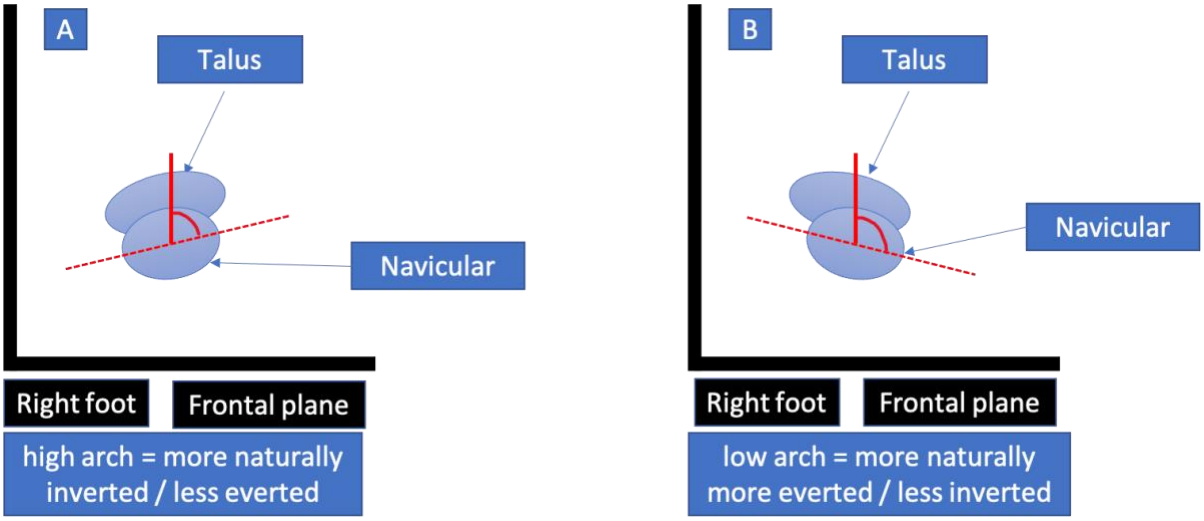

Figure 98 Showing relative differences of the talonavicular joint between foot types, A: Describing the high arch foot type as more naturally everted and B: the low arch foot type as more naturally everted.

Distinctions between the high and low arch foot types for talonavicular eversion could be related to systematic differences in morphology between foot populations. Specifically, where the primary bones the talus and navicular spatially relate to their foot groups i.e., bones for the low arch group show a medial and posterior rotation leading to more eversion and, for the high group rotate lateral and anteriorly leading to less eversion at this joint. Statistical parametric mapping shows relevant differences between high and low arch groups at particular times in the stance phase of gait for talonavicular eversion, with a greater proportion of significant difference along the time series between 14% and 97% compared to the normal and low arch groups, where difference observed between 64% and 90% of stance. These results suggest that for the talonavicular joint the model developed in chapter five is sensitive to capturing systematic differences between low and high arch foot types.

6.4.5 Talonavicular abduction / adduction

The results demonstrated in this chapter largely agree with previous literature from Oosterwaal et al., (2016), Nester et al., (2007) and Lundgren et al., (2008) who report values for normal talonavicular RoM in the transverse plane, in the present study was the RoM was 14.18° (4.96). However, Arndt et al., (2007) found different results with a mean RoM of 8.7° (1.4).

The model developed and evaluated by Oosterwaal et al., (2016) which reported a mean RoM of 14.6° of talonavicular abduction is most comparable to the results produced by the 26-segment foot model developed in this thesis. In a study by Nester et al using a cadaver experiment reported a mean RoM of 16.8° (9.2), which is similar to bone-pin study by Lundgren et al., (2008) who reported a mean RoM of 16.3° (6.5), while study by Arndt et al., (2007) found a smaller mean RoM 8.7° (1.4).

The high, normal and low arch groups from the current study yielded mean RoM (SD) values for the talonavicular abduction joint of 18.21° (3.22); 14.18° (4.96); 15.05° (4.34) degrees, respectively, see Appendix B for further clarification. The larger RoM observed in the high group indicates more motion occurring at the talonavicular joint compared to either low or normal arch groups. These differences may be due to the rigid nature of the high foot type dissipating forces into the joint area causing the bone to move more in comparison to normal or low arch groups. In the low foot type flexibility is more prevalent, forces and movement could be redistributed to other joints of the foot, causing less RoM at this joint.

Statistical parametric mapping was able to show the high arch group to have significantly less talonavicular dorsiflexion angle between 61% and 100% of stance phase ($p = 0.026$) compared to the normal arch group and between 0% and 40% and 56% and 100% compared to the low arch group ($p = 0.007$). Finding distinctive differences between low arch and high groups, highlights the capabilities of the 26-segment foot model in detecting differences between theoretical opposite ends of the foot posture spectrum in the small bones of the foot. Figure 99 A and B describe the observed differences between high arch feet which has been noted to be more naturally adducted and low arch feet which has been noted to be more abducted.

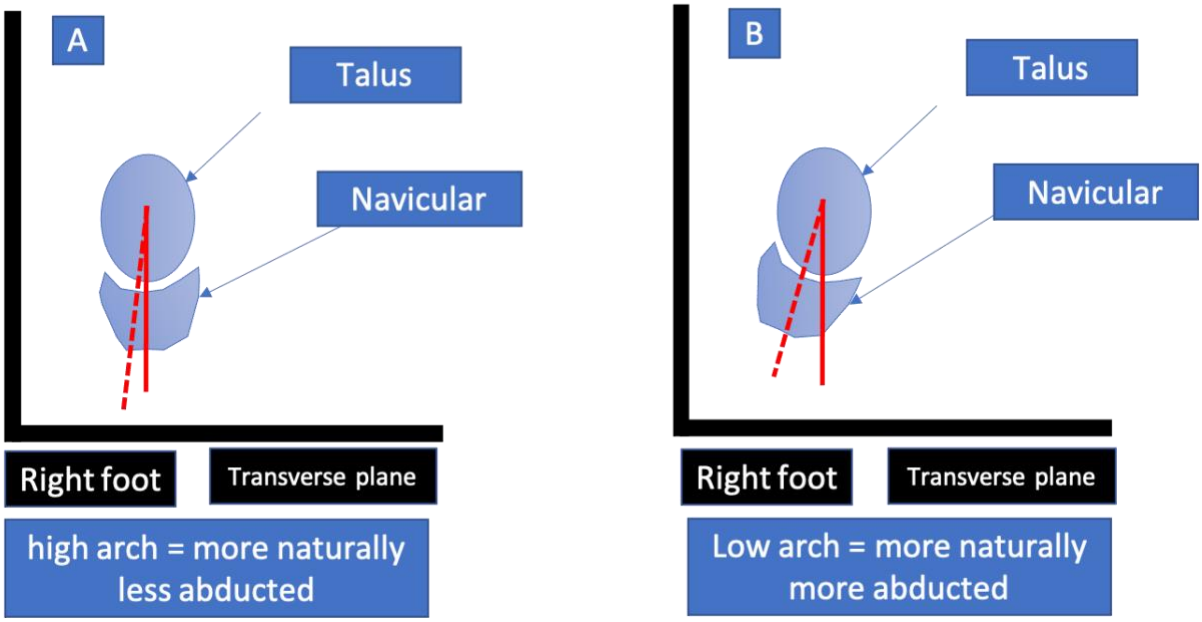

Figure 99 Showing relative differences of the talonavicular joint between foot types, A: Describing the high arch foot type as more naturally adducted and B: the low arch foot type as more naturally abducted.

6.4.6 First metatarsophalangeal dorsiflexion / plantarflexion

The results generated from the biomechanical model for the first metatarsal phalanx normal foot type dorsiflexion in this study had a mean RoM of 44.14° (3.81) degrees which are comparable to cadaver study (Nester et al., 2007) and other studies using multi segment foot models (MacWilliams et al., 2003; Simon et al., 2006; De Mits et al., 2012). The most comparable model evaluated in Oosterwaal et al., (2016) reported a population mean RoM of 40.0°, which closely aligns with the normal arch foot type results in the present study. Furthermore, shape characteristics of the kinematic profiles were similar to those found by Oosterwaal et al., (2016).

For independent groups high, normal and low arch, their reported mean RoM was 36.89° (7.92); 44.14° (3.81) and 39.33° (11.21) respectively. These results indicate that the high group had less RoM than the low arch group, which had less RoM than

the normal arch group. These findings contradict results from in a study by Buldt et al., (2015) who found the high group to have the greatest RoM for the first metatarsal phalanx. However, data produced by Caravaggi et al found that normal foot types have a greater RoM than low arch footed types. Both studies consisted of adolescent foot types, however each study had a different approach to categorising the feet, alongside the use of different models to capture kinematics. Statistical parametric mapping analysis showed the high group to have significantly more first metatarsal phalanx dorsiflexion angle between 42% and 79% of stance phase compared to the low arch group ($p < 0.001$). Using a 3 segment foot model and independent time-point t-tests Saraswat et al., (2014) found hallux flexion of planovalgus foot type to be significantly less to typically developing foot types, between approximately 30% and 40% and 77% and 100% of stance phase. Although significant differences were not observed between normal and low arch foot types in this study, similar to a study by Saraswat et al., (2014) which found the low arch population was less dorsiflexed over the time series compared to the typically developing foot type.

For the first metatarsal the high group, the impact of anatomically relevant differences on joint kinematics could be explained by the slight medial and anterior tilt of the bone described in chapter four. For the low arch group, a lateral and posterior tilt in position and orientation could also explain the difference in kinematics at this joint. This agrees with the conjecture of a high arch feet being more naturally plantarflexed / less dorsiflexed at the head of the first metatarsal see Figure 100 A, compared to a low arch foot see Figure 100 B which describes the foot as being in a more dorsiflexed position relative to the first phalanx.

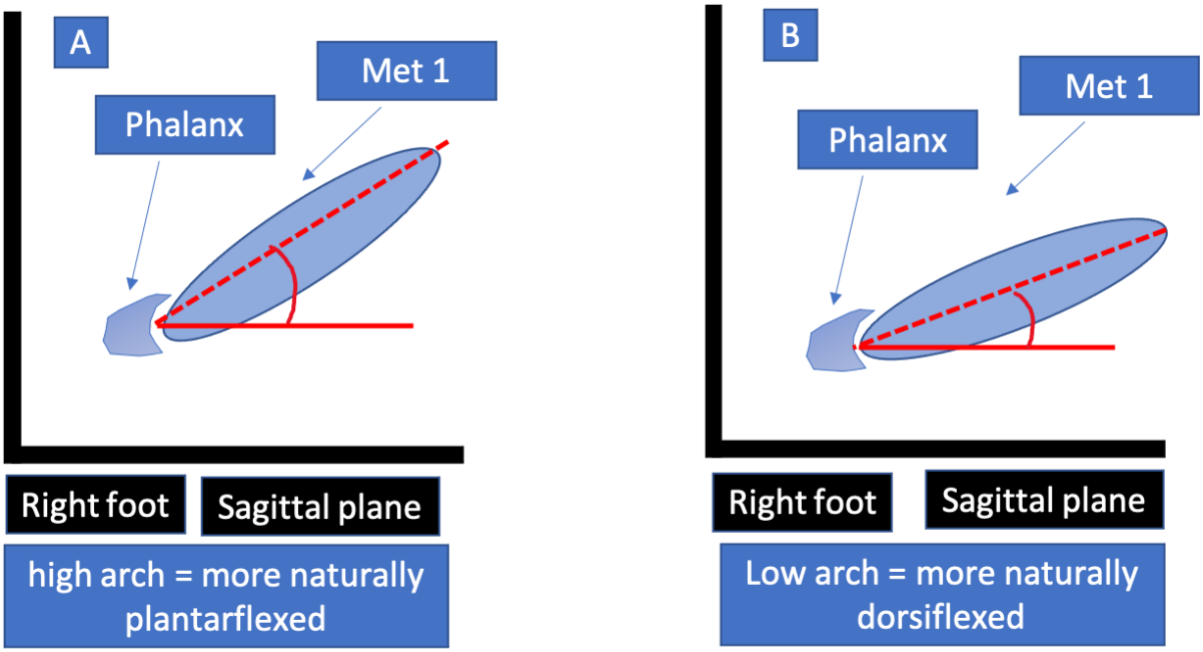

Figure 100 Showing relative differences between of the first metatarsal phalanx joint between foot types, A: Describing the high arch foot type as more naturally dorsiflexed and B: the low arch foot type as more naturally plantarflexed

6.4.7 Lesser joints of the foot

Most prominent structural variations occur in the medial ray of the foot, however other smaller joints appear to have less obvious association with arch type, this may indicate differences between foot types. As lesser joints are small the signal to noise ratio maybe lower when compared to larger joints, such as those found in the medial ray of the foot. Table 15 shows joints with potential systematic and non-systematic variation, and the plane of motion. Most of the other joints showed more noise than signal when looking to determine systematic offsets between low, normal and high arch foot types.

Table 15 Showing a summary of foot joints, not including the medial ray, that have systematic and non-systematic variation between low arch normal and high groups

Plane of motion	Systematic	Non-systematic
Sagittal plane		
	Distal phalange 2	Calcaneo-cuboid Naviculo-intermedite cuneiform Naviculo-lateral cuneiform Tarso-metatarsal 2 Tarso-metatarsal 3 Tarso-metatarsal 4 Tarso-metatarsal 5 Metatarsophalangeal 2 Metatarsophalangeal 3 Metatarsophalangeal 4 Metatarsophalangeal 5 Distal phalange 3 Distal phalange 4 Distal phalange 5
Frontal plane		
	Metatarsophalangeal 4 Metatarsophalangeal 5	Calcaneo-cuboid Metatarsophalangeal 2 Metatarsophalangeal 3

6.5 **Limitations**

Although the present study demonstrates valuable technological advances in using a statistical shape modelling bone morphing workflow with a 26-segment foot model, there are several limitations.

The foremost limitation of the results presented in this chapter include the extreme variance with respect to the inversion-eversion angles reported. The large variance seen especially in the subtalar joint is not typical of clinically reported values and the result of this is most likely due to the joint centres not being recalibrated after the scaling and morphing process has been applied to each patient model. The focus of the thesis was on the developing a pipeline that could be applied to the foot and ankle of which an MSK model was a modular component, future research could focus on developing and applying methods similar to those mentioned by Marra et al., 2015, based on work by Parra et al., 2012 calculating the axis of rotation.

The sample size was very small which severely limits statistical power and the clinical findings presented here cannot be extrapolated to wider foot populations as a much larger sample of foot types would be needed to achieve this. However, given the depth and complexity of engineering development, the sample size was appropriate for the research question of whether the model could detect differences. It was effective in applying processed MRI scans into a statistical shape model, as seen in chapter 4. The shape model generated patient specific geometry that can be integrated into the 26-segment foot model, developed in chapter 5, this demonstrates the potential of the workflow to uncover kinematic differences between low normal and high arch foot types. While the model outputs show promising results that indicate some significant differences between foot types, the evidence is not strong enough, therefore detailed model validation including, for example, biplanar fluoroscopy would be necessary. The adapted GM foot model makes several assumptions about the local movement of joints based on a healthy population as developed by Oosterwaal et al., (2011) and these assumptions might not hold true when studying pathological feet. However, the model was adapted using the same

subject specific bone morphing workflow for all participants and therefore any differences observed between groups were relative. Furthermore, the impact of soft tissue artifact was not studied in this thesis, and previous work by Oosterwaal, (2016) found the effect of marker positions ranged from 1.9 mm – 6.7 mm, with midfoot markers exhibiting more motion, but with no significant difference.

Before interpreting the kinematic measures from this analysis, it is important to note the reference frames for both kinematic measures and a ‘neutral’ position for comparative analysis between groups; this is a generally accepted challenge to overcome in foot biomechanics. This work did not apply a neutral position for comparative analysis and instead relied on reference frames, local to the bones of which were included in the joint. Due to the natural anatomical variation seen between low arch and high arch foot types, it was implied that differences seen between these groups would be related to anatomical changes in bone orientation. As each patient was assigned a group based on their clinical foot posture index score, kinematic outputs were aggregated into one of three categories, while appropriate in clinical practice, this may not be the optimum approach to classifying foot types.

6.6 **Conclusion**

This study demonstrates the applicability of a 26-segment foot model to describe biomechanics of low, normal and high arch foot types using subject specific bone morphologies derived from a statistical shape model. This was achieved by integrating the point correspondence between each of the subjects with 12 bones of the 26-segment foot model. This study also demonstrates the potential to detect and extract systematic differences between foot types of medial ray bone kinematics. The relevance of this work goes some way towards integrating disparate technologies applied to the complex foot and ankle to uncover the specific quantitative relationships that exist between foot structure and function.

In future, this research would benefit from increasing the sample size of the study participants and the study group of interest. This approach would lead to a greater understanding of the specific nuance that exists across the spectrum of foot types

and help in determining appropriate clinical treatments. An interesting yet broad approach from possible adjacent domains, such as machine learning (ML) and deep learning (DL) could provide tools to classify biomechanical parameters associated with the study groups. However, these classification techniques often require large samples to provide meaningful information. While papers that apply ML and DL techniques have benefits (Halilaj et al., 2018) reported that sample sizes among other issues are associated with the test, train and holdout sets specific to ML and DL workflows can be a limiting factor. The benefits of aggregating appropriate biomechanical data from various sources into ML models that can be tuned, known as *'transfer learning'* for a specific problem (i.e., regression, classification, association, predictive, or prescriptive analysis) is already leading to extensive clinical benefits in the field of medicine. While this is application of technology is an attractive proposal, the application of statistical based outcomes requires a range of domains to align with ethical and social considerations to safely implement these tools on a large scale. The advances made in this chapter demonstrate the sensitivity of the model developed in chapter five, using a statistical shape modelling approach to scaling and morphing bones developed in chapter four to capturing systematic differences of low, normal and high arch foot types.

Chapter 7 Overall Discussion

7.1 Introduction

The overall aim of this thesis was divided into two parts. Firstly, a statistical shape model was developed to analyse variation in bone position and shape between low, normal and high arch foot types, which was carried out to investigate the principal modes of variation in the talus, calcaneus, navicular, medial cuneiform and first metatarsal bones. Secondly, a dynamic 26-segment foot model was developed to analyse differences between foot types in a number of kinematic joints including ankle plantarflexion, subalar eversion, talonavicular dorsiflexion, talonavicular abduction, talonavicular eversion and dorsiflexion at the first metatarsophalangeal joints. The other available joints in the foot were graphically represented in appendix A and described in tabular format per foot type; low, normal and high in appendix B, but not analysed in detail. This model also used, for the first time in this type of application, a novel bone morphing technique derived from twelve statistical shape models including the calcaneus, talus, navicular, three cuneiforms, cuboid and five metatarsals, developed in chapter four.

This novel approach combined information from shape analysis from advanced imaging techniques with kinematics from a detailed multibody model. Data to answer the overall research question exploring relationships between foot posture and mechanical function was collected using MRI scans of the patient's foot, and a motion capture system described in chapter three. Initially shape characteristics were investigated in chapter four, where a statistical shape model was constructed from segmented of patients' feet which were categorised into low, normal and high foot arch, using the Foot Posture Index, a validated clinical approach. The results of the SSM studies revealed positional and morphological differences between different foot posture categories. Using the same cohort of patients, a 26-segment foot model was developed in chapter five. Kinematic outputs were derived from markers placed on the foot which determined the movement of bone segments and the data generated was used to quantify functional differences between foot types in chapter six.

Overall, this thesis demonstrates feasibility of a novel, integrated analytical pipeline to quantify positional and morphological variation with corresponding kinematic differences between flat, normal and high arch foot type. This work provides a basis for a larger sample of patients with varying foot postures to be researched in the future. This could lead to population-based generalisations to be made about systematic morphological and kinematic differences in the foot posture spectrum, with further potential for inverse dynamic analysis aimed at understanding the variance in particular muscles or joint contact forces between low, normal and high arch foot types.

Statistical analysis of shape geometry is an active area of research and a methodology used across research domains. Medical challenges can build on knowledge or software generated from similar problems, such as driverless cars, plant diseases or identification of animal species in the wild. A potential reason aforementioned domains are used to develop and prove analytical techniques, could be due to that fact these data are easier to obtain. Conversely, it is difficult to get large amounts of morphological data within the medical domain in a reasonable amount of time, due to labour involved in collecting and labelling the images sufficiently. One immediate challenge ubiquitous to medical imaging and anatomical modelling is generating a large enough sample to adequately capture population variation; consequently, the study in chapter three does not aim to generalise to low, normal or high arch foot postures, but aims to provide a pipeline which could be applied to each of these populations with substantial sample sizes. Furthermore, images generated were non-weight bearing, reflecting current radiological practice and technical limitations of MR imaging, which may influence results from positional variance in shape analysis. Although using a foot coil increases signal to the foot during MRI scanning, it also reduces the field of view, thus distal phalanges were not analysed for shape variance or used to scale the foot model for kinematic analysis. This model uses several motion markers on the foot to constrain motion of the distal segments.

In chapter six, only 13 out of 15 participants were used for kinematic analysis, with exclusion of the other two participants due to marker dropout during walking trials. To generate motion data to drive the 26-segment foot model a detailed and

complicated opto-reflective marker set-up was required, alongside the image acquisition; however, it should be noted the detailed analytical pipeline is too costly for routine clinical usage.

The scaling approach used in this thesis is particularly interesting, because it filled a gap presented in the Oosterwaal et al., (2016) study, that being the need to experiment with sensitivity of the scaling technique. To avoid skewing the variance between foot types, the kinematic model from the repository used in chapter six was compiled in an SSM, separate to the analysis undertaken in chapter four. Taking this approach made it possible to create a corresponding point map between the patients bones and the model template. The 26-segment foot model initially had issues with the repository meshes from the AMMR, as there were holes, and were of low quality. This was then rectified, by filling in the holes, to allow the SSM pipeline to integrate properly with the 26-segment foot model.

Furthermore, the 26-segment foot model from the repository was originally developed to scale based on surface points generated on the skin of the foot (Oosterwaal et al., 2016). Given this thesis research question was aimed at developing an analytical pipeline capable of capturing the relationship between low, normal and high arch foot types and foot function, the bones including talus, calcaneus, navicular, three cuneiforms, cuboid and 5 metatarsals, were scaled individually. As the process for scaling bones in the AMS relies on a point correspondence between source and target meshes with a radial basis inter/extrapolation, an investigation into the error of three approaches was carried out. In chapter five, when comparing the methods used to scale the kinematic model to a patient specific geometry, the largest error was present in the published scaling approach defined in Oosterwaal et al., (2016). The smallest error was observed in the SSM morphing method. This demonstrates the feasibility of using a SSM approach for creating patient specific foot geometries for future research associated with 26-segment GM foot model.

7.2 **Summary of findings**

7.2.1 Shape analysis

Chapter four revealed significant positional and morphological differences within the bones of the medial ray between high and low arched foot types. Differences included a slight medial and anterior positional rotation of the talus, calcaneus, navicular and medial cuneiforms, compared to the high arched foot population. In the forefoot, the low arched group's first metatarsal had positional differences resulting in a lateral and slightly posterior rotation relative to the high-arch population. Changes in morphology mapped to changes in position and orientation, but with less magnitude and more subtle differences. Overall these positional findings reflect clinical observations in shape characteristics of high (Kim, 2017; Osher and Shook, 2021) and low arch foot types (Manaster, 2016). Statistical shape modelling is a valid well established technique and has been successfully applied to the foot and ankle (Melinska et al., 2015; Melinska et al., 2017; Grant et al., 2020; Krähenbühl et al., 2020) and recently to variations in foot posture for the hind foot (Moore et al., 2019) and the metatarsals (Telfer et al., 2016). The analytical approach carried out to determine shape characteristics of low and high arch foot types in this thesis was most similar to the method detailed in Krähenbühl et al., (2020) using ShapeWorks Studio software developed at the university of Utah to create a baseline model for which pathologies could be compared.

To the authors knowledge, this is the first published SSM of the calcaneus, talus, navicular, medial cuneiform and first metatarsal bones combined to target variance between low and high arch foot types, accompanied with subsequent individual SSMs for each bone. A compelling finding, with regards to the medial ray, was the height of the medial longitudinal arch as the first principal model of variation without Procrustes analysis. A rising of the medial arch radius was closely linked to the mean high arch foot type, and a lowering of the medial arch was associated with a mean low arch foot type. Comparing morphological differences within individual bones revealed areas of morphological variation between bones from the three different groups that followed a similar variation to non-procrustean analysis, but with seemingly less magnitude.

Calcaneus

Considering the calcaneus, the positional and morphological changes associated with positional changes in medial lateral rotation and calcaneal pitch in the high arch group are an interesting finding of this thesis. Notably, they are in agreement with clinical concepts which could be due to the loading conditions on the bone in this foot type which is known to have an increased calcaneal pitch (Kim, 2017; Osher and Shook, 2021) while the opposite has been found for low arched foot types (Manaster, 2016).

Talus

The talus exhibited overall difference in the medial lateral angle of the talar dome, and the morphological redistribution of bone on the medial and lateral sides of the talar head. Moore et al., (2019) found the high-arched group to have extended lateral and medial tubercles, whereas the average shape of the high-arch talus in morphology study within this thesis had an extended medial tubercle and the lateral tubercle was extended in the average shape of the low arch foot, thus demonstrating differences in morphology between foot types. The reason for these differences may be due to loading patterns, or possibly bone remodelling following a combination of movement and loading patterns.

Navicular

The positional and morphological variance associated with mediolateral rotation with a focus on the medial aspect of the bone, was interpreted as aligning with superior inferior tilt. In the context of mean differences this shows the low arch foot group to exhibit a thickened lower medial posterior quadrant of the talar articulating surface. In addition, the navicular drop in low arch foot populations is mentioned within the literature as an anatomical feature of a low arch populations (Caravaggi et al., 2018) and could be due to the medialised talar head altering the loading of the navicular bone. The higher relative position of the navicular tuberosity in high arch feet is a well-recognised clinical feature (Kim, 2017; Osher and Shook, 2021).

Medial Cuneiform

The mediolateral and subtle anterior posterior tilt variation between high and low arch foot types showed the average low arched foot type exhibits an increase of bone on the lower left quadrant of the naviculo-medial cuneiform articulating surface

in comparison to the high arched group. These findings align conceptually with the hind and mid foot rotating medially in a low arch foot type (Manaster, 2016), and a high arch mid foot rotating laterally, with the forefoot rotating medially (Kim, 2017; Osher and Shook, 2021)

Metatarsal 1

The first two PCs showed 68.4% variance with the first PC linking to positional changes in medial lateral rotation, while the second PC was linked to the anterior-posterior tilt. In the low arched foot population, the first metatarsal bone rotates laterally and posteriorly relative to the high-arched population; this shape characteristic agrees with clinical observations. This type of rotation of the first metatarsal bone shows a decrease of the radius of the medial longitudinal arch contributing to lower arch height, this finding is in agreement with Manaster, (2016) findings for a low arch foot type. The opposite was observed for the high arch group where the first metatarsal bone rotated medially also aligning with clinical observations from (Kim, 2017; Osher and Shook, 2021)

7.2.2 Kinematic analysis

There is a relationship between bone position and shape with respect to intersegment angles between the joints of the foot. However, the exact relationship is not clear due to the small sample sizes in this thesis, and so interpretations are purely speculative. Taking the shape characteristics from the SSM and comparing to the kinematic joint profiles could indicate a relationship between structure and function and the two approaches identified some systematic trends that were consistent across the three groups for both shape and function. However, suggesting such a relationship with the data analysed in this thesis may not be appropriate based on extraneous variables omitted from the analysis, such as muscle and ligamentous tissue and lack of model validation.

Considering kinematic measures reported and analysed, SPM revealed significant differences for all joints between low and high arch foot types, the two extremes. Many kinematic foot models with clinical applications exist (Leardini et al., 2019), but relatively few have been applied to extremes of foot posture or using detailed analytical pipeline described within this thesis. Comparing the kinematic outputs of

other foot models is challenging due to the reference frames and discontinuity between methods used as described by Lenz et al., (2021). This could be a strong reason for the disparities in results amongst research in creating kinematic profile bounds for extremes of foot posture.

The approach taken in chapter five to morph foot bones in this thesis creates opportunities to individually model the impact of different treatments on biomechanical outcomes based on individual patient's bones. If more data was available, it may be possible to generalise findings to clinical strata based on foot posture. The results in chapter six demonstrate the applicability of the analytical pipeline to variations in foot posture and show statistical differences between high and flat foot types.

7.2.3 Shape and Kinematics

The common morphological variation between flat and high arch foot types indicates a general trend where the calcaneus, talus, navicular and medial cuneiform have a medial and posterior anatomical change in the low arch group relative to the high arch. In addition, the first metatarsal exhibits a lateral and anterior change. Considering the ankle, the calcaneus and talus for the average low arch foot type are 'flatter' or more anteriorly positioned relative to the talus and calcaneus for the mean high arch foot type. This is represented by the lower starting angles for ankle plantarflexion and differences in statistical parametric mapping in chapter six. In addition, the average low arch foot, specifically the calcaneus and talus sit more everted relative to the mean high arch talus and calcaneus. This is represented by increased eversion in the subtalar eversion angle, presented in chapter six, with differences observed in the statistical parametric mapping. At the talonavicular joint the average talus and navicular shape for the low arch foot had medial and posterior tilt. Appendages were observed on the navicular tuberosity and on the superior surface on of the bone relative to the high arch foot type. Kinematic angles at this joint for the mean low arch population could be related to the observed morphological difference. However, the flexibility of a flat foot type may result in different positional variance from statistical shape modeling, for example, if medical images were taken in a body weight loaded standing position as opposed to using a

foot coil within this work. Considering the first metatarsophalangeal joint, the first metatarsal in the average low arch group had a lateral and anterior tilt relative to the high arch group and the kinematics at this joint showed the low arch population to be significantly different at mid stance. This could relate to morphology changes, although soft tissues can also impact the rigidness of the foot, thus studying differences of muscle and tendon differences between these groups would be needed to draw any firmer conclusion.

7.2.4 Implications of foot shape analysis

Knowing shape characteristics of a population and predefined subsets for each of the bones that make up the medial ray would create an opportunity for researchers and clinicians to mathematically identify treatments targeted at the specific anatomical variations. Furthermore, there are more general applications in categorising a patient based on a distribution of variance, this would provide a basis to redefine, or sub-group patients based on features in latent space (similar patient bones grouped closer together) and has the potential to generate new information on anatomical features that may be unknown. This could create a comprehensive index or measure for foot types. In addition, implant manufacturers e.g., for total ankle replacement or metatarsophalangeal arthroplasty, would be interested in knowing how to design their products based on the shape of their target populations. This product design could be made specific to all bones within the foot.

7.2.5 Implications of foot kinematic modelling

The model developed in chapter five has potential to generalise kinematics of foot pathologies based on a spectrum of foot postures in great detail. With further development work and the addition of inverse dynamic simulations the impacts of interventions on joint forces and medical interventions could be investigated and optimised for each patient. In this thesis, the development of a virtual gait laboratory in the form of a scripted force plate and pressure platform could extend the usage of the model to other gait research laboratories. Sensitivity analysis in scaling the foot

model demonstrates that a SSM approach could be capable of capturing complex non-uniform shapes of foot bones and arguably has greater efficacy than current published literature on scaling the GM model.

7.3 Limitations

7.3.1 Shape analysis modelling limitations

Making direct comparisons between different statistical shape models can be challenging, primarily because there are several approaches taken to define anatomical landmarks and how these are optimised for correspondence between shapes. For example Moore et al., (2019) used landmarks, 14, 11, 14 and 9 on the calcaneus, talus, navicular and cuboid based on Bookstein's approach to anatomical landmarking, this differs from the approach taken within this thesis. This thesis used a particle entropy-based optimisation to correspond landmarks between the bone shapes. Another aspect which holds significant weight in the interpretation of the results is the method used to categorise foot type prior to shape analysis. The process for labelling foot types was pre-determined by clinical observation in the study by Moore et al, contrastingly this thesis took the Foot Posture Index and divided the foot types into 3 discrete subgroups. A standardised method to accurately label a foot, flat, normal or high does not currently exist due to the complexity in the foot's architecture, however clinically useful indices, such as the FPI are suitable for the type of application described here. The FPI is applicable as it has statistically derived definitions of foot types with normative values which are routinely used in clinical practice.

The image acquisition process is time-consuming and requires the patient to be still for a prolonged period, which is not always possible and can lead to unwanted artifacts potentially rendering an image obsolete. As the foot is a flexible structure the use of an 8-channel foot coil enhanced the signal to the extremity and mitigated artifacts; however, using a coil reduces the field of view. While omitting the most distal parts of the foot reduces the amount of information, this was not the

hypothesised area of greatest difference between low and high arch foot types, therefore does not impact the aims of the thesis.

It is well established that MRI scans provide rich information about the local anatomy, however extracting information from an MRI through segmentation requires more advanced algorithmic approaches compared to CT scans where a thresholding approach is usually sufficient to segment bone. Segmenting foot and ankle MRI scans based on an active contour approach using the robust statistical segmentation (RSS) algorithm developed by Gao et al., (2012) within 3D Slicer, performed adequately well in the current study, with the addition of manual tuning to the masks, an expected scenario in biomedical image segmentation tasks.

The input to the statistical shape modelling process in this thesis requires pre-processing MRI images of bones including the talus, calcaneus, navicular, three cuneiforms, cuboid and 5 metatarsals. Although only the talus, calcaneus, navicular, medial cuneiform and first metatarsal were compared for shape analysis, as they make up the medial ray. The additional bones were used to create the patient specific foot kinematic model. Generating enough data to use a SSM with the patient specific foot model required 12 bones from 15 patients totalling 180 separate segmentations taking approximately 3-5 hours per patient, with a partially automated approach. This time-consuming process demonstrates need for releasing or sharing statistical shape models within the research community to accelerate segmentation for similar bones. Such precedents have been set with recent deep learning frame works and neural networks by releasing the neural network pretrained weights into a ‘model zoo’ which is an online area that curates pretrained model weights for deep learning models for a variety of uses. From the model zoo another deep learning practitioner can use the algorithm for closely related tasks. The biomedical imaging community has not seen pretrained weights released as often as general image segmentation tasks, such as identification of objects for self-driving cars; however architectures that allow the development of models and their weights to be calculated, such as a UNET (Ronneberger et al., 2015) are available to researchers. Although neural network architectures are available for research, they are not useful without sufficient data and as previously mentioned this is a challenge often seen in medical imaging projects. Steps have been made towards sharing and releasing

data, binary segmentations or STL files used to create shape models using repositories like Zendo or DOI's.

Statistical shape models reconstruct the binary segmentations into smoothed, mathematical representations, and validating these representations is an important part of the process to determine an aspect of quality. Efforts have been made in this thesis to quantify the error between patient segmentations and generated patient bone shapes from the SSM. Having a clear understanding of this error is also important for downstream applications of the SSM, in particular in chapter six where the spawned outputs from the SSM were used to morph a template 26-segment foot mode to a patients' geometry.

Initial registration in the SSM process involved initially aligning the images based on their centre of mass and a feature-based alignment process based on vertices using the Iterative Closest Point (ICP) of the meshes. Following this process, particles on the surface of each of the shapes were optimised using an entropy-based cost function with Procrustes alignment to normalize the shapes for size, determining any variation related to morphology.

7.3.2 Kinematic foot modelling limitations

The foot model developed in this thesis used commercial software, limiting the userbase to institutions with resources to spend, and also reducing ease at which the community can contribute to model development.

Recent foot and ankle kinematics applied to extremes of foot posture; including planus, planovalgus, cavus, have been derived from several foot models in the literature (Saraswat et al., 2014; Buldt et al., 2015; Caravaggi et al., 2018; Kruger et al., 2019) each varying in complexity in the number of segments and particular populations. Pathological foot types vary from typical feet in terms of their structure and kinematics; therefore, care must be taken when applying models which are developed using 'normal' populations. Nevertheless, models such as the one developed in chapter five, facilitate systematic patient specific modelling. Through mesh morphing they provide reasonable grounds for exploration and application to pathological foot types and could provide adequate mathematical approximations of pathologies given an adequate sample size. The kinematics were generated using

‘healthy’ motion rhythms which were not adapted from the AMMR GM foot model. Given the ambiguity in agreed motion characteristics in the foot, knowing how to meaningfully alter these rhythms is challenging and a limitation of this work.

The main points to consider in the interpretation of kinematic findings are primarily concerned with the difference in definitions of joint axes for comparison among studies. In a systematic review of local coordinate systems to calculate ankle kinematics, Lenz et al., (2021) highlights how advances in bi-planar fluoroscopy provide a means for evaluating the motion of particular joints *in vivo*. This provides a validation benchmark for which multi-segment models can be evaluated against for derived kinematic motions. However, this type of validation for each patient means the model would be individually and statically valid. This static validity does not take into consideration the dynamic alterations and changes that occur to a patient or population over time. The statistical shape modelling pipeline in chapter four could be used to create a reference, by which longitudinal observations of shape changes could be captured and manifestation of pathologies studied. It could also facilitate the level of detail needed to generate a referencing system.

7.4 Future research

7.4.1 Future research for shape analysis

Although work in this thesis shows that shape and positional characteristics between low and high arch foot types exist, future research could be carried out to explore further the findings in this thesis with larger sample sizes per group.

Generating discrete categories underpinned by valid clinical measures such as the Foot Posture Index does not fully capture the minutiae associated with individual bone anatomy. Therefore, applying PCA to bones to determine where similarities or differences exist between patients’, could lead to the development of new information in the form of clustering of anatomical features and broader set of categories beyond the current clinical reasoning. For example, planus, planovalgus, cavus, cavovarus are categories, or subcategories similar, but with subtly different

anatomical variations. By following this approach, entire foot pathologies, including those associated with neurological conditions, or subtle anatomical nuance with diabetic feet for example could be mapped in latent space, which could be useful in the identification of similar anatomical representations within the data.

In addition, more than bone shape can be represented in a statistical shape model, for example within the MSK model the generation of patient specific models uses a RBF to morph the bone geometries and associated muscle origin and insertion points which error associated with this process has been studied (Pellikaan et al., 2014). Statistical shape models and specifically the point distribution models could assign point correspondence between the muscle tracking of the MSK model and the patients models which could further reduce the error associated with muscle attachment site and improve the accuracy of the modelling process.

For such latent spaces to be representative, there is a reliance on accurately extracting the area of interest from the image through segmentation. Manual segmentation is a time consuming, but a necessary process to generate masks for shape analysis and is the first step in generating automatic, or semi-automatic approach to segmenting an image. Efforts from the deep learning community have been made to develop methods to auto-segment images, however typically these need large class sample sizes in order of 1000’s and at present the sample size suggested is not fulfilled. The number of samples can be reduced when using models with pretrained weights i.e., a model trained on a different, but similar task, however there are few of these available for the medical images community. During any automation of medical segmentation, post-hoc tuning with a ‘human in the loop’ is required to ensure the region is correctly segmented. Data augmentation for medical imaging is an active area of research. A focus on general adversarial networks (GAN’s) as a mechanism to generate data from a small sample size could provide a means for population analysis. This is however subject to the initial samples containing the variance required for the task. Further efforts could focus specifically on the image voxels and masks created by segmenting the medical images (Yi et al., 2019). The premise here would be to generate more instances of the plausible bone shapes resulting in a more generalisable SSM such as has been demonstrated by Adams et al., (2020)

7.4.2 Future research for kinematic analysis

Although work in this thesis shows the applicability of the 26-segment foot model applied to low, normal and high arch foot types, future work should consider larger sample sizes per group. Kinematic rhythms used in the model could be adapted to account for a typical pathological movement as opposed to the ‘healthy’ kinematic rhythms used in the repository model.

The numerous approaches to co-ordinate system definition reviewed by Lenz et al., (2021) suggests that a single universal co-ordinate system should be agreed upon among researchers. Given the ambiguity surrounding the ‘true’ movement of individual bones in the foot created by individual differences, the most enticing point of reference would be a mathematical representation of an individual’s bones or set of bones at any given point in time. A dynamic, shape-based co-ordinate system mapping to the patients’ bones, potentially makes more intuitive sense over palpable bony prominences on the skin surface, as it captures unique attributes of a patient’s pathology or typically functioning foot.

One approach to asserting goodness of fit of a kinematic model would be the use of biplanar fluoroscopy to capture the motion of bones (Iaquinto et al., 2014), as opposed to the motion of bones derived from skin-markers, which are known to be subject to skin-motion artefact (Maslen and Ackland, 1994). Once links between kinematics of a model are validated with fluoroscopy, further work could investigate muscle and ligament forces and their subtle differences between foot pathologies, creating a mathematical test bed for simulating treatments on patients while optimising for ‘more appropriate’ biomechanics.

7.5 Conclusion

In conclusion, this thesis presents the application of a novel analytical pipeline to a real-world clinical challenge of linking bone shape and foot function using a statistical shape model and a 26-segment patient specific foot model.

Advances made in shape analysis of low, normal and high arch foot types include:

- Application of a semi-automatic segmentation algorithm of 12 bones from 15 MRI scans summing to 180 separate segmentations of bones in low, normal and high arch foot types.
- Development of a multi-domain statistical shape model including the calcaneus, talus, navicular, medial cuneiform and first metatarsal consisting of 15 patients 5 low, 5 normal and 5 high arch foot types.
- Generation of 5 individual bone statistical shape models including, calcaneus, talus, navicular, medial cuneiform and first metatarsal applied to 15 patients 5 low, 5 normal and 5 high arch foot types.
- Generation of 12 individual bone statistical shape models including calcaneus, talus, cuboid, navicular, three cuneiforms and five metatarsals, used to generate patient specific foot geometry, enabling kinematic analysis of patients of three subgroups low, normal and high arch types.
- Identifying shape differences associated with orientation and position between low, normal and high arch foot types.
- Identifying shape differences associated with morphology between low, normal and high arch foot types
- Development of model that facilitates linkage of shape and function that could be used to identify new latent space features in foot bone shapes and multi-domain SSM's.

Advances made in kinematic modeling of low, normal and high arch foot types include:

- Developing a 26-segment foot model to work with a new laboratory including the deployment of a virtual force plate using and AMTI device and pressure platform using Emed that could be used to run inverse dynamic models Opening the research potential to other institutions and creating a basis for further work on analysis of interventions
- Implementing a non-linear bone scaling and morphing approach using 12 separate SSM's including the calcaneus, talus, cuboid, navicular, three

cuneiforms and five metatarsals of 15 patients ranging from low to high arch foot types and

- Performing sensitivity tests with a previous foot surface scaling approach, showing that a SSM approach results in less error than other approaches.

Advances made in this thesis demonstrate a modelling workflow capable of capturing anatomical and pathological shape features associated in latent space, providing a potentially interesting advancement to the concept of ‘flat’ or ‘high’ as a paradigm. New anatomical features of similar representations based on individual bone shape (position and morphology) could be identified if the method was applied to a larger cohort of foot bones from various pathologies. Vector deformations could also be modelled, i.e., the change in shape between the metatarsals of a diabetic foot and paediatric low-arched foot type, creating linkages between different, but related phenomena, adding information to the lineage of a particular pathology and predicting potential future pathologies. Incorporating shape representation through the SSM models into a pipeline that can be used to scale a generic dynamic patient foot model, opens possibilities to identifying relationships between the shape representations and their associated movement patterns. Developing a 26-segment foot model that could be used to run inverse dynamic models, opens the research potential of this model to other institutions. For example, clinical and research gait laboratories and commercial footwear companies. Implementing a non-linear bone scaling and morphing approach using a SSM of 15 patients, ranging from low to high arch foot types and performing sensitivity tests with a previous foot surface scaling approach, demonstrates the benefits of extra computational resources. This would a more efficient approach for future research in the domain of dynamic MSK foot and ankle research.

Bibliography

Adams, J., Bhalodia, R. and Elhabian, S. 2020. Uncertain-DeepSSM: From Images to Probabilistic Shape Models. *Lecture Notes in Computer Science (including subseries Lecture Notes in Artificial Intelligence and Lecture Notes in Bioinformatics)*. **12474 LNCS**, pp.57–72.

Al-Munajjed, A.A., Bischoff, J.E., Dharia, M.A., Telfer, S., Woodburn, J. and Carbes, S. 2016. Metatarsal Loading During Gait—A Musculoskeletal Analysis. *Journal of Biomechanical Engineering*. **138**(3), p.034503.

Aminian, A. and Sangeorzan, B.J. 2008. The Anatomy of Cavus Foot Deformity. *Foot and Ankle Clinics*. **13**(2), pp.191–198.

Andersen, M.S., Damsgaard, M. and Rasmussen, J. 2009. Kinematic analysis of over-determinate biomechanical systems. *Computer Methods in Biomechanics and Biomedical Engineering*. **12**(4), pp.371–384.

Apkarian, J., Naumann, S. and Cairns, B. 1989. A three-dimensional kinematic and dynamic model of the lower limb. *Journal of Biomechanics*. **22**(2), pp.143–155.

Arndt, A., Wolf, P., Liu, A., Nester, C., Stacoff, A., Jones, R., Lundgren, P. and Lundberg, A. 2007. Intrinsic foot kinematics measured in vivo during the stance phase of slow running. *Journal of biomechanics*. **40**(12), pp.2672–8.

Barnes, A., Wheat, J. and Milner, C. 2008. Association between foot type and tibial stress injuries: A systematic review. *British Journal of Sports Medicine*. **42**(2), pp.93–98.

Bischoff, J.E., Dai, Y., Goodlett, C., Davis, B. and Bandi, M. 2014. Incorporating Population-Level Variability in Orthopedic Biomechanical Analysis: A Review. *Journal of Biomechanical Engineering*. **136**(2), p.021004.

Blana, D., Hincapie, J.G., Chadwick, E.K. and Kirsch, R.F. 2008. A musculoskeletal model of the upper extremity for use in the development of neuroprosthetic systems. *Journal of Biomechanics*. **41**(8), pp.1714–1721.

Bowes, M. a, Vincent, G.R., Wolstenholme, C.B. and Conaghan, P.G. 2015. A novel method for bone area measurement provides new insights into osteoarthritis

and its progression. *Annals of the rheumatic diseases*. **74**(3), pp.519–25.

Buhmann, M.D. (Martin D. and Buhmann, M.D. 2003. *Radial basis functions : theory and implementations* [Online]. Cambridge University Press. [Accessed 1 June 2017]. Available from: http://dl.acm.org/citation.cfm?id=945834.

Buldt, A.K., Forghany, S., Landorf, K.B., Levinger, P., Murley, G.S. and Menz, H.B. 2018. Foot posture is associated with plantar pressure during gait: A comparison of normal, planus and cavus feet. *Gait & Posture*. **62**, pp.235–240.

Buldt, A.K., Levinger, P., Murley, G.S., Menz, H.B., Nester, C.J. and Landorf, K.B. 2015. Foot posture is associated with kinematics of the foot during gait: A comparison of normal, planus and cavus feet. *Gait and Posture*. **42**(1), pp.42–48.

Buldt, A.K., Murley, G.S., Butterworth, P., Levinger, P., Menz, H.B. and Landorf, K.B. 2013. The relationship between foot posture and lower limb kinematics during walking: A systematic review. *Gait & Posture*. **38**(3), pp.363–372.

Burns, J., Crosbie, J., Hunt, A. and Ouvrier, R. 2005. The effect of pes cavus on foot pain and plantar pressure. *Clinical Biomechanics*. **20**(9), pp.877–882.

Burns, J., Keenan, A.M. and Redmond, A. 2005. Foot type and overuse injury in triathletes. *Journal of the American Podiatric Medical Association*. **95**(3), pp.235–241.

Burns, J., Redmond, A., Ouvrier, R. and Crosbie, J. 2005. Quantification of muscle strength and imbalance in neurogenic pes cavus, compared to health controls, using hand-held dynamometry. *Foot & ankle international*. **26**(7), pp.540–4.

Cappozzo, A., Catani, F., Croce, U. Della and Leardini, A. 1995. Position and orientation in space of bones during movement: anatomical frame definition and determination. *Clinical biomechanics (Bristol, Avon)*. **10**(4), pp.171–178.

Caravaggi, P., Sforza, C., Leardini, A., Portinaro, N. and Panou, A. 2018. Effect of plano-valgus foot posture on midfoot kinematics during barefoot walking in an adolescent population. *Journal of Foot and Ankle Research*. **11**(1), p.55.

Carbes, S., Tørholm, S., Telfer, S., Woodburn, J., Oosterwaal, M. and Rasmussen,

J. 2011. A new multisegmental foot model and marker protocol for accurate simulation of the foot biomechanics during walking. *Proceedings of ISB 2011 Congress XXIII*., pp.1–2.

Carbone, V., Fluit, R., Pellikaan, P., van der Krogt, M.M., Janssen, D., Damsgaard, M., Vigneron, L., Feilkas, T., Koopman, H.F.J.M. and Verdonschot, N. 2015. TLEM 2.0 – A comprehensive musculoskeletal geometry dataset for subject-specific modeling of lower extremity. *Journal of Biomechanics*. **48**(5), pp.734–741.

Carson, M.C., Harrington, M.E., Thompson, N., O'Connor, J.J. and Theologis, T.N. 2001. Kinematic analysis of a multi-segment foot model for research and clinical applications: a repeatability analysis. *Journal of Biomechanics*. **34**(10), pp.1299–1307.

Cates, J., Elhabian, S. and Whitaker, R. 2017. ShapeWorks: Particle-Based Shape Correspondence and Visualization Software *In*: *Statistical Shape and Deformation Analysis: Methods, Implementation and Applications*. Elsevier Inc., pp.257–298.

Cates, J., Fletcher, P.T., Styner, M., Shenton, M. and Whitaker, R. 2007. Shape modeling and analysis with entropy-based particle systems. *Information processing in medical imaging : proceedings of the ... conference*. **20**, pp.333–45.

Chao, E.Y.S., Armiger, R.S., Yoshida, H., Lim, J. and Haraguchi, N. 2007. Virtual Interactive Musculoskeletal System (VIMS) in orthopaedic research, education and clinical patient care. *Journal of orthopaedic surgery and research*. **2**, p.2.

Chen, Z., Zhang, Z., Wang, L., Li, D., Zhang, Y. and Jin, Z. 2016. Evaluation of a subject-specific musculoskeletal modelling framework for load prediction in total knee arthroplasty. *Medical Engineering & Physics*. **38**(8), pp.708–716.

Chilvers, M. and Manoli, A. 2008. The Subtle Cavus Foot and Association with Ankle Instability and Lateral Foot Overload. *Foot and Ankle Clinics*. **13**(2), pp.315–324.

Cobb, S.C., Tis, L.L., Johnson, J.T., Wang, Y.T., Geil, M.D. and McCarty, F.A. 2009. The effect of low-mobile foot posture on multi-segment medial foot model gait

kinematics. *Gait and Posture*. **30**(3), pp.334–339.

Cootes, T.F., Taylor, C.J., Cooper, D.H. and Graham, J. 1995. Active Shape Models-Their Training and Application. *Computer Vision and Image Understanding*. **61**(1), pp.38–59.

Damsgaard, M., Rasmussen, J., Christensen, S.T., Surma, E. and de Zee, M. 2006. Analysis of musculoskeletal systems in the AnyBody Modeling System. *Simulation Modelling Practice and Theory*. **14**(8), pp.1100–1111.

Dryden, L. and Mardia, K. V. 1998. Statistical Shape Analysis *In*: *John Wiley & Son*. John Wiley & Sons, p.347.

Dube, B., Bowes, M.A., Barr, A.J., Hensor, E.M., Kingsbury, S.R. and Conaghan, P.G. 2018. The relationship between two different measures of osteoarthritis bone pathology, bone marrow lesions and 3D bone shape: data from the osteoarthritis initiative. *Osteoarthritis and Cartilage*. **26**, p.S444.

Dyal, C.M., Feder, J., Deland, J.T. and Thompson, F.M. 1997. Pes planus in patients with posterior tibial tendon insufficiency: asymptomatic versus symptomatic foot. *Foot & ankle international*. **18**(2), pp.85–8.

Fang, L., Jia, X. and Wang, R. 2007. Modeling and simulation of muscle forces of trans-tibial amputee to study effect of prosthetic alignment. *Clinical Biomechanics*. **22**(10), pp.1125–1131.

Franco, a H. 1987. Pes cavus and pes planus. Analyses and treatment. *Physical therapy*. **67**(5), pp.688–694.

Gao, Y., Kikinis, R., Bouix, S., Shenton, M. and Tannenbaum, A. 2012. A 3D interactive multi-object segmentation tool using local robust statistics driven active contours. *Medical Image Analysis*. **16**(6), pp.1216–1227.

van de Giessen, M., Foumani, M., Streekstra, G.J., Strackee, S.D., Maas, M., van Vliet, L.J., Grimbergen, K.A. and Vos, F.M. 2010. Statistical descriptions of scaphoid and lunate bone shapes. *Journal of Biomechanics*. **43**(8), pp.1463–1469.

Goodall, C. 1991. Procrustes Methods in the Statistical Analysis of Shape. *Journal of*

the Royal Statistical Society. Series B (Methodological). **53**(2), pp.285–339.

Grant, T.M., Diamond, L.E., Pizzolato, C., Killen, B.A., Devaprakash, D., Kelly, L., Maharaj, J.N. and Saxby, D.J. 2020. Development and validation of statistical shape models of the primary functional bone segments of the foot. *PeerJ*. **2020**(2), p.e8397.

Gray, H. 1918. Gray, Henry. 1918. Anatomy of the Human Body. *Anatomy of the Human Body*. [Online]. Available from: http://bartleby.com/107/.

Groves, D. 2015. Groves, Dawn (2015) Geometric Variances in Hip Osteoarthritis and Tribology of the Natural Hip. PhD thesis, University of Leeds - Google Search.

Halilaj, E., Rajagopal, A., Fiterau, M., Hicks, J.L., Hastie, T.J. and Delp, S.L. 2018. Machine learning in human movement biomechanics: Best practices, common pitfalls, and new opportunities. *Journal of Biomechanics*. **81**, pp.1–11.

Hawes, M.R., Nachbauer, W., Sovak, D. and Nigg, B.M. 1992. Footprint parameters as a measure of arch height. *Foot & ankle*. **13**(1), pp.22–6.

Heimann, T. and Meinzer, H.-P. 2009. Statistical shape models for 3D medical image segmentation: a review. *Medical image analysis*. **13**(4), pp.543–63.

Hicks, J.H. 1954. The mechanics of the foot: II. The plantar aponeurosis and the arch. *Journal of Anatomy*. **88**(Pt 1), p.25.

Hillstrom, H.J., Song, J., Kraszewski, A.P., Hafer, J.F., Mootanah, R., Dufour, A.B., Chow, B.S. and Deland, J.T. 2013. Foot type biomechanics part 1: Structure and function of the asymptomatic foot. *Gait & Posture*. **37**(3), pp.445–451.

Van Houcke, J., Schouten, A., Steenackers, G., Vandermeulen, D., Pattyn, C. and Audenaert, E.A. 2017. Computer-based estimation of the hip joint reaction force and hip flexion angle in three different sitting configurations. *Applied Ergonomics*. **63**, pp.99–105.

Hughes, P., Miranda, R. and Doyle, A.J. 2019. MRI imaging of soft tissue tumours of the foot and ankle. *Insights into Imaging*. **10**(1).

Hunt, A.E., M. Smith, R., Torode, M. and Keenan, A.M. 2001. Inter-segment foot

motion and ground reaction forces over the stance phase of walking. *Clinical Biomechanics*. **16**(7), pp.592–600.

Hunt, A.E. and Smith, R.M. 2004. Mechanics and control of the flat versus normal foot during the stance phase of walking. *Clinical Biomechanics*. **19**(4), pp.391–397.

Hunt, A.E., Smith, R.M. and Torode, M. 2001. Extrinsic muscle activity, foot motion and ankle joint moments during the stance phase of walking. *Foot & ankle international / American Orthopaedic Foot and Ankle Society [and] Swiss Foot and Ankle Society*. **22**(1), pp.31–41.

Iaquinto, J.M., Tsai, R., Haynor, D.R., Fassbind, M.J., Sangeorzan, B.J. and Ledoux, W.R. 2014. Marker-based validation of a biplane fluoroscopy system for quantifying foot kinematics. *Medical Engineering and Physics*. **36**(3), pp.391–396.

Jarvis, H.L., Nester, C.J., Bowden, P.D. and Jones, R.K. 2017. Challenging the foundations of the clinical model of foot function: Further evidence that the root model assessments fail to appropriately classify foot function. *Journal of Foot and Ankle Research*. **10**(1), p.7.

Jung, M. 2014. *Comparison of mid foot forces between flatfoot and metatarsalgia patients using the Glasgow-Maastricht AnyBody foot model Wearable sensors for assessment of function: Development, validation & application of wearable sensors View project KNEEMO, an In* [Online]. [Accessed 25 October 2018]. Available from: https://www.researchgate.net/publication/263441353.

Kadaba, M.P., Ramakrishnan, H.K. and Wootten, M.E. 1990. Measurement of lower extremity kinematics during level walking. *Journal of Orthopaedic Research*. **8**(3), pp.383–392.

Kaufman, K.R., Brodine, S.K., Shaffer, R.A., Johnson, C.W. and Cullison, T.R. 1999. The effect of foot structure and range of motion on musculoskeletal overuse injuries. *American Journal of Sports Medicine*. **27**(5), pp.585–593.

Kidder, S.M., Abuzzahab, F.S., Harris, G.F. and Johnson, J.E. 1996. A system for the analysis of foot and ankle kinematics during gait. *IEEE transactions on*

rehabilitation engineering : a publication of the IEEE Engineering in Medicine and Biology Society. **4**(1), pp.25–32.

Kikinis, R., Pieper, S.D. and Vosburgh, K.G. 2014. 3D Slicer: A Platform for Subject-Specific Image Analysis, Visualization, and Clinical Support *In*: *Intraoperative Imaging and Image-Guided Therapy* [Online]. New York, NY: Springer New York, pp.277–289. [Accessed 18 April 2018]. Available from: http://link.springer.com/10.1007/978-1-4614-7657-3_19.

Kim, B.S. 2017. Reconstruction of Cavus Foot: A Review. *The open orthopaedics journal*. **11**, pp.651–659.

Kohls-Gatzoulis, J., Angel, J.C., Singh, D., Haddad, F., Livingstone, J. and Berry, G. 2004. Tibialis posterior dysfunction: a common and treatable cause of adult acquired flatfoot. *BMJ (Clinical research ed.)*. **329**(7478), pp.1328–33.

Krähenbühl, N., Lenz, A.L., Lisonbee, R.J., Peterson, A.C., Atkins, P.R., Hintermann, B., Saltzman, C.L., Anderson, A.E. and Barg, A. 2020. Morphologic analysis of the subtalar joint using statistical shape modeling. *Journal of Orthopaedic Research*. **38**(12), pp.2625–2633.

Kruger, K.M., Graf, A., Flanagan, A., McHenry, B.D., Altiok, H., Smith, P.A., Harris, G.F. and Krzak, J.J. 2019. Segmental foot and ankle kinematic differences between rectus, planus, and cavus foot types. *Journal of Biomechanics*. **94**, pp.180–186.

Landorf, K., Keenan, A.M. and Louise Rushworth, R. 2001. Foot orthosis prescription habits of Australian and New Zealand podiatric physicians. *Journal of the American Podiatric Medical Association*. **91**(4), pp.174–183.

Leardini, A., Belvedere, C., Nardini, F., Sancisi, N., Conconi, M. and Parenti-Castelli, V. 2017. Kinematic models of lower limb joints for musculo-skeletal modelling and optimization in gait analysis. *Journal of Biomechanics*. **62**, pp.77–86.

Leardini, A., Benedetti, M.G., Berti, L., Bettinelli, D., Nativo, R. and Giannini, S. 2007. Rear-foot, mid-foot and fore-foot motion during the stance phase of gait. *Gait & Posture*. **25**(3), pp.453–462.

Leardini, A., Benedetti, M.G., Catani, F., Simoncini, L. and Giannini, S. 1999. An

anatomically based protocol for the description of foot segment kinematics during gait. *Clinical Biomechanics*. **14**(8), pp.528–536.

Leardini, A., Caravaggi, P., Theologis, T. and Stebbins, J. 2019. Multi-segment foot models and their use in clinical populations. *Gait and Posture*. **69**, pp.50–59.

Leardini, A., Chiari, A., Della Croce, U. and Cappozzo, A. 2005. Human movement analysis using stereophotogrammetry: Part 3. Soft tissue artifact assessment and compensation. *Gait & Posture*. **21**(2), pp.212–225.

Ledoux, W.R., Shofer, J.B., Ahroni, J.H., Smith, D.G., Sangeorzan, B.J. and Boyko, E.J. 2003. Biomechanical Differences among Pes Cavus, Neutrally Aligned, and Pes Planus Feet in Subjects with Diabetes. *Foot and Ankle International*. **24**(11), pp.845–850.

Lenz, A.L., Strobel, M.A., Anderson, A.M., Fial, A. V., MacWilliams, B.A., Krzak, J.J. and Kruger, K.M. 2021. Assignment of local coordinate systems and methods to calculate tibiotalar and subtalar kinematics: A systematic review. *Journal of Biomechanics*. **120**, p.110344.

Levinger, P., Murley, G.S., Barton, C.J., Cotchett, M.P., McSweeney, S.R. and Menz, H.B. 2010. A comparison of foot kinematics in people with normal- and flat-arched feet using the Oxford Foot Model. *Gait and Posture*. **32**(4), pp.519–523.

Lindner, C., Thiagarajah, S., Wilkinson, J.M., Wallis, G.A. and Cootes, T.F. 2013. Development of a fully automatic shape model matching (FASMM) system to derive statistical shape models from radiographs: application to the accurate capture and global representation of proximal femur shape. *Osteoarthritis and Cartilage*. **21**(10), pp.1537–1544.

Liu, W., Siegler, S., Hillstrom, H. and Whitney, K. 1997. Three-dimensional, six-degrees-of-freedom kinematics of the human hindfoot during the stance phase of level walking. *Human Movement Science*. **16**(2), pp.283–298.

Lobmann, R., Kayser, R., Kasten, G., Kasten, U., Kluge, K., Neumann, W. and Lehnert, H. 2001. Effects of preventative footwear on foot pressure as determined by pedobarography in diabetic patients: A prospective study.

Diabetic Medicine. **18**(4), pp.314–319.

Lu, Y.C. and Untaroiu, C.D. 2013. Statistical shape analysis of clavicular cortical bone with applications to the development of mean and boundary shape models. *Computer Methods and Programs in Biomedicine*. **111**(3), pp.613–628.

Lundgren, P., Nester, C., Liu, A., Arndt, A., Jones, R., Stacoff, A., Wolf, P. and Lundberg, A. 2008. Invasive in vivo measurement of rear-, mid- and forefoot motion during walking. *Gait & Posture*. **28**(1), pp.93–100.

Lynch, J.A., Parimi, N., Chaganti, R.K., Nevitt, M.C. and Lane, N.E. 2009. The association of proximal femoral shape and incident radiographic hip OA in elderly women. *Osteoarthritis and Cartilage*. **17**(10), pp.1313–1318.

MacWilliams, B.A., Cowley, M. and Nicholson, D.E. 2003. Foot kinematics and kinetics during adolescent gait. *Gait and Posture*. **17**(3), pp.214–224.

Mahfouz, M., Abdel Fatah, E.E., Bowers, L.S. and Scuderi, G. 2012. Three-dimensional Morphology of the Knee Reveals Ethnic Differences. *Clinical Orthopaedics and Related Research®*. **470**(1), pp.172–185.

Manaster, B.J. 2016. Pes Planus (Flatfoot) *In*: *Diagnostic Imaging: Musculoskeletal Non-Traumatic Disease*. Elsevier, pp.738–743.

Manders, C., New, A. and Rasmussen, J. 2008. VALIDATION OF MUSCULOSKELETAL GAIT SIMULATION FOR USE IN INVESTIGATION OF TOTAL HIP REPLACEMENT. *Journal of Biomechanics*. **41**, p.S488.

Marra, M.A., Vanheule, V., Fluit, R., Koopman, B.H.F.J.M., Rasmussen, J., Verdonschot, N. and Andersen, M.S. 2015. A Subject-Specific Musculoskeletal Modeling Framework to Predict In Vivo Mechanics of Total Knee Arthroplasty. *Journal of Biomechanical Engineering*. **137**(2), p.020904.

Maslen, B.A. and Ackland, T.R. 1994. Radiographic study of skin displacement errors in the foot and ankle during standing. *Clinical Biomechanics*. **9**(5), pp.291–296.

Mayich, D.J., Novak, A., Vena, D., Daniels, T.R. and Brodsky, J.W. 2014. Gait analysis in orthopedic foot and ankle surgery--topical review, part 1: principles

and uses of gait analysis. *Foot Ankle Int*. **35**(1), pp.80–90.

McCarthy, E., Morrison, W.B. and Zoga, A.C. 2017. MR Imaging of the Diabetic Foot. *Magnetic Resonance Imaging Clinics of North America*. **25**(1), pp.183–194.

McGinley, J.L., Baker, R., Wolfe, R. and Morris, M.E. 2009. The reliability of three-dimensional kinematic gait measurements: A systematic review. *Gait & Posture*. **29**(3), pp.360–369.

Mei, Z., Ivanov, K., Zhao, G., Wu, Y., Liu, M. and Wang, L. 2020. Foot type classification using sensor-enabled footwear and 1D-CNN. *Measurement*. **165**, p.108184.

Melinska, A.U., Romaszkiewicz, P., Wagel, J., Antosik, B., Sasiadek, M. and Iskander, D.R. 2017. Statistical shape models of cuboid, navicular and talus bones. *Journal of Foot and Ankle Research*. **10**(1), p.6.

Melinska, A.U., Romaszkiewicz, P., Wagel, J., Sasiadek, M. and Iskander, D.R. 2015. Statistical, Morphometric, Anatomical Shape Model (Atlas) of Calcaneus H. He, ed. *PLOS ONE*. **10**(8), p.e0134603.

Menz, H.B. 1995. Clinical hindfoot measurement: a critical review of the literature. *The Foot*. **5**(2), pp.57–64.

Menz, H.B., Dufour, A.B., Riskowski, J.L., Hillstrom, H.J. and Hannan, M.T. 2013. Association of planus foot posture and pronated foot function with foot pain: The Framingham foot study. *Arthritis Care and Research*. **65**(12), pp.1991–1999.

De Mits, S., Segers, V., Woodburn, J., Elewaut, D., De Clercq, D. and Roosen, P. 2012. A clinically applicable six-segmented foot model. *Journal of Orthopaedic Research*. **30**(4), pp.655–661.

Moore, E.S., Kindig, M.W., McKearney, D.A., Telfer, S., Sangeorzan, B.J. and Ledoux, W.R. 2019. Hind- and midfoot bone morphology varies with foot type and sex. *Journal of Orthopaedic Research*. **37**(3), pp.744–759.

Mortimer, J.A., Bouchard, M., Acosta, A. and Mosca, V. 2020. The Biplanar Effect of the Medial Cuneiform Osteotomy. *Foot and Ankle Specialist*. **13**(3), pp.250–257.

Neogi, T., Bowes, M.A., Niu, J., De Souza, K.M., Vincent, G.R., Goggins, J., Zhang, Y. and Felson, D.T. 2013. Magnetic resonance imaging-based three-dimensional bone shape of the knee predicts onset of knee osteoarthritis: Data from the osteoarthritis initiative. *Arthritis and Rheumatism*. **65**(8), pp.2048–2058.

Nester, C.J., Liu, A.M., Ward, E., Howard, D., Cocheba, J., Derrick, T. and Patterson, P. 2007. In vitro study of foot kinematics using a dynamic walking cadaver model. *Journal of Biomechanics*. **40**(9), pp.1927–1937.

Nigg, B.M., Fisher, V., Allinger, T.L., Ronsky, J.R. and Engsberg, J.R. 1992. Range of Motion of the Foot as a Function of Age. *Foot & Ankle International*. **13**(6), pp.336–343.

Nolte, D., Tsang, C.K., Zhang, K.Y., Ding, Z., Kedgley, A.E. and Bull, A.M.J. 2016. Non-linear scaling of a musculoskeletal model of the lower limb using statistical shape models. *Journal of Biomechanics*. **49**(14), pp.3576–3581.

Novak, A.C., Mayich, D.J., Perry, S.D., Daniels, T.R. and Brodsky, J.W. 2014. Gait Analysis for Foot and Ankle Surgeons-- Topical Review, Part 2: Approaches to Multisegment Modeling of the Foot. *Foot & Ankle International*. **35**(2), pp.178–191.

Oliveira, F.P.M.M. and Tavares, J.M.R.S.S. 2014. Medical image registration: a review. *Computer methods in biomechanics and biomedical engineering*. **17**(2), pp.73–93.

Oosterwaal, M. 2016. *The Glasgow-Maastricht Foot Model Development, repeatability and sources of error of a 26 segment multi-body foot model* [Online]. [Accessed 26 May 2021]. Available from: https://cris.maastrichtuniversity.nl/en/publications/the-glasgow-maastricht-foot-model-development-repeatability-and-s.

Oosterwaal, M., Carbes, S., Telfer, S., Woodburn, J., Tørholm, S., Al-Munajjed, A.A., van Rhijn, L. and Meijer, K. 2016. The Glasgow-Maastricht foot model, evaluation of a 26 segment kinematic model of the foot. *Journal of foot and ankle research*. **9**, p.19.

Oosterwaal, M., Telfer, S., Tørholm, S., Carbes, S., van Rhijn, L.W., Macduff, R.,

Meijer, K. and Woodburn, J. 2011. Generation of subject-specific, dynamic, multisegment ankle and foot models to improve orthotic design: a feasibility study. *BMC musculoskeletal disorders*. **12**(1), p.256.

Osher, L. and Shook, J.E. 2021. Imaging of the Pes Cavus Deformity. *Clinics in Podiatric Medicine and Surgery*. **38**(3), pp.303–321.

P. Cignoni, M. Callieri, M. Corsini, M. Dellepiane, F. Ganovelli, G.R. 2008. MeshLab. *MeshLab: an Open-Source Mesh Processing Tool*., pp.129–136.

Parra, W.C.H., Chatterjee, H.J. and Soligo, C. 2012. Calculating the axes of rotation for the subtalar and talocrural joints using 3D bone reconstructions. *Journal of Biomechanics*. **45**(6), pp.1103–1107.

Pataky, T.C. 2012. One-dimensional statistical parametric mapping in Python. *Computer Methods in Biomechanics and Biomedical Engineering*. **15**(3), pp.295–301.

Pataky, T.C., Robinson, M.A. and Vanrenterghem, J. 2013. Vector field statistical analysis of kinematic and force trajectories. *Journal of Biomechanics*. **46**(14), pp.2394–2401.

Pataky, T.C., Vanrenterghem, J. and Robinson, M.A. 2015. Zero- vs. one-dimensional, parametric vs. non-parametric, and confidence interval vs. hypothesis testing procedures in one-dimensional biomechanical trajectory analysis. *Journal of Biomechanics*. **48**(7), pp.1277–1285.

Pedoia, V., Lansdown, D.A., Zaid, M., McCulloch, C.E., Souza, R., Ma, C.B. and Li, X. 2015. Three-dimensional MRI-based statistical shape model and application to a cohort of knees with acute ACL injury. *Osteoarthritis and Cartilage*. **23**(10), pp.1695–1703.

Pellikaan, P., van der Krogt, M.M., Carbone, V., Fluit, R., Vigneron, L.M., Van Deun, J., Verdonschot, N. and Koopman, H.F.J.M. 2014. Evaluation of a morphing based method to estimate muscle attachment sites of the lower extremity. *Journal of Biomechanics*. **47**(5), pp.1144–1150.

Rankine, L., Long, J., Canseco, K. and Harris, G.F. 2008. Multisegmental foot modeling: a review. *Critical reviews in biomedical engineering*. **36**(2–3), pp.127–

81.

Rattanaprasert, U., Smith, R., Sullivan, M. and Gilleard, W. 1999. Three-dimensional kinematics of the forefoot, rearfoot, and leg without the function of tibialis posterior in comparison with normals during stance phase of walking. *Clinical Biomechanics*. **14**(1), pp.14–23.

Razeghi, M. and Batt, M.E. 2002. Foot type classification: a critical review of current methods. *Gait & Posture*. **15**(3), pp.282–291.

Redmond, A.C. 2005. THE FOOT POSTURE INDEX Easy quantification of standing foot posture Six item version FPI-6 USER GUIDE AND MANUAL Foot Posture Index -User guide and manual.

Redmond, A.C., Crane, Y.Z. and Menz, H.B. 2008. Normative values for the Foot Posture Index. *Journal of foot and ankle research*. **1**(1), p.6.

Renkawitz, T., Weber, T., Dullien, S., Woerner, M., Dendorfer, S., Grifka, J. and Weber, M. 2016. Leg length and offset differences above 5mm after total hip arthroplasty are associated with altered gait kinematics. *Gait & Posture*. **49**, pp.196–201.

Ring, J., Davies, H.G., Chadwick, C., Blundell, C.M. and Davies, M.B. 2019. Trauma to the medial ray of the foot: A classification of patterns of injury and their management. *Injury*. **50**(8), pp.1483–1488.

Ronneberger, O., Fischer, P. and Brox, T. 2015. U-Net: Convolutional Networks for Biomedical Image Segmentation. *Lecture Notes in Computer Science (including subseries Lecture Notes in Artificial Intelligence and Lecture Notes in Bioinformatics)*. **9351**, pp.234–241.

Saltzman, C.L. and Nawoczenski, D.A. 1995. Complexities of Foot Architecture as a Base of Support. *Journal of Orthopaedic & Sports Physical Therapy*. **21**(6), pp.354–360.

Sangeorzan, B.J., Mosca, V. and Hansen, S.T. 1993. Effect of calcaneal lengthening on relationships among the hindfoot, midfoot, and forefoot. *Foot and Ankle*. **14**(3), pp.136–141.

Saraswat, P., Andersen, M.S. and MacWilliams, B.A. 2010. A musculoskeletal foot model for clinical gait analysis. *Journal of Biomechanics*. **43**(9), pp.1645–1652.

Saraswat, P., MacWilliams, B.A. and Davis, R.B. 2012. A multi-segment foot model based on anatomically registered technical coordinate systems: method repeatability in pediatric feet. *Gait & posture*. **35**(4), pp.547–55.

Saraswat, P., MacWilliams, B.A., Davis, R.B. and D'Astous, J.L. 2013. A multi-segment foot model based on anatomically registered technical coordinate systems: method repeatability and sensitivity in pediatric planovalgus feet. *Gait & posture*. **37**(1), pp.121–5.

Saraswat, P., MacWilliams, B.A., Davis, R.B., D'Astous, J.L. and D'Astous, J.L. 2014. Kinematics and kinetics of normal and planovalgus feet during walking. *Gait & posture*. **39**(1), pp.339–45.

Schallig, W., Streekstra, G.J., Hulshof, C.M., Kleipool, R.P., Dobbe, J.G.G., Maas, M., Harlaar, J., van der Krogt, M.M. and van den Noort, J.C. 2021. The influence of soft tissue artifacts on multi-segment foot kinematics. *Journal of Biomechanics*. **120**, p.110359.

Schuberth, J.M. and Babu-Spencer, N. 2009. The Impact of the First Ray in the Cavovarus Foot. *Clinics in Podiatric Medicine and Surgery*. **26**(3), pp.385–393.

Seth, A., Sherman, M., Reinbolt, J.A. and Delp, S.L. 2011. OpenSim: A musculoskeletal modeling and simulation framework for in silico investigations and exchange *In*: *Procedia IUTAM*. Elsevier B.V., pp.212–232.

Sharma, U.K., Dhungel, K., Pokhrel, D., Tamang, S. and Parajuli, N.P. 2018. Magnetic Resonance Imaging Evaluation of Musculoskeletal Diseases of Ankle and Foot. *Kathmandu University medical journal (KUMJ)*. **16**(61), pp.28–34.

Shibuya, N., Jupiter, D.C., Ciliberti, L.J., VanBuren, V. and La Fontaine, J. 2010. Characteristics of Adult Flatfoot in the United States. *The Journal of Foot and Ankle Surgery*. **49**(4), pp.363–368.

Shultz, R., Kedgley, A.E. and Jenkyn, T.R. 2011. Quantifying skin motion artifact error of the hindfoot and forefoot marker clusters with the optical tracking of a multi-segment foot model using single-plane fluoroscopy. *Gait and Posture*.

34(1), pp.44–48.

Simkin, A., Leichter, I., Giladi, M., Stein, M. and Milgrom, C. 1989. Combined Effect of Foot Arch Structure and an Orthotic Device on Stress Fractures. *Foot & Ankle International*. **10**(1), pp.25–29.

Simon, J., Doederlein, L., McIntosh, A.S., Metaxiotis, D., Bock, H.G. and Wolf, S.I. 2006. The Heidelberg foot measurement method: Development, description and assessment. *Gait & Posture*. **23**(4), pp.411–424.

Sonka, M., Hlavac, V. and Boyle, R. 1993a. Image understanding *In*: *Image Processing, Analysis and Machine Vision* [Online]. Boston, MA: Springer US, pp.316–372. [Accessed 10 February 2017]. Available from: http://link.springer.com/10.1007/978-1-4899-3216-7_8.

Sonka, M., Hlavac, V. and Boyle, R. 1993b. Segmentation *In*: *Image Processing, Analysis and Machine Vision* [Online]. Boston, MA: Springer US, pp.112–191. [Accessed 10 February 2017]. Available from: http://link.springer.com/10.1007/978-1-4899-3216-7_5.

Sonka, M., Hlavac, V. and Boyle, R. 1993c. Texture *In*: *Image Processing, Analysis and Machine Vision* [Online]. Boston, MA: Springer US, pp.477–506. [Accessed 10 February 2017]. Available from: http://link.springer.com/10.1007/978-1-4899-3216-7_13.

Telfer, S., Kindig, M.W., Sangeorzan, B.J. and Ledoux, W.R. 2016. Metatarsal shape and foot type: a geometric morphometric analysis. *Journal of Biomechanical Engineering*.

Tørholm, S., Carbes, S., Rasmussen, J. and Al-Munajjed, A.A. 2013. The Glasgow-Maastricht AnyBody Foot Model to predict internal loads in the foot 1 *In*: *Combined Orthopedic Research Societies 2013* [Online]. [Accessed 20 April 2016]. Available from: https://www.researchgate.net/publication/263441453_The_Glasgow-Maastricht_AnyBody_Foot_Model_to_predict_internal_loads_in_the_foot_1.

Vincent, G., Wolstenholme, C., Scott, I. and Bowes, M. 2010. Fully Automatic Segmentation of the Knee Joint using Active Appearance Models. *Medical*

Image Analysis for the Clinic: A Grand Challenge., pp.224–230.

Waarsing, J.H., Rozendaal, R.M., Verhaar, J.A.N., Bierma-Zeinstra, S.M.A. and Weinans, H. 2010. A statistical model of shape and density of the proximal femur in relation to radiological and clinical OA of the hip. *Osteoarthritis and Cartilage*. **18**(6), pp.787–794.

Wang, C., Wang, H., Cao, S., Wang, S., Ma, X., Wang, X., Huang, J., Zhang, C., Chen, L., Geng, X. and Wang, K. 2019. Pathological kinematic patterns of the tarsal complex in stage II adult-acquired flatfoot deformity. *Journal of Orthopaedic Research*. **37**(2), pp.477–482.

Westblad, P., Hashimoto, T., Winson, I., Lundberg, A. and Arndt, A. 2002. Differences in ankle-joint complex motion during the stance phase of walking as measured by superficial and bone-anchored markers. *Foot & ankle international*. **23**(9), pp.856–63.

Winfeld, M.J. and Winfeld, B.E. 2019. Management of pediatric foot deformities: an imaging review. *Pediatric Radiology*. **49**(12), pp.1678–1690.

Wolf, P., Stacoff, A., Liu, A., Nester, C., Arndt, A., Lundberg, A. and Stuessi, E. 2008. Functional units of the human foot. *Gait & Posture*. **28**(3), pp.434–441.

Wu, G., Siegler, S., Allard, P., Kirtley, C., Leardini, A., Rosenbaum, D., Whittle, M., D'Lima, D.D., Cristofolini, L., Witte, H., Schmid, O. and Stokes, I. 2002. ISB recommendation on definitions of joint coordinate system of various joints for the reporting of human joint motion—part I: ankle, hip, and spine. *Journal of Biomechanics*. **35**(4), pp.543–548.

Yi, X., Walia, E. and Babyn, P. 2019. Generative adversarial network in medical imaging: A review. *Medical Image Analysis*. **58**.

Younger, A.S.E. and Hansen, S.T. 2005. Adult cavovarus foot. *The Journal of the American Academy of Orthopaedic Surgeons*. **13**(5), pp.302–15.

Zheng, G. 2010. Statistical shape model-based reconstruction of a scaled, patient-specific surface model of the pelvis from a single standard AP x-ray radiograph. *Medical Physics*. **37**(4), pp.1424–1439.

Appendix A

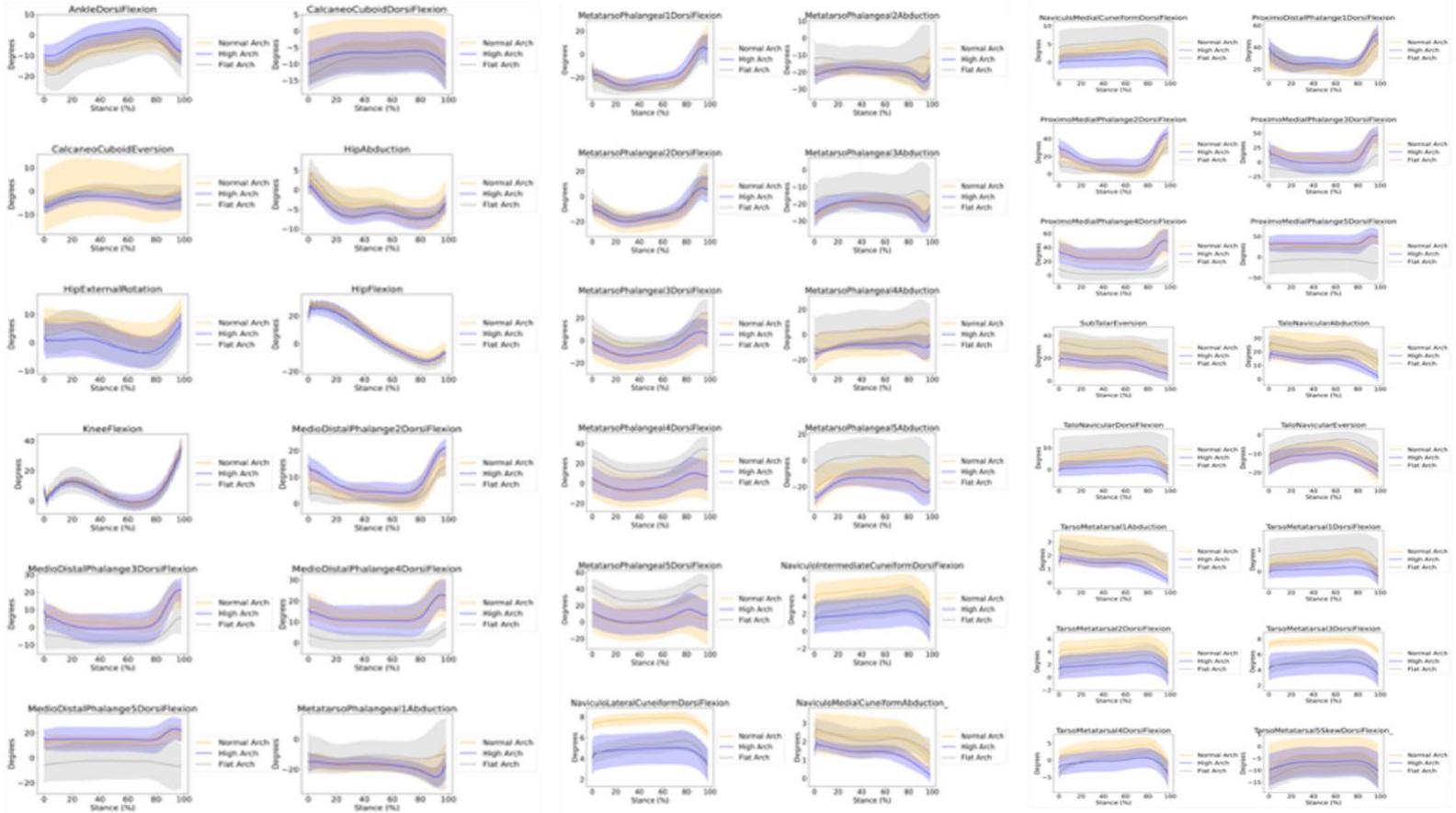
AnkleDorsiFlexion
CalcaneoCuboidDorsiFlexion
CalcaneoCuboidEversion
HipAbduction
HipExternalRotation
HipFlexion
KneeFlexion
MedioDistalPhalange2DorsiFlexion
MedioDistalPhalange3DorsiFlexion
MedioDistalPhalange4DorsiFlexion
MedioDistalPhalange5DorsiFlexion
MetatarsoPhalangeal1Abduction
MetatarsoPhalangeal1DorsiFlexion
MetatarsoPhalangeal2Abduction
MetatarsoPhalangeal2DorsiFlexion
MetatarsoPhalangeal3Abduction
MetatarsoPhalangeal3DorsiFlexion
MetatarsoPhalangeal4Abduction
MetatarsoPhalangeal4DorsiFlexion
MetatarsoPhalangeal5Abduction
MetatarsoPhalangeal5DorsiFlexion
NaviculoIntermediateCuneiformDorsiFlexion
NaviculoLateralCuneiformDorsiFlexion
NaviculoMedialCuneiformAbduction
NaviculoMedialCuneiformDorsiFlexion
ProximoDistalPhalange1DorsiFlexion
ProximoMedialPhalange2DorsiFlexion
ProximoMedialPhalange3DorsiFlexion
ProximoMedialPhalange4DorsiFlexion
ProximoMedialPhalange5DorsiFlexion
SubTalarEversion
TaloNavicularAbduction
TaloNavicularDorsiFlexion
TaloNavicularEversion
TarsoMetatarsal1Abduction
TarsoMetatarsal1DorsiFlexion
TarsoMetatarsal2DorsiFlexion
TarsoMetatarsal3DorsiFlexion
TarsoMetatarsal4DorsiFlexion
TarsoMetatarsal5SkewDorsiFlexion
Normal Arch
High Arch
Flat Arch
Degrees
Stance (%)

Appendix B

	POPULATION				High				Normal				Flat			
	MEAN ROM	S.D	MAX ROM	MIN ROM	MEAN ROM	S.D	MAX ROM	MIN ROM	MEAN ROM	S.D	MAX ROM	MIN ROM	MEAN ROM	S.D	MAX ROM	MIN ROM
Ankle Dorsiflexion	15.53	2.81	19.57	8.53	15.60	1.06	17.18	13.86	14.19	3.51	18.09	8.53	16.79	2.92	19.57	11.96
Calcaneocuboid Dorsiflexion	5.95	2.24	9.79	1.75	5.47	2.08	9.00	2.75	4.59	1.75	6.48	1.75	7.92	1.34	9.79	6.02
Calcaneocuboid Eversion	7.46	2.06	11.26	3.91	6.79	1.40	8.42	4.58	7.07	0.79	8.42	6.44	8.70	2.90	11.26	3.91
Hip Abduction	10.70	2.46	15.68	8.22	9.70	1.11	11.58	8.63	9.66	1.68	12.43	8.22	12.99	2.79	15.68	8.62
Hip External Rotation	11.49	2.83	17.69	8.14	11.33	3.33	17.69	8.52	11.01	2.62	15.21	8.14	12.16	2.17	14.64	8.68
Hip Flexion	40.00	4.87	48.39	33.75	37.71	3.93	45.13	33.75	39.31	4.94	47.47	34.18	43.56	3.70	48.39	38.39
Knee Flexion	38.59	2.67	43.27	34.72	38.40	3.42	43.27	34.72	39.13	1.77	42.19	37.96	38.29	2.24	40.75	35.69
MedioDistalPhalange 2 Dorsiflexion	16.90	3.10	21.71	10.75	18.46	2.53	21.71	14.19	16.15	1.65	18.59	14.59	15.69	3.92	20.06	10.75
MedioDistalPhalange 3 Dorsiflexion	21.00	4.65	30.03	12.64	24.68	4.09	30.03	18.24	19.45	2.39	22.77	16.03	17.96	3.87	23.22	12.64

MedioDistalPhalange 4 Dorsiflexion	12.89	4.25	20.80	4.99	14.65	3.56	20.80	10.82	12.36	3.47	15.08	6.44	11.22	4.90	17.53	4.99
MedioDistalPhalange 5 Dorsiflexion	11.34	3.03	16.41	6.64	12.70	2.19	16.41	10.73	10.86	2.75	14.34	6.64	10.11	3.50	15.98	7.08
Metatarsophalangeal 1 Abduction	14.08	5.60	27.72	5.70	13.13	3.05	16.73	8.28	11.98	3.53	15.92	8.01	17.36	7.86	27.72	5.70
Metatarsophalangeal 1 Dorsiflexion	39.87	8.74	52.51	27.00	36.89	7.92	51.27	27.00	44.14	3.81	50.04	40.69	39.33	11.21	52.51	27.58
Metatarsophalangeal 2 Abduction	12.75	4.63	21.48	4.23	11.69	2.60	13.77	6.62	11.51	2.94	15.65	8.05	15.30	6.58	21.48	4.23
Metatarsophalangeal 2 Dorsiflexion	32.73	7.73	45.15	21.91	30.40	7.26	43.18	22.87	33.92	2.61	36.96	29.80	34.45	10.51	45.15	21.91
Metatarsophalangeal 3 Abduction	14.32	3.42	20.01	8.19	15.27	3.64	20.01	9.12	14.31	0.15	14.54	14.12	13.15	4.35	18.50	8.19
Metatarsophalangeal 3 Dorsiflexion	26.50	8.11	42.74	14.88	24.85	7.31	35.65	14.88	24.20	3.35	29.30	19.91	30.86	10.39	42.74	15.66
Metatarsophalangeal 4 Abduction	13.92	3.63	19.44	7.64	14.28	2.35	18.36	11.68	15.47	3.95	19.44	9.01	11.93	3.71	17.57	7.64

Metatarsophalangeal 4 Dorsiflexion	22.36	8.68	40.44	12.96	21.87	6.63	30.57	12.96	16.69	4.41	24.25	13.53	28.64	9.93	40.44	13.06
Metatarsophalangeal 5 Abduction	16.91	5.53	26.84	7.75	20.68	5.22	26.84	13.12	16.25	4.59	22.97	10.42	12.87	3.12	16.14	7.75
Metatarsophalangeal 5 Dorsiflexion	23.08	6.70	38.30	15.48	22.31	5.49	28.82	15.48	18.49	1.45	20.01	16.18	28.63	7.31	38.30	17.87
NaviculoIntermediateCuneiform Dorsiflexion	2.80	1.30	5.30	1.38	2.08	0.58	3.14	1.51	2.79	1.03	4.43	1.57	3.70	1.59	5.30	1.38
NaviculoLateralCuneiform Dorsiflexion	2.30	1.28	5.78	0.92	1.91	0.65	3.18	1.44	1.72	0.54	2.45	0.92	3.39	1.67	5.78	1.13
NaviculoMedialCuneiform Abduction	1.60	0.45	2.29	0.66	1.82	0.32	2.29	1.33	1.42	0.50	1.96	0.66	1.51	0.43	2.21	1.05
NaviculoMedialCuneiform Dorsiflexion	4.85	2.58	10.19	1.00	3.39	1.54	5.44	1.00	6.62	1.78	9.25	4.92	4.92	3.10	10.19	2.45
ProximoDistalPhalange 1 Dorsiflexion	27.07	7.42	39.33	15.71	30.86	5.83	38.13	26.01	26.80	8.39	39.33	17.61	22.62	5.31	30.64	15.71
ProximoMedialPhalange 2 Dorsiflexion	37.18	6.81	47.77	23.66	40.62	5.56	47.77	31.21	35.53	3.62	40.91	32.09	34.53	8.63	44.13	23.66

ProximoMedialPhalange 3 Dorsiflexion	46.20	10.22	66.07	27.81	54.31	8.99	66.07	40.13	42.78	5.26	50.10	35.27	39.50	8.51	51.08	27.81
ProximoMedialPhalange 4 Dorsiflexion	28.35	9.36	45.76	10.97	32.22	7.83	45.76	23.80	27.20	7.64	33.17	14.16	24.68	10.78	38.56	10.97
ProximoMedialPhalange 5 Dorsiflexion	24.95	6.67	36.10	14.60	27.95	4.82	36.10	23.61	23.89	6.05	31.54	14.60	22.25	7.71	35.16	15.57
SubTalar Eversion	13.51	4.00	19.98	5.57	14.57	2.96	19.98	11.00	12.35	4.99	19.21	5.57	13.36	3.66	18.06	8.60
Talonavicular Abduction	16.00	4.53	22.94	6.57	18.21	3.22	22.94	13.34	14.18	4.96	19.56	6.57	15.05	4.34	22.13	10.53
Talonavicular Dorsiflexion	8.09	4.29	16.98	1.66	5.65	2.57	9.06	1.66	11.04	2.97	15.42	8.20	8.19	5.16	16.98	4.08
Talonavicular Eversion	11.53	4.73	20.68	5.17	10.80	2.36	13.78	6.52	11.84	5.24	20.68	7.35	12.13	6.09	20.21	5.17
TarsoMetatarsal 1 Abduction	1.60	0.45	2.29	0.66	1.82	0.32	2.29	1.33	1.42	0.50	1.96	0.66	1.51	0.43	2.21	1.05
TarsoMetatarsal 1 Dorsiflexion	0.81	0.43	1.70	0.17	0.57	0.26	0.91	0.17	1.10	0.30	1.54	0.82	0.82	0.52	1.70	0.41
TarsoMetatarsal 2 Dorsiflexion	2.80	1.30	5.30	1.38	2.08	0.58	3.14	1.51	2.79	1.03	4.43	1.57	3.70	1.59	5.30	1.38
TarsoMetatarsal 3 Dorsiflexion	2.30	1.28	5.78	0.92	1.91	0.65	3.18	1.44	1.72	0.54	2.45	0.92	3.39	1.67	5.78	1.13
TarsoMetatarsal 4 Dorsiflexion	6.98	2.84	13.10	1.78	5.37	1.99	7.40	1.78	7.09	1.61	8.70	4.86	8.87	3.44	13.10	4.35
TarsoMetatarsal 5 Skew Dorsiflexion	5.95	2.24	9.79	1.75	5.47	2.08	9.00	2.75	4.59	1.75	6.48	1.75	7.92	1.34	9.79	6.02